ISSN 1451 - 9372(Print)
ISSN 2217 - 7434(Online)
APRIL-JUNE 2021
Vol.27, Number 2, 107-206

Chemical Industry & Chemical Engineering Quarterly

Belgrade SERBIA AChE

The AChE Journal for Chemical Engineering, Biochemical Engineering, Chemical Technology, New Materials, Renewable Energy and Chemistry

www.ache.org.rs/ciceq

Journal of the
Association of Chemical Engineers of
Serbia, Belgrade, Serbia

Chemical Industry & Chemical Engineering Quarterly

CI&CEQuarterly

EDITOR-In-Chief

Vlada B. Veljković
Faculty of Technology, University of Niš, Leskovac, Serbia
E-mail: veljkovicvb@yahoo.com

ASSOCIATE EDITORS

Jonjaua Ranogajec
Faculty of Technology, University of Novi Sad, Novi Sad, Serbia

Srđan Pejanović
Department of Chemical Engineering, Faculty of Technology and Metallurgy, University of Belgrade, Belgrade, Serbia

Milan Jakšić
ICEHT/FORTH, University of Patras, Patras, Greece

EDITORIAL BOARD (Serbia)

Đorđe Janaćković, Sanja Podunavac-Kuzmanović, Viktor Nedović, Sandra Konstantinović, Ivanka Popović
Siniša Dodić, Zoran Todorović, Olivera Stamenković, Marija Tasić, Jelena Avramović, Goran Nikolić, Dunja Sokolović

ADVISORY BOARD (International)

Dragomir Bukur
Texas A&M University, College Station, TX, USA

Milorad Dudukovic
Washington University, St. Luis, MO, USA

Jiri Hanika
Institute of Chemical Process Fundamentals, Academy of Sciences of the Czech Republic, Prague, Czech Republic

Maria Jose Cocero
University of Valladolid, Valladolid, Spain

Tajalli Keshavarz
University of Westminster, London, UK

Zeljko Knez
University of Maribor, Maribor, Slovenia

Igor Lacik
Polymer Institute of the Slovak Academy of Sciences, Bratislava, Slovakia

Denis Poncelet
ENITIAA, Nantes, France

Ljubisa Radovic
Pen State University, PA, USA

Peter Raspor
University of Ljubljana, Ljubljana, Slovenia

Constantinos Vayenas
University of Patras, Patras, Greece

Xenophon Verykios
University of Patras, Patras, Greece

Ronnie Willaert
Vrije Universiteit, Brussel, Belgium

Gordana Vunjak Novakovic
Columbia University, New York, USA

Dimitrios P. Tassios
National Technical University of Athens, Athens, Greece

Hui Liu
China University of Geosciences, Wuhan, China

FORMER EDITOR (2005-2007)

Professor Dejan Skala
University of Belgrade, Faculty of Technology and Metallurgy, Belgrade, Serbia

Journal of the
Association of Chemical Engineers of
Serbia, Belgrade, Serbia

Chemical Industry & Chemical Engineering Quarterly

Vol. 27 | Belgrade, April-June 2021 | No. 2

Chemical Industry & Chemical Engineering Quarterly (ISSN 1451-9372) is published quarterly by the Association of Chemical Engineers of Serbia, Kneza Miloša 9/I, 11000 Belgrade, Serbia

Editor:
Vlada B. Veljković
veljkovic@yahoo.com

Editorial Office:
Kneza Miloša 9/I, 11000 Belgrade, Serbia
Phone/Fax: +381 (0)11 3240 018
E-mail: shi@yubc.net
www.ache.org.rs

For publisher:
Ivana T. Drvenica

Secretary of the Editorial Office:
Slavica Desnica

Marketing and advertising:
AChE Marketing Office
Kneza Miloša 9/I, 11000 Belgrade, Serbia
Phone/Fax: +381 (0)11 3240 018

Publication of this Journal is supported by the Ministry of Education, Science and Technological Development of the Republic of Serbia

Subscription and advertisements make payable to the account of the Association of Chemical Engineers of Serbia, Belgrade, No. 205-2172-71, Komercijalna banka a.d., Beograd

Computer typeface and paging:
Vladimir Panić

Printed by:
Faculty of Technology and Metallurgy, Research and Development Centre of Printing Technology, Karnegijeva 4, P.O. Box 3503, 11120 Belgrade, Serbia

Abstracting/Indexing:
Articles published in this Journal are indexed in *Thompson Reuters* products: *Science Citation Index - Expanded*™ - access *via Web of Science*®, part of *ISI Web of Knowledge*℠

CONTENTS

Activities of the Association of Chemical Engineers of Serbia are supported by:

- Ministry of Education, Science and Technological Development, Republic of Serbia
- Hemofarm Koncern AD, Vršac, Serbia
- Faculty of Technology and Metallurgy, University of Belgrade, Belgrade, Serbia
- Faculty of Technology, University of Novi Sad, Novi Sad, Serbia
- Faculty of Technology, University of Niš, Leskovac, Serbia
- Institute of Chemistry, Technology and Metallurgy, University of Belgrade, Belgrade, Serbia

CI&CEQ
Chemical Industry & Chemical Engineering Quarterly

Available on line at
Association of the Chemical Engineers of Serbia *AChE*
www.ache.org.rs/CICEQ

Chem. Ind. Chem. Eng. Q. 27 (2) 107–112 (2021) CI&CEQ

N. DEEPA PRIYA[1]
K. SARAVANAN[2]

[1]Department of Chemical Engineering, Sri Venkateswara College of Engineering, Sriperumbudur, India
[2]Department of Chemical Engineering, Kongu Engineering College, Perundurai, India

SCIENTIFIC PAPER

UDC 66.096.5:544

HYDRODYNAMIC STUDIES IN TWO-PHASE STIRRED FLUIDIZED BED WITH THREE TYPES OF IMPELLERS

Article Highlights

- Stirring the bed provides the required energy to breakdown interparticle bonds
- Stirring enhances the performance of fluidization and reduces the minimum fluidization velocity
- Using three types of impellers provides efficient mixing
- Pressure drop and power increase with increase in gas velocity and stirrer speed
- Fluidization performance is enhanced in the stirred bed

Abstract

Fluidized beds are extensively used in petrochemical, chemical process industries, pharmaceutical, food and biotechnology industries. They are preferred to process materials with a wide range of particle size distribution and offer even temperature distribution and excellent heat and mass transfer. To improve the quality of the fluidized bed, mechanical stirring can be employed along with aeration. Hence, an attempt was made to study the hydrodynamics of stirred fluidized bed using air-water system. The characteristics of the fluidized bed can be well understood by studying its hydrodynamics. Pressure drop is one of the vital factors which affect the performance of fluidized bed. Hence, the effects of gas velocity and stirrer speed on pressure drop and power were studied for both stirred and unstirred bed conditions. It was observed that pressure drop and power increases with increase in gas velocity and stirrer speed. Also, the pressure drop and power are lower for the stirred bed condition than the unstirred bed condition.

Keywords: hydrodynamics, stirred fluidized bed, stirrer speed, gas velocity, two-phase system.

In the fluidized bed, excellent fluidization quality is necessary for gas-solid contact, heat and mass transfer. But often it is very difficult to maintain fluidization due to particle agglomeration [1]. Though aeration of the bed gives better fluidization, too much aeration leads to slugging and bubble formation. So, mechanical stirring can be employed along with aeration in fluidized beds for improving fluidization performance. Particle size distribution plays a major role in easiness on which the particle gets fluidized and withstand fluidization. Generally, fine particles agglomerate and defluidize the bed [2]. So, a mechanical stirrer [3] can be employed and the bed can be operated at higher gas velocities to eradicate agglomeration.

Mechanical agitation enhances the performance of fluidized bed with respect to gas-solid contact in heat transfer, catalytic reaction, homogeneous mixing of powders [4]. Stirred fluidized bed is an excellent device for solids blending (Leve 1960). Stirring decreases porosity and minimum fluidization velocity, controls sticking of particles and overheating in case of sticky materials [5]. Various efforts were made to alter the particle and bubble behaviour by external means inside a fluidized bed. Acoustic fields are used to improve the fluidization quality of cohesive powders [6]. Also, ferromagnetic particles are exposed to magnetic fields and they alter the way the bed fluidizes, extending the bubble free operation in fluidization

Correspondence: N. Deepa Priya, Department of Chemical Engineering, Sri Venkateswara College of Engineering, Sriperumbudur - 602117, India.
E-mail: dppriya1984@gmail.com
Paper received: 5 March, 2020
Paper revised: 22 July, 2020
Paper accepted: 30 July, 2020

https://doi.org/10.2298/CICEQ200305029D

state [7]. Agitated fluidized bed dryer is used to dry oil palm frond particles [8]. Inter-bond properties of fibre prevent flow of air within the bed and agitation of the bed results in reducing the bond, thereby the state of fluidization is attained [9]. Furthermore, using special methods like gas injection also improves the fluidization quality. Use of a rotary distributor can improve solids mixing and bubble distribution in fluidized bed [10]. The use of a distributor reduces bubble channelling and stimulated particle radial dispersion in the fluidized bed. Fluidization of nanoparticles can be significantly improved by both vibration and stirring [11]. Addition of a stirring device into the fluidized bed reduces the dead zone of gas-solids fluidized beds [12]. The particle mixing and fluidization quality can also be improved by inclined injection of the fluidizing air [13].

Stirred fluidized beds find application in the recovery of lysozyme from chicken egg white [14,15], operations related with particle separation [16], etc. The application of fluidized beds can be extended to wet and sticky materials and drying of granular materials [17] by introducing vibration in the fluidized bed. Some applications of agitated beds are fluidization of bentonite particles [18] and phosphor particles [19], drying of apple pulp [20] and pharmaceutical products [21].

Due to extreme agglomeration and channelling, the improvement in fluidization requires a design that should be capable to offer high levels of energy in the entire bed volume. Hence, mechanical stirring is employed to overcome the difficulties in a conventional fluidized bed. Stirring the bed offers the required energy to break the interparticle bonds, eradicate channelling and reduces agglomeration. Very few studies have been reported on hydrodynamics in a stirred fluidized bed. Therefore, the present study deals with the hydrodynamic studies in a stirred fluidized bed with three types of impellers using air-water system. The three types of impellers used are pitched blade upflow, pitched blade downflow and Rushton turbine. The effects of gas velocity and stirrer speed on pressure drop and power were studied.

MATERIALS AND METHODS

The photographic view experimental setup is shown in Figure 1. The acrylic column is 1 m in height with 0.05 m internal diameter and 0.06 m outside diameter. U-tube manometer is used to measure the pressure drop across the column. A compressor driven by 5 hp motor is used to supply air. Water is drawn from the surge tank located at the bottom through a motor. Water flow rate and air flowrate are measured by flow meters with a range of 0-5 L/min and 0-10 L/min, respectively. The stirrer is 1 m in length and 0.06 m in diameter and it is rotated by a Tullu motor with a speed regulator. Three different impellers namely, Rushton turbine (1 no.), pitched blade upflow (1 no.) and pitched blade downflow (4 nos.) are used for stirring the bed and are placed at equal distance. The diagrammatic view of impellers and its location in stirrer is shown in Figures 2 and 3, respectively. Compressed air and tap water were used as gas and liquid phases, respectively. Table 1 shows the specifications of the experimental setup.

Figure 1. Photographic view of the experimental setup.

Using the above laboratory setup, hydrodynamic studies on two phase stirred fluidized bed were carried out using an air-water system. Water pumped from the surge tank flowed at a continuous flow rate of 2 L/min. Air from the compressor was introduced at the bottom of the column. The gas velocity was varied from 0.02 to 0.09 m/s. Stirrer speed was varied from 600-1400 rpm and the speed were measured by a digital tachometer. A differential manometer with carbon tetrachloride as manometric fluid was used to measure pressure drop across the column. Power is calculated as the product of volumetric flow rate and pressure drop. The effect of gas velocity and stirrer speed on pressure drop and power was studied without and with stirrer.

RESULTS AND DISCUSSIONS

Hydrodynamic studies are vital to understand the design and operation of fluidized bed. The charac-

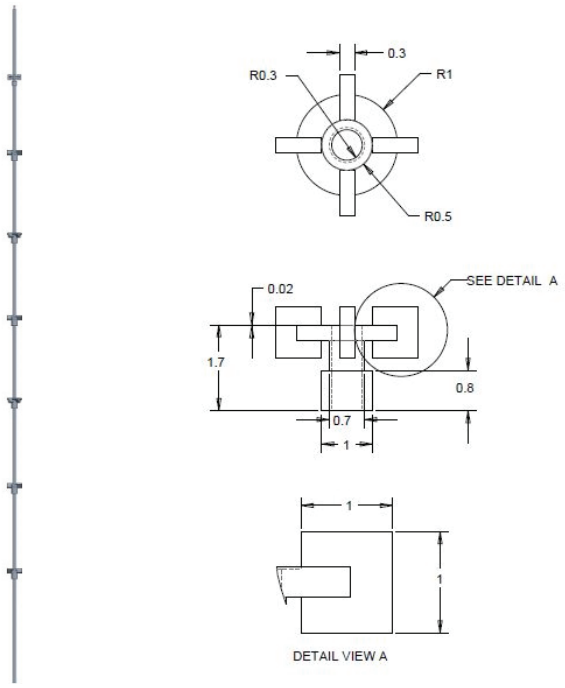

Figure 2. Stirrer with impeller.

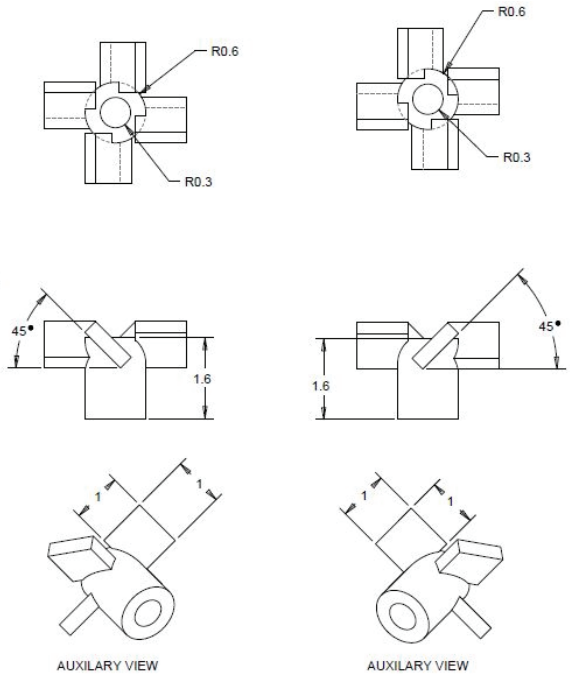

Figure 3. Schematic view of impellers.

Table 1. Specifications of the experimental setup

Acrylic Column	
Column height	1 m
Inner Diameter	0.05 m
Outer diameter	0.06 m
Wall thickness	0.005 m
Stirrer details	
Stirrer height	1 m
Stirrer diameter	0.06 m
Impeller types	
Rushton turbine	1 no.
Pitched blade down flow 45o	4 nos.
Pitched blade up flow	1 no.
Rotameter	
Gas	0-10 L/min
Liquid	0 - 5 L/min

teristics of fluidized bed can be enhanced by understanding the hydrodynamics. The most important parameter which affects the fluidization quality is the pressure drop, which measures the drag in combination with phase holdups and buoyancy. Pressure drop controls the slug formation and channelling.

Effects of gas velocity and stirrer speed on pressure drop

Figure 4 shows the effect of gas velocity on pressure drop for various stirrer speeds. It is observed from the figure that pressure drop increases with gas velocity and stirrer speed. This is because when air is pumped from the bottom of the column larger size bubbles will be produced. The bubble reaches the top of the column quickly due to higher buoyancy force, hence the fractional holdup is low for an unstirred bed. At low gas velocity, the bubble size is larger. Further increase in velocity leads to breakage of bubbles, its size gets reduced and due to lower buoyancy force the bubble reach the top of the column very slowly. At higher velocity, the pressure drop should be constant, but due to slugging and channelling the pressure drop increases to some amount. By increasing the velocity further, the pressure drop

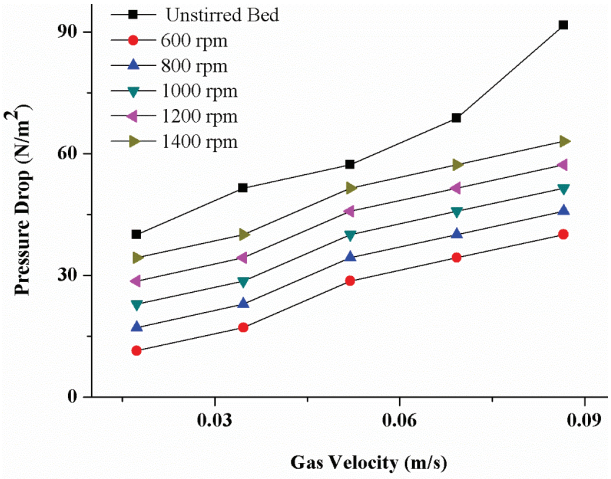

Figure 4. Effect of gas velocity on pressure drop for various stirrer speeds.

inside the column also increases. Pressure drop is lesser in the stirred bed than in unstirred bed conditions, since the stirred bed reduces bubble size thereby resulting in reduction of the bulk density and the same is confirmed from the graph.

Figure 5 depicts the effect of stirrer speed on pressure drop for various gas velocities. It is observed that on increasing the stirrer speed the pressure drop increases. This effect is due to the fact that bulk density of the fluid in the column is inversely proportional to the fractional holdup. Further increase in stirrer speed results in increase in fractional hold up and there is decrease in bulk density of the fluid in the column. The stirrer is designed in such a way that the pitched blade downflow impeller is placed at the top of the column, which pushes the liquid down the column resulting in an increase in pressure drop.

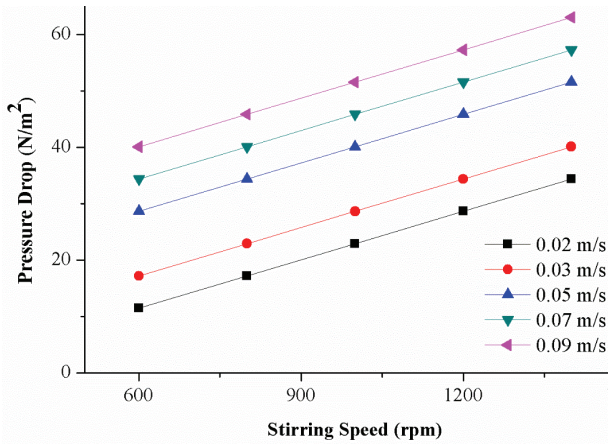

Figure 5. Effect of stirrer speed on pressure drop for various gas velocities.

Two observations were made from the experimental results: one is reduction in bubble size and the other is downflow of the fluid at a higher stirrer speed. The reduction in bubble size reduces the bulk density of the fluid. The downflow of fluid at higher velocity is mainly due to the type of blade. In axial flow impellers, when the particle is pushed up there will be increase in bed density or when the particle is pushed down there will be decrease in density; these effects are mainly due to blade type [22]. In this study, the stirrer has pitched blade downflow impeller at the top, hence the effect of downflow is greater which increases the pressure drop, on increasing the stirrer speed. The outcomes are in good agreement with the study on effect of agitation in fluidized bed done by Reed III and Fenske [23], in which they stated that pressure drop rises due to agitation by the stirrer. Thus, the pressure drop increases with increase in stirrer speed.

Effects of gas velocity and stirrer speed on power

The effect of gas velocity and stirrer speed on power is depicted in Figures 6 and 7. It is observed that power increases with increase in gas velocity and stirrer speed. At low gas velocity, the bubble size will be relatively large and it reaches top of the column quickly and hence the power requirement is low. When the gas velocity increases, the power requirement is also high. Similar report was reported by Leva *et al.* in studies on pressure drop and power requirement in stirred fluidized bed [24]. The requirement of power for stirring the aerated bed depends on the stirrer design and sense of operation [24]. Also, reduction in inter-blade distance rises the power requirement [3]. In the present study, three types of impellers are used, namely, pitched blade downflow, pitched blade upflow (4 nos.) and Rushton turbine. The impellers are positioned at equal distance. The power requirement for stirring depends on the arrangement

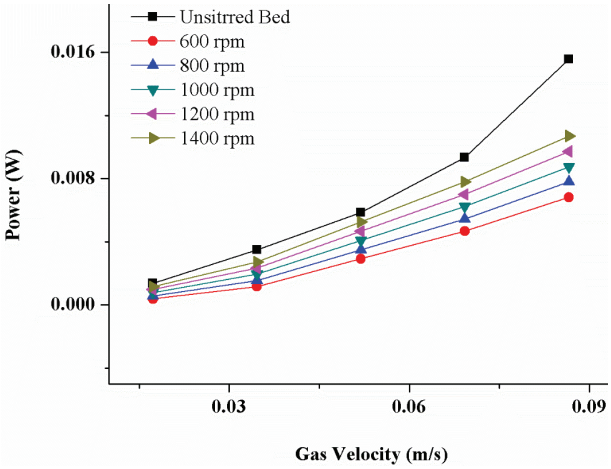

Figure 6. Effect of gas velocity on power for various stirrer speeds.

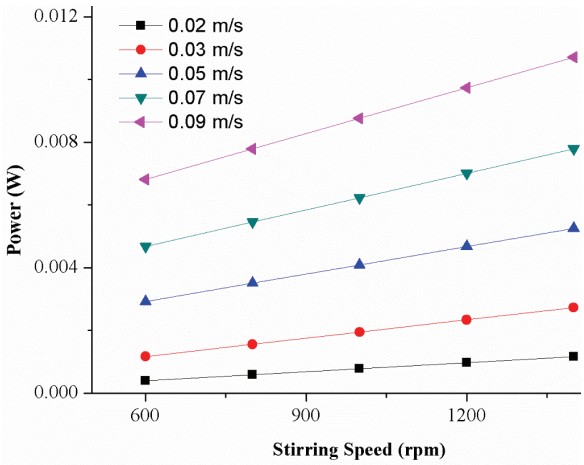

Figure 7. Effect of stirrer speed on power for various gas velocities.

and types of impellers. Power is directly proportional to the third power of stirrer speed and hence, power increases with the increase in stirrer speed. Also, the total power consumed in a stirred vessel increases with the pressure drop [25]. This is in good agreement with the results reported by Joshi and Sharma [26]. Although mechanical agitation increases the power consumption it significantly enhances the quality of fluidization [20].

CONCLUSIONS

Hydrodynamics study in a two-phase stirred fluidized bed was carried out using an air-water system. The effects of gas velocity and stirrer speed on pressure drop and power were studied for stirred and unstirred bed conditions. It was observed that the pressure drop and power increases with increase in gas velocity. This is due to the fact that at higher gas velocity the bubble size will be reduced and would take a longer time to reach the top of the column due to a lesser buoyancy force, which results in increase in pressure drop across the column. With the increase in stirrer speed, both the pressure drop and power increase; this effect is mainly due to the arrangement of impellers. On comparing stirred and unstirred conditions of the bed, it is evident that though pressure drop and power are increased in the stirred bed more than in the unstirred bed, the fluidization performance is enhanced in the stirred bed.

REFERENCES

[1] Y. Han, J.-J. Wang, X.-P. Gu, L.-F. Feng, G.-H. Hu, Homogeneous fluidization of Geldart D particles in a gas--solid fluidized bed with a frame impeller, Ind. Eng. Chem. Res. 51 (2012) 16482-16487

[2] J.R. van Ommen, J.M. Valverde, R. Pfeffer, Fluidization of nanopowders: a review, J. Nanoparticle Res. 14 (2012) 737

[3] N. Kuipers, E. Stamhuis, A. Beenackers, Fluidization of potato starch in a stirred vibrating fluidized bed, Chem. Eng. Sci. 51 (1996) 2727-2732

[4] J. Murthy, P. Sekhar, K. Haritha, P. Balaram, S. Anjani, Hydrodynamic Characteristics of Stirred Gas-solid Fluidized Beds, J.-Ins. Eng. India Part CH Chem. Eng. Divis. (2003) 39-44

[5] W.-C. Yang, Handbook of fluidization and fluid-particle systems, CRC press, Boca Raton, FL, 2003

[6] W. Nowak, Fluidization and heat transfer of fine particles in an acoustic field, AIChE Symp. Ser., 1993, pp. 137-149

[7] R.E. Rosensweig, Fluidization: Hydrodynamic stabilization with a magnetic field, Science 204 (1979) 57-60

[8] I. Puspasari, M.Z.M. Talib, W.R.W. Daud, S.M. Tasirin, Drying kinetics of oil palm frond particles in an agitated fluidized bed dryer, Dry. Technol. 30 (2012) 619-630

[9] I. Puspasari, M.Z.M. Talib, W.R.W. Daud, S.M. Tasirin, Fluidization characteristics of oil palm frond particles in agitated bed, Chem. Eng. Res. Des. 91 (2013) 497-507

[10] C. Sobrino, J.A. Almendros-Ibáñez, D. Santana, M. De Vega, Fluidization of Group B particles with a rotating distributor, Powder Technol. 181 (2008) 273-280

[11] T. Zhou, H. Kage, S. Funaoka, H. Ogura, Y. Matsuno, Fluidization behavior of glass beads under different vibration modules, Adv. Powder Technol. 12 (2001) 559-575

[12] X. Xu, J. Chen, Z. Luo, L. Tang, Y. Zhao, B. Lv, Y. Fu, C. Chen, Fluidization characteristics of air dense medium agitated separation fluidized bed with different distributors, Min. Proc. Ext. Met. Rev. 40 (2019) 299-306

[13] H. Nakamura, T. Kondo, S. Watano, Improvement of particle mixing and fluidization quality in rotating fluidized bed by inclined injection of fluidizing air, Chem. Eng. Sci. 91 (2013) 70-78

[14] Y.-K. Chang, I.-P. Chang, Method development for direct recovery of lysozyme from highly crude chicken egg white by stirred fluidized bed technique, Biochem. Eng. J. 30 (2006) 63-75

[15] K.-H. Chen, S.-Y. Chou, Y.-K. Chang, Rapid purification of lysozyme by mixed-mode adsorption chromatography in stirred fluidized bed, Food Chem. 272 (2019) 619-627

[16] Z. Zhang, J. Beeckmans, Segregation in a stirred fluidized bed, Can J. Chem. Eng. 68 (1990) 932-937

[17] A.S. Mujumdar, Handbook of industrial drying, CRC press, Boca Raton, FL, 2014

[18] D.-H. Bae, H.-J. Ryu, D.-W. Shun, G.-T. Jin, D.-K. Lee, J.-H. Choi, Effects of agitation speed and temperature on minimum fluidization velocity of cohesive particles in a mechanically agitated fluidized bed, Korean Chem. Eng. Res. 40 (2002) 237-245

[19] J. Kim, G.Y. Han, Effect of agitation on fluidization characteristics of fine particles in a fluidized bed, Powder Technol. 166 (2006) 113-122

[20] A. Reyes, G. Diaz, F.-H. Marquardt, Analysis of mechanically agitated fluid-particle contact dryers, Dry. Technol. 19 (2001) 2235-2259

[21] S. Watano, N. Yeh, K. Miyanami, Drying of granules in agitation fluidized bed, J. Chem. Eng. Jpn. 31 (1998) 908--913

[22] J.J. Wang, Y. Han, X.P. Gu, L.F. Feng, G.H. Hu, Effect of agitation on the fluidization behavior of a gas-solid fluidized bed with a frame impeller, AIChE J. 59 (2013) 1066--1074

[23] T. Reed III, M. Fenske, Effects of agitation on gas fluidization of solids, Ind. Eng. Chem. 47 (1955) 275-282

[24] M. Leva, Pressure drop and power requirements in a stirred fluidized bed, AIChE J. 6 (1960) 688-692

[25] T. Sridhar, O.E. Potter, Gas holdup and bubble diameters in pressurized gas-liquid stirred vessels, Ind. Eng. Chem. Fundam. 19 (1980) 21-26

[26] J. Joshi, M.M. Sharma, Mass transfer and hydrodynamic characteristics of gas inducing type of agitated contactors, Can. J. Chem. Eng. 55 (1977) 683-695.

N. DEEPA PRIYA[1]
K. SARAVANAN[2]

[1]Department of Chemical Engineering, Sri Venkateswara College of Engineering, Sriperumbudur, India
[2]Department of Chemical Engineering, Kongu Engineering College, Perundurai, India

NAUČNI RAD

ISTRAŽIVANJE HIDRODINAMIKE DVOFAZNIH FLUIDIZIRANIH SLOJEVA MEŠANIH TRIMA VRSTAMA MEŠAČA

Fluidizirani slojevi se široko koriste u petrohemijskoj, hemijskoj procesnoj industriji, farmaceutskoj, prehrambenoj i biotehnološkoj industriji. Poželjni su za obradu materijala sa širokim spektrom raspodele veličine čestica i nude ravnomernu raspodelu temperature i odličan prenos toplote i mase. Da bi se poboljšao kvalitet fluidizovanog sloja u sistemima vazduh-voda, može se primeniti mehaničko mešanje. U ovom radu, proučavana je hidrodinamika fluidizovanog sloja u sistemu vazduh-voda sa mehaničkim mešanjem. Karakteristike fluidizovanog sloja mogu se objasniti proučavanjem njegove hidrodinamike. Pad pritiska je jedan od važnih faktora koji utiče na performanse fluidizovanog sloja. Otuda su proučavani uticaji brzine gasa i brzine obrtanja mešača na pad pritiska i snagu u slojevima sa mešanjem i bez mešanja. Zapaženo je da se pad pritiska i snaga povećavaju sa povećanjem brzine gasa i brzine obrtanja mešalice. Takođe, pad pritiska i snaga su manji za sloj sa mehaničkim mešanjem.

Ključne reči: hidrodinamika, fluidizovani sloj sa mehaničkim mešanjem, brzina mešača, brzina gasa, dvofazni sistem.

CI&CEQ
Chemical Industry & Chemical Engineering Quarterly

Available on line at
Association of the Chemical Engineers of Serbia *AChE*
www.ache.org.rs/CICEQ

Chem. Ind. Chem. Eng. Q. 27 (2) 113–119 (2021) CI&CEQ

AHMED MAHROU[1]
R. JOURAIPHY[2]
H. MAZOUZ[3]
A. BOUKHAIR[1,4]
MOHAMMED FAHAD[1]

[1]Laboratory of Physics and Nuclear, Atomic, Molecular, Mechanic and Energy, Department of Physics, Faculty of Sciences; University Chouaïb Doukkali, El Jadida, Morocco
[2]Environmental Sciences and Development Laboratory, Faculty of Science and Techniques, University Hassan I, Settat, Morocco
[3]OCP. SA Jorf Lasfar, El Jadida, Morocco
[4]Regional Center for Education and Training Trades, Casablanca--Settat, El Jadida, Morocco

SCIENTIFIC PAPER

UDC 546.18-3:546.6:66.066.7

MAGNESIUM REMOVAL FROM PHOSPHORIC ACID BY PRECIPITATION: OPTIMIZATION BY EXPERIMENTAL DESIGN

Article Highlights

- High magnesium contents in phosphoric acid increase in the viscosity of the acid
- The removal of magnesium from the acid has important advantages in the phosphoric industry
- The reduction of magnesium by precipitation was achieved by the addition of aluminum and fluorine
- The magnesium is precipitated in one of the following forms: $MgAlF_5$ or $MgAl_2F_8$
- The parameters influencing the removal of magnesium are temperature, fluorine form and F/Mg ratio

Abstract

High content of magnesium in phosphate and phosphoric acid affects negatively the performance and operating conditions in phosphate industry. A content of more than 0.3% in phosphate increases the P_2O_5 losses during phosphate digestion and filtration, and also increases steam consumption and solid settling kinetics during concentration. In this work, the removal of magnesium from phosphoric acid by precipitation in one of the compounds, $MgAlF_5$ or $MgAl_2F_8$, was studied. Magnesium precipitation is achieved by the simultaneous addition of aluminum and fluorine. The experimental design methodology was used to carry out this work. Tests were conducted according to the NEMRODW software using industrial quality phosphoric acid. The screening study of parameters affecting the removal efficiency of magnesium from industrial wet phosphoric acid showed that from the following parameters: temperature, F/Mg and Al/Mg ratios, aluminum form and fluorine form, only temperature and F/Mg ratio have an effective influence on magnesium removal. The optimization of magnesium removal from phosphoric acid was performed according to the response surface methodology using a composite matrix. By applying this methodology, the optimum parameters corresponding to a maximum magnesium removal efficiency in phosphoric acid were determined. The values of the optimum parameters obtained by this method are T = 80 °C, ratios: Al/Mg = 1 and F/Mg = 16.

Keywords: phosphoric acid, impurities, magnesium, optimization, design of experiments.

The manufacture of phosphoric acid by the wet process is carried out by contacting the phosphate rock with sulfuric acid. During this operation, most of the impurities contained in the rock dissolve in the phosphoric acid produced. The presence of magnesium in phosphoric acid affects its quality and the operating conditions in fertilizer and phosphoric production units.

Various works have been published focusing on phosphoric acid treatment and purification in order to remove impurities such as heavy metals, organic matter and uranium [1,2]. Koopman developed a new in-line technique for the removal of impurities from the product acid, and simultaneously avoid their incorporation into the calcium sulfate solids [3]. Other authors

Correspondence: H. Mazouz, OCP. SA Jorf Lasfar, El Jadida, Marocco.
E-mail: h.mazouz@ocpgroup.ma
Paper received: 1 January, 2020
Paper revised: 7 April, 2020
Paper accepted: 6 August, 2020

https://doi.org/10.2298/CICEQ200101030M

were focused on a specific impurity, such as cadmium, iron, aluminum, magnesium, etc. [4–7]. Berglund, for example, described a method for removing cadmium. This method relates to a separation in a solid using sulphur compounds added to the phosphate-containing medium after its neutralization. Abdennebi studied the iron and aluminum removal from phosphoric acid at low pH by the precipitation of an organometallic complex. The latter is formed using an organophosphorus reagent [8]. Nevertheless, no work has tackled the problem of MgO with the method of experimental design.

Phosphate magnesium solubilizes almost entirely in phosphoric acid during the phosphate rock attack by sulfuric acid [9,10]. High magnesium contents in phosphoric acid result in an increase in the viscosity of the acid, making its handling and concentration difficult. It leads also to a decrease in extraction efficiency during phosphoric acid purification and clogging equipment by magnesium-based solid. The removal of magnesium from phosphoric acid, therefore, has important advantages in the phosphoric industry.

Several techniques have been developed for the removal of magnesium from phosphoric acid. Numerous researches on the purification of the acid involved liquid-liquid extraction for the recovery of MgO and other impurities [11,12]. Moreover, Berry and Baroody [13] used a continuous ion exchange approach to recover the magnesium as a minor element. This technique allows the reduction of minor elements with minimal phosphate losses and dilution to produce a phosphoric acid that is suitable for the production of fertilizer products. Mills [14] and Parks [15] argue that the magnesium can be recovered by precipitation. The magnesium is removed by adding calcium or fluoride ion donating compound, such as hydrofluoric acid. The latter was the most widely used [16]. Magnesium can precipitate in phosphoric acid under several compounds such as: $MgSiF_6$; $MgAlF_5$; $MgAl_2F_8$; $NH_4MgAl(F,OH)\cdot H_2O$, $Na_xMg_xAl_{2-x}(F,OH)_6\cdot H_2O$ [17].

The aim of this work is to study the optimization of the removal of magnesium from weak phosphoric acid by its precipitation in one of the forms, $MgAlF_5$ and $MgAl_2F_9$, by applying experimental designs. The experimental design method consists in organizing the experimental approach and decision analysis by applying rigorous rules based on the exploitation of the algebraic and statistical properties of the matrices describing the experiments [18,19]. The parameters were selected to determine their influence in the fixed experimental plan, using Hadamard matrices. Then, the mathematical model explaining the phenomenon was established by using complete factorial designs to determine the interaction effects of the parameters and the experimental conditions corresponding to an optimum (maximum or minimum) of the studied response.

EXPERIMENTAL

The removal of magnesium from weak industrial phosphoric acid 28-30% P_2O_5, by precipitation of the compounds $MgAl_2F_8$, $MgAlF_5$, is achieved by the simultaneous addition of aluminum and fluorine under specific conditions. The tests for the removal of magnesium from industrial weak phosphoric acid by precipitation were carried out in 20 L double-jacketed stirred reactor. The acid is stirred at 350 rpm and heated to 60 and 80 °C. Heating was provided by thermal oil circulation using a thermostat bath. Aluminum and fluorine are added at the same time, according to the Al/Mg and F/Mg ratios given in Table 1. After 2 h, the agitation is stopped; the time agitation was fixed in this work. The precipitate is recovered by vacuum filtration. According to the analysis of the industrial phosphoric acid used in laboratory tests, it is mainly composed of 0.36% of Al_2O_3, 0.52% of CaO, 0.42% of MgO, 1.53% of SO_3, 1.96% of F and 27.10% of P_2O_5; this composition leads to Al/Mg ratio of 0.79 and F/Mg ratio of 7.78. During our tests we used one source quality of industrial wet phosphoric acid, which lead to fixing the P_2O_5 content, with an objective to gives a MgO content less than 1% MgO.

Table 1. Experimental plan used for the removal of magnesium by phosphoric acid precipitation

Name	U1	U2	U3	U4	U5
	Al/Mg	F/Mg	Al Form	F Form	Temperature
Unit	-	-	-	-	°C
Level -1	1	5	Metallic	NaF	60
Level +1	2	16	Salt	HF	80

The tests were carried out according to the experimental design matrix proposed by the NEMRODW software at each stage. The solid formed after each test is separated from the phosphoric acid by settling. The treated phosphoric acid is analyzed by ICP to evaluate magnesium removal efficiency.

Asymmetric screening study

The objective of this part of the study is to select the most influential parameters on the magnesium removal from phosphoric acid by precipitation. In order to evaluate their effects on the response of variations in the factor levels, an asymmetric screening

design was used [15]. The asymmetric screening design allows a rapid examination of factors at different numbers of levels. Among different parameters influencing the reaction, the following parameters were selected for the screening study: Al/Mg and F/Mg concentration ratios, forms of added aluminum and fluorine, and temperature. For each parameter the two levels (-1) and (+1) were indicated. Table 1 presents the experimental plan set for screening study. The experiment matrix is constructed from the Hadamard matrix for a number of factor k equal to 5; the experiment matrix in this case consists of 8 experiments. The experimental design is obtained by replacing the -1 and +1 values of the variables in the experimental matrix with the actual values of the corresponding factors (Table 2). These matrices were edited by the NEMRODW.

RESULTS AND DISCUSSION

The tests were performed according to the experimental design in Table 2. The results of the magnesium removal efficiency from phosphoric acid are summarized in Table 3.

The effect of the parameters is estimated by calculating the coefficients of the assumed mathematical model (1):

$$Y = b_0 + b_1U_1 + b_2U_2 + b_3U_3 + b_4U_4 + b_5U_5 \quad (1)$$

Y represents the magnesium removal efficiency from phosphoric acid.

The coefficients of the model (1) are calculated by the least-squares method. The coefficient b_0 represents the average value of the response to the 8 experiments. It is equal to 25.875. The main effect b_1 represents the variation in response Y when the variable U_1 changes from level -1 to level +1. The values of the coefficients b_0 to b_5 obtained are presented in Eq. (2):

$$Y = 25.875 - 4.375U_1 + 24.125U_2 + \\ +3.875U_3 - 9.625U_4 + 7.875U_5 \quad (2)$$

From the results of Eq. (2) and Figure 1, it is noticed that the value b_1 is equal to -4.375, which means that the elimination efficiency of magnesium in phosphoric acid decreases on average by 8.75% when the ratio Al/Mg was increased from value 1 to 2. The value b_2 = 24.12 means that, on average, the efficiency increases by 48.24% when the ratio F/Mg was increased from 5 to 16. The value b_3 = 3.87 means that, on average, the efficiency increases by 3.9% when switching from the metallic aluminum form to the salt form ($Al_2(SO_4)_3$). The value b_4 = -9.62 means that, on average, the yield decreases by 19.24% when switching from the fluorine NaF form to the HF form. The value b_5 = 7.87 means that, on average, the efficiency increases by 15.74% when going from 60 to 80 °C. Analysis of the data in Figure

Table 2. Eight-run asymmetric screening matrix and experimental design used in the screening study

No. Exp.	U_1	U_2	U_3	U_4	U_5	Al/Mg	F/Mg	Aluminum form	Fluorine form	Temperature, °C
1	1	1	1	-1	1	2	16	Salt	NaF	80
2	-1	1	1	1	-1	1	16	Salt	HF	60
3	-1	-1	1	1	1	1	5	Salt	HF	80
4	1	-1	-1	1	1	2	5	Metallic	HF	80
5	-1	1	-1	-1	1	1	16	Metallic	NaF	80
6	1	-1	1	-1	-1	2	5	Salt	NaF	60
7	1	1	-1	1	-1	2	16	Metallic	HF	60
8	-1	-1	-1	-1	-1	1	5	Metallic	NaF	60

Table 3. Experimental design

No. Exp.	Al/Mg	F/Mg	Aluminium form	Fluorine form	Temperature, °C	*Rd* (%)
1	2	16	Salt	NaF	80	65.00
2	1	16	Salt	HF	60	49.00
3	1	5	Salt	HF	80	0.00
4	2	5	Metallic	HF	80	0.00
5	1	16	Metallic	NaF	80	70.00
6	2	5	Salt	NaF	60	5.00
7	2	16	Metallic	HF	60	16.00
8	1	5	Metallic	NaF	60	2.00

2 shows that the parameter F/Mg has a contribution rate in the response of 75.15%, followed by the fluorine form at a rate of 12.02% and then the temperature at a rate of 8.05. The parameters aluminum form and Al/Mg have a low contribution rate in response *Y*. This means that the magnesium removal efficiency of phosphoric acid depends, essentially, on the variation of the F/Mg parameter. These results can be approved by different studies [13-15]. According to the authors, the precipitation and the recovery of magnesium depends on the temperature, Al/Mg ratio, and F/Al ion ratio.

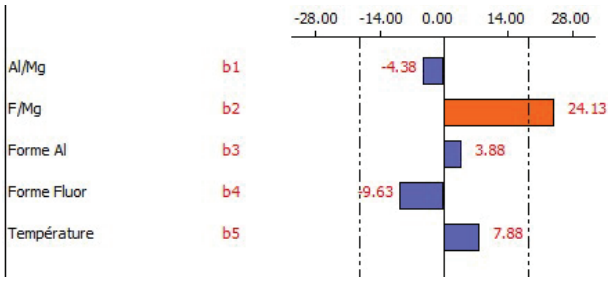

Figure 1. Individual Pareto effects of parameters on Y responses.

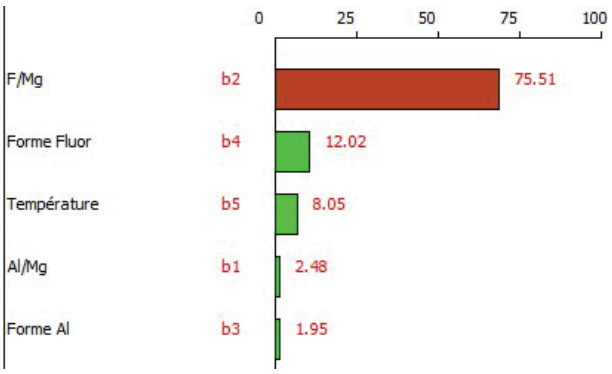

Figure 2. Cumulative Pareto effects of the parameters on the Y response.

The P_2O_5 content does not change during the precipitation of MgO. The choice of doping with alumina and fluorine allows targeting the precipitation of the two compounds $MgAlF_5$ or $MgAl_2F_8$. However, a slight decrease in uranium and calcium has been observed.

Optimization for the MgO removal efficiency from phosphoric acid

The optimization of magnesium removal from phosphoric acid was carried out according to the response surface methodology using the second-degree composite matrix. The objective is to achieve the optimum (maximum or minimum) of the *Y* response (efficiency removal) in the set experimental domain. The parameters selected for the optimization study were as follows: ratios (Al/Mg and F/Mg) and temperature shown in Table 4 with the experimental plan. The postulated model is a complete second-degree plan with the following Eq. (3):

$$Y = b_0 + \sum b_i X_i + \sum b_{ii} X_i^2 + \sum b_{ij} X_i X_j \quad (3)$$

Table 4. Factors studied and experimental field

Variable	Factor	Center	Pace
U_1	Temperature	65	15
U_2	Al/Mg	1.5	0.5
U_3	F/Mg	10.5	5.5

The tests were carried out according to the experimental plan edited by the software and presented in Table 4. The results of the elimination efficiency obtained for each test performed are presented in the 5th column of Table 5.

From the experimental results of the value of the *Y* response, the software was used, to estimate the model coefficients and statistical analysis. Table 6 presents the values of the model's coefficients and Table 7 presents the result of the statistical analysis. It should be noted that the determination of the coefficients is carried out by the least-squares method.

For the validation of the model, it is required that $0<R^2<1$ and R^2 adjusted $<R^2$. The values of R^2 and R^2 adjusted obtained following the regression analysis are mentioned in Table 7 and show that the model is valid because of $R^2 = 0.981$ ($0<R^2<1$); and R^2 adjusted = $0.953<R^2$. After the validation of the model, the variation of the response was studied in the plan (F/Mg; temperature) and (F/Mg; Al/Mg).The results are presented in Figures 3 and 4.

The analysis of the results in Figure 3 shows that the value of the response *Y* in the plan (F/Mg; temperature) varies with the variation in the F/Mg ratio and is independent of the variation in temperature in the experimental domain studied. This explains why the magnesium removal efficiency in the plan (F/Mg; Temperature) depends only on the variation in the F/Mg ratio.

The analysis of Figure 4 shows that the value of the response *Y* in the experimental design (F/Mg; Al/Mg) varies with the variation in the F/Mg ratio and is independent of the variation in the Al/Mg ratio in the experimental domain studied. This explains why the magnesium removal efficiency in the plan (F/Mg; Al/Mg) depends only on the variation in the F/Mg ratio. According to these results, only the parameter F/Mg affects the value of the response in the experimental domain. These results were approved by Mills

Table 5. Design of experiments with the response values obtained for each test performed

No. Exp.	Temperature, °C	Al/Mg	F/Mg	*Y* (%)
1	50.00	1.00	5.00	10.90
2	80.00	1.00	5.00	0.00
3	50.00	2.00	5.00	10.90
4	80.00	2.00	5.00	2.20
5	50.00	1.00	16.00	56.50
6	80.00	1.00	16.00	71.70
7	50.00	2.00	16.00	63.00
8	80.00	2.00	16.00	56.50
9	50.00	1.50	10.50	10.90
10	80.00	1.50	10.50	0.00
11	65.00	1.00	10.50	10.90
12	65.00	2.00	10.50	8.70
13	65.00	1.50	5.00	10.90
14	65.00	1.50	16.00	52.20
15	65.00	1.50	10.50	8.70
16	65.00	1.50	10.50	6.50

Table 6. Estimation of the value of the coefficients

No. Exp.	Coefficient	Inflation factor	Standard deviation	t_{exp}	Signif., %
b_0	6.948		2.649	2.62	3.87 *
b_1	-2.180	1.00	1.769	-1.23	26.4
b_2	-0.870	1.00	1.769	-0.49	64.3
b_3	26.500	1.00	1.769	14.98	< 0.01***
b_{11}	-1.172	1.42	3.445	-0.34	74.2
b_{22}	3.178	1.42	3.445	0.92	39.5
b_{33}	24.928	1.42	3.445	7.23	0.0515***
b_{12}	-2.437	1.00	1.978	-1.23	26.4
b_{13}	3.537	1.00	1.978	1.79	12.2
b_{23}	-1.363	1.00	1.978	-0.69	52.2

explaining that the MgO to F ratio is the primordial criterion for the removal of MgO [14].

Using the validated model, the values of the factors were determined at the optimum and then calculated the optimal value of the response in these coordinates. According to the values of the factors edited by the software the optimal temperature is 79.66 °C, the optimal Al/Mg ratio is 1.00 and the optimal F/Mg ratio is 15.99. Tests at the conditions related to the optimum (*Y*) were performed, then com-

Table 7. Statistics of responses

Standard deviation of the response	5.594
R^2	0.981
R^2 Adjusted	0.953
R^2 Predicted	0.732
PRESS	2667.680
Number of degrees	6

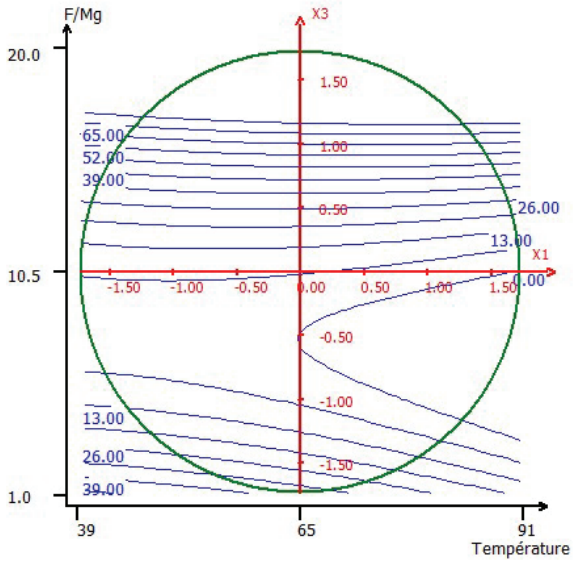

Figure 3. Same response curve variation of in plan (F/Mg; temperature).

pared the calculated *Y* value with the experimental value obtained. The results obtained are presented in Table 8.

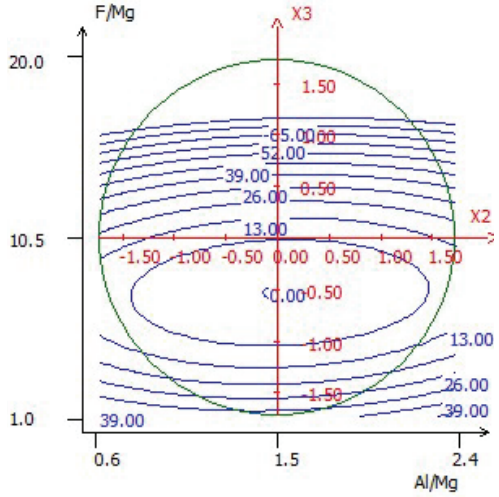

Figure 4. Same response curves variation in plan (F/Mg; Al/Mg).

Table 8. Ycal and Yexp values at optimum

Response	Response name	Value (%)	Residue (*Yexp* - *Ycal*)
Ycal	Calculated yield	66.10	3.2
Yexp	Experimental yield	69.3	

CONCLUSION

The optimization of the reduction of the magnesium concentration in phosphoric acid by experimental designs was the subject of this study. The reduction of magnesium by precipitation was achieved by the simultaneous addition of aluminum and fluorine to precipitate it in one of the following forms: $MgAlF_5$ or $MgAl_2F_8$. With the use of experimental designs, through the postulated models, the most influential parameters on the magnesium elimination phenomenon, and the optimum parameters corresponding to the optimal magnesium elimination efficiency in phosphoric acid were defined. The parameters influencing the removal efficiency of magnesium in phosphoric acid, determined during the screening study, are temperature, fluorine form, and F/Mg ratio. The latter has an influence rate of 75% in relation to all the parameters used. The optimum parameter values determined during the optimization study are temperature T = 80 °C, ratio Al/Mg = 1 and F/Mg = 16. The predictive model for the study of magnesium removal from phosphoric acid by precipitation has been validated. The prediction of the value of the response Y to the optimum was performed with a low residue compared to the experiment of about 3.2.

REFERENCES

[1] A.B. Gerber, (FED PHOSPHORUS COMPANY), US No. 44224721A, 1921

[2] C.F. Booth, J.E. Malowan, (Monsanto Chemicals), US No. 74282634A, 1937

[3] C. Koopman, G.J. Witkamp, Sep. Sci. Technol. 37 (2007)1273-1290

[4] H. Berglund, (WIPO (PCT)), WO No. 1980002418A, 1980

[5] A.M. Cornelis, A. Johannes, (Stamicarbon B.V. (NL)), No. 07/0912, 1989

[6] S.D. Ukeles, E. Ben-yoseph, N. Philip, (Norsk Hydro ASA), US No. 4986970A, 1991

[7] P.Becker, (Office, Togolais Des Phosphates (Kpeme-Togo, TG), No. 07/793369, 1994

[8] N. Abdennebi, K. Benhabib, C. Goutaudier, M. Bagane, JMES 8 (2017) 557-565

[9] J. Yu, D. Liu, Chem. Eng. Res. Des. 88 (2010) 712-717

[10] I.T. Shamshidinov, K.G. Gafurov, M.M. Ikramov, J. Chem. Technol. Metall 51 (2016) 157-162

[11] H. Ahmed, H. Diamonta, C. Chaker, R. Abdelhamid, Sep. Purif. Technol. 55 (2007) 212-216

[12] R. Hamdi, A. Hannachi, J. Chem. Eng. Process Technol. 3 (2012) 134

[13] W.W. Berry, T.E. Baroody, (K-Technologies Inc), US No. 20150166343A1, 2015

[14] H.E. Mills, (White Springs Agricultural Chemicals Inc), US No. 4243643A, 1978

[15] K.L. Parks, K.D. Clevenger, D.P. Mcdonald, (Agrico Chemical Company), US No. 4299804, 1981

[16] D. Goldstein, (FMC Corp), US 3819810A, 1994

[17] J.R. Lehr, A. W. Frazier, J.P. Smith, J. Agric. Food Chem. 14 (1966) 522-529

[18] G. Jaxques, Introduction aux plans d'expériences, DUNOD Ed, Paris, 2001, p.18

[19] O.W. Gooding, Curr. Opin. Chem. Biol. 28 (2004) 297-304.

AHMED MAHROU[1]
R. JOURAIPHY[2]
H. MAZOUZ[3]
A. BOUKHAIR[1,4]
MOHAMMED FAHAD[1]

[1]Laboratory of Physics and Nuclear, Atomic, Molecular, Mechanic and Energy, Department of Physics, Faculty of Sciences; University Chouaïb Doukkali, El Jadida, Morocco
[2]Environmental Sciences and Development Laboratory, Faculty of Science and Techniques, University Hassan I, Settat, Morocco
[3]OCP. SA Jorf Lasfar, El Jadida, Marocco
[4]Regional Center for Education and Training Trades, Casablanca-Settat, El Jadida, Morocco

NAUČNI RAD

STATISTIČKA OPTIMIZACIJA UKLANJANJA MAGNEZIJUMA IZ FOSFORNE KISELINE PRECIPITACIJOM

Visok sadržaj magnezijuma u fosfatu i fosfornoj kiselini negativno utiče na performanse i radne uslove u industriji fosfata. Dok sadržaj veći od 0,3% u fosfatu povećava gubitke P_2O_5 tokom digestije i filtracije fosfata, a i povećava potrošnju pare i kinetiku taloženja čvrstih čestica tokom koncentrisanja. U ovom radu, proučavano je uklanjanje magnezijuma iz fosforne kiseline taloženjem u obliku jedinjenja $MgAlF_5$ ili $MgAl_2F_8$ primenom metode statističke optimizacije. Taloženje magnezijuma postiže se istovremenim dodavanjem aluminijuma i fluora. Istraživanja su sprovedena prema softveru NEMRODV koristeći fosfornu kiselinu industrijskog kvaliteta. Skrining parametara koji utiču na efikasnost uklanjanja magnezijuma iz industrijske vlažne fosforne kiseline pokazao je da od više parametara (temperatura, odnosi F/Mg i Al/Mg, oblik aluminijuma i oblik fluora), samo temperatura i odnos F/Mg imaju efektivni uticaj na uklanjanje magnezijuma. Optimizacija uklanjanja magnezijuma iz fosforne kiseline izvedena je prema metodologiji površine odziva kombinovanom sa kompozitnim planom. Primenom ove metodologije utvrđeni su optimalni parametri koji odgovaraju maksimalnoj efikasnosti uklanjanja magnezijuma iz fosforne kiseline. Vrednosti optimalnih parametara dobijenih ovom metodom su 80 °C, odnos Al/Mg = 1 i odnos F/Mg = 16.

Ključne reči: fosforna kiselina, nečistoće, magnezijum, optimizacija, planiranje eksperimenata.

CI&CEQ
Chemical Industry & Chemical Engineering Quarterly

Available on line at
Association of the Chemical Engineers of Serbia *AChE*
www.ache.org.rs/CICEQ

Chem. Ind. Chem. Eng. Q. 27 (2) 121–130 (2021) CI&CEQ

ATHEER M. AL-YAQOOBI[1]
MUNA N. AL-RIKABEY[2]
MAHMOOD K.H. AL-MASHHADANI[1]

[1]Department of Chemical Engineering, Collage of Engineering, University of Baghdad, Iraq
[2]Department of Biochemical Engineering, Al-Khwarizmi Collage of Engineering, University of Baghdad, Iraq

SCIENTIFIC PAPER

UDC 574.583:544.6

ELECTROCHEMICAL HARVESTING OF MICROALGAE: PARAMETRIC AND COST-EFFECTIVITY COMPARATIVE INVESTIGATION

Article Highlights

- The current research highlighted the commercial feasibility of electrochemical harvesting
- The high harvesting efficiency was obtained in short electrolysis time with aluminum
- However, similar harvesting efficiency could be obtained with graphite with lower operating cost
- The operating cost can be optimized by controlling pH of the broth
- The operation cost achieved in this method is distinctly lower than that of traditional methods

Abstract

The cost of microalgae harvesting constitutes a heavy burden on the commercialization of biofuel production. The present study addressed this problem through economic and parametric comparison of electrochemical harvesting using a sacrificial electrode (aluminum) and a nonsacrificial electrode (graphite). The harvesting efficiency, power consumption, and operation cost were collected as objective variables as a function of applied current and initial pH of the solution. The results indicated that high harvesting efficiency obtained by using aluminum anode is achieved in short electrolysis time. That harvesting efficiency can be enhanced by increasing the applied current or the electrolysis time for both electrode materials, where 98% of harvesting efficiency can be obtained. The results also demonstrated that the power consumption with the graphite anode is higher than that of aluminum. However, at 0.2 A the local cost of operation with graphite (0.036 US$/m^3) is distinctly lower than that of aluminum (0.08 US$/m^3). Furthermore, the harvesting efficiency reached its higher value at short electrolysis time at an initial pH of 6 for aluminum, and at an initial pH of 4 for graphite. Consequently, the power consumption of the harvesting process could be reduced at acid- nature conditions to around 0.46 kWh/kg for aluminum and 1.12 kWh/kg for graphite.

Keywords: electrochemical harvesting, electrocoagulation, microalgae, sacrificial electrode, cost efficiency, energy consumption.

The growing concern for biomass as a source of renewable energy is a response to vast global demands for energy and uneasy prices of fossil fuels due to the deficiency of its reserve, beside the reinforcement of greenhouse gases resulting from utilizing fossil fuels[1].

Due to the high growth rate and lipid accumulation capability of microalgae, they are recognized as an important feedstock for biofuels, food, feed and fine chemicals. Furthermore, microalgae contribute in the reduction of greenhouse gas emissions employing their ability of CO_2 capture [2,3]. However, the biorefinery processing of biofuel production from microalgae sources is facing serious challenges that must be taken into consideration. The high cost of harvesting comes as the primary challenge for commer-

Correspondence: A.M. Al-Yaqoobi, Department of Chemical Engineering, Collage of Engineering, University of Baghdad, Iraq.
E-mail: atheer.ghaleb@coeng.uobaghdad.edu.iq
Paper received: 13 December, 2019
Paper revised: 12 June, 2020
Paper accepted: 14 August, 2020

https://doi.org/10.2298/CICEQ191213031A

cialization of the biofuel industry, which may require investment up to 30% of the total cost of biofuel production due to high-energy consumption [4].

The high capital cost and energy consumption of microalgae harvesting comes due to the fact that the algae concentration in the solution is very low (1-2 g/l); consequently, a large volume is required. The small size of microalgal cells, most of which are less than 10 μm in diameter, further complicate the separation process [5,6].

Researchers have adopted various microalgae harvesting techniques that include gravity flotation and flocculation, sedimentation, filtration and screening and centrifugation. However, all of these techniques have disadvantages associated with power consumption and process efficiency that affect the overall economic feasibility of the process [6-9].

Electrocoagulation accompanied with electroflotation of microalgae comes into view as a promising harvesting technique. The harvesting process starts with the formation of coagulants through dissolving of a metallic anode due to the electrochemical oxidation reaction. Simultaneously, hydrogen and oxygen microbubbles are produced on the anode and cathode [10-12].

The following reactions occur during the process at the anode when an aluminum anode is used:

$$Al \rightarrow Al^{+3} + 2e^{-}$$

$$2H_2O \rightarrow 4H + O_2 + 4e^{-}$$

$$x\,Al^{+3} + y\,OH^{-} \rightarrow Al_x(OH)_y^{z+}$$

The main reaction at the cathodes is reduction of water:

$$2H_2O + 2e^{-} \rightarrow H_2 + 2OH^{-}$$

The flocs are formed by the reaction of the negative surface charge microalgae and the positive charge coagulants. These algal flocs can be lifted to the surface of the solution by the aid of the bubbles [5,6].

Low energy consumption and no direct addition of chemicals are the major advantages that distinguish this technique from the other traditional harvesting methods. The process is also considered eco-friendly, easy to control, and mostly cost-efficient [7]. However, the main drawback of the electrocoagulation process is the periodical replacement of the metallic anodes which are usually Al or Fe. Researchers also indicate the negative effect of the excessive doses of dissolved anode material on the biomass [8,9]. Consequently, electrochemical harvesting could be enhanced by adopting nonsacrificial anode material for the process.

It is well known that the electrode material has a massive effect on the electrochemical harvesting process, where it is directly related to the removal efficiency and energy consumption of the process [6]. Aluminum and iron have extensively been used as electrode materials in the electrocoagulation process for harvesting strains of microalgae. Electrochemical harvesting was also investigated using other anode materials like boron-doped diamond [6] and carbon electrodes [10,11]. However, limited information is available about the comparison of the electrochemical harvesting of microalgae with sacrificial and non-sacrificial anode material.

The current work focuses on exploration and comparison of the performance of electrochemical harvesting of microalgae with using sacrificial anode material (aluminum) and nonsacrificial anode material (graphite). The influence of key parameters, including applied current and initial pH of the solution on the harvesting process, was investigated. The results were assessed based on harvesting efficiency, energy consumptions, and the total operation cost. The operation cost was estimated according to local prices of energy input (kWh) and aluminum.

METHODS

Cultivation of microalgae

Chlorella microalgae were provided kindly by the department of Biology, Ibn-Haitham College of Education, University of Baghdad. First, the microalgae were inoculated in two 250 ml flasks in Chu-13 media at 25±2 °C. Then the microalgae were incubated into two 5-L glass containers in a fresh culture medium. Cultures were grown at 16/8 h light/dark at a controlled temperature of 25±2 °C. The light intensity was 2500 lux measured by a photometer (Milwaukee/ /China). The air was supplied to each reactor at 500 mL/min flowrate for six hours daily.

Electrocoagulation experiments

The experiments of microalgae harvesting were conducted using a cylindrical cell made of plexiglass with a diameter of 9 cm and a height of 10.5 cm. Two types of anode material were used in the current study which are graphite and aluminum. A horizontal aluminum plate was used as a cathode. All electrodes in experiments had the same dimensions of 9.5 cm×6 cm×1 cm.

The distance between the anode and cathode was 15 mm. The anode was connected to the positive

pole and cathode was connected to the negative pole of DC power supply (Smart Power System, model EMA-01-32-15-P, USA). All experiments were conducted at constant current mode, and the applied current was changed in the range of (0.2-1 A).

The experiments were performed with 450 ml of broth at room temperature (25±2 °C). The effect of initial acidity of microalgal broth was studied by changing pH of the solution (2, 4, 6, 8 and 10). The initial pH of microalgal broth was adjusted by adding 0.1 M of H_2SO_4 and 0.1 M of NaOH. The pH of broth was measured by (Basic pH Crison, USA). The reactor was constantly stirred at speed of 200 rpm by a magnetic stirrer (Corning, model PC-410, USA).

Before each run, the aluminum electrode was kept in a 1 M HCl solution for a half-hour, mechanically ground with abrasive paper, and then washed with distilled water.

Determination of electrochemical harvesting efficiency

The microalgae harvesting efficiency was determined based on the change in optical density and the turbidity of the microalgal suspension. Samples were collected periodically during the ECH process. The samples were taken at a distance of 5 cm from the liquid surface. The flocs of microalgae floated to the top surface of microalgal broth by the action of gases formed at the anode and cathode.

After 10 min of salting time, the optical density of samples was measured using UV-Vis spectrometer (Bio-Rad, SmartSpec Plus, USA) measured at 680 nm.

The harvesting efficiency was subsequently calculated as:

$$ECH\% = 100\frac{OD_i - OD_t}{OD_i} \quad (1)$$

where OD_i is the optical density of the initial suspension, and OD_t is the optical density of the suspension at a time t.

Calculation of power consumption and operation cost

The power consumption PC (in kWh/kg of recovered microalgae) was estimated according to the following formula:

$$PC = \frac{Pt}{1000V\mu_a C_i} \quad (2)$$

where P is the power (W), t the electrolysis time (h), V the volume of the microalgal broth treated (m^3), μ_a the microalgae recovery efficiency, and C_i the initial microalgae biomass concentration (kg/m^3).

The operating costs OC in US\$/m^3 was expressed in terms of the energy consumption and electrode dissolved and is calculated by the following relation [15,16]:

$$OC = Ep_e + Wp_{Al} \quad (3)$$

The unit price of electricity p_e equivalent to 0.03 US\$/kWh in Iraq in 2019 [17], and the price of aluminum p_{Al} equivalent to 1.93 US\$/kg in Iraq in 2019.

The energy consumption E (kWh/m^3) can be calculated according to the following relation [5,10,11]:

$$E = \frac{IUt}{V} \quad (4)$$

where I is the applied current (A), U is the cell voltage (V) which assumed to be constant.

Faraday's Law was used to calculate the theoretical amount of aluminum dissolved W during the harvesting process [13]:

$$W = \frac{I\,t\,M}{nFV} \quad (5)$$

where W = aluminum dissolved (g/m^3); M = molecular weight of aluminum (M = 27 g/mol); n = number of electrons involved in the oxidation reaction (n = 3); F = Faraday's constant, 96,500 C/mol.

RESULTS AND DISCUSSION

Effect of applied current

The applied current is found to be an essential factor that influences the electrochemical harvesting process of microalgae as it affects process efficiency, time and power consumption.

In the investigation, the experiments of effects of current density on harvesting efficiency were carried out with a range of 0.2-1 A, at constant initial pH of 10. The microalgae concentration was fixed for all experiments.

For the aluminum anode, the removal efficiency of microalgae increased with the rising of current density, as shown in Figure 1. At a current density of 1 A, around 99% removal efficiency was achieved within the first 2 min and remained around this value for the rest of electrolysis time. Reducing the applied current to 0.2 A led to a decline in the removal efficiency, where it took 15 min of electrolysis time to reach around 95% efficiency.

That behavior could be attributed to the fact that the increase in current density resulted in an abundance of aluminum that was released from the electrodes according to Faraday's law. The amount of positively charged dissolved metal hydroxides neut-

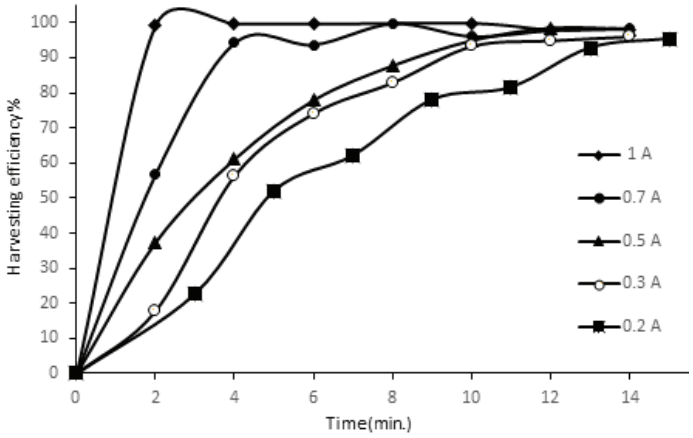

Figure 1. Effect of current on harvesting efficiency for aluminum electrode.

ralized the negative charge surface microalgae which promoted the formation of low-density flocs. In addition, increases in the applied current increase the microbubble producing rate by the electrodes, which results in higher upward momentum flux and speed up algae flotation [18].

The performance of aluminum and graphite electrodes for the effect of applied current is compared in Figure 2. The trend of removal efficiency for the graphite electrode is similar to that of the aluminum electrode where the efficiency increased with increasing of applied current; however, the removal efficiency for aluminum is higher than that of graphite for the same applied current. With applied current of 0.5 A, the graphite electrode achieved removal efficiency of 98.5% after 12 min of electrolyte time, while it was about 91% for the graphite in the same electrolysis time. Furthermore, for low applied current of 0.2 A, harvesting efficiency of 95% was achieved in 15 min, while it was around 85% for graphite during the same electrolysis time.

With nonsacrificial electrodes like graphite, the principle of electroflotation of microalgae is based on the migration of negative charge cells of microalgae by the action of the electric field. The algae accumulate on the positive anode's surface and the negative charge of the algae cells is neutralized resulting in the formation of algal aggregates. The microbubbles generated on both electrodes in electrolysis of water will cause flocculation and flotation of the microalgae aggregates [9,15]. With the increasing of applied current, the electrical charges produced by the electrode increase the generation of bubbles as well. This results in an increase in the effective harvesting of microalgae with applied current [20]. In electrocoagulation-flocculation, using a sacrificial electrode like aluminum, the process mechanism is different, when Al^{3+} released from the electrode react with water to form -BNm soluble monomeric and polymeric hydroxo-metal complexes which act as chemical flocculants [15,17]. In both types of anodes (sacrificial and nonsacrificial), the microbubbles do the same action.

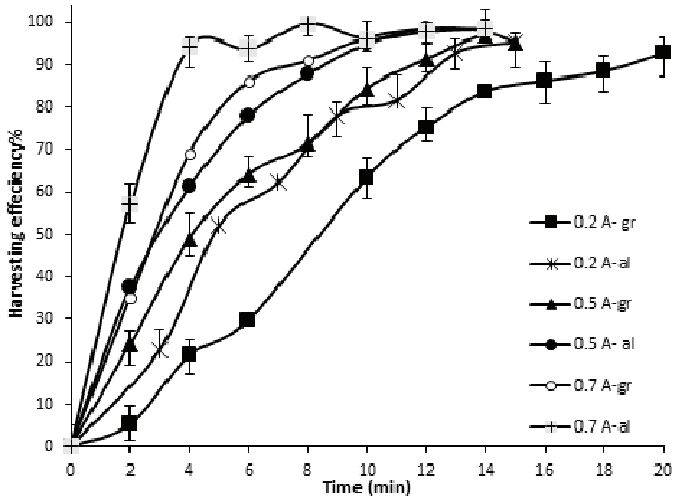

Figure 2. Removal efficiency of microalgae at different applied currents for aluminum and graphite anodes, at initial pH of 10.

From the results above, it seems that the physical and chemical process involved in electrocoagulation-flocculation with sacrificial anodes (aluminum) has an advantage over the electro-flotation with sacrificial anodes, where the harvesting efficiency of aluminum achieved higher values than that obtained with graphite at the same operating conditions.

The results of the influence of applied current on the harvesting process in the current work were found to be harmonious with those observed in several researches that used aluminum, carbon and other anode materials [8,9,16,18]

Effect of acidity

The influence of initial pH has been recognized to be a decisive parameter on the microalgae harvesting process. Natural acidic conditions were found to be optimum for harvesting processes using carbon anode [20]. In addition, with the aluminum anode, the microalgae harvesting efficiency could be enhanced by decreasing the initial pH of the solution [5,19]. Despite that, some researchers found that alkaline conditions are more suitable for algal harvesting [17,20]. The effect of broth acidity on electrocoagulation was investigated by varying the starting of acidity from 2 to 10. From Figure 3, it can be observed that the harvesting efficiency reached its higher value at natural acidic conditions. For an initial pH of 6, the removal efficiency achieved 94% after 10 min of electrolysis time and around 98% after 13 min. On the other hand, in the alkaline range of initial pH, the efficiency process faded. The harvesting efficiency decreased to 81% after 10 min with increase of pH to 8 and reached 88% after 13 min.

In acidic and neutral conditions, the aluminum hydroxide precipitates and monomeric hydroxo-aluminum and polymeric cations like $Al_{13}O_4(OH)_{24}^{+7}$, $Al_6(OH)_{15}^{+3}$, $Al_7(OH)_{17}^{+4}$, $Al_8(OH)_{20}^{+4}$, $Al_{13}O_4(OH)_{24}^{+7}$ are present significantly in the bulk. Consequently, the negative surface charge microalgae are readily neutralized by those cations. Increasing initial pH to alkaline conditions, the negatively charged aluminum hydroxide $Al(OH)_4^-$ is dominant in solution, which does not react with the surface of microalgae, resulting in slower removal of microalgae [5,19,21]. The $Al(OH)_4^-$ species are not active for most water treatment applications [26]. However, for extremely acidic conditions of pH 2, it seems that the removal efficiency reached its lowest value. It may be due to the changing in microalgae surface properties at this pH value. The cell surface charge of microalgae is a result of the existence of ionizable functional groups, which are part of the cell wall, or may be found in the attached extracellular algogenic organic matter (AOM). The pH value of the surrounding medium forces these groups to become protonated or deprotonated. For green algae, zeta potential was found to be electronegative for pH 4-10, while for pH around 3-4, isoelectric point is determined [15,22]. In addition, it is found that the surface charge of the cell is a function of the species life cycle [19].

The effect of initial solution pH was also investigated using graphite anode. Figure 4 shows that the harvesting efficiency increased by decreasing initial solution pH, except for pH 2. The highest removal efficiency of 90.2% is achieved at pH 4 at electrolysis time of 13 min. Similar behavior was also obtained at electrolysis time of 10 min, where the curve has a

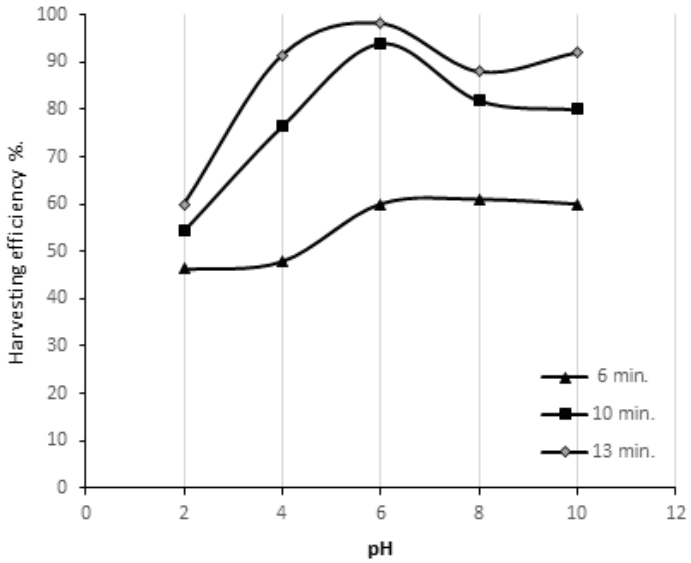

Figure 3. Effect of pH on the harvesting efficiency for aluminum electrode.

sharp peak at pH 4 and the removal efficiency of 78.3%. The current results are concordant with those obtained in electrochemical harvesting of oleaginous green microalgae *S. obliquus* [20]. It was found that the harvesting efficiency achieved maximum values at pH 5, and it has been attributed to the formation of positively charged ions in acid conditions. However, increasing the electrolysis time results in increasing of harvesting efficiency, which applied for both types of anode material.

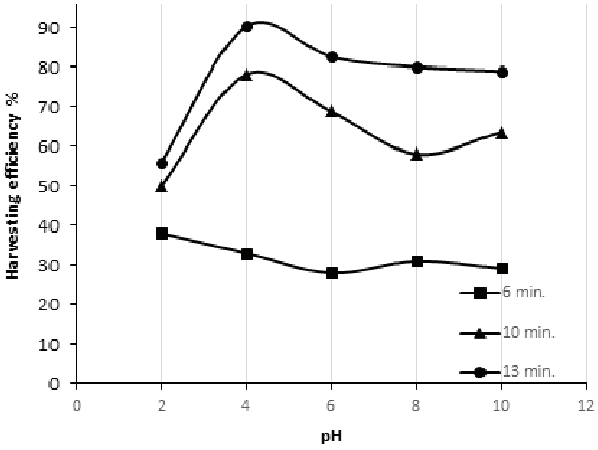

Figure 4. Effect of pH on harvesting efficiency for graphite electrode.

From the results obtained with the aluminum and graphite electrodes, it seems that the acidic to natural conditions are the most favorable for harvesting *Chlorella* microalgae by using both electrodes, except in extremely acidic conditions, around pH 2, where the harvesting is inhibited.

The experimental results also show that the recovery efficiencies achieved with applying a high current or low pH during a short electrolysis time could be obtained by applying a low current density or high pH during a longer electrolysis time. Bearing in mind that when an industrial scale is the aim, a long electrolysis time requires a bigger reactor volume and may affect the quality of the microalgae in the process [23].

Power consumption and operation cost

Assessing the economic feasibility of the harvesting process using both types of electrodes is the ultimate goal of the research. In addition to the harvesting efficiency, the effect of the key parameters should be highlighted in terms of electrical energy consumption and local cost of operation.

The results demonstrate that the high removal efficiency of microalgae obtained with aluminum electrodes is accompanied with low energy consumption during the harvesting process. Figure 5 shows the average energy consumption for both types of anodes with different applied currents. The estimation of the average energy consumption based on 92% harvesting efficiency.

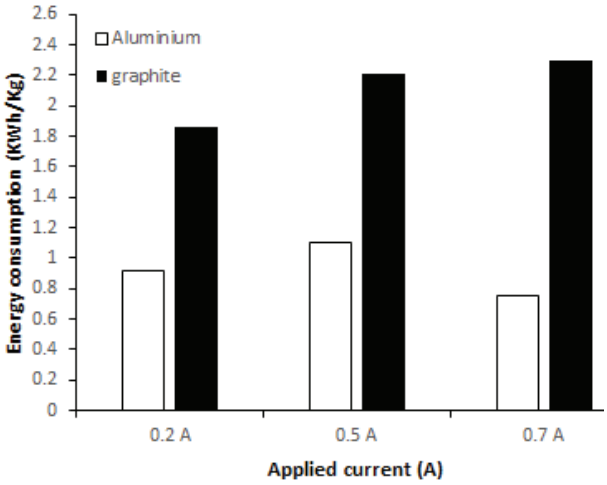

Figure 5. Power consumption with different applied currents for aluminum and graphite anodes.

It is obvious from Eq. (2) that the energy consumption increased with the increasing of applied current for both electrode materials, which isusually accompanied by increases in total cell potential. However, the time required to reach to the desired harvesting efficiency is an effective parameter to determine energy consumption. The results reveal that the graphite associated with high energy consumption in comparison with that obtained with aluminum. It can be observed from Figure 5 that with aluminum anode, the energy consumption is 0.759 kWh/kg of microalgae for applied current of 0.7 A, while it's around 2.3 kWh/kg of microalgae for the graphite anode. Likewise, at a low applied current of 0.2 A, the energy consumption for the aluminum anode is 67% lesser from that obtained with graphite. The reason behind relatively low energy consumption of aluminum anodes maybe due to a high overpotential of oxygen evaluation for graphite anodes. Also, Al^{3+} released by aluminum anodic oxidation increases the electrical conductivity of the solution that reduces electrical power consumption.

The optimization of process energy consumption is crucial to reflect its impact on the total cost of operation and the economic feasibility of the process. The operation cost of microalgae harvesting in the current study is expressed by Eq. (3), which expresses the total cost in terms of the energy cost and the cost of consumable anode materials. The microalgae separation efficiency of 92% is taken as a reference to estimate the total cost of operation. Figure 6

shows the operation cost of aluminum and graphite anodes at different applied currents. The figure demonstrates that the cost of operation is obviously high for aluminum for the applied currents of 0.2, 0.5 and 0.7 A, despite that the time for achieving the required separation efficiency is obviously shorter, and the power consumption is much lower, which can be noticed from Figures 1 and 6. The high cost of power consumption obtained with the graphite anode is vanquished by the cost of aluminum dissolved during the harvesting process, which raises the total cost operation of the aluminum electrodes. The percentage of dissolved electrode cost is about 78% of the total process cost at applied current of 0.2 A, while this percentage increases to about 82% when the applied current increases to 0.7 A.

However, it has been recognized that the operation cost of electrocoagulation process using aluminum electrodes is obviously lower than that of iron electrode at different applied currents [15].

It can be observed from Figure 7 that alteration of microalgae broth acidity from an energy consumption point of view, the harvesting process with aluminum anode shows a clear superiority over the graphite anode. Generally, the energy consumption (kWh/kg) is reduced with the decrease of pH values, where the values energy consumption for pH 4 and 6 are lower than those obtained with pH 8 and 10 for both aluminum and graphite. That may be due to the addition of H_2SO_4 that enhances the conductivity of the mixture, which typically reduces the overpotential. In addition, the power consumption estimated at the point in time corresponded to 92% recovery efficiency, which gives lower energy consumption for the acidic region. Consequently, the power consumption achieved minimal value for aluminum of 0.46 kWh/kg at pH 6, which is due to shorter electrolysis time to reach 92% recovery efficiency.

The high cell potential obtained with graphite anode reflects on the overall behavior of power

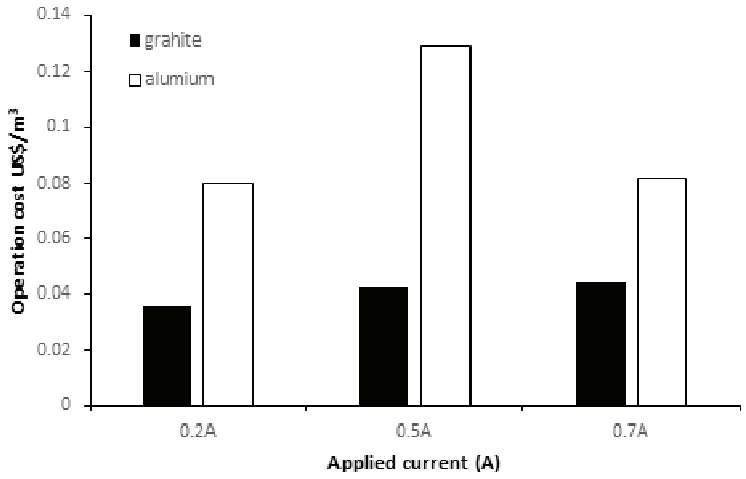

Figure 6. Operation cost at different applied currents for aluminum and graphite anodes.

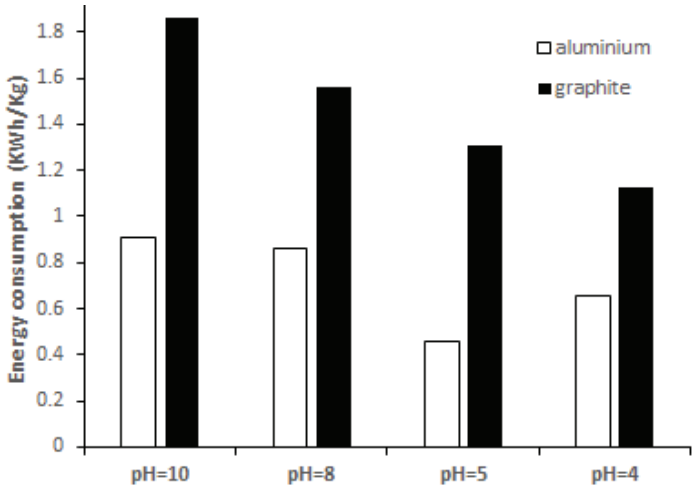

Figure 7. Power consumption at different initial pH for aluminum and graphite anodes.

consumption for the harvesting process. Where at pH 4, the power consumption of graphite is 1.127 kWh/kg and for aluminum 0.657 kWh/kg, that disparity in energy consumption is applied for all pH range. However, the power consumption at pH 2 is eliminated from the calculation due to insufficient harvesting process efficiency at that pH value.

In spite of effective harvesting of algae and minimal power consumption achieved by using aluminum anode for all pH range, the harvesting process provided higher operation cost values in comparison to that obtained with graphite which can be observed clearly from Figure 8. The lowest operation cost for graphite anodes was at pH 4 which is 0.0218 US$/m^3, while it was 0.075 US$/m^3 for the aluminum anode at the same conditions, while the lowest operation cost for aluminum is 0.056 US$/m^3 obtained at pH 6, which refers to the best broth pH condition.

However, the medium of microalgae growth is usually in alkaline condition, and accordingly, lowering the pH of the medium toward the acidic-natural region will require additional cost. It's required to add chemicals to adjust the required pH value for the broth, *i.e.*, H_2SO_4 (24 $/L), which adds extra cost to the process. However, this cost was equal for both modes of operation with both electrodes (Al or graphite) at a certain pH value. For instance, it required ~0.28 $/m^3 to adjust the broth acidity to pH 2, ~0.2 $/m^3 for pH 4, ~0.14 $/m^3 for pH 6 and ~0.06 $/m^3 for pH 8.

Both electrolysis time and cell potential played important roles in the optimization of operation cost. However, the local prices of the aluminum and the electricity power, which differ from place to another, have the lion's share of the impact on optimization of the operation cost.

In comparison to other harvesting technology, the performance of the electrochemical harvesting process of microalgae could be optimized to be a promising harvesting technology in which minimum energy is consumed [9]. Technologies like tangential flow filtration, polymer flocculation, and centrifugation require high energy for operation [14,23]. On the other hand, pressure filters and vacuum filters require to be periodically replaced [29]. Sedimentation may require low power for operation but it is denoted with low separation efficiency (up to 66%) [30]. The present work showed that the target of low energy consumption and long-life parts could be met in the electrochemical harvesting process.

The operation cost obtained in current study was relatively lower than in other electrocoagulation processes. That comes from low applied current, the high harvesting efficiency in relatively low electrolysis time, the local prices of electrical energy, local electrodes materials, and the composition of electrolyte. The operation cost for electrocoagulation process of kaolinite and bentonite suspensions using aluminum electrode was 0.1-1 US$/m^3 and depends on operation conditions [31]. The operation cost reduced to 0.768 US$/m^3 when the technique was applied for the treatment of waste metal cutting fluids [26]. It was concluded that around 1.190 US$/m^3 was required for the electrocoagulation process of metalworking fluid wastewater treatment at the optimum study conditions [32]. Similarly the operating cost of treatment of dyehouse wastewater using aluminum electrode was 1.851 US$/m^3 [33].

Generally, for non-sacrificial anode like graphite, the low cost of operation compensates the relatively long electrolysis time to fulfill high harvesting efficiency. In addition, the metallic electrodes as aluminum will need periodic process shutdown for electrode replacement, while with the non-sacrificial electrode like graphite the replacement process will be omitted. Furthermore, the graphite electrodes will not conta-

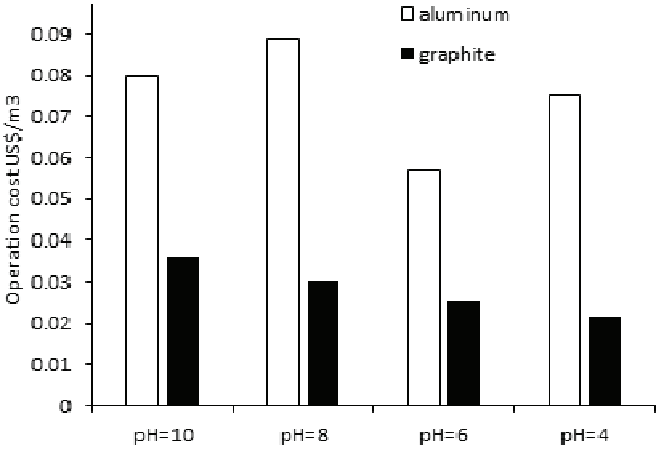

Figure 8. Operation cost at different initial pH for aluminum and graphite anodes.

minate the water or microalgae biomass as will metallic electrodes [8,22].

CONCLUSION

The electrochemical harvesting of microalgae was investigated using two types of anode materials, aluminum and graphite anodes. Based on the experimental results, the study concluded that high harvesting efficiency could be achieved either by applying high current at short electrolysis time and *vice versa*. Consequently, the electrolysis time and the applied current can be optimized to obtained lower power consumption. The comparison between the behaviors of the two types of electrodes showed that a higher harvesting efficiency could be obtained with electro-coagulation-flotation using aluminum anode with relatively short electrolysis time.

Despite the power consumption obtained, the graphite was generally higher than that of the aluminum, and the operation cost of the harvesting process with the graphite was considerably lower.

The electrochemical harvesting exhibited higher harvesting efficiency under acidic-natural initial pH conditions for both anode materials. Consequently, the power consumption can be reduced to lower values. In addition, the operation cost could be shifted to a lower value at the optimum pH values.

The process of microalgae electrochemical harvesting could be optimized to be cost-competitive and an environment-friendly process with a lower operation cost of 0.037 US$/m^3, which may contribute to the development and deployment of the marketing of this biorefinery process.

REFERENCES

[1] S.M.A. Mobin, Energy Procedia 160 (2019) 752–760

[2] D. Moreira, J.C.M. Pires, Bioresour. Technol. 215 (2016) 371–379

[3] S.M.A. Mobin, F. Alam, A Review of Microalgal Biofuels, Challenges and Future Directions, in: M.M.K. Khan, A.A. Chowdhury, N.M.S. Hassan (Eds.), Appl. Thermo-Fluid Process. Energy Syst. Key Issues Recent Dev. a Sustain. Futur., Springer Singapore, Singapore, 2018, pp. 83–108

[4] X. Lei, Y. Chen, Z. Shao, Z. Chen, Y. Li, H. Zhu, J. Zhang, W. Zheng, T. Zheng, Bioresour. Technol. 198 (2015) 922–925

[5] S. Gao, J. Yang, J. Tian, F. Ma, G. Tu, M. Du, J. Hazard. Mater. 177 (2010) 336–343

[6] B.G. Ryu, J. Kim, J.I. Han, K. Kim, D. Kim, B.K. Seo, C.M. Kang, J.W. Yang, Algal Res. 31 (2018) 497–505

[7] C.G. Alfafara, K. Nakano, N. Nomura, T. Igarashi, M. Matsumura, J. Chem. Technol. Biotechnol. 77 (2002) 871–876

[8] N. Uduman, V. Bourniquel, M.K. Danquah, A.F.A. Hoadley, Chem. Eng. J. 174 (2011) 249–257

[9] R. Misra, A. Guldhe, P. Singh, I. Rawat, F. Bux, Chem. Eng. J. 255 (2014) 327–333

[10] F. Baierle, D.K. John, M.P. Souza, T.R. Bjerk, M.S.A. Moraes, M. Hoeltz, A.L.B. Rohlfes, M.E. Camargo, V.A. Corbellini, R.C.S. Schneider, Chem. Eng. J. 267 (2015) 274–281

[11] A. Alyaqoobi, J. Eng. 16 (2010) 6198–6205

[12] M. Khemis, G. Tanguy, J.P. Leclerc, G. Valentin, F. Lapicque, Process Saf. Environ. Prot. 83 (2005) 50–57

[13] F. Akbal, S. Camcidotless, Desalination 269 (2011) 214–222

[14] E. Brillas, C.A. Martínez-Huitle, Appl. Catal., B 166–167 (2015) 603–643

[15] M. Bayramoglu, M. Kobya, O.T. Can, M. Sozbir, Sep. Purif. Technol. 37 (2004) 117–125

[16] F. Ozyonar, B. Karagozoglu, 20 (2011) 173–179 (http://www.pjoes.com/pdf/20.1/pol.j.environ.stud.vol.20.no.1.173-179.pdf)

[17] GlobalPetrolPrices.com, (n.d.) https://www.globalpetrolprices.com/Iraq/electricity_prices/ (accessed July 19, 2019)

[18] P.K. Holt, G.W. Barton, M. Wark, C.A. Mitchell, Colloids Surfaces A Physicochem. Eng. Asp. 211 (2002) 233–248

[19] I. Branyikova, G. Prochazkova, T. Potocar, Z. Jezkova, T. Branyik, Fermentation 4 (2018) 93

[20] R. Misra, A. Guldhe, P. Singh, I. Rawat, T.A. Stenström, F. Bux, Bioresour. Technol. 176 (2015) 1–7

[21] M.G. Kiliç, Ç. Hoşten, Ş. Demirci, J. Hazard. Mater. 171 (2009) 247–252

[22] J. Kim, B.G. Ryu, B.K. Kim, J.I. Han, J.W. Yang, Bioresour. Technol. 111 (2012) 268–275

[23] D. Vandamme, S.C.V. Pontes, K. Goiris, I. Foubert, L.J.J. Pinoy, K. Muylaert, Biotechnol. Bioeng. 108 (2011) 2320–2329

[24] D. Ghernaout, C. Benblidia, F. Khemici, Desalin. Water Treat. 54 (2015) 3328–3337

[25] M.Y.A. Mollah, R. Schennach, J.R. Parga, D.L. Cocke, J. Hazard. Mater. 84 (2001) 29–41

[26] M. Kobya, C. Ciftci, M. Bayramoglu, M.T. Sensoy, Sep. Purif. Technol. 60 (2008) 285–291

[27] R. Henderson, S.A. Parsons, B. Jefferson, Water Res. 42 (2008) 1827–1845

[28] M.K. Danquah, L. Ang, N. Uduman, N. Moheimani, G.M. Forde, J. Chem. Technol. Biotechnol. 84 (2009) 1078–1083

[29] E.M. Grima, F.G. Acie, A.R. Medina, Y. Chisti, Biotech. Adv. 20 (2003) 491–515

[30] H. AL-Hattab M, ghaly A, J Fundam Renew. Energy. 154 (2015) 1–26

[31] J.C. Donini, J. Kan, J. Skynnarkarczuk, T.A. Hassan, K.L. Kar, Can. J. Chem. Eng. 72 (1994) 1007

[32] E. Demirbas, M. Kobya, Process Saf. Environ. Prot. 105 (2017) 79–90

[33] M. Kobya, E. Gengec, E. Demirbas, Chem. Eng. Process. Process Intensif. 101 (2016) 87–100.

ATHEER M. AL-YAQOOBI[1]
MUNA N. AL-RIKABEY[2]
MAHMOOD K.H. AL-MASHHADANI[1]

[1]Department of Chemical Engineering, Collage of Engineering, University of Baghdad, Iraq
[2]Department of Biochemical Engineering, Al-Khwarizmi Collage of Engineering, University of Baghdad, Iraq

NAUČNI RAD

ELEKTROHEMIJSKO IZDVAJANJE MIKROALGI: UPOREDNO ISTRAŽIVANJE EFEKTIVNOSTI PARAMETARA I TROŠKOVA

Troškovi izdvajanja mikroalgi predstavljaju veliko opterećenje za komercijalizaciju proizvodnje biogoriva. Ovaj rad se bavio ekonomskim i parametarskim upoređivanjem elektrohemijskog izdvajanja pomoću žrtvene (aluminijum) i nežrtvene (grafit) elektrode. Efikasnost izdvajanja, potrošnja energije i operativni troškovi korišćeni su kao objektivne promenljive u zavisnosti od primenjene struje i početnog pH rastvora. Rezultati su pokazali da se visoka efikasnost izdvajanja postiže aluminijumskom anodom za kratko vreme. Ova efikasnost izdvajanja može se povećati povećanjem primenjene struje ili vremena trajanja elektrolize za oba elektrodna materijala, pri čemu se može postići efikasnost izdvajanja od 98%. Rezultati su, takođe, pokazali da je potrošnja energije veća sa grafitnom nego sa aluminijumskom anodom. Međutim, pri 0,2 A, okalni troškovi rada sa grafitnom elektrodom (0,036 USD/m^3) su znatno niži od troškova rada sa aluminijumskom elektrodom (0,08 USD/m^3). Dalje, efikasnost izdvajanja dostiglo je bila veća za kratko vreme elektrolize pri početnom pH 6 za aluminijumsku elektrodu, odnosno pri početnom pH 4 za grafitnu elektrodu. Shodno tome, potrošnja energije procesa izdvajanja može se smanjiti u uslovima kisele sredine na 0,46 kWh/kg za aluminijumsku elektrodu i 1,12 kWh/kg za grafitnu elektrodu.

Ključne reči: elektrohemijsko izdvajanje, elektrokoagulacija, mikroalge, žrtvena elektroda, efikasnost troškova, potrošnja energije.

CI&CEQ
Chemical Industry & Chemical Engineering Quarterly

Available on line at
Association of the Chemical Engineers of Serbia *AChE*
www.ache.org.rs/CICEQ

Chem. Ind. Chem. Eng. Q. 27 (2) 131–142 (2021) CI&CEQ

JOVANA GRAHOVAC
IVANA PAJČIN
VANJA VLAJKOV
ZORANA RONČEVIĆ
JELENA DODIĆ
DRAGOLJUB CVETKOVIĆ
ALEKSANDAR JOKIĆ

University of Novi Sad, Faculty of Technology Novi Sad, Novi Sad, Serbia

SCIENTIFIC PAPER

UDC 633.42:632.3:66

Xanthomonas campestris BIOCONTROL AGENT: SELECTION, MEDIUM FORMULATION AND BIOPROCESS KINETIC ANALYSIS

Article Highlights

- Antagonists from 7 genera were tested to select the most promising black rot biocontrol agent
- *B. velezensis* has showed the highest potential for suppression of *X. campestris*
- Glycerol and yeast extract were selected as optimal nutrients in *B. velezensis* cultivation medium
- Cultivation of *B. velezensis* was performed in a laboratory-scale bioreactor (2 L working volume)
- Bioprocess kinetics of biomass growth and carbon source consumption was investigated

Abstract

Black rot, caused by Xanthomonas campestris pv. campestris, is one of the most important diseases of cruciferous crops which causes significant yield losses. Biological control of black rot by microbial biocontrol agents represents a promising alternative to chemical treatments and good agricultural practices which show only limited success. This study was carried out to assess a potential of different antagonists, including Bacillus, Pseudomonas, Lactobacillus, Streptomyces, Saccharomyces and Trichoderma genera, for biological control of black rot. Cultivation broth samples and their filtrates were examined against seven X. campestris strains, isolated from diseased cruciferous plants, using the diffusion-disc method. Bacillus velezensis has showed the highest inhibition zone diameter of 35.62±3.76 mm. Afterwards, different combinations of carbon and nitrogen sources were used in the cultivation medium to maximize antagonistic activity of B. velezensis. The best combinations were glycerol and yeast extract, lactose and peptone, as well as sucrose and yeast extract, suggesting the potential of biodiesel, dairy and sugar industry effluents in the production of bioactive compounds effective against the black rot pathogen. The validation experiment was performed in a laboratory-scale bioreactor, in order to investigate bioprocess kinetics of biomass growth and carbon source consumption, using the cultivation medium containing the optimal carbon and nitrogen source.

Keywords: Bacillus, biological control, black rot, carbon source, cultivation, organic nitrogen source.

Black rot is one of the most economically important diseases of *Brassica* species, other members of *Brassicaceae* family and wild *Capparales* species [1]. The causal agent of this disease is *Xanthomonas campestris* pv. *campestris* (*Xcc*), Gram-negative aerobic bacteria which is known for producing extracellular polysaccharide xanthan. The most important host plants of this pathogen are cabbage, cauliflower, kale, broccoli and Brussels sprouts, where *Xcc* causes significant yield losses [2] because diseased crops have poor market value and rot fast after har-

Correspondence: I. Pajčin, University of Novi Sad, Faculty of Technology Novi Sad, Bulevar cara Lazara 1, 21000 Novi Sad, Serbia.
E-mail: ivana.pajcin@uns.ac.rs
Paper received: 8 May, 2020
Paper revised: 29 July, 2020
Paper accepted: 26 August, 2020

https://doi.org/10.2298/CICEQ200508032G

vest. Black rot is primarily a seed-borne disease, but infected transplants, soil and crop remains could also represent a reservoir of contamination. Bacterial pathogens can be carried over from plant to plant by wind, irrigation water, aerosol, rain, insects, and by equipment and people. *Xcc* enters the plant through hydathodes on leaf margins by reabsorption of guttation droplets into the leaf [2]. Some races can infect the plant entering through stomata and colonizing apoplastic space before penetrating into the vascular tissue. This mode of infection is rare because it requires reduced hydrophobicity, *i.e.*, modification of cuticular waxes around stomata. Other sites of infection include wounds or roots, but in any case, the final destination of the pathogen is vascular tissue [1]. Infection could be latent at low temperatures, where pathogens rest in the vascular system without producing symptoms. When the temperature rises over 25 °C bacteria move through the vascular system, simultaneously producing xanthan, which plugs xylem vessels and restricts water flow, resulting in chlorotic yellow V-shaped lesions on leaves and roots. The name black rot originates from dark veins which ensue due to pathogen movement through vascular tissue. Affected tissues could become necrotic and cause premature leaves falling. Secondary infection by other pathogenic bacteria, such as *Erwinia carotovora* or *Pseudomonas marginalis*, is responsible for the rotting of the diseased plant [2]. Disease management usually includes usage of assayed healthy planting material (seeds and transplants), crop rotation, elimination of other potential inoculum sources (infected crop remains and weeds) and use of resistant cultivars, but these methods have showed only limited success in practice [3]. Reduction of disease spreading is achieved by avoiding overhead irrigation and by usage of chlorine dioxide in the irrigation water. Physical and chemical seed treatments, such as application of hot water, sodium hypochlorite, zinc sulfate, acidified cupric acetate, hydrogen peroxide and antibiotics, are also used, but these treatments are not completely efficient [2]. Therefore, researchers have been looking for alternative ways to control black rot disease, among which biological control represents the promising solution.

Biological control is one of the ecologically acceptable solutions for management of different plant diseases. It represents the usage of beneficial microorganisms and/or their metabolites for control of different plant pathogens by several mechanisms that include competition for nutrients and space, antibiosis, induced plant resistance or parasitism [4]. Utilization of bio-based agents implies reduction of chemical compounds usage in agricultural production, which leads to lower environmental pollution and decreases risks for negative effects of pesticides to human and animal health [5]. Besides, several antagonistic microorganisms used for biological control of plant pathogens show the ability to promote plant growth and induce its defensive mechanisms against pathogens [6]. Root antagonists have also proven to enrich the rhizosphere of plants with essential nutrients, providing a favorable environment for growth and multiplication of beneficial microorganisms. Many of these antagonists have also been investigated for adoption of soil contaminants [7].

Bacteria of the genus *Bacillus* are among the mostly favorable microorganisms for biological control of black rot, due to their high potential for application as biocontrol agents [8-11]. The formation of endospores is one of the desirable characteristics due to their tolerance to high temperatures, desiccation, UV radiation and organic solvents, which imply higher viability compared to vegetative cells, as well as suitability for formulation [11]. One of the most important characteristics of these bacteria is the ability to produce a wide spectrum of antibiotics and other metabolites with antagonistic activity against fungal and bacterial phytopathogens [12]. *Bacillus* species are commonly found in soil, the rhizosphere and the phyllosphere, therefore they are well adjusted to conditions where they should be applied [13]. Bacteria of this genus are known for plant growth-promoting capabilities and they have also showed ability to colonize plants endophytically, which is an important feature for biocontrol of vascular pathogens [11]. Among the *Bacillus* species, the most commonly used are *Bacillus subtilis*, *Bacillus amyloliquefaciens* and *Bacillus pumilus* [14]. *Pseudomonas* species are also suitable candidates for biological control of black rot [15]. Pseudomonads produce several bioactive metabolites, such as antibiotics, siderophores and volatile compounds [16]. There have been several mechanisms proposed for plant growth promoting activity of *Pseudomonas* spp.: stimulation of nutrients adoption, production of phytohormones, antagonistic activity against pathogens and induction of systemic resistance response [17]. *Lactobacillus* spp. have been considered as biocontrol agents due to production of different antimicrobial compounds, such as bacteriocins, organic acids, antimicrobial peptides and hydrogen peroxide [18]. Due to generally regarded as safe (GRAS) status, they usually comply with all recommendations for food and agricultural products. Different lactic acid bacteria are examined for biological control of *Xcc* [19]. Streptomycetes are

also considered as potential candidates for biological control of black rot [20], due to their beneficial trait of producing large number of different metabolites, enzymes and antibiotics with antagonistic activities against microbial pathogens [21]. Different yeasts are also investigated as biological control agents for black rot [22]. Genus *Trichoderma* represents hemibiotrophic fungi, whose main biocontrol traits are antagonism or mycoparasitism against plant pathogens and induction of systemic or localized resistance in plants. Also, fungi of the genus *Trichoderma* produce over 40 secondary metabolites that play a role in plant-microbe interaction and phytopathogen suppression [23]. *Trichoderma viride* [20] and *Trichoderma harzianum* [13] were investigated for biological control of *Xcc*.

The aim of this study was the selection of the antagonistic microorganism with the highest potential for biological control of black rot, whose antimicrobial activity was tested against seven phytopathogenic *Xcc* strains isolated from diseased cruciferous plants. After the selection of the best producing microorganism, another aim of this study was the determination of an optimal combination of carbon and organic nitrogen sources in the cultivation medium for the production of bioactive agents effective against black rot causers. Selected carbon sources were representative for different industrial waste streams in order to evaluate the potential of these waste streams in production of biocontrol agents. Validation experiment was carried out in a laboratory-scale bioreactor using the cultivation medium containing optimal carbon and nitrogen source, where the aim was to investigate bioprocess kinetics. The aims set in this study represent important steps in defining of a techno-economically viable bioprocess solution for the production of biocontrol agent for black rot management, which is a basis for potential commercialization of this product.

EXPERIMENTAL

Pathogens

Test microorganisms used in this study were pathogenic isolates of the genus *Xanthomonas*, isolated from diseased plants of *Brassicaceae* family. The pathogens were isolated using standard phytopathological techniques. All isolates were characterized according to their pathogenic, morphological and ecological characteristics as the members of *X. campestris* species [24]. Microorganisms were stored on YMA (yeast maltose agar) medium (glucose 15.0 g/L, yeast extract 3.0 g/L, malt extract 3.0 g/L, peptone 5.0 g/L and agar 20.0 g/L) at 4 °C and subcultured every four weeks. Working cultures were prepared by subculturing pathogens on YMA medium, and by incubating at 26 °C for 48 h. Test suspensions of pathogens were obtained by suspending microorganisms from YMA medium in 20 ml of sterile NaCl solution (9 g/L).

Antagonists

Antagonistic microorganisms used in this study were: *Bacillus subtilis* ATCC 6633 (M 1), *Bacillus cereus* ATCC 10876 (M 2), *Bacillus amyloliquefaciens* (M 3), *Bacillus* sp. (M 4) and *Bacillus velezensis* (M 5) isolated from soil, *Pseudomonas aeruginosa* ATCC 27853 (M 6), *Pseudomonas aeruginosa* isolated from water (M 7), *Pseudomonas putida* isolated from water (M 8), three isolates of genus *Lactobacillus* isolated from food (M 9-M 11), *Streptomyces hygroscopicus* isolated from soil (M 12), *Saccharomyces cerevisiae* (M 13) and *Trichoderma reesei* QM 9414 (M 14). Antagonists were stored on appropriate media at 4 °C and subcultured every four weeks. The selected antagonist with the highest potential to suppress *X. campestris* was identified using 16S rDNA sequencing, based on query coverage of 100% and sequence homology of 99%.

Media and cultivation conditions for screening of producing microorganisms

Media used for growth and biosynthesis of antimicrobial compounds by antagonistic microorganisms were: nutrient broth (HiMedia, India) for *Bacillus* and *Pseudomonas* strains, MRS (de Man, Rogosa and Sharpe) broth (HiMedia, India) for *Lactobacillus* strains, SM (Sabouraud maltose) broth (HiMedia, India) for *T. reesei*, while *S. hygroscopicus* and *S. cerevisiae* were grown in semi-synthetic media. Medium used for cultivation of *S. hygroscopicus* contained (g/L): glucose (5.0), soybean defatted flour (10.0), $(NH_4)_2HPO_4$ (0.5), K_2HPO_4 (1.0), $CaCO_3$ (3.0), NaCl (3.0) and $MgSO_4$ (0.5). Medium for *S. cerevisiae* cultivation contained (g/L): barley malt extract (14.0) (Malteks®, Prena-M Inžinjering, Serbia), glucose (2.0) and peptone (0.1). Volume of each medium was 50 mL, while the volume of the Erlenmeyer flasks was 200 mL. Inoculation was performed directly from tubes with microorganisms previously grown on the same medium that was used for cultivation, but containing agar (20 g/L) for 48 h at 28 °C, except for *Pseudomonas* strains, which were grown at 37 °C. Cultivation was carried out at 30 °C during 96 h, with aeration on a laboratory shaker (KS 4000i control, IKA® Werke, Germany) at agitation rate of 150 rpm.

Media and cultivation conditions for determination of an optimal carbon-organic nitrogen source combination

Inoculum was prepared by transferring the selected producing microorganism using inoculation loop from nutrient agar to an Erlenmeyer flask containing 50 mL of nutrient broth. Incubation was carried out at 28 °C for 24 h, with spontaneous aeration and agitation (150 rpm) on a laboratory shaker. After 24 h, the liquid culture was poured into an Erlenmeyer flask containing 150 mL of nutrient broth under sterile conditions, which was then incubated at 28 °C for 24 h, with spontaneous aeration and agitation (150 rpm) on a laboratory shaker. Liquid media used for production of bioactive agents by the selected producing microorganism contained (g/L): carbon source (15.0), organic nitrogen source (3.0), $(NH_4)_2SO_4$ (1.5), $MgSO_4 \cdot 7H_2O$ (0.3), K_2HPO_4 (3.0), and pH value was adjusted to 7.0±0.2 prior to sterilization performed by autoclaving at 121 °C and 2.1 bar (20 min). Varied carbon sources were glucose, sucrose, lactose, starch and glycerol, while varied organic nitrogen sources were yeast extract, peptone, soybean meal, L-glutamic acid and urea. Inoculum volume was equal to 10 vol.% of cultivation medium volume. Production of bioactive compounds was carried out in Erlenmeyer flasks (200 mL) containing 50 mL of cultivation medium at 28 °C during 96 h, with an agitation rate of 150 rpm under aerobic conditions on a laboratory shaker (KS 4000i control, IKA® Werke, Germany).

Validation experiment

Cultivation of the selected producing microorganism was carried out in a laboratory-scale bioreactor (Biostat® Aplus, Sartorius AG, Germany) using cultivation medium containing selected optimal carbon and organic nitrogen sources. Inoculum in this experimental stage was prepared in the same way as in the previous stage. Working volume of the bioreactor was 2 L, where 10 vol.% of inoculum was added compared to cultivation medium volume. Cultivation parameters were set to temperature of 28 °C, agitation rate of 250 rpm and aeration rate of 1 vvm (volume of air/volume of medium/min) using sterile air. During 96 h of cultivation, cultivation broth was sampled at predefined time intervals (12 h) to determine biomass concentration, carbon source content and antimicrobial activity of the produced bioactive agents, as well as the kinetics of microbial growth and carbon source consumption.

In vitro assaying of antimicrobial activity

In this study, antimicrobial activities of cultivation broth samples and their filtrates obtained after cultivation of the aforementioned antagonists were examined against seven *X. campestris* pathogenic isolates using the diffusion-disc method. Suspensions containing phytopathogens were prepared using sterile saline to achieve 10^8 CFU/mL. Biomass concentration in these suspensions was measured using the calibration curve between plate count and spectrophotometric measurement at 600 nm (UV 1800, Shimadzu, Japan). Each cultivation broth was filtered through nylon filter (Agilent Technologies, Germany) with pore diameter of 0.22 μm to obtain biomass-free filtrates. Commercial discs containing 30 μg of streptomycin (Torlak, Serbia) (K) were used as control to compare antimicrobial activity of the tested antimicrobial agents. Cultivation media used for antimicrobial activity assaying were prepared by adding suspension of pathogens (1 mL) to melted YMA media, which were previously tempered at 50±1 °C. After homogenization, prepared media were poured into Petri dishes. Every cultivation broth sample and its filtrate were examined against each pathogenic strain using three diffusion discs in triplicate tests. Each sample volume was 15 μL. Petri dishes were incubated at 26 °C during 72 h, and afterwards inhibition zone diameters were measured using a ruler for accurate zone reading (Antibiotic ZoneScale, Himedia®, India). *In vitro* assaying of antimicrobial activity of bioactive agents produced by the selected producing microorganism was carried out in triplicate tests against each pathogenic isolate using cultivation broth samples (15 μL) with different combinations of carbon and organic nitrogen sources.

Quantification of glycerol content

Supernatants obtained after centrifugation of cultivation broth samples at 10000 rpm during 10 min (Rotina 380R, Hettich, Germany) were used for determination of glycerol content. Glycerol content was determined using the HPLC instrument (Thermo Scientific Dionex UltiMate 3000 series, Thermo Fisher Scientific, MA, USA), which was equipped with the pump HPG-3200SD/RS, the autosampler WPS--3000(T)SL (10 μL injection loop), the column Zorbax NH2 (250 mm×4.6 mm, 5 μm) (Agilent Technologies, Germany) and the refractive index detector (ERC RefractoMax520, Germany). The mobile phase was mixture of acetonitrile and bidistilled water (70:30 volume ratio) and the conditions of analysis were: eluent flow rate 1 mL/min, elution time 20 min and temperature 30 °C.

Quantification of biomass content

Biomass content was determined using DCW (dry cell weight) method. Cultivation broth samples

(20 mL) were centrifuged (10000 rpm, 10 min) to separate biomass from the liquid phase. The obtained biomass pellets were dried at 105 °C until reaching constant weight. Biomass concentration (g/L) was calculated based on the measured dry cell weight and initial volume of cultivation broth sample (20 mL).

Experimental data analysis

In vitro assaying of the produced antimicrobial agents' activity was performed in triplicate tests, and mean values of inhibition zone diameters along with standard deviations were calculated using Microsoft Excel 2010 (Microsoft Corporation, WA, USA). Obtained results were analyzed using several different statistical tests. Levene's test was applied for testing homogeneity of variances, followed by ANOVA and Duncan's multiple range tests. Statistical analysis using all applied tests was carried out at significance level of $\alpha = 0.05$ in Statistica software 13.0 (StatSoft, OK, USA).

Bioprocess kinetics investigation

Bioprocess kinetic parameters were determined using the GraphPad Prism software, v. 8.1.0 (GraphPad Software, Inc., CA, USA). Biomass growth kinetics was described using the Gompertz model (Eq. (1)):

$$X(t) = X_{\max}\left(\frac{X_0}{X_{\max}}\right)^{e^{-\mu t}} \tag{1}$$

where biomass concentration $X(t)$ during cultivation could be calculated using initial biomass concentration X_0, maximal biomass concentration $X_{\max}$, and specific growth rate μ.

Glycerol consumption was described using modified Luedeking-Piret equation (Eq. (2)):

$$S(t) = S_0 - \gamma X_0\left(\frac{e^{\mu t}}{1-\frac{X_0}{X_{\max}}\left(1-e^{\mu t}\right)}-1\right) - \delta\frac{X_{\max}}{\mu}\ln\left(1-\frac{X_0}{X_{\max}}\left(1-e^{\mu t}\right)\right) \tag{2}$$

where glycerol concentration $S(t)$ during cultivation could be calculated using initial glycerol concentration S_0, kinetic parameters previously determined using the Gompertz equation (X_0, $X_{\max}$ and μ), as well as by using γ and δ, considered as glycerol consumption constants related to growth and metabolites production, respectively [25].

RESULTS AND DISCUSSION

Analysis of antimicrobial activity of antagonistic agents against phytopathogenic *X. campestris* isolates

Production of preparations based on different microorganisms and their products for protection of agricultural crops has been gaining increasing interest in the last decade. Since microorganisms are an almost inexhaustible source of different bioactive compounds, great efforts are still invested in the development of new and efficient preparations. Therefore, this research investigates the possibility of applying different microbial antagonist for suppressing phytopathogenic isolates of *X. campestris* species. Cultivation broth samples obtained after cultivation of 14 antagonists and their filtrates, as well as commercial streptomycin discs, were tested against seven *X. campestris* isolates. Mean values of inhibition zone diameters obtained due to antimicrobial activity of cultivation broth samples and filtrates were calculated. Experimental results were analyzed using several statistical tests in order to adequately asses which preparation is the most efficient against phytopathogenic *X. campestris* isolates.

Results of the Levene's test for inhibition zone diameters measured after testing of cultivation broth samples have confirmed homogeneity of variances ($p = 0.9970$). Considering that the antagonistic effect can be expressed by both microorganisms' cells and its metabolites, inhibition zone diameters formed by the cultivation broth samples and their filtrates were compared (Figure 1). Filtration was carried out using filters with pore diameter of 0.22 μm in order to remove cells of antagonistic microorganisms.

Filtrates obtained by filtration of cultivation broth after cultivation of *B. subtilis* ATCC 6633 (M 1), *B. cereus* (M 2), *P. aeruginosa* ATCC 27853 (M 6), *Lactobacillus* sp. (M 10), *S. hygroscopicus* (M 12) and *S. cerevisiae* (M 13) didn't show antimicrobial activity against tested phytopathogenic isolates, which clearly indicates that the bioactive compound in these preparations is the biomass of cultivated antagonists. Monteiro *et al.* [11] and Issazadeh *et al.* [26] have showed similar antimicrobial activity of *B. subtilis* and *B. cereus* cultivation broths against *X. campestris* phytopathogenic strains. Research of *P. aeruginosa* strains activity has shown that bioactive compounds effective against *Xcc* [15] are metabolites contained in biomass-free filtrates or supernatants of cultivation broth, which is opposite to the results of this research. Different *Lactobacillus* strains were examined for their antimicrobial activity against pathogenic *Xantho-*

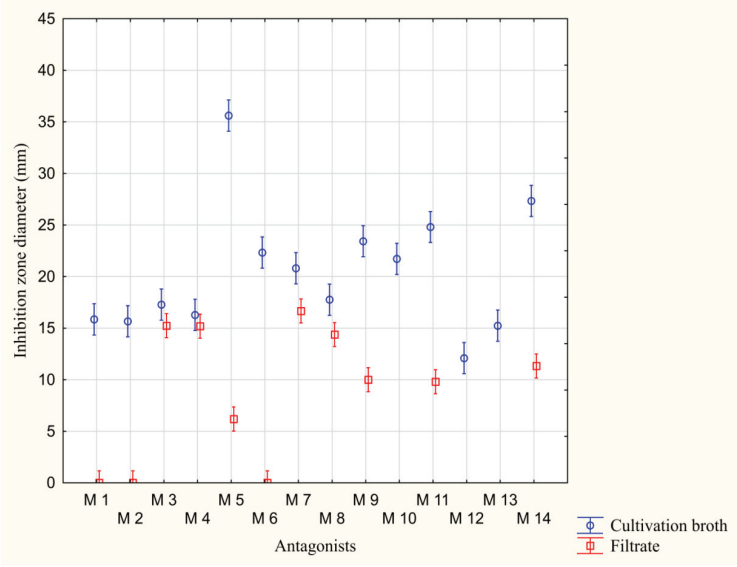

Figure 1. Inhibition zone diameters against seven Xanthomonas campestris strains for cultivation broth samples and filtrates obtained after cultivation of 14 antagonists.

monas strains. Kannan *et al.* [27] demonstrated antimicrobial activity of extracellular bioactive compounds of *Lactobacillus* against *X. campestris*. Encheva-Malinova *et al.* [28] demonstrated that cultivation broths of different *Streptomyces* isolates show antimicrobial activity against few *Xanthomonas* species. Biomass of *T. harzianum* has been shown to suppress growth of *Xcc* [13], while Deivamani and Muthamilan [20] showed antagonistic activity of different *Trichoderma* species' spores against black rot pathogen. The same authors have shown antagonistic activity of *S. cerevisiae* against *Xcc* [20].

Filtrates of cultivation broth samples obtained by cultivation of other antagonists showed certain antimicrobial activity, but in case of each antagonist, inhibition zone diameter obtained by cultivation broth testing was larger than the inhibition zone diameter obtained by filtrate testing. Statistical analysis of the presented results has showed that only for strain M 4 (*Bacillus* sp.) there wasn't statistically significant difference between inhibition zone diameters resulting from cultivation broth and filtrate activity (p = 0.2919). These results indicate that the bioactive compound is synthesized extracellular antimicrobial metabolite. On the other hand, preparations based on *Bacillus* spp. (M 3, M 5), *P. aeruginosa* from water (M 7), *P. putida* (M 8), *Lactobacillus* spp. (M 9, M 11) and *T. reesei* QM 9414 (M 14) have showed statistically significant larger inhibition zone diameters when applied as unfiltered cultivation broth, which is confirmed by p-values of 0.0023, 0.0956, 0.0051, 0.0182, 0.0000, 0.0000 and 0.0039, respectively. Higher antimicrobial activity of cultivation broth could suggest that biomass is more likely to be the bioactive agent against phytopathogenic *X. campestris* isolates.

Homogenous groups of antagonists and significance of differences were established using Duncan's multiple range test (Table 1).

Table 1. Mean values of inhibition zone diameters obtained by assaying cultivation broth samples of tested antagonists against Xanthomonas campestris isolates; values marked with the same superscript letter are at the same level of significance with confidence level of 95% (Duncan's test)

Antagonist	Inhibition zone diameter, mm
M 12	12.10±3.28[a]
M 13	15.24±3.40[b]
M 2	15.67±3.32[bc]
M 1	15.86±3.31[bc]
M 4	16.29±3.49[bc]
M 3	17.29±3.36[bc]
M 8	17.76±3.85[c]
M 7	20.81±3.72[d]
M 10	21.71±3.48[de]
M 6	22.33±3.29[de]
M 9	23.43±3.44[ef]
M 11	24.81±3.72[f]
M 14	27.33±3.80[g]
M 5	35.62±3.76[h]
K[a]	36.10±3.53[h]

[a]Commercial streptomycin disks

Results presented in Table 1 show that cultivation broth samples for each examined antagonist have manifested antimicrobial activity against tested phytopathogenic *X. campestris* isolates and that there

was statistically significant difference between their activities. The antagonist that has showed the weakest antimicrobial activity (the smallest inhibition zone diameter) against tested phytopathogens was *S. hygroscopicus* (M 12), while the best antagonist for this purpose was *B. velezensis* (M 5), which has shown the highest potential for suppressing infections caused by phytopathogenic *X. campestris* strains. In order to confirm antagonistic activity of biomass of *B. velezensis*, centrifugation of the cultivation broth sample was performed (10000 rpm, 10 min). The obtained solid phase after the supernatant had been discarded was resuspended in the same volume of sterile saline and homogenized using vortex. Antimicrobial activity of resuspended biomass was also tested using the diffusion-disc method against the tested phytopathogenic *X. campestris* strains under the previously defined conditions. Mean value and standard deviation of the obtained inhibition zone diameters was 32.85±3.82 mm, suggesting that the most of *B. velezensis* antimicrobial effect arises from biomass activity. Furthermore, presented results point out that there was no statistically significant difference between antimicrobial activity of this antagonist and bactericidal activity of commercial streptomycin discs (K) (p = 0.6615), indicating that *B. velezensis* has a great potential for application in biological control of diseases caused by phytopathogenic *X. campestris* strains.

Analysis of different carbon and organic nitrogen sources' effects on antimicrobial activity of *B. velezensis* against phytopathogenic *X. campestris* isolates

Since *B. velezensis* has arisen as the best potential antagonistic agent among tested antagonists, the next step was to determine the optimal combination of carbon and organic nitrogen sources in the medium for its cultivation. Cultivation broth samples of this isolate were tested against phytopathogenic *X. campestris* strains in further assays, since they have shown a larger inhibition zone diameter compared to filtrate. The chosen carbon sources were selected to represent the main nutrients in effluents of different food industries in order to estimate the potential of application of different waste streams in production of bioactive agents effective against black rot pathogens. Glucose was selected as the main carbon source in effluents from fruits and vegetables processing, as well as in vinery wastewaters, simultaneously being most widely used sugar in biotechnological production. Industrial waste containing high levels of glucose was used for biosurfactant production by *B. subtilis* [29]. Sucrose is the main component of molasses, a by-product of sugar beet and sugar cane processing. Molasses has been mainly used as cultivation medium for biosurfactants production by different *Bacillus* strains [30]. Płaza *et al.* [31] investigated antifungal activity of Bacilli cultivated on different agro-industrial wastes, including molasses. Lactose is mainly distributed in waste streams from the dairy industry. Gomaa [32] investigated antimicrobial activity of biosurfactant produced by *B. licheniformis* M104 using whey as cultivation medium. Starch can be found in wastewaters and effluents of grains, cassava and potato processing. Cassava wastewater was proved as good cultivation medium for production of surfactant by *B. subtilis* [33]. Starch processing water was used for production of *B. thuringiensis* biopesticide [34]. Glycerol is obtained in significant amount as by-product of continuously growing biodiesel industry and there has been significant scientific interest in its conversion to different value-added products using microorganisms [35]. Crude glycerol from biodiesel synthesis was used as carbon source in cultivation medium for production of biosurfactants by *B. subtilis* ATCC 6633 [36]. Examined organic nitrogen sources were commonly used yeast extract, peptone, soybean flour, L-glutamic acid and urea.

Two-way ANOVA was employed to determine whether there were significant differences between inhibition zone diameters obtained by assaying cultivation broth samples of *B. velezensis* against seven *X. campestris* phytopathogenic isolates, as a result of using different carbon and organic nitrogen sources in the cultivation medium. ANOVA results have showed that the effects of carbon and organic nitrogen sources, as well as their interaction, were significant (p-values less than 0.05, Table 2).

Table 2. Two-way ANOVA of inhibition zone diameter obtained by assaying Bacillus velezensis cultivation broth samples against Xanthomonas campestris isolates; SS - sum of squares; DF - degree of freedom; MS - mean square

Source of variability	SS[1]	DF[2]	MS[3]	F	p-value
Carbon source	717.7	4	177.9	13.63	0.0000
Nitrogen source	1506.0	4	376.5	28.85	0.0000
Carbon source*Nitrogen source	1954.1	16	122.1	9.36	0.0000
Error	1631.5	125	13.1	-	-

In order to determine which combination of carbon and organic nitrogen source is the most suitable for production of bioactive agents effective against tested *X. campestris* isolates by *B. velezensis*, Figures 2 and 3 were generated, which present the mean values of inhibition zone diameters for each carbon and organic nitrogen source, respectively. As it can be seen in Figure 2, the best carbon sources were glycerol and lactose, followed by starch and sucrose, while the presence of glucose in the cultivation medium has resulted in the lowest inhibition zone diameter. These results indicate the high potential of glycerol, as the by-product of biodiesel production, and dairy waste streams, which contain lactose, for production of bioactive agents by *B. velezensis* for biological control of black rot. Considering that the ability to degrade β-1→4 glycosidic bond of lactose is not a common characteristic among microorganisms [37], utilization of dairy industry waste streams by microbial conversion is therefore limited. Since the dairy industry generates one liter of wastewater per one liter of produced milk [38], the fact that *B. velezensis* metabolize lactose as a carbon source opens up a new chapter of possibilities for dairy industry waste streams utilization for the production of value-added microbial products. On the other hand, the ability of *B. velezensis* to metabolize glycerol presents a basis for utilization of raw glycerol from biodiesel industry. This effluent represents a major problem since it has been generated in large amounts (10% compared to the produced biodiesel amount) and contains very high concentrations of different impurities arising from raw materials used for biodiesel production, as well as from the biodiesel production process itself [39]. There is an ongoing scientific challenge to reveal possible routes for raw glycerol exploitation, where microbial conversion into different microbial products represents one of the attractive solutions [39]. Therefore, further research of production of biocontrol agents by *B. velezensis* will include the investigation of suitability of raw glycerol as a carbon source in this bioprocess.

When it comes to organic nitrogen sources (Figure 3), yeast extract was shown to be the best solution, followed by peptone, L-glutamic acid and urea. Since amino acids are the preferred nitrogen source for the most *Bacillus* species, yeast extract, that contains variety of amino acids, and peptone, which contains peptides and amino acids, were shown to be the best nitrogen sources for *B. velezensis*. Although yeast extract has been considered an expensive nitrogen source, further optimization of cultivation medium composition in terms of nutrients' content would show the required amount of this nitrogen source and the economical profitability of its application in cultivation medium. Also, the usage of complex carbon sources, such as dairy wastewater and molasses, could satisfy producing microorganism's nutritional requirements for amino acids, therefore optimization could show that the required amount of organic nitrogen source could be low. Soybean flour, although the economically most payable organic nitrogen source, was shown to be the least suitable solution in this particular case.

Mean values of inhibition zone diameters obtained by testing *B. velezensis* cultivation broth

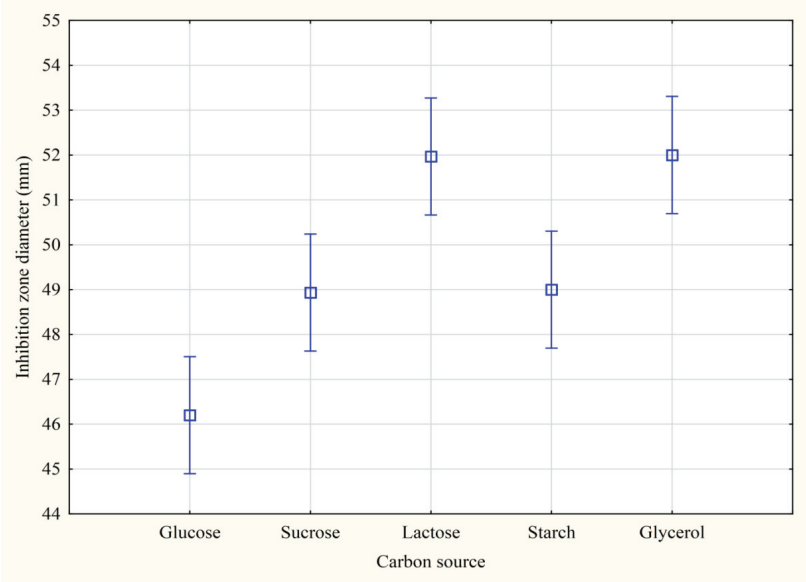

Figure 2. Inhibition zone diameters against seven Xanthomonas campestris strains obtained using different carbon sources in cultivation medium for Bacillus velezensis.

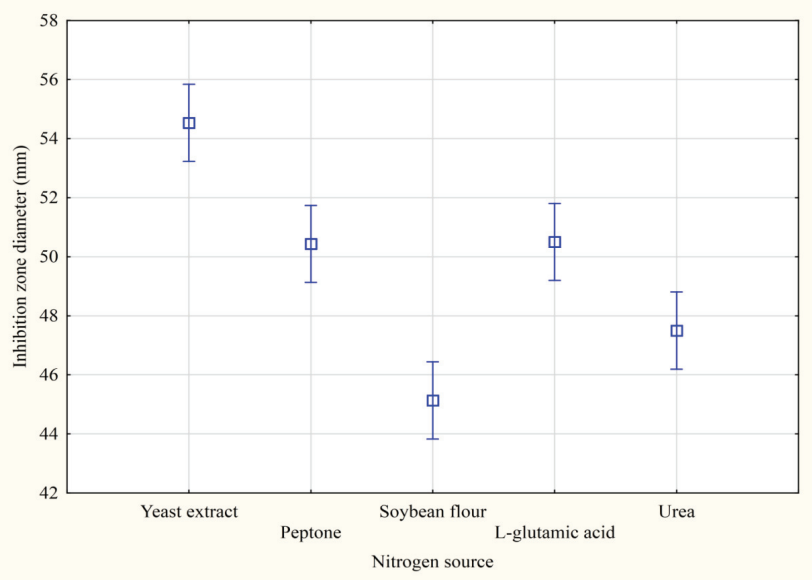

Figure 3. Inhibition zone diameters against seven Xanthomonas campestris strains obtained using different nitrogen sources in cultivation medium for Bacillus velezensis.

samples against seven *X. campestris* isolates for each investigated combination of carbon and organic nitrogen sources and the results of Duncan's test are given in Table 3. Duncan's test was performed to examine whether any combinations of carbon and organic nitrogen sources are at the same level of statistical significance.

As the results presented in Table 3 show, the lowest antimicrobial activity of *B. velezensis* was evinced when sucrose and L-glutamic acid were used as carbon and organic nitrogen sources in the cultivation medium. The highest inhibition zone diameter was obtained when a combination of glycerol and yeast extract was used, but data also suggests that combinations of lactose and peptone, as well as sucrose and yeast extract, are at the same level of statistical significance, indicating that the potential of these carbon sources, *i.e.*, dairy effluents and molasses, is only slightly lower than the potential of glycerol when it comes to the production of biocontrol agents. Since molasses, as a sucrose source, and dairy wastewater, as a lactose source, contain significantly smaller amounts of amino acids compared to standard organic nitrogen sources, as yeast extract, these cultivation media should be supplemented with yeast extract or peptone as the preferred nitrogen sources by *B. velezensis*.

Bioprocess kinetics

Since the previously discussed experimental results suggest that biomass of *B. velezensis* presents the major biocontrol agent against phytopathogenic *X. campestris* strains, it is of a great importance

Table 3. Mean values of inhibition zone diameters obtained by assaying Bacillus velezensis cultivation broth samples against Xanthomonas campestris isolates, obtained due to usage of different carbon and organic nitrogen sources in cultivation medium; values marked with the same superscript letter are at the same level of significance with confidence level of 95% (Duncan's test)

Carbon source	Nitrogen source	Inhibition zone diameter, mm
Sucrose	L-Glutamic acid	40.83 ± 0.41^{a}
Glucose	Soybean flour	41.33 ± 2.66^{ab}
Lactose	Urea	44.00 ± 1.26^{abc}
Starch	Soybean flour	44.83 ± 0.75^{abc}
Sucrose	Soybean flour	44.83 ± 0.98^{abc}
Glucose	Yeast extract	45.83 ± 1.33^{bcd}
Glycerol	Peptone	45.83 ± 1.33^{bcd}
Glucose	Peptone	46.50 ± 3.08^{cde}
Starch	Urea	46.67 ± 2.25^{cde}
Lactose	Soybean flour	46.83 ± 4.31^{cde}
Glucose	Urea	47.50 ± 0.84^{cdef}
Glycerol	Soybean flour	47.83 ± 5.31^{cdef}
Starch	Peptone	48.67 ± 1.21^{cdef}
Sucrose	Urea	48.83 ± 0.98^{cdef}
Glucose	L-Glutamic acid	49.83 ± 4.75^{defg}
Glycerol	Urea	50.50 ± 3.56^{defgh}
Starch	L-Glutamic acid	51.33 ± 5.20^{efghi}
Sucrose	Peptone	51.67 ± 0.52^{fghi}
Starch	Yeast extract	53.50 ± 6.32^{ghi}
Lactose	Yeast extract	54.00 ± 5.55^{ghi}
Glycerol	L-Glutamic acid	55.00 ± 2.61^{hij}
Lactose	L-Glutamic acid	55.50 ± 1.76^{ijk}
Sucrose	Yeast extract	58.50 ± 3.87^{jkl}
Lactose	Peptone	59.50 ± 7.15^{kl}
Glycerol	Yeast extract	60.83 ± 6.21^{l}

to investigate the kinetics of biomass growth, as well as the kinetics of carbon source (*i.e.*, glycerol) consumption, and to establish kinetic models suitable for description of these bioprocess outcomes. Data required for determination of bioprocess kinetic parameters are biomass concentration and glycerol content in different periods during the bioprocess. These data were gathered by sampling the cultivation broth during a validation experiment in a laboratory-scale bioreactor at predefined time intervals. The obtained kinetic parameters using the Gompertz model for biomass growth and modified Luedeking-Piret Equation for glycerol consumption are given in Table 4.

Experimental data fitting using the obtained parameters of Gompertz biomass growth model and modified Luedeking-Piret equation for glycerol consumption are given in Figures 4 and 5, respectively.

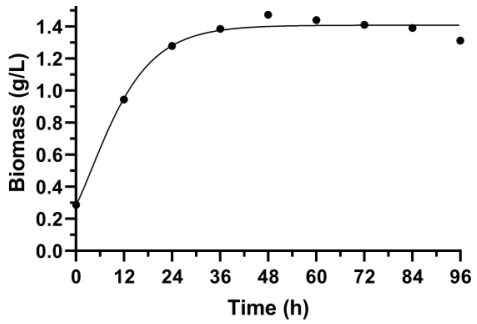

Figure 4. Experimental data fitting for Bacillus velezensis biomass concentration using Gompertz growth model.

Initial biomass concentration obtained using the Gompertz growth model was 0.282 g/L, which is in accordance with the experimental value of 0.287 g/L. Exponential growth phase could be observed until the 48th hour of cultivation, when the predicted value of maximal biomass concentration was 1.409 g/L (Figure 4). Afterwards, a slight decrease of biomass content was noticed until the end of the bioprocess. Calculated average specific growth rate for *B. velezensis* was 0.118 1/h. Coefficient of determination for the Gompertz growth model was 0.9860, indicating very good fitting of the experimental data using this equation. Since the maximal biomass content was observed at 48th hour of cultivation, there is a possibility to shorten bioprocess duration from 96 to 48 h. In this way, significant savings could be made when it comes to the bioprocess cost, especially considering the possibility of bioprocess scale-up to pilot or industrial scale, which would be the ultimate goal of bioprocess development.

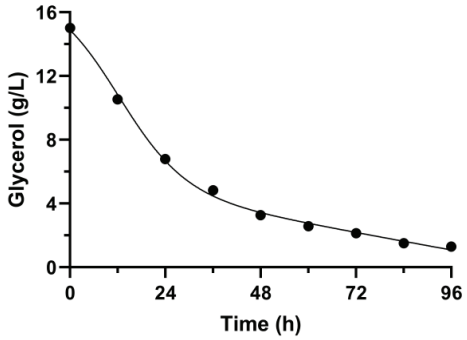

Figure 5. Experimental data fitting for glycerol consumption by Bacillus velezensis using modified Luedeking-Piret equation.

When it comes to the usage of modified Luedeking-Piret Equation for describing glycerol consumption during batch cultivation of *B. velezensis* (Figure 5), it could be concluded that the given equation has shown satisfying fitting ability of the obtained experimental data, with coefficient of determination of 0.9979. Also, initial glycerol content predicted by this equation was 14.89 g/L, which is in a very good accordance with 15 g/L of glycerol initially added during cultivation medium preparation. Glycerol consumption constant related to growth (γ), being significantly higher than constant related to metabolites production (δ), has also suggested that the major amount of glycerol was utilized for growth of *B. velezensis*, while only a minor amount of glycerol was used for metabolites production. These kinetic parameters confirm previously discussed results, where only slight difference of inhibition zone diameters could be observed during testing of antimicrobial activity of cultivation broth samples and *B. velezensis*

Table 4. Bioprocess kinetic parameters and model predicted values for biomass growth and glycerol consumption during cultivation of Bacillus velezensis in the laboratory-scale bioreactor

Model	Parameter	Value of the kinetic parameter	R^2 value
Gompertz – biomass concentration	X_{max} (g/L)	1.409	0.9860
	X_0 (g/L)	0.282	
	μ (1/h)	0.118	
Modified Luedeking-Piret – glycerol concentration	S_0 (g/L)	14.89	0.9979
	Y (g_S/g_X)	8.916	
	δ ($g_S/g_X \cdot h^{-1}$)	0.032	

biomass, indicating that biomass of *B. velezensis* is the main biocontrol agent effective against tested phytopathogenic *X. campestris* strains.

Further steps in bioprocess development should include optimization of cultivation medium composition in terms of main nutrients' quantity aiming at maximal yield of *B. velezensis* biomass, as well as investigation of cultivation parameters effect on bioprocess outcomes. Also, since the literature data suggest that *B. velezensis* shows supreme ability to synthesize a wide range of different antimicrobial metabolites [40], including lipopeptide antibiotics, further research will include analysis of cultivation broth supernatants using LC-MS and MALDI-TOF in order to identify and characterize antimicrobial compounds produced by this strain. The reason for further investigation in this field is the fact that the biomass-free filtrate from the first experimental stage in this study has also shown antimicrobial activity against tested phytopathogenic *X. campestris* strains isolated from plants with black rot symptoms, suggesting the presence of some antimicrobial compounds biosynthesized by *B. velezensis*. Further optimization of cultivation medium composition and cultivation conditions could also be aimed at directing metabolic activity of *B. velezensis* towards synthesis of targeted antimicrobial compounds in larger amounts. Formulation of final biocontrol product could be adjusted for biomass of the producing microorganism or targeted, separated and purified antimicrobial compounds, but as well as for product containing both biomass and bioactive compounds, depending on the requirements of eventual product application in the field.

CONCLUSION

B. velezensis has shown the greatest potential among tested antagonists to be used as biocontrol agent against phytopathogenic *X. campestris* strains, causing black rot of cruciferous crops. The optimal combinations of nutrients in the cultivation medium for production of bioactive compounds by *B. velezensis* were glycerol and yeast extract, lactose and peptone, as well as sucrose and yeast extract. Kinetic study performed during the validation experiment in the laboratory-scale bioreactor, using optimal carbon and nitrogen sources in the cultivation medium, has confirmed the results which indicate that biomass of *B. velezensis* presents the major bioactive agent effective against phytopathogenic *Xanthomonas* spp. Since the biomass-free filtrate has also shown antimicrobial activity against tested phytopathogens, further research will also include LC-MS and MALDI-TOF analysis to identify the produced antimicrobial compounds. The results of this study confirm biocontrol potential of *B. velezensis* and represent a basis for further bioprocess development in terms of optimization of cultivation medium composition and cultivation parameters, including investigation of different industrial waste streams, ultimately aimed at defining of a techno-economically viable bioprocess solution applicable at industrial scale.

Acknowledgement

This research was supported by the Ministry of education, science and technological development of the Republic of Serbia, project: 451-03-68/2020-14/200134.

REFERENCES

[1] A. Aires, C.S.P. Dias, R. Carvalho, M.H. Oliveira, A.A. Monteiro, M.V. Simões, E.A.S. Rosa, R.N. Bennett, M.J. Saavedra, Sci. Hortic. 129 (2011) 503–510

[2] J.G. Vicente, E.B. Holub, Mol. Plant Pathol. 14 (2013) 2–18

[3] J.D. Taylor, J. Conway, S.J. Roberts, D. Astley, J.G. Vicente, Phytopathology 92 (2002) 105–111

[4] C.A. Nunes, Eur. J. Plant Pathol. 133 (2012) 181–196

[5] R.R. Sharma, D. Singh, R. Singh, Biol. Control 50 (2009) 205–221

[6] A. Pérez-García, D. Romero, A. de Vicente, Curr. Opin. Biotechnol. 22 (2011) 187–193

[7] S. Compant, B. Duffy, J. Nowak, C. Clément, E.A. Barka, Appl. Environ. Microbiol. 71 (2005) 4951–4959

[8] C.L. Luna, R.L.R. Mariano, A.M. Souto-Maior, Braz. J. Chem. Eng. 19 (2002) 133–140

[9] E.G. Wulff, J.W.L. van Vuurde, J. Hockenhull, Plant Soil 255 (2003) 463–474

[10] S.M.S. Massomo, C.N. Mortensen, R.B. Mabagala, M.A. Newman, J. Hockenhull, J. Phytopathol. 152 (2004) 98–105

[11] L. Monteiro, R.D.R. Mariano, A.M. Souto-Maior, Braz. Arch. Biol. Technol. 48 (2005) 23–29

[12] P. Zhao, Y. Xue, W. Gao, J. Li, X. Zu, D. Fu, X. Bai, Y. Zuo, Z. Hu, F. Zhang, Peptides 101 (2018) 10-16

[13] I. Nikolić, Ž. Ivanović, J. Blagojević, S. Živković, T. Popović, Zašt. Bilja 64 (2013) 189–197

[14] E.G. Wulff, C.M. Mguni, C.N. Mortensen, C.L. Keswani, J. Hockenhull, Eur. J. Plant Pathol. 108 (2002) 317–325

[15] S. Mishra, N.K. Arora, World J. Microbiol. Biotechnol. 28 (2012) 693–702

[16] F.R. Spago, C.S.I. Mauro, A.G. Oliveira, J.P.O. Beranger, M.V.T. Cely, M.M. Stanganelli, A.S. Simionato, J.A.B. San Martin, C.G.T.J. Andrade, J.C.P. Mello, G. Andrade, Crop Prot. 62 (2014) 46–54

[17] Shivalingaiah, S. Umesha, Can. J. Physiol. Pharmacol. 1 (2013) 147–153

[18] R. Vaitkevičienė, D. Žadeikė, E. Bartkienė, V. Krunglevičiūtė, V. Baliukoniene, S. Supronienė, G. Juodeikienė, Zemdirbyste 106 (2019) 59-64

[19] R. Trias, L. Baneras, E. Montesinos, E. Badosa, Int. Microbiol. 11 (2008) 231-236

[20] M. Deivamani, M. Muthamilan, J. Innov. Agric. 2 (2015) 1-9

[21] T. Veličković, Z. Rončević, J. Grahovac, A. Jokić, I. Mitrović, B. Bajić. J. Dodić, Chem. Ind. Chem. Eng. Q. 24 (2018) 399-410

[22] S.M.P. Assis, R.L.R. Mariano, S.J. Michereff, G. Silva, E.A.A. Maranhão, Rev. Microbiol. 30 (1999) 191-195

[23] N. Ortuño, J. A. Castillo, C. Miranda, M. Claros, X. Soto, Renew. Agr. Food Syst. 32 (2016) 366-375

[24] G.S. Saddler, J.F. Bradbury, in Bergey's Manual® of Systematic Bacteriology, Vol. 2: The Proteobacteria, Part B: The Gammaproteobacteria, Springer-Verlag GmbH, Wien, 2005, pp. 63-122

[25] A. Mohsin, K. Zhang, J. Hu, Salim-ur-Rehman, M. Tariq, W. Q. Zaman, I. M. Khan, Y. Zhuang, M. Guo, Carbohydr. Polym. 181 (2018) 793-800

[26] K. Issazadeh, S.K. Rad, S. Zarrabi, M.R. Rahimibashar, Afr. J. Microbiol. Res. 6 (2012) 1615-1620

[27] N. M. Kannan, Abhiramy, P. Rajvanshi, IJAPBC 3 (2014) 1016-1027

[28] M. Encheva-Malinova, M. Stoyanova, H. Avramova, Y. Pavlova, B. Gocheva, I. Ivanova, P. Moncheva, Biotechnol. Biotechnol. Equip. 28 (2014) 721-727

[29] J.F.F. Secato, D.F. Coelho, N.G.J. Rosa, L.D.L. Costa, E.B. Tambourgi, Chem. Eng. Trans. 49 (2016) 103-108

[30] S.N. Al-Bahry, Y.M. Al-Wahaibi, A.E. Elshafie, A.S. Al--Bemani, S.J. Joshi, H.S. Al-Makhmari, H.S. Al-Sulaimani, Int. Biodeterior. Biodegradation 81 (2013) 141-146

[31] G.A. Płaza, E. Król, M. Pacwa-Płociniczak, Z. Piotrowska-Seget, L.R. Brigmon, Acta Sci. Pol. Hortorum Cultus 11 (2012) 169-182

[32] E.Z. Gomaa, Braz. Arch. Biol. Technol. 56 (2013) 259--268

[33] M. Nitschke, G.M. Pastore, Bioresour. Technol. 97 (2006) 336-341

[34] M. Chang, S.G. Zhou, N. Lu, J.R. Ni, World J. Microbiol. Biotechnol. 24 (2008) 441-447

[35] C. Li, K. L. Lesnik, H. Liu, Energies 6 (2013) 4739-4768

[36] M. de Sousa, I.T. Dantas, A.K.N. Felix, H.B. de Sant'Ana, V.M.M. Melo, L.R.B. Gonçalves, Braz. Arch. Biol. Technol. 57 (2014) 295-301

[37] Sumithra, A.V.N. Swamy, V.V. Basava Rao, IJAR 4 (2016) 2196-2200

[38] M. Priyadharshini, R.S. Kumar, IJMTST 3 (2016) 133-138

[39] V.K. Garlapati, U. Shankar, A. Budhiraja, Biotechnol. Rep. 9 (2016) 9-14

[40] L. Chen, H. Shi, J. Heng, D. Wang, K. Bian, Microbiol. Res. 218 (2019) 41-48.

JOVANA GRAHOVAC
IVANA PAJČIN
VANJA VLAJKOV
ZORANA RONČEVIĆ
JELENA DODIĆ,
DRAGOLJUB CVETKOVIĆ
ALEKSANDAR JOKIĆ

Univerzitet u Novom Sadu, Tehnološki fakultet Novi Sad, Novi Sad, Srbija

NAUČNI RAD

BIOKONTROLNI AGENS PATOGENA *Xanthomonas campestris*: ODABIR, FORMULACIJA HRANLJIVE PODLOGE I ANALIZA KINETIKE BIOPROCESA

Crna trulež uzrokovana patogenom Xanthomonas campestris pv. campestris je jedna od najznačajnijih bolesti biljaka iz porodice kupusnjača, koja izaziva značajne gubitke prinosa. Biološka kontrola crne truleži mikrobiološkim biokontrolnim agensima predstavlja obećavajuću alternativu hemijskim tretmanima i dobroj poljoprivrednoj praksi, koji pokazuju samo ograničenu uspešnost u suzbijanju bolesti. U ovom radu ispitan je potencijal različitih antagonista iz rodova Bacillus, Pseudomonas, Lactobacillus, Streptomyces, Saccharomyces i Trichoderma za biološku kontrolu crne truleži. Antimikrobna aktivnost uzoraka kultivacione tečnosti i njihovih filtrata testirana je protiv sedam sojeva Xanthomonas campestris, izolovanih iz obolelih biljaka, primenom disk-difuzione metode. Najveći prečnik zone inhibicije (35,62±3,76 mm) pokazao je izolat Bacillus velezensis. Nakon toga su ispitane različite kombinacije izvora ugljenika i azota u kultivacionom medijumu u cilju maksimizacije antagonističke aktivnosti odabranog soja. Najbolje kombinacije su bile glicerol i ekstrakt kvasca, laktoza i pepton, kao i saharoza i ekstrakt kvasca, što ukazuje na potencijal efluenata industrije biodizela, mleka i šećera kao sirovina za proizvodnju bioaktivnih komponenti efikasnih protiv izazivača crne truleži. Validacioni eksperiment je izvršen u laboratorijskom bioreaktoru u cilju ispitivanja kinetike bioprocesa u pogledu rasta biomase i potrošnje izvora ugljenika, primenom kultivacionog medijuma koji sadrži optimalni izvor ugljenika i azota.

Ključne reči: Bacillus, biološka kontrola, crna trulež, izvor ugljenika, kultivacija, organski izvor azota.

CI&CEQ
Chemical Industry & Chemical Engineering Quarterly

Available on line at
Association of the Chemical Engineers of Serbia *AChE*
www.ache.org.rs/CICEQ

Chem. Ind. Chem. Eng. Q. 27 (2) 143–153 (2021) CI&CEQ

SHAMA MUSTAFA HAYDER
SALMAN HUSSAIN
WASIM AHMAD
MIRZA JAHANZAIB
ABAID ULLAH

University of Engineering and Technology, Taxila, Punjab, Pakistan

SCIENTIFIC PAPER

UDC 66.081.3:661.183.2:502/504

OPTIMIZATION OF LOW-COST COW DUNG BASED ACTIVATED CARBON FOR THE REMOVAL OF CARBOFURAN FROM AQUEOUS SOLUTION

Article Highlights

- Cow dung can be utilized to produce low-cost activated carbon by waste-to-wealth concept
- Cow dung-based activated carbon can be employed for removing pesticides from aqueous solution
- Maximum activated carbon yield and pesticide removal were 16 and 94%, respectively
- The optimized activated carbon yield and pesticide removal were 14.78 and 89.187%, respectively
- Most significant factors include activation temperature and impregnation ratio

Abstract

Water pollution has become a serious issue of this century due to increased industrialization. Several methods have been adopted to tackle this issue, including adsorption by activated carbon (AC). Conventional sources of AC preparation are costly and non-renewable as well. Several fruit and agricultural wastes have characteristics to become sustainable feedstock for AC preparation. This study aims to prepare cost effective AC from sustainable raw material, cow dung. The preparation has been analyzed and optimized by utilizing central composite design (CCD). The effect of activation temperature, time, and impregnation ratio (IR) on responses of percent yield (R_1) and percent pesticide removal (R_2) has been analyzed. Quadratic models have been suggested with R^2, adjusted R^2, and predicted R^2 values of 0.98, 0.96, 0.89 for R_1, and 0.97, 0.94, 0.87 for R_2, respectively. Activation temperature and KOH/Feedstock ratio significantly influence the yield and pesticide removal. Optimized conditions of activation temperature, KOH/Feedstock ratio, and activation time are 708.07 °C, 1.22 and 0.66 h, respectively. These conditions produced 14.78% yield and 89.18% pesticide removal. SEM and BET analysis of optimized AC also confirmed porosity development and large surface area availability due to activation process. Findings of this study suggest that cow dung can be used to prepare low-cost AC for pesticide removal from aqueous solution.

Keywords: adsorbent, activated carbon, biowaste, cow dung, pesticides, wastewater treatment.

Pesticides are synthetic substances used to mitigate the attacks of pests to avail the maximum yield of crops. However, along with the benefits of pesticides, there exist some hazards associated with their use. Most of the pesticides are toxic for living organisms and some of these are persistent in the environment posing a great hazard. Their persistence in environmental bodies like food, soil and water have potential to bio-accumulate and ultimately bio-magnify in living organisms causing detrimental effects [1]. Moreover, inappropriate and excessive use of pes-

Correspondence: S.M. Hayder, University of Engineering and Technology, Taxila, Taxila, Punjab, Pakistan
E-mail: shamamustafahayder@gmail.com
Paper received: 27 April, 2020
Paper revised: 11 August, 2020
Paper accepted: 26 August, 2020

https://doi.org/10.2298/CICEQ200427033H

ticide pollutes the water bodies endangering the aquatic life and rendering the water bodies unsuitable for routine operations [2].

The global amount of sprayed pesticide has reached above 4.6 million tons per annum. The effective amount accounts for only 1% and the rest 99% ends up in different environmental bodies. A report of United States' EPA says that out of 127 pesticides at least one is present in many rural wells. A study reported the presence of pesticides in 90 different sites, from the equator to cold regions. Considerable amounts have also been found in Greenland ice sheets and Antarctic penguins [3].

In Pakistan, 245 metric tons of pesticides were consumed in 1954 and by 2011 it has reached up to 70,000 tons. The extra amount applied, the careless handling and storage, improper transportation and use of outdated and banned pesticides have led to a number of environmental problems [4]. Some studies have indicated the presence of pesticides in water bodies of different agricultural areas of Pakistan [5-11].

Carbofuran is a carbamate pesticide, widely used for a variety of fruits and vegetables. It is highly toxic to humans, birds and aquatic life, having acute and chronic effects. It causes cholinesterase inhibition in humans and animals and has been found to be responsible for escalated risks of diabetes [12]. The World Health Organization (WHO) has recommended the drinking water standard of 3 μg/L for carbofuran [5]. However, in Pakistan it has been found in some water samples above permissible limits [5,7]. So, there is dire need to regulate its exposure into the environment and to eliminate the existing quantities from environmental bodies.

Various processes have been proposed for the treatment of contaminated water to make it potable and safe for other applications. These processes include adsorption, membrane filtration and advanced electrochemical oxidation methods. Adsorption is extensively studied and applied due to lower cost, easy operation and higher efficiency than the other methods [13]. Activated carbon has been used as adsorbent material and it provides exceptional results. A recent study employed an activated carbon fixed bed setup for adsorption of Ni ions from aqueous solution. The effects of different parameters were studies and the adsorption mechanism was determined by CFD analysis. The study concluded that activated carbon is capable of 90% removal of metal ions from solution [14]. Activated carbons available on the market are expensive owing to their reliance on conventional non-sustainable and non-renewable raw materials and hence the high cost of production cannot be justified for use in wastewater treatment. So, in search of inexpensive and renewable raw materials, researchers have successfully prepared activated carbons for water treatment from fruit and agricultural bio-wastes like orange tree leaves [15], hemp fibers [16], and corncobs [17] following the waste-to--wealth concept [18]. However, due to a large spectrum of pollutants it is highly desirable to produce very specific activated carbon for specific application.

The major factors controlling the qualities of carbon are its preparation conditions which can be manipulated to get suitable properties. The effect of various factors can easily be analyzed through an appropriate experimental design. Response surface methodology (RSM) is an opposite tool to analyze the interaction of different factors. RSM can also be used to optimize the experimental conditions and it has been used for many processes and preparation of activated carbons as well [19].

Cow dung is an abundantly available waste material due to a huge livestock industry. The composition of cow dung (35.97% holocellulose and 19.02% lignin) implies that it can be a worthy feedstock for activated carbon preparation [20].

Bhattacharjya *et al.* prepared cow dung-based activated carbon for electrodes of capacitors. Surface area of 1500-2000 m^2/g with different KOH ratios and maximum capacitance of 124 F/g was obtained [21]. Demiral *et al.* studied the surface properties of cow dung-based activated carbon and reported that surface area as high as 1916 m^2/g can be achieved with KOH activation [22]. Elaigwu prepared activated carbon from cow dung to remove metallic ions from simulated water solution and described that cost effective adsorbent can be prepared by cow dung having good capability to remove lead(II) ions [23]. Li *et al.* carried out activation of cow dung using various activating agents and stated that $ZnCl_2$, KOH and K_2CO_3 produced good activated carbons. Moreover, sewage from cow farm was treated to remove chemical and biological oxygen demand effectively and it was showed that after treatment the sewage met the discharge standards [20].

Limited studies were found utilizing the cow dung-based activated carbon for water treatment, especially using RSM. Thus, the novelty of the current work is to produce a low-cost, highly selective and sustainable cow dung-based KOH-activated AC for carbofuran removal from simulated water solution using RSM. Moreover, the effect of different variables and optimal conditions for maximum pesticide removal and yield are also a point of interest. Potassium hydroxide (KOH) is used for activation of cow dung as

it is an environment-friendly activating agent and it keeps tar formation at minimum. It reacts with carbon in the feedstock to make K_2CO_3 which upon reaction with more carbon produces potassium, potassium oxide, carbon monoxide and carbon dioxide. All these reactions produce porosity and large volumes of activated carbon [24,25].

EXPERIMENTAL

Materials and instruments

Analytical grade 99% pure carbofuran ($C_{12}H_{15}NO_3$) and ≥85% pure potassium hydroxide (KOH) were utilized, purchased from a local dealer of Sigma Aldrich. Distilled water and hydrochloric acid (37%, Sigma Aldrich) were used for washing of samples. All solutions were made in distilled water. Cow dung was fetched from a local dairy farm in dried form. Scanning electron microscope (Tescan Vega LMU) was used for surface morphology of AC. Surface area and porosity measures were taken by using BET surface area and porosity analyzer (Tristar II 3020).

Preparation of activated carbon

Dry cow dung fetched from a local dairy farm has been used as feedstock for AC preparation following the steps given in Figure 1. The feedstock was pulverized using mortar and pestle and sieved to get uniformity of particles. The powdered feedstock was dried in oven at 100 °C to eliminate the moisture content until constant weight. The dried feedstock was mixed with KOH in different ratios (KOH: Feedstock) and activated at different conditions according to experimental design in a furnace at constant heating rate. The obtained material was allowed to cool down to room temperature and rinsed with water to eliminate the activating agent. Washing with 0.5 M HCl was also carried out to remove the ash contents. Washing with water was continued till the pH of washed solution reached about 6-7. Washed carbon was dried in an oven at 1000 °C until it attained constant weight.

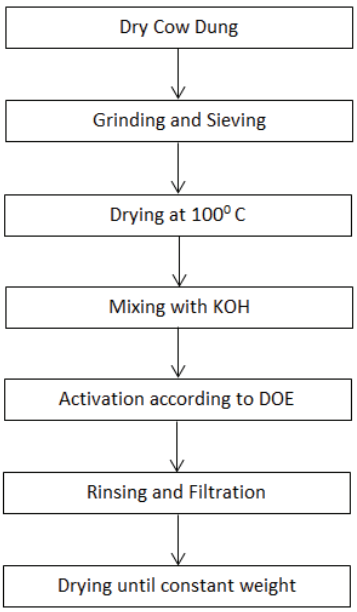

Figure 1. Steps of cow dung-based activated carbon preparation.

Performance measurements

Percentage yield

Yield of cow dung-based AC was computed on dry basis. Eq. (1) [26, 27] was used to calculate the percentage yield of prepared samples:

$$Yield = 100\frac{w_o}{w_i} \quad (1)$$

where w_o and w_i are final weights of dry AC and dry feedstock, respectively.

Percentage pesticide removal

Batch tests were conducted to evaluate the adsorption capacity of prepared activated carbons. Carbofuran solution having 100 mg/L concentration was taken in an Erlenmeyer flask and 0.30 g of cow dung-based AC (pH around 7.8) was mixed with it. The flask was kept in an isothermal shaker at 250 °C and 100 rpm and was occasionally checked for normal operation until the attainment of equilibrium which was around 6 h. The solution was then filtered to separate the AC and the remaining concentration of solution was measured by UV-1800 Perkin Elmer 750 nm spectrophotometer. The wavelength of carbofuran for maximum absorption was determined by taking 100 µg/mL in a cuvette and measuring its absorption at different wavelengths. It was found near 275 nm for carbofuran as evident from spectrum given in Figure 2. The calibration curve for carbofuran was found by measuring the absorbance of standard solutions of

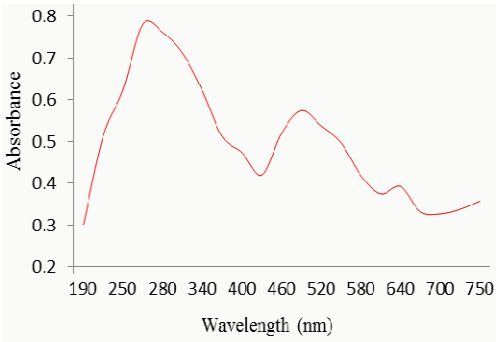

Figure 2. Maximum absorption spectrum for carbofuran.

carbofuran and the regression coefficient (R^2) for the calibration curve was 0.998. The calibration curve was used to measure the unknown concentration of solutions. The removal of carbofuran was determined by using Eq. (2) [27,28]:

$$\text{Percentage removal} = 100\frac{C_0 - C_f}{C_f} \quad (2)$$

where C_0 and C_f (mg/l) refer to initial and final concentrations of carbofuran in solution, respectively.

Design of experiments

Central Composite Design (CCD) was employed to study the effect of selected factors on activated carbon preparation. CCD is an efficient design able to employ appropriate mathematical models to study and optimize the effect of different factors on preparation of a product with a minimum number of experiments. It is a vital tool for experimentation as it allows modeling the data points with minimum number of experiments in a limited time and cost. Besides data fitting in an appropriate model, RSM is capable of optimization of results for desired outcome or to produce a highly specific product. Usually, it involves three types of points; (1) "2^k" Factorial/Cube (2) "$2k$" Axial/Star and (3) "C" Center points. The minimum number of experimental runs required for given number of factors (k) can be calculated by Eq. (3) [27]:

$$n = 2^k + 2k + C \quad (3)$$

Three important factors with their ranges were selected from literature. These factors included activation temperature, impregnation ratio (IR) and activation time. The total numbers of experiments for three factors based on Eq. (3) were 20, with 6 center points. These factors are important in deciding the characteristics of AC [29]. Cow dung-based AC yield and carbofuran removal were two responses measured and used to develop polynomial mathematical equations showing the relationship between the response and selected factors. Second order polynomial equation (Eq. (4)) was used to model the data points and to estimate the regression equation for both responses [28]:

$$R_i = \alpha_0 + \sum \alpha_i X_i + \sum \alpha_{ii} X_i^{\,2} + \sum_{i<j} \sum \alpha_{ij} X_i X_j + \varepsilon \quad (4)$$

where R_i, α_0, α_{ii}, α_{ij}, X_i, X_j and ε are the i-th response, constant, linear coefficient, square coefficient, interaction coefficient, i-th variable, j-th variable and random error, respectively. ANOVA along with other model adequacy checks were performed to check the significance of variables. Design Expert 7.0.0 was employed for data analysis. Selected factors for AC preparation and responses are given in the Table 1. The α values refer to the axial points of design.

ANALYSIS OF RESULTS

The design matrix of cow dung-based AC along with two responses is given in the Table 2, and the

Table 2. Design matrix with responses of yield and pesticide removal

Run	Variable factor			R_1	R_2 / %
	(A)	(B)	(C)		
1	500	1	1	16.33	62.90
2	700	1	1	13.33	87.00
3	500	3	1	13.40	85.00
4	700	3	1	10.53	94.60
5	500	1	2	14.80	70.00
6	700	1	2	11.73	81.60
7	500	3	2	13.20	84.30
8	700	3	2	10.20	91.00
9	432	2	1.5	13.80	69.80
10	768	2	1.5	9.00	93.60
11	600	0.32	1.5	15.20	61.00
12	600	3.68	1.5	10.33	89.10
13	600	2	0.66	14.10	88.30
14	600	2	2.34	12.33	88.70
15	600	2	1.5	11.40	93.60
16	600	2	1.5	11.13	88.40
17	600	2	1.5	10.86	88.20
18	600	2	1.5	10.66	88.00
19	600	2	1.5	10.80	88.10
20	600	2	1.5	11.10	91.00

Table 1. Selected factors and responses

Factor	$-\alpha$	Lower level	Center point	Upper level	$+\alpha$
Activation temperature (°C) (A)	432	500	600	700	768
Impregnation ratio (B)	0.32	1	2	3	3.68
Activation time (h) (C)	0.66	1	1.5	2	2.34
Responses					
1	Yield of AC, %			(R_1)	
2	Removal of pesticide, %			(R_2)	

coded factor-based models for responses are given by Eqs. (5) and (6). The magnitude of coefficients of the equation indicates the relative effect of factors on response. These equations can be used to predict the response at given levels of factors. The usefullness and quality of models can be assessed through the value of R^2. Usually the value of R^2 ranges from 0 to 1 and indicates good or bad fit of expermental data in the suggested model. A value closer to 1 suggests a good fit of experimental data in the model. However, adjusted and predicted R^2 is a better indicator of good fit as contrary to simple R^2, as simple R^2 always increases with the addition of the independent factor. Adjusted R^2 improves only when the new term in the model improves it. The predicted R^2 is calculated by deleting response points one by one and then re-estimating them using the developed model and hence it represents how accurately the developed model estimates the data point. With an increased number of factors the value of simple R^2 may increase due to random noise, providing the likelihood of overfitting of model with a high R^2 value but with a poor ability of making predictions. So, reporting the other two R^2 values for the validation of model becomes of great significance in such scenarios. For Eq. (5) the values of R^2, adjusted and predicted R^2 are 0.98, 0.96 and 0.89, respectively. The high value of R^2 suggests a good fit of the data in the suggested model. The adequately high values of adjusted R^2 and predicted R^2 suggests that the model is accurate and can be used to estimate the response. For Eq. (6) the values are 0.97, 0.94 and 0.87, respectively. The adequacy of the model is confirmed by these appropriate values and hence it is suggested that the model can used to predict the response accurately.

$$R_1 = 10.98 - 1.47A - 1.25B - 0.49C + 0.025AB - \\ -0.025AC + 0.33BC + 0.23A^2 + 0.71B^2 + 0.87C^2 \quad (5)$$

$$R_2 = 89.53 + 6.74A + 7.37B - 0.14C - 2.42AB - \\ -1.92AC - 0.75BC - 2.61A^2 - 4.96B^2 - 0.21C^2 \quad (6)$$

Eq. (4) can be used to predict the impact on R_1 by putting the levels of each factor and then changing the level of one factor to estimate its impact on R_1. The code for upper level is 1 and -1 for lower level. Below is given the calculation for R_1 for lower level (-1) of factor '*A*' and upper level (1) of factor '*B*' and '*C*':

R_1 = 10.979 - 1.4654*(-1) -1.2485*(1) - 0.486*(1) +
+ 0.025*(-1)*(1) - 0.025*(-1)*(1) +0.325*(1)*(1) +
+ 0.22686*$(-1)^2$+0.70946*$(1)^2$+0.86856*$(1)^2$

Hence, the value of R_1 comes out to be 12.8398.

By taking upper level (1) of factor '*A*' with higher levels (1) of factor '*B*' and '*C*', the R_1 becomes 9.9089:

R_1 = 10.979 - 1.4654*(1) -1.2485*(1) - 0.486*(1) +
+ 0.025*(1)*(1) - 0.025*(1)*(1) + 0.325*(1)*(1) +
+ 0.22686*$(1)^2$ + 0.70946*$(1)^2$ + 0.86856*$(1)^2$

It can be seen that by switching the factor '*A*' from lower to upper level, the value of response decreases. Hence it can be predicted that yield (R_1) decreases by increasing the activation temperature (*A*).

Similarly, the effect of factor level can be estimated for R_2 by taking lower level (-1) of factor '*A*' and upper level (1) of factor '*B*' and '*C*'. By putting the level values in Eq. (5):

R_2 = 89.53 + 6.74*(-1) + 7.37*(1) - 0.14*(1) -
- 2.42*(-1)*(1) - 1.92*(-1)*(1) - 0.75*(1)*(1) -
- 2.61*$(-1)^2$ - 4.96*$(1)^2$ - 0.21*$(1)^2$

R_2 = 85.83

Now Eq. (5) can be solved for upper level (1) of all factors to analyze the effect of factor level:

R_2 = 89.53 + 6.74*(1) + 7.37*(1) - 0.14*(1) -
- 2.42*(1)*(1) - 1.92*(1)*(1) - 0.75*(1)*(1) -
- 2.61*$(1)^2$ - 4.96*$(1)^2$ - 0.21*$(1)^2$

R_2 = 90.63

It is evident from the above calculation that carbofuran removal (R_2) is lower for lower level (-1) of activation temperature (*A*) and it becomes higher for upper level (1) of activation temperature (*A*) keeping the other two factor levels constant. It can be inferred that more activation is achieved at higher temperature due to which more removal is observed.

Analysis of variance (ANOVA)

ANOVA is another check of the model and it also provides information about significant terms. The significant terms have considerable effect on responses and play an important role in predicting the overall response. Ignoring any significant term renders the model less precise to estimate the response. The ANOVA results of R_1 and R_2 are provided in the Tables 3 and 4, respectively. *F*-value is defined as the ratio of source variability to residual variability. A high *F*-value suggests that residual variability is lower and the selected model can better explain the behavior of response. The *P*-value, smaller than 0.05, suggests that the specific term is significant. *P*-value is the probability of null hypothesis to be true for the observed *F*-value. Hence *P*-value lower than 0.05 suggests the rejection of the null hypothesis which states that an additional term would not render the model better. Rejection of the null hypothesis means that

Table 3. ANOVA for percent yield

Source	Sum of squares	Degrees of freedom	Mean square	*F*-Value	*P*-value
Model	71.323	9	7.924	62.698	< 0.0001
A	29.326	1	29.326	232.021	< 0.0001
B	21.287	1	21.287	168.417	< 0.0001
C	3.225	1	3.225	25.517	0.0005
AB	0.005	1	0.005	0.039	0.8463
AC	0.005	1	0.005	0.039	0.8463
BC	0.845	1	0.845	6.685	0.0272
A^2	0.742	1	0.741	5.868	0.0359
B^2	7.254	1	7.253	57.389	< 0.0001
C^2	10.872	1	10.871	86.015	< 0.0001

Table 4. ANOVA for percent carbofuran removal

Source	Sum of squares	Degrees of freedom	Mean square	*F*-Value	*P*-value
Model	1867.22	9	207.47	40.94	< 0.0001
A	620.12	1	620.12	122.36	< 0.0001
B	741.91	1	741.91	146.39	< 0.0001
C	0.27	1	0.27	0.05	0.8215
AB	47.04	1	47.04	9.28	0.0123
AC	29.64	1	29.64	5.85	0.0361
BC	4.50	1	4.50	0.89	0.3682
A^2	98.34	1	98.34	19.40	0.0013
B^2	355.02	1	355.02	70.05	< 0.0001
C^2	0.62	1	0.62	0.12	0.7330

additional terms have effect on the response and are called significant terms.

From Table 3, the *F*-value for R_1 is 62.698 suggesting that the model is significant. The terms "*A*, *B*, *C*, *BC*, A^2, B^2, C^2" are significant for R_1.

The *F*-value of 40.94 for R_2 presented in Table 4 specifies significance of the suggested model. Other significant terms of the model include "*A*, *B*, *AB*, *AC*, A^2, B^2".

The root mean square error (*RMSE*), mean absolute percentage error (*MAPE*), coefficient of variance (C.V) and variance accounted for (*VAF*) values are 0.25, 1.819, 2.91 and 98.26 for R_1, and 1.59, 1.59, 2.67 and 97.34 for R_2, respectively. The coefficient of variance *C.V* measures the dispersion of data around the mean and a lower values of *C.V* for R_1 and R_2 indicate a precise estimate of data and less dispersion around the mean. Lower *RMSE* and *MAPE* value are desirable for model adequacy. The obtained values of *RMSE* and *MAPE* are considerably low and hence suggest an accurate reproducibilty of data. The higher values of *VAF* for both models implies the closeness of experimental and predicted data [30].

Model diagnostics

Normal probability plots are employed to examine that if the data is normally distributed or not. The data is assumed to be normally distributed if all the residuals are adequately near to the straight line [31]. It can be seen from Figures 3 and 4 that for both responses the residual points are sufficiently close to the standard line suggesting the normality of data. Figure 5 presents the actual *vs*. predicted values of yield and pesticide removal data. The closeness of the points with the straight line discloses that actual and predicted values differ slightly. It also confirms the model adequacy.

Factor effects on cow dung AC yield (R_1)

Temperature of activation has the highest effect as indicated by a highest F-value of 232.02 from Table 3. Impregnation ratio and activation time also have an effect on yield but to a lesser extent than the temperature. It is observed that all three factors have a negative effect on the yield as evident from Table 2. The effect of activation time and impregnation ratio on R_1 with constant activation temperature at center point (T=600 °C) is shown in Figure 6(a). It is evident that higher yield is obtained at lower activation time and impregnation ratio. However, IR seems to have more effect than activation time on yield. Figure 6(b) depicts the response graph of activation time and temperature with constant IR at center point (IR=2). A higher value of these factors produces lower yield.

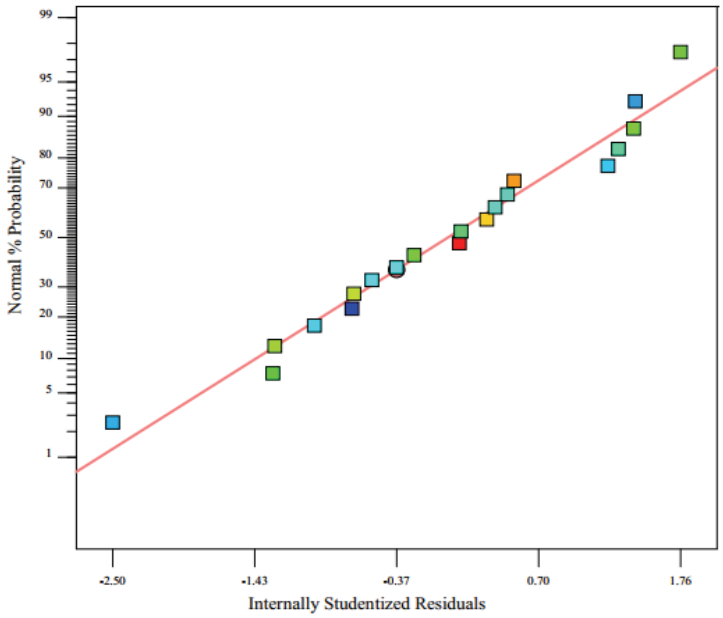

Figure 3. Normal probability plot for % yield.

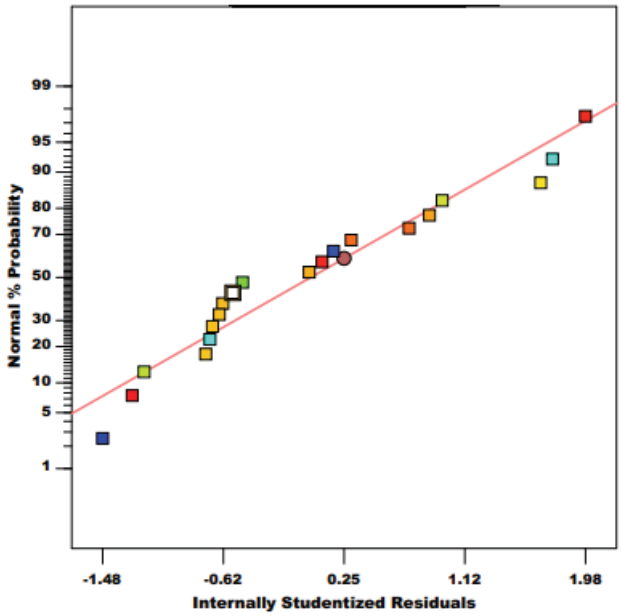

Figure 4. Normal probability plot for % carbofuran removal.

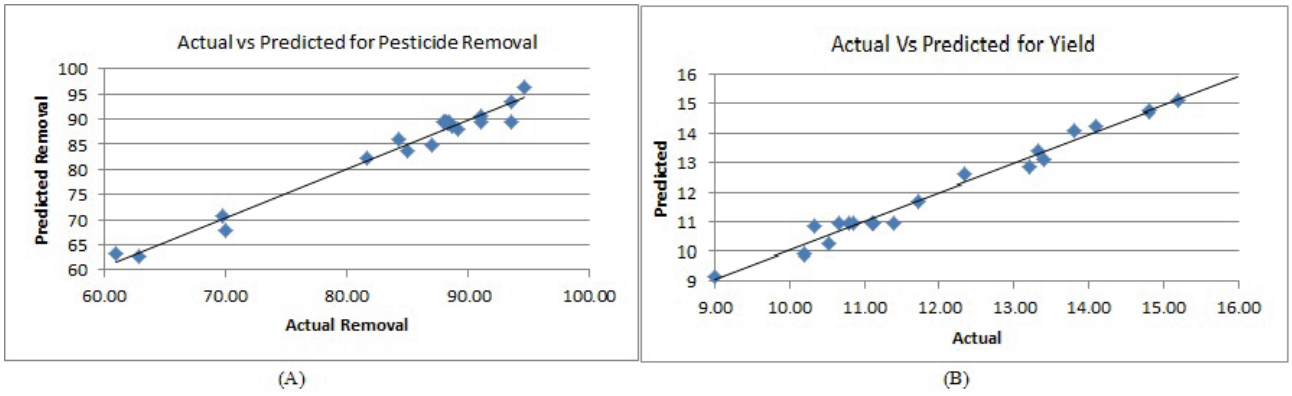

Figure 5. Parity chart (A) pesticide removal (B) yield.

Activation temperature seems to have more significant effect than time. Figure 6c presents the response graph of activation temperature and *IR* with constant activation time at center point (t = 1.5 h). A higher value of both factors lowers the yield considerably. Both have almost same effect on yield but relatively higher than activation time.

The increase in temperature increases the discharge of volatile matter owing to enhanced elimination reactions along with increased C-KOH and C-CO_2 reaction, thus causing a lower yield [32]. Higher *IR* also produces a lower yield due to excessive burn-off of surface carbon atoms and emission of volatile matter. At higher amounts of KOH, the gasification of surface carbon atoms is increased resulting in a lower carbon yield [33].

In the present study, the percentage yield obtained varies from 9 to 16.33%. In another study a yield of (12.58±1.2)% was obtained using KOH as activating agent at 800 °C [19]. Percentage yield of the present study is comparable with the stated work and the difference can be attributed to small differences in preparation techniques.

Factor effects on pesticide removal (R_2)

Activation temperature and *IR* seem to have higher effect on R_2 as it can be noticed in Table 4. Activation time has been found insignificant in this case. Interaction effect of *IR*, activation temperature, and activation time is moderate while that of *IR* and activation time is not significant. The quadratic effect of *IR* is higher than the quadratic effect of activation temperature, while for activation time it is insignificant.

Figure 7a depicts the response graph of activation temperature and *IR* for R_2 with constant activation time at center point (t = 1.5 h). It reveals that at the lower end of these factors, a lesser amount of removed carbofuran is obtained while the reverse is true when both factors are at the higher end. Individually, these factors affect the response in same fashion. Figure 7b describes the response graph of activation temperature and time with constant IR at center point (*IR* = 2). It is clearly visible that activation time has constant response at all values while activation temperature has a positive effect. A higher removal is obtained at higher temperature. From Figure 7c it is apparent that activation time has a constant response at all values while *IR* has significant positive effect on the response as higher removal is obtained at higher IR.

Sudaryanto *et al.* [34] also stated the insignificance of activation time towards pore development and structure and hence it had no effect on adsorption

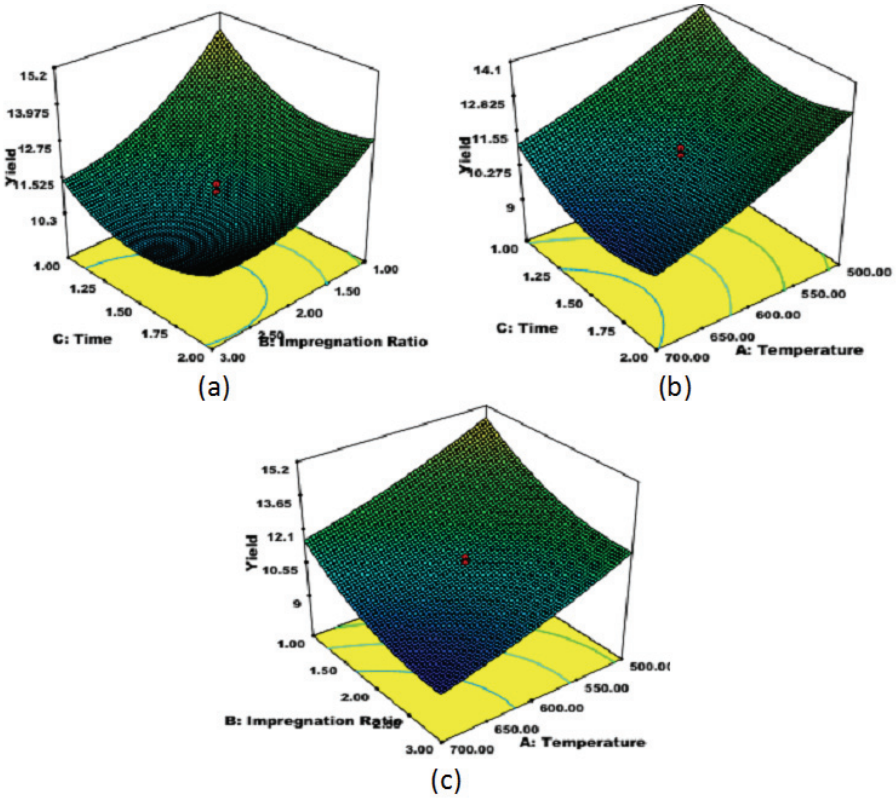

Figure 6. Three-dimensional graph of AC yield with: a) activation time and IR; b) activation temperature and time; c) activation temperature and IR.

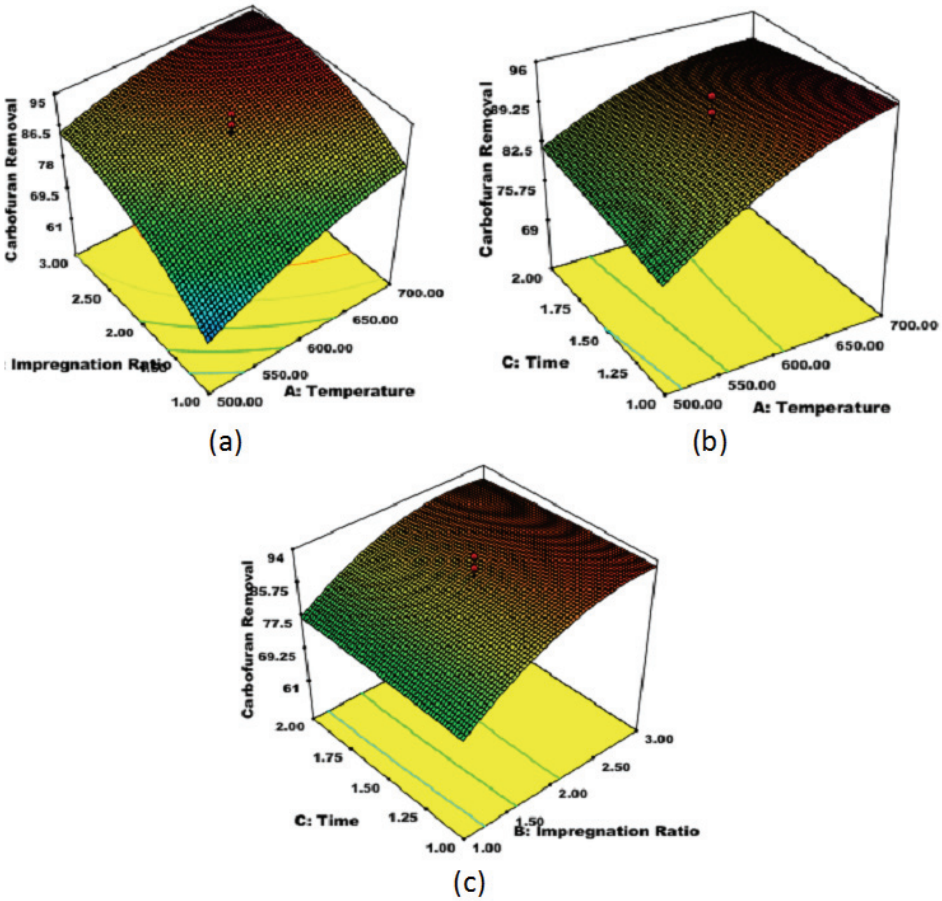

Figure 7. Three-dimensional graph of pesticide removal with: a) activation temperature and IR; b) activation temperature and time; c) IR and activation time.

capability of AC. The higher pesticide removal at higher *IR* and activation temperature is credited to higher activation of AC and porosity development. Shoaib *et al.* [35] also reported that activation at higher temperature increases the porosity and hence the uptake capacity of the product. Porosity development at higher temperature is due to the increased C-KOH, gasification and de-volatilization reactions. The higher *IR* favors oxidation reaction due to which porosity is developed [36].

Optimization of responses

It has been seen that the activated carbon yield and pesticide removal results have a conflicting situation. The conditions favoring higher activated carbon yield produce lower pesticide removal capacity and *vice versa*. To overcome this conflict, a tradeoff is necessary to get acceptable results. The desirability function of Design Expert 7.0.0 is used to get optimal results in this situation. The result with maximum desirability value is selected as optimal among all feasible solutions. Table 5 presents the optimized results for the preparation of cow-dung based activated carbon to have optimal responses.

Characterization of activated carbon

Figure 8 represents the SEM image (x1000) of cow dung-based AC prepared under obtained optimized conditions. Well-developed porosity can be observed from the image and it can be attributed to the activation process. These pores are responsible for adsorption of carbofuran molecules on AC surface. BET and Langmuir surface area were found to be 1123.37 and 1563.28 m^2/g, respectively. The prepared AC had total pore volume of 0.631 cm^3/g and average pore diameter of 2.53 nm. The prepared AC was classified as mesoporous as its pore diameter was found to be 2.53 nm. The high surface area and

Table 5. Optimized preparation conditions

Activation temperature (°C)	Impregnation ratio	Activation time (h)	Yield (%)	Carbofuran removal (%)
708.07	1.22	0.660	14.785	89.187

pore volume are achieved due to chemical activation process and these are directly related to enhanced adsorption of carbofuran onto the surface of AC. Porosity also adds to the available surface area and can be improved by using higher amounts of activating agent.

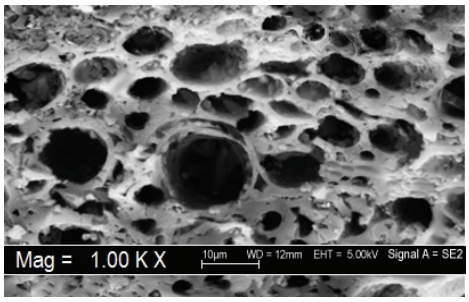

Figure 8. SEM Image of cow dung-based activated carbon under optimum conditions.

Validation of developed models

Some additional experimental runs were performed to validate the proposed models after data analysis. The selected data points for experimentation were different than the design points previously employed for experimentation and analysis. Percentage error was measured between the predicted and actual values. An absolute percent error of below 5% was observed for all validation runs, thus validating the adequacy of proposed models. Table 6 shows the validation data points along with percent error. Percent error was calculated by using Eq. (7):

$$\text{Percent Error} = \\ = 100\frac{|\text{Actual value - Predicted value}|}{\text{Predicted value}} \quad (7)$$

Table 6. Validation runs

Factor	Run		
	1	2	3
A	550	650	708
B	1.50	1.50	1.22
C	1.25	1.8	0.66
Actual yield	13.55	10.72	14.4
Predicted yield	13.11	11.01	14.784
Error, %	3.35	2.67	2.60
Actual removal	77.600	89.110	87.2
Predicted removal	79.318	87.407	89.187
Error, %	2.166	1.949	2.25

CONCLUSION

Cow dung was utilized to make AC and tested to remove pesticide from simulated contaminated water. CCD was employed to model and optimize the experimental results. *IR* and activation temperature had a significant effect on AC yield and uptake capacity. Higher values of both factors favor the removal of pesticide at the cost of AC yield. The optimized conditions of 708.07 °C activation temperature, 1.22 *IR*, and 0.66 h of activation time produced 14.78% yield and 89.18% pesticide removal. SEM image of optimized AC revealed that it has numerous pores on its surface which aid in adsorption. BET analysis confirmed the availability of large surface area and pore volume for better adsorption. These optimized conditions not only produce best results but are also economical from a cost point of view. Hence a low-cost and highly selective AC can be obtained from cow dung and the problem of water contamination by carbofuran can be addressed by exploiting an apparent waste following the waste-to-wealth concept.

Acknowledgements

The authors are highly grateful to the Environmental Engineering Department, UET, Taxila, for providing laboratory and necessary equipment to carry out the experimentation for this work.

REFERENCES

[1] R. Kumar, S. Mukherji, Curr. Org. Chem. 22 (2018) 954--972

[2] V.L. Zikankuba, G. Mwanyika, J. E. Ntwenya, A. James, Cogent Food Agric. 5 (2019) 1-15

[3] W. Zhang, F. Jiang, J. Ou, Proc. Int. Acad. Ecol. Environ. Sci. 1 (2011) 125-144

[4] A. Azizullah, M.N.K. Khattak, P. Richter, D.P. Häder, Environ. Int. 37 (2011) 479-497

[5] K. Ahad, A. Mohammad, H. Khan, I.Ahmad, Y. Hayat, Environ. Monit. Assess. 166 (2010) 191-199

[6] A. Ulhassan, A.B. Tabinda, M. Abbas, A.M. Khan, Pak. J. Agric. Sci. 51 (2014) 321-325

[7] M.I. Tariq, S. Afzal, I. Hussain, Environ. Int. 30 (2004) 471-479

[8] M.N. Qureshi, Pak. J. Sci. Ind. Res., A 60 (2017) 101-105

[9] G. Riaz, A.M. Tabinda, M. Kashif, A. Yasar, A. Mahmood, R. Rasheed, M.I. Khan, J. Iqbal, S. Siddique, Y. Mahfooz, Environ. Sci. Pollut. Res. 25 (2018) 22584-22597

[10] S. Mahboob, F. Niazi, K. AlGhanim, S. Sultana, F. Al--Misned, Z. Ahmed, Environ. Monit. Assess. 187 (2015) 1-10

[11] A.Jabbar, S.Z. Masud, Z. Parveen, M. Ali, Bull. Environ. Contam. Toxicol. 51 (1993) 268-273

[12] S. Salim, S. Satar, A. Sebe, H, Yesilagac, Mt. Sinai J. Med. 72 (2005) 389-392

[13] S. Wong, N.A.N. Yac'cob, N. Ngadi, O. Hassan, I.M. Inuwa, Chin. J. Chem. Eng. 26 (2018) 870-878

[14] S.A. Maddodi, H.A. Alalwan, A.H. Alminshid, M.N. Abbas, S. Afr. J. Chem. Eng. 32 (2020) 5-12

[15] N. Nourbakhsh, H.Z. Mousavi, E. Kolvari, A. Khaligh, Chem. Ind. Chem. Eng. Q. 25 (2019) 107-117

[16] S.S. Konstantinović, M.G. Kodrić, R. Ničić, D.M. Đorđević, Chem. Ind. Chem. Eng. Q. 25 (2019) 11-19

[17] D.D. Milenković, A.Lj. Bojić, V.B. Veljković, Ultrason. Sonochem. 20 (2013) 955-962

[18] A.Pandiarajan, R. Kamaraj, S. Vasudevan, S. Vasudevan, Bioresour. Technol. 261 (2018) 329-341

[19] G.D. Vyavahare, R.G. Gurav, P.P. Jadhav, R.R. Patil, C.B. Aware, J.P. Jadhav, Chemosphere 194 (2018) 306--315

[20] H. Li, S. Yang, H. Sun, X. Liu, Bioresources 13 (2018) 3135-3143

[21] D. Bhattacharjya, J.S. Yu, J. Power Sources 262 (2014) 224-231

[22] H. Demiral, I. Demiral, Surf. Interface Anal. 40 (2008) 612-615

[23] S.E. Elaigwu, L.A.Usman, G.V. Awolola, G.B. Adebayo, R.M.K. Ajayi, Adv. Nat. Appl. Sci. 3 (2009) 442-446

[24] N.B. Azmi, M.J. Bashir, S. Sethupathi, N.C. Aun, G.C. Lam, Environ. Earth Sci. 75 (2016) 902

[25] X. Chen, H. Zhang, Y. Guo, Y. Cao, F. Cheng, Chin. J. Chem. Eng. 28 (2020) 299-306

[26] I. Izhab, M. Asmadi, N.A.S. Amin, Int. J. Hydrogen Energy 46 (2020) 24754-24767

[27] F. Ghorbani, S. Kamari, S. Zamani, S. Akbari, M. Salehi, Surf. Interfaces. 18 (2020) 100444

[28] S. Kamari, F. Ghorban, A.M. Sanati, Sustainable Chem. Pharm. 13 (2019) 100153

[29] A.Baçaoui, A.Yaacoubi, A.Dahbi, C.Bennouna, R.P.T. Luu, F.J. Maldonado-Hodar, J. Rivera-Utrilla, C. Moreno--Castilla, Carbon 39 (2001) 425-432

[30] Z. Ilbay, A. Haşimoğlu, O.K. Ozdemir, F. Ateş, S. Şahin, J. Mol. Liq. 246 (2017) 208-214

[31] J. Antony, Design of experiments for engineers and scientists, Butterworth-Heinemann, New York, 2003, p. 38

[32] D. Adinata, W.M.A.W. Daud, M.K. Aroua, Bioresour. Technol. 98 (2007) 145-149

[33] Y. Sudaryanto, S.B. Hartono, W. Irawaty, H. Hindarso, S. Ismadji, Bioresour. Technol. 97 (2006) 734-739

[34] C.D. Şentorun-Shalaby, M.G. Uçak-Astarlıog˘lu, L. Artok, Levent, C. Sarıcı, Microporous Mesoporous Mater. 88 (2006) 126-134

[35] M. Shoaib, H.M. Al-Swaidan, Biomass Bioenergy 73 (2015) 124-134

[36] Z. Ab. Ghani, M.S. Yusoff, N.Q. Zaman, M.F.M.A Zamri, J. Andas, Waste Manage. (Oxford, U. K.) 62 (2017) 177--187.

SHAMA MUSTAFA HAYDER
SALMAN HUSSAIN
WASIM AHMAD
MIRZA JAHANZAIB
ABAID ULLAH

University of Engineering and Technology, Taxila, Punjab, Pakistan

NAUČNI RAD

OPTIMIZACIJA JEFTINOG AKTIVNOG UGLJA OD KRAVLJE BALEGE ZA UKLANJANJE KARBOFURANA IZ VODENOG RASTVORA

Zagađenje vode postalo je ozbiljno pitanje ovog veka zbog povećane industrijalizacije. Usvojeno je nekoliko metoda za rešavanje ovog problema, uključujući adsorpciju aktivnim ugljem. Konvencionalni izvori dobijanja aktivnog uglja su, takođe, skupi i neobnovljivi. Nekoliko voćnih i poljoprivrednih otpadaka ima karakteristike održivih sirovina za dobijanje aktivnog uglja. Cilj ovog istraživanja je dobijanje isplativog aktivnog uglja iz održive sirovina - kravlje ibalege. Postupak dobijanja je analiziran i optimizovan primenom centralnog kompozitnog dizajna. Analiziran je uticaj temperature aktivacije, vremena i odnosa impregnacije na odgovore prinos (R_1) i stepen uklanjanja pesticida (R_2). Predloženi su kvadratni modeli sa koeficijentima determinacija R^2, R_{adj}^2 i R_{pred}^2 od 0,98, 0,96, 0,89 za prinos pesticida i 0,97, 0,94 i 0,87 za stepen uklanjanja pesticida, redom. Temperatura aktivacije i odnos KOH/sirovina značajno utiču na prinos i stepen uklanjanje pesticida. Optimizovani uslovi temperature aktivacije, odnosa KOH/sirovina i vremena aktivacije su 708 °C, 1,22 i 0,66 h, redom. Pri ovim uslovima, ostvern us prinos 14,78% i stepen uklanjanje pesticida 89,18%. SEM i BET analize optimizovanog aktivnog uglja su, takođe, potvrdile njegovu poroznost i veliku površinu. Rezultati ovog istraživanja sugerišu da se kravlja balega može koristiti za dobijanje jeftinog aktivnog uglja za uklanjanje pesticida iz vodenog rastvora.

Ključne reči: adsorbent, aktivni ugalj, biootpad, kravlja balega, pesticidi, prečišćavanje otpadnih voda.

CI&CEQ
Chemical Industry & Chemical Engineering Quarterly

Available on line at
Association of the Chemical Engineers of Serbia *AChE*
www.ache.org.rs/CICEQ

Chem. Ind. Chem. Eng. Q. 27 (2) 155–163 (2021) CI&CEQ

LUIZ DANIEL DA SILVA NETO[1]
PAULO VICTOR FERREIRA LOZ[2]
JOÃO INÁCIO SOLETTI[2]
DAYANA DE GUSMÃO COÊLHO[2]

[1]Department of Chemical Engineering, Federal University of São Carlos Rodovia Washington Luís, São Carlos - São Paulo, Brazil
[2]Laboratory of Separation and Process Optimization Systems, Technology Center, Federal University of Alagoas, Maceió, Alagoas, Brazil

SCIENTIFIC PAPER

UDC 662.756.3:66

FACTORIAL DESIGN AND SURFACE METHOD TO OPTIMIZE ETHYLIC BIODIESEL PRODUCTION FROM CHICKEN WASTES

Article Highlights

- Ethylic biodiesel production from chicken wastes
- Production optimization
- *Physical and chemical properties of chicken wastes oil biodiesel*

Abstract

To produce biodiesel, one of the most important factors is the quality of the oil used in the production. However, other factors such as price and availability should also be taken into consideration. Chicken wastes oil shows a very promising option for this sector, since it comes from a waste. The aim of the present study was a methodology for extraction and characterization of chicken wastes oil for production of biodiesel by ethylic transesterification, besides presenting the characterization and optimization of the process variables of the production of biodiesel, the applying of RSM involving CCD. The investigation was performed following evaluation of the characterization parameters for the oil: viscosity, density, acidity index, moisture of the sample, refractive index, and saponification index. For biodiesel, viscosity, density, acidity index and ester content were evaluated. An optimum point was reached for the production of chicken biodiesel where the concentration of the catalyst is 2.1% by mass, the oil/ethanol ratio is 1:5.5 and the reaction temperature of 30 °C; at that point, a 95% conversion was achieved. At the optimum point obtained from the statistical technique for a p-value of 0.05 the results found for the physical-chemical characterization of biodiesel are found in the ANP standards.

Keywords: biodiesel; chicken wastes; ethyl transesterification; optimization.

Over the years, diesel motors became one of the main sources of power generation around the world, due to the efficiency and economy, being used in transport, agriculture, etc. However, with technological advancement and population growth, the high consumption and rapid depletion of fossil fuels compel the energy sector to adapt to this new reality [1,2]. In this way, also aiming at the significant reduction of the emission of polluting gases and, consequently, to contribute to the minimization of the environmental impacts on the planet, several energy sources were studied and implemented over the years [3].

Biodiesel, with an energy efficiency equivalent to that of diesel oil obtained from petroleum refining, is derived from vegetable oils and animal fats. They present advantages to petroleum diesel for not emitting carbon monoxide, sulfur and hydrocarbons, have low emission of vapors, are biodegradable and non-flammable [4]. Some raw materials used for the production of biodiesel are vegetable oil [5], algae biomass [6-9], residual cooking oil [10-13], and animal fats [14-16]. Many countries use methanol as an alcoholic reagent to produce biodiesel. However, by producing a fuel with raw materials from fully renewable sources, ethanol can be used in the transesterification of biodiesel.

Correspondence: L.D. da Silva Neto, Department of Chemical Engineering, Federal University of São Carlos Rodovia Washington Luís, km 235 - SP-310 São Carlos - São Paulo, P.O. Box: 13565--905, Brazil.
E-mail: ld_neto@hotmail.com
Paper received: 17 November, 2019
Paper revised: 1 July, 2020
Paper accepted: 7 September, 2020

https://doi.org/10.2298/CICEQ191117034S

In Brazil, although most of the biofuel is ethanol, obtained from sugarcane, biodiesel is already part of the energy matrix. Currently, 10% of the percentage of diesel oil sold to the consumer is biodiesel and the estimated consumption was 5.3 billion L in 2018. Most of the oils used in biodiesel production in Brazil come from traditional oleaginous oils such as soybean oil. However, the inclusion of other raw materials in this matrix is important and aims to reduce confrontation with the food industry.

According to the report of the Brazilian Association of Animal Proteins (ABPA), Brazil is the second largest producer of poultry meat in the world, with a production of 13,056 million tons, behind only the 18,596 million tons produced by the United States of America [17]. Thus, the meat processing industries produce a large amount of animal fat, where part of this by-product is destined for the chemical, pharmaceutical and chemical industries [16]. However, just a part of the animal fat receives suitable management and reaches its destination, especially the ones that come from chicken slaughterhouses that do not have a processing unit to deal with them, which makes them have problems for the elimination of those residues.

The study of process variables such as the use of ethyl route from an environmental point of view is more attractive because ethanol can be obtained from renewable sources. It is important to consider that other factors influence biodiesel yield and multivariate optimization has stood out for evaluating the interaction between variables in the process response.

In this study, a Central Composite Design (CCD) to optimize the reaction parameters was used to get the best yield in the production of biodiesel from chicken wastes. The parameters considered were the oil/ethanol mass ratio, catalyst concentration and temperature on the production of ethylic biodiesel via basic catalysis.

MATERIALS AND METHODS

Raw materials

The residues used on this work, which resulted from cutting chicken meat, were provided by Cortez Supermarket, Coruripe, Brazil. From these residues we were able to extract the raw materials (chicken fatty oils).

For the realization of the analytical methodologies and reaction transesterification, ethyl alcohol, heptane, hydrogen gas and sodium hydroxide were analytical grade and purchased commercially and used without any prior purification. The materials were weighed on a precision balance (Mars, model AM220, Brazil) that had an uncertainty of ±0.0001g.

Obtaining the oil

The crude residue was obtained from chicken wastes from the supermarket ground. The cooking of the residue was carried out in a vessel with water, in a ratio of 2:1 water/fat. The oil was separated by decantation and filtered through a vacuum filter to melt the fat. The obtained fat was then filtered to remove impurities and stored in bottles kept under refrigeration. This oil was taken to a greenhouse where any residual water was removed to be used in transesterification reactions.

Gas chromatography

For the identification of the fatty acids in chicken oil, a transesterification reaction was carried out with NaOH to form ethyl esters. These samples of ethyl esters were then analyzed by gas chromatography, by adapting the method prescribed by the European standard EN 14103, where approximately 0.05 g of the sample was dissolved in 1.0 mL of heptane. CG--2010/Shimadzu was used equipped with a split/splitless injection system operating at 250 °C, split ratio of 100:1, sample volume of 1.0 μL and flame ionization detector operating at 250 °C. A 30-meter-long apolar capillary column ZB-WAXplus, with a 0.32 mm internal diameter and 0.25 micron-thick film and high purity hydrogen gas, used as drag, was used. The temperature programming was constant temperature of 200 °C (10 min). The fatty acid composition was calculated based on the identification and integration of the peak areas by normalization.

Transesterification process

Biodiesel from chicken wastes was obtained by transesterification reaction, where anhydrous ethanol was used as the alcoholic agent and sodium hydroxide was used as the catalyst. The reactions were carried out in 1500 mL reactors with a magnetic stirrer and equipped with temperature control. Initially, the catalyst was dissolved in the anhydrous alcohol and subsequently added to the chicken waste oil. The reaction time was 30 min. Subsequently, the mixture was transferred to a separating funnel and allowed to stand for 12 h. The lower layer of the glycerol was removed, and the upper phase of the biodiesel subjected to the washing process with distilled water, at room temperature. After that, the oven was dried for a total time of 24 h to remove water and alcohol present.

Optimization and data analysis

Experiment planning techniques were used to optimize the operating conditions of the production of biodiesel from fatty residues of chicken. To determine

the experimental conditions optimizing the experiment, the effect of variables and their interactions were evaluated, which influence the yield of the transesterification reaction [12,18]. In this step, the oil/ethanol ratio, amount of catalyst and temperature in the conversion of the reaction were evaluated. In literature reports, experiments were carried out on agitation speed, the type of paddles, temperature, catalyst and alcohol/molar ratio; the factors that presented a greater significance for chicken waste biodiesel were temperature, catalyst and alcohol mole ratio [19,20]. The experimental data obtained by following the above procedures were analyzed by the response surface regression procedure using the following second-order polynomial equation, Eq (1):

$$y = \beta_0 + \sum_j \beta_j x_j + \sum_{i<j} \beta_{ij} x_i x_j + \sum_j \beta_{jj} x_j^2 + e \quad (1)$$

where y is the response (percentage conversion); x_i and x_j are the uncoded independent variables and β_0, β_i, β_{ii} and β_{ij} are intercept, linear, quadratic and interaction constant coefficients, respectively. Design Expert software package was used for regression analysis and analysis of variance (ANOVA) [21]. The software used for evaluation and validation of the data obtained was Statistica® 13.0 Statsoft, Inc.

Physical and chemical properties

The physicochemical properties were evaluated according to the methods established by the American Society for Testing and Materials (ASTM), the results compared to the European standards and the Brazilian National Agency of Petroleum, Natural Gas and Biofuels (ANP).

The investigation was performed following parameter characterization for the oil: viscosity, humidity, acidity index, and saponification index were evaluated, presented in Eqs. (2)-(5):

$$v = tK \quad (2)$$

where v is a viscosity (mm²/s), t is the time (s); K is constant (0,1125 mm^2/s^2).

The humidity was determined in Eq. (3), where U is humidity, N is difference between final and initial mass, P is initial mass:

$$U = \frac{100N}{P} \quad (3)$$

Eq. (4) presented the acidity index, where IA is acidity index (mg NaOH/g), V is the volume of NaOH (ml), f is correction factor, M is molarity and m is the mass of the sample.

$$IA = \frac{28.2VfM}{m} \quad (4)$$

The saponification index, IS, is presented in Eq. (5) where A is volume of the sample titration, B is volume of the white sample, f is correction factor of the solution HCl 0,5 M, P is initial mass of the sample:

$$IS = \frac{26.6f(B-A)}{P} \quad (5)$$

The density was analyzed by ASTM D 4052 and the refraction index was checked by Abbe refractometer.

RESULTS AND DICUSSION

Physical and chemical properties

Transesterification is influenced by the physical and chemical characteristics of the raw materials, so some properties of biodiesel can be predicted from the analysis. The results found in this study are shown in Table 1.

Table 1. Physical-chemical properties of chicken oil and biodiesel of chicken oil

Property	Chicken oil	Chicken biodiesel
Refractive index	1.4646±0.0001	-
Viscosity 40 °C (mm²/s)	48.46±0.2	5.839±0.2
Density 20 °C (kg/m³)	917.30±0.5	884.35±0.5
Humidity (%)	0.398±0.0018	-
Acidity index (mg KOH/g)	0.759±0.05	0.716±0.05
Saponification index (mg KOH/g)	191.51±0.8	-

Compared with soybean oil, which is the main raw material for biodiesel production in Brazil (ANP), the oil of chicken had similar density and a lower viscosity, which is satisfactory for the production of biodiesel, since high values of viscosity and density can cause problems related to the fuel injection in the engine, damaging its performance [22,23].

For base-catalyzed transesterification, the glycerides and alcohol must be substantially anhydrous; the water causes partial saponification that produces soap, consuming the catalyst and reducing the catalytic efficiency, in addition to causing increased viscosity, gel formation and difficulty in reaching separation of glycerol [19,24]. Humidity in biodiesel acts increasing the acidity and subsequent formation of soap, as well as causing corrosion of fuel supply systems, microbiological growth and hydrolysis of the methyl ester [25]. Humidity was not a problem, neither in terms of favoring side reactions nor reagent consumption.

The acid number is defined as the number of mg of potassium hydroxide needed to neutralize 1 g of the sample. For transesterification to be efficient, the amount of free fatty acids present in the raw material must be less than 3% [26]. Researchers suggest that to use an alkaline catalyst, the level of free fatty acids in the raw materials should be reduced to less than 1% [27,28], but as can be seen in Table 1, the index found was less than 1 mass%, thus, no oil treatment step was necessary.

Most of the raw materials used for biodiesel production have higher values than the one found in this study. The chicken oil had an adequate acid index, with a low presence of free fatty acids, indicating a good raw material for the biodiesel production, without compromising the transesterification process.

The saponification index of the chicken oil found in this study was 190.51 mg KOH/g. Like the viscosity and the density, the saponification index does not have a standard value set in resolution of the ANP, but compared to the literature, the value found is within the parameters [29]. A lower saponification index leads to a higher yield in the reaction, due to the decrease of the parallel reactions that can lead to the formation of soap. This index directly influences the amount of alcohol in the transesterification since an excess of alcohol is used to avoid the formation of soap.

Gas chromatography

The gas chromatography technique is used to determine the fatty acid profile of the raw material. Table 2 shows the oil profile used as raw material for this study. Chicken oil is composed of 25 to 35% of saturated fatty acids and 40 to 75% of unsaturated fatty acids [30,31]. Thus, with the known composition and after a transesterification reaction, the respective triglycerides were obtained. Thus, through the percentage of each component of the oil, the molar mass was obtained (Table 2). With 95.5% of the oil composition known and that this percentage corresponds to 820.592 g/mol, this basis of calculation was used to obtain the total molar mass of 859.26 g/mol.

Ester content and optimization

The variables studied in the experimental design, their respective levels, and the results of ester concentration in the biodiesel of chicken oil obtained are shown in Table 3.

Table 3. Experimental matrix for factorial design 2^3, with triplicate at the central point and 6 axial points, with maximum conversion of esters

Case	Temperature °C	Proportion	Catalyst content %	Ester content %
B1	35 (-1)	1;5.0238 (-1)	1.25 (-1)	73.46
B2	65 (1)	1;5.0238 (-1)	1.25 (-1)	51.82
B3	35 (-1)	1;10.9762 (1)	1.25 (-1)	58.28
B4	65 (1)	1;10.9762 (1)	1.25 (-1)	86.83
B5	35 (-1)	1;5.0238 (-1)	2.25 (1)	92.88
B6	65 (1)	1;5.0238 (-1)	2.25 (1)	52.88
B7	35 (-1)	1;10.9762 (1)	2.25 (1)	91.59
B8	65 (1)	1;10.9762 (1)	2.25 (1)	67.91
B9	50 (0)	1;8 (0)	1.75 (0)	88.99
B10	50 (0)	1;8 (0)	1.75 (0)	89.02
B11	50 (0)	1;8 (0)	1.75 (0)	89.09
B12	24.8 (-1.68)	1;8 (0)	1.75 (0)	86.67
B13	75.2 (1.68)	1;8 (0)	1.75 (0)	59.52
B14	50 (0)	1;3 (-1,68)	1.75 (0)	68.95
B15	50 (0)	1;13 (1,68)	1.75 (0)	75.34
B16	50 (0)	1;8 (0)	0.91 (-1.68)	68.86
B17	50 (0)	1;8 (0)	2.59 (1.68)	41.34

The data obtained in the experimental design were treated statistically and, in this way, it was observed the need of adding the axial points to the planning due to the non-representativeness of the linear model to the obtained data was observed.

Through CCD planning it was possible to analyze the effects of the studied variables, allowing to verify statistically their significance for biodiesel production. The Pareto graph (Figure 1) shows the effects of variables that are statistically important, as well as presenting the effects of two-to-two interactions between these variables.

Table 2. Composition of fatty acids and triglycerides present in chicken oil

Fatty acid	Content (%)	Triglyceride	Correspondent molar mass (g/mol)
Myristic	0.6	Trimyristate	4.332
Palmitic	22.3	Tripalmitate	179.738
Palmitoleic	4.5	Tripalmitoleate	36.000
Stearic	4.9	Triestearate	43.610
Oleic	35.4	Trioleate	312.936
Linoleic	26	Trilinoleate	228.280
Linolenic	1.8	Trilinolenate	15.592
Others	4.5	-	-

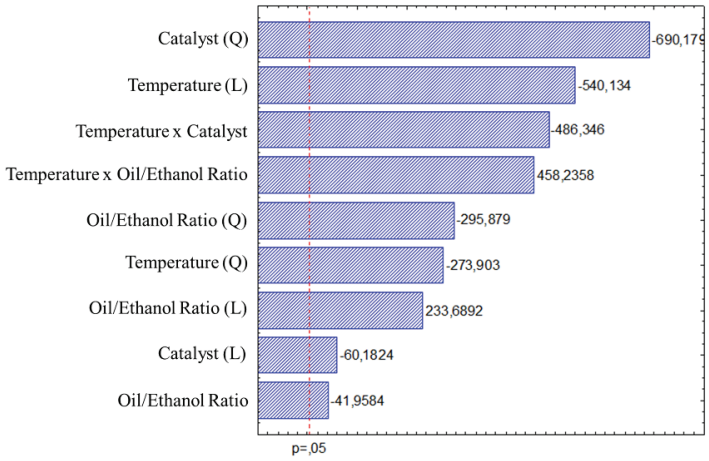

Figure 1. Pareto graph.

The effect of a variable is more significant the further it is on the right side of the line $p = 0.05$, which represents a significance level of 95%, so those behind the line are not considered to be statistically significant. Once the significant effects have been defined, we can evaluate their interference in the response variable by studying the Response Surface Methodology (RSM), analyzing two variables simultaneously. For the comparison of ester conversion in biodiesel as a function of catalyst concentration and reaction temperature, the oil/ethanol ratio was kept fixed at the center point (Figure 2).

For the comparison of the ester conversion as a function of the oil/ethanol ratio and catalyst concentration, the reaction temperature was maintained at the central point of the planning (Figure 3).

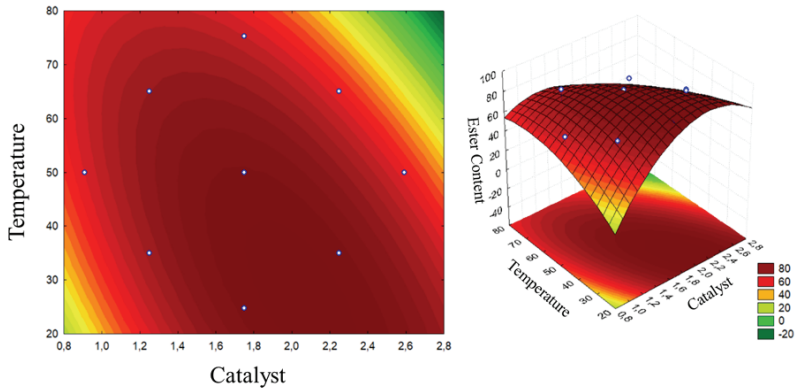

Figure 2. Response surface for ester conversion as a function of catalyst concentration and temperature with a fixed oil/ethanol ratio of 1:8.

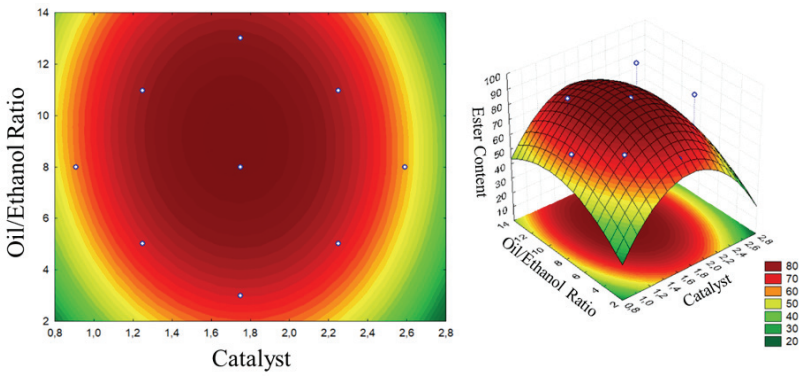

Figure 3. Response surface for ester conversion as a function of catalyst concentration and the oil/ethanol ratio with a fixed temperature of 50 °C.

Finally, the ester conversion was evaluated as a function of the oil/ethanol ratio and reaction temperature, with the catalyst concentration at the center point (Figure 4).

In Figures 2 and 3 we can see that the optimum biodiesel conversion range is between 1.8 and 2.2%, for the catalyst concentration. High concentrations of the catalyst tend to form salts of fatty acids, making the purification process difficult and causing product losses. The low concentrations of the catalyst are insufficient for the reaction to occur, reducing the yield [32].

Figures 3 and 4 show that the optimum biodiesel conversion range is between 1:5 and 1:9, for the oil/ /ethanol ratio. Low oil/ethanol ratios reduce the yield due to the reversibility of the reaction and, on the other hand, the excess alcohol deactivates the performance of the catalyst [33]. Thus, an optimized mole ratio will reduce the cost of producing biodiesel, decreasing the amount of ethanol used. In Figures 2 and 4 it is observed that the temperature extremes reduce the reaction yield for some analyses and the optimum conversion range is between 20 and 40 °C.

Because it is a fat, at low temperatures the chicken oil is in a solid state, which makes the reaction difficult. The reaction temperature is normally dependent on the type of alcohol used, so the temperature is kept below the boiling point of the alcohol, keeping its level constant in the reaction bottle [3].

With the obtained data it was possible to obtain an optimization for biodiesel production for the variables and levels studied, that can be expressed by Eq. (6) (Table 4):

$$C_{Ester} = -136.203 + 1.930T_L - 0.019T_Q + 0,.43R_L - \\ -0.511R_Q + 208.924C_L - 42.94C_Q + 0.186T_LR_L - \\ -1.176T_LC_L - 0.512R_LC_L \quad (6)$$

where C_{Ester} corresponds to ester concentration in biodiesel (g/g), R_L, the linear ratio oil/ethanol (g/g), R_Q, the quadratic ratio oil/ethanol (g/g), C_L, the linear catalyst concentration (g of cat./g of oil), C_Q, the quadratic catalyst concentration (g of cat./g of oil), T_L, the linear temperature (°C) and T_Q, the quadratic temperature (°C).

Table 4. Regression coefficients of predicted quadratic polynomial model

Term		Regression coefficient	Standard error
Intercept	β_0	-136.203	96.02255
Linear	β_1	1.930	1.83354
	β_2	0.843	8.57747
	β_3	208.924	56.11116
Quadratic	β_{11}	-0.019	0.01433
	β_{22}	-0.511	0.36412
	β_{33}	-42.194	12.90127
Interaction	β_{12}	0.186	0.08576
	β_{13}	-1.176	0.51050
	β_{23}	-0.512	2.57290

Physical-Chemical properties of biodiesel

Table 1 shows data on the physicochemical characterization of biodiesel obtained from optimized operating conditions (temperature: 30 °C, catalyst concentration: 2.1%, oil/ethanol ratio: 1:5.5). It can be observed that the biodiesel of chicken oil is in accordance with the specifications of the *ANP* Resolution Nº 45/2014 in all the tests.

The value obtained for the specific mass, 884.35 kg/m³, complies with *ANP* Resolution 45/2014, which defines the limit between 850 and 900 kg/m³. The value obtained is close to the diesel value of 853 kg/m³. The density of the oil varies according to the nature of the raw material and, in determining the

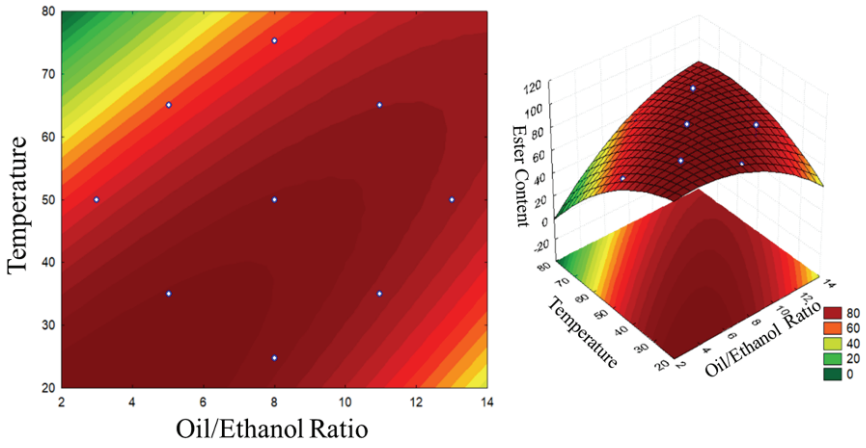

Figure 4. Response surface for ester conversion as a function of temperature and the oil/ethanol ratio with a fixed catalyst concentration of 1.75%.

density of the biodiesel, it is possible to guarantee the longevity and the good functioning of the engine due to the influence on the fuel atomization efficiency [15,34,35].

The value obtained for the viscosity, 5.839 mm²/s, complies with the ANP Resolution 45/2014, which defines the limit between 3.0 and 6.0 mm²/s, the value of the range established for conventional diesel. The viscosity of the biodiesel is influenced mainly by the experimental conditions and the extension of the transesterification reaction. It is a parameter that affects the atomization of the fuel at the time of injection in the combustion chamber and, ultimately, the formation of deposits in the engine [3,15,24,36].

Viscosity and density are important parameters in the biodiesel quality and may be related to the purity of the product obtained, assuming that there are no possible interactions between the ethyl ester and the glycerides. Factors such as incomplete reaction, the presence of mono-, di- and triglycerides or the presence of glycerin, due to inefficient purification, promote changes in viscosity and density. In this way, we can associate one of these physical properties with the degree of purity of the prepared biodiesel oil, being an efficient, fast, and low-cost analytical method for determining the quality and purity of biodiesel.

For the acid value, the obtained value of 0.716 mg KOH/g is within the limits allowed by the *ANP*. The acid control is extremely important to prevent corrosion of the engine. In addition, the monitoring of the acidity of biodiesel is also of great importance for its storage since the change of values in this period can mean the presence of water. Viscosity and, mainly, the period of induction of Rancimat are parameters that can be used to monitor the oxidative degradation of the biodiesel during the time of storage [15].

About 3.33 chickens are produced per m^2, so about 33,300 chickens per ha are produced. The average unit weight of chicken is 2.7 kg, where 8% is greasy residue. As 43.8% (data obtained in this work), about 3,150 kg are obtained per ha. As the production of chicken for slaughter occurs five times a year, we have a final value of about 15,750 kg of oil per ha per year. Comparing this yield with those of other oilseeds, we can theoretically produce about 25 times more chicken oil per ha than soybean oil, the main raw material for biodiesel production in Brazil [11,24,34].

CONCLUSION

The studies show that the reuse of the fatty residues of chicken is a viable alternative for the production of biodiesel, since it has an excellent extraction yield and a high productivity - approximately 25 times higher than soybean oil per hectare, the most used raw material for biodiesel production in Brazil. The factorial design was efficient in the screening of significant variables to a 95% confidence interval and it was possible to describe the process. The central composite design resulted in optimized conditions being determined for the maximum biodiesel chicken wastes yield where the concentration of the catalyst is 2.1% by mass, the oil/ethanol ratio is 1:5.5 and the reaction temperature is 30 °C. From the equation obtained (Eq. (6)) it is possible to predict the conditions required to obtain a higher yield.

The biodiesel of chicken oil presented adequate characteristics for its use, since its specifications agree with specification parameters listed in Technical Regulation Nº 7/2008 of the National Agency of Petroleum, Natural Gas and Biofuels.

Nomenclature

A	Volume of the sample titration, mL
ABPA	Brazilian Association of Animal Proteins
ANOVA	Analysis of Variance
ANP	Brazilian National Agency of Petroleum, Natural Gas and Biofuels
ASTM	American Society for Testing and Materials
B	Volume of the white sample, mL
β_i	Linear coefficient
β_{ii}	Quadratic coefficient
β_{ij}	Interaction coefficient
β_0	Intercept coefficient
CCD	Central composite design
C_{Ester}	Ester concentration, g/g
C_L	Linear coefficient of catalyst concentration, g of cat./g of oil
C_Q	Quadratic coefficient of catalyst concentration, g of cat./g of oil
f	Correction factor
IA	Acidity index, mg NaOH/g
IS	Saponification index, mg KOH/g
K	Constant, mm^2/s^2
m	Mass of the sample, g
M	Molarity, mol/mL
N	Final and initial mass difference, m
P	Initial mass, m
R_L	Linear coefficient of ratio oil/ethanol, g/g
R_Q	Quadratic coefficient of ratio oil/ethanol, g/g
RSM	Response Surface Methodology
t	Time, s
T_L	Linear coefficient of temperature, °C
T_Q	Quadratic coefficient of temperature, °C
U	Humidity, %

ν Viscosity, mm²/s
V Volume of NaOH, mL
x_i Independent variable
x_j Independent variable
y Model response

REFERENCES

[1] S. Kumar, P. Dinesha, I. Bran, Energy 140 (2017) 98-105.

[2] M. Kirubakaran, V. Arul Mozhi Selvan, J. Environ. Chem. Eng. 6 (2018) 4490-4503

[3] M. Kirubakaran, V. Arul Mozhi Selvan, Renew. Sustain. Energy Rev. 82 (2018) 390-401

[4] M. Mofijur, M.G. Rasul, J. Hyde, A.K. Azad, R. Mamat, M.M.K. Bhuiya, Renew. Sustain. Energy Rev. 53 (2016) 265-278

[5] V. Singh, M. Yadav, Y.C. Sharma, Fuel 203 (2017) 360--369

[6] B.C. Klein, A. Bonomi, R.M. Filho, Renew. Sustain. Energy Rev. 82 (2018) 1376–1392

[7] P.R. Pandit, M.H. Fulekar, J. Environ. Manage. 198 (2017) 319-329

[8] U. Rajak, P. Nashine, T.N. Verma, Fuel. 268 (2020) 117305

[9] S. Salam, T.N. Verma, Energy Convers. Manage. 180 (2019) 496-510

[10] A.B. Fadhil, I.K. Saeed, L.I. Saeed, M.H. Altamer, Energy Sources, Part A Recover. Util. Environ. Eff. 38 (2016) 2883-2890

[11] A. Piker, B. Tabah, N. Perkas, A. Gedanken, Fuel. 182 (2016) 34-41

[12] M. Gülüm, M.K. Yesilyurt, A. Bilgin, Environ. Sci. Pollut. Res. 27 (2020) 10351-10366

[13] T.S. Singh, T.N. Verma, Energy Convers. Manage. 182 (2019) 383-397

[14] T. Ito, Y. Sakurai, Y. Kakuta, M. Sugano, K. Hirano, Fuel Process. Technol. 94 (2012) 47-52

[15] G.I. Martins, D. Secco, H.A. Rosa, R. Bariccatti, B.D. Dolci, S.N.M. Souza, R.F. Santos, T.R.B. Silva, F. Gurgacz, Renew. Sustain. Energy Rev. 42 (2015) 154-157

[16] A. Cunha, V. Feddern, M.C. De Prá, M.M. Higarashi, P.G. De Abreu, Fuel. 105 (2013) 228-234

[17] Brazilian Association of Animal Proteins, Brazilian statistical yearbook, http://abpa br.com.br/storage/files/ /relatorio-anual-2018.pdf (accessed 20 February 2018)

[18] M.K. Yesilyurt, M. Arslan, T. Eryilmaz, Int. Journal Green Energy 16 (2019) 60-71

[19] A. Rojas-González, E. Girón-Gallego, Ing. Univ. 15 (2011) 197-218

[20] D.C. Antonio, L.P. Amancio, I.G. Rosset, Catal. Lett. 148 (2018) 3214-3222

[21] B. Barros Neto, I.S. Scarminio, R.E. Bruns, Como fazer experimentos: pesquisa e desenvolvimento na ciência e na indústria, B. Barros Neto, Ed., Editora Unicamp, Campinas, 2002, p. 251

[22] A. Amin, A. Gadallah, A.K. El Morsi, N.N. El-Ibiari, G.I. El-Diwani, Egypt. J. Pet. 25 (2016) 509-514

[23] W. Yuan, A.C. Hansen, Q. Zhang, Z. Tan, J. Am. Oil Chem. Soc. 82 (2005) 195-199

[24] D. Bajpai, V.K. Tyagi, J. Oleo Sci. 55 (2006) 487-502

[25] B.R. Moser, Vitr. Cell. Dev. Biol. Plant. 45 (2009) 229-266

[26] L.C. Meher, D. Vidya Sagar, S.N. Naik, Renew. Sustain. Energy Rev. 10 (2006) 248-268

[27] B. Freedman, E. Pryde, T. Mounts, J. Am. Oil Chem. Soc. 61 (1984) 1638–1643

[28] K.S. Liu, J. Am. Oil Chem. Soc. 71 (1994) 1179–1187

[29] M.C. Chiu, R. Grimaldi, L.A. Gioielli, Rev. Bras. Ciencias Farm. J. Pharm. Sci. 43 (2007) 421-434

[30] M.C. Chiu, L.A. Gioielli, Ciênc. Tecnol. Aliment. 22 (2002) 151-157

[31] S. Gugule, F. Fatimah, Y. Rampoh, Anim. Prod. 13 (2009) 115–121

[32] T.M. Mata, N. Cardoso, M. Ornelas, S. Neves, N.S. Caetano, Energy and Fuels. 25 (2011) 4756-4762

[33] K.-H. Chung, J. Kim, K.-Y. Lee, Biomass Bioenergy 33 (2009) 155–158

[34] I.B. Banković-Ilić, I.J. Stojković, O.S. Stamenković, V.B. Veljkovic, Y.T. Hung, Renew. Sustain. Energy Rev. 32 (2014) 238-254

[35] A. Sagiroglu, Ş.S. Isbilir, H.M. Ozcan, H. Paluzar, N.M. Toprakkiran, Chem. Ind. Chem. Eng. Q. 17 (2011) 53-58

[36] G. Simonelli, C. Moraes, C.A. de Moraes Pires, L.C.L. dos Santos, Chem. Ind. Chem. Eng. Q. 25 (2019) 183--192.

LUIZ DANIEL DA SILVA NETO[1]
PAULO VICTOR FERREIRA LOZ[2]
JOÃO INÁCIO SOLETTI[2]
DAYANA DE GUSMÃO COÊLHO[2]

[1]Department of Chemical Engineering, Federal University of São Carlos Rodovia Washington Luís, São Carlos - São Paulo, Brazil
[2]Laboratory of Separation and Process Optimization Systems, Technology Center, Federal University of Alagoas, Maceió, Alagoas, Brazil

NAUČNI RAD

STATISTIČKA OPTIMIZACIJA PROIZVODNJE BIODIZELA IZ PILEĆEG OTPADA I ETANOLA

Za dobijanje biodizela, jedan od najvažnijih faktora je kvalitet ulja koje se koristi u proizvodnji. Međutim, i druge faktore, kao što su cena i raspoloživost, treba, takođe, uzeti u obzir. Otpadno pileće ulje je vrlo obećavajuća mogućnost za ovu proizvodnju, jer potiče iz otpada. Cilj ovog rada bio je razvoj metodologije za ekstrakciju i karakterizaciju otpadnog pilećeg ulja i njegovu primenu za proizvodnju biodizela etanolizom, kao i optimizacija procesnih uslova proizvodnje biodizela primenom metodologiji površine odziva kombinovanom sa centralnim kompozitnim planom. Određene su karakteristike ulja: viskozitet, gustina, kiselost, vlažnost uzorka, indeks refrakcije i saponifikacioni broj, kao i karakteristike biodizela: viskozitet, gustina, kiselost i sadržaj estra. Pri optimalnim uslovima proizvodnju biodizela iz pilećeg ulja (koncentracija katalizatora 2,1%, odnos ulje/etanol 1:5,5 i reakciona temperatura 30 °C) postignuto je 95% konverzije. Fizičko-hemijske karakteristike dobijenog biodizela zadovoljavaju ANP standarde.

Ključne reči: biodizel; ileći otpad; etanoliza; optimizacija.

CI&CEQ
Chemical Industry & Chemical Engineering Quarterly

Available on line at
Association of the Chemical Engineers of Serbia *AChE*
www.ache.org.rs/CICEQ

Chem. Ind. Chem. Eng. Q. 27 (2) 165–176 (2021) CI&CEQ

CLÁUDIA JÉSSICA DA SILVA CAVALCANTI[1]
JOÃO PAULO DA SILVA QUEIROZ[2]
LUIZ STRAGEVITCH[1]
FLORIVAL RODRIGUES DE CARVALHO[1]
MARIA FERNANDA PIMENTEL[1]

[1]Department of Chemical Engineering, Federal University of Pernambuco, Recife-PE, Brazil
[2]Department of Chemical Engineering, Federal University of São Carlos, São Carlos-SP, Brazil

SCIENTIFIC PAPER

UDC 662.754.2:544:66

MULTIVARIATE STATISTICAL OPTIMIZATION OF THE ETHANOL FUEL DEHYDRATION PROCESS USING IONIC LIQUIDS

Article Highlights

- The desirability function assesses simultaneously several variables and their effects on responses
- Ionic liquids are promising solvents for the ethanol dehydration process
- Significant improvements in the processes with only minor modifications of a preexisting design

Abstract

In this work, the ethanol fuel dehydration process was optimized using the Aspen Plus® simulator and a multivariate statistical technique based on the desirability function. The suitability of the ionic liquids 1-methylimidazolium chloride ([Mim][Cl]), 1-ethyl-3-methylimidazolium chloride ([Emim][Cl]), 1-butyl--3-methylimidazolium chloride ([Bmim][Cl]) and 1-hexyl-3-methylimidazolium chloride ([Hmim][Cl]), as extractive distillation entrainers, was also evaluated and compared to the conventional solvents, ethylene glycol and cyclohexane. Among the solvents studied, [Mim][Cl] required the lowest energy consumption, about 8% less energy use when compared to the optimized process using ethylene glycol. The multivariate statistical techniques employed were effective in the optimization of the extractive distillation processes as the process energy consumption could be minimized while achieving ethanol purity in agreement with the current specifications as well as obtaining a high solvent recovery. With the desirability approach it was possible to improve the process performance with little or no modification of existing processing plants.

Keywords: bioethanol, desirability, energy, extractive distillation, ionic liquid, optimization.

The increasing contribution of liquid biofuels to the world energy matrix is a consequence of the growing concern about environmental issues and the adoption of public policies to reduce fossil fuel usage. One important liquid biofuel is ethanol. Ethanol can be used directly or as ethanol/gasoline blends in internal combustion engines with spark ignition. The former is hydrated ethanol fuel (HEF), containing about 5 vol.% water, while the latter is dehydrated ethanol fuel (DEF) with a water content of about 0.5 vol.% [1].

Brazil and the United States of America together account for 85% of the global ethanol fuel production [2], two largest producers of ethanol fuel in the world, with distillation still as the dominant ethanol recovery process [3,4,5]. Particularly in the northeast region of Brazil, the process of ethanol dehydration by azeotropic distillation continues to be the most used as the majority of industrial plants are very old. However, the adoption of the molecular sieve technology is growing, especially for new industrial units.

In those units where DEF is produced by azeotropic and extractive distillation, the solvents cyclohexane [6] and ethylene glycol (EG) [7-9] are widely used. As the use of cyclohexane presents environmental and exposure risks, new technologies to dehydrate ethanol are preferred, among which are the

Correspondence: M.F. Pimentel, Department of Chemical Engineering, Federal University of Pernambuco, Recife-PE, Brazil.
E-mail: mfernanda.pimentel@gmail.com, mfernanda.pimentel@ufpe.br
Paper received: 10 April, 2020
Paper revised: 17 August, 2020
Paper accepted: 15 September, 2020

https://doi.org/10.2298/CICEQ200410035C

use of molecular sieves, membranes and extractive distillation using less toxic and more efficient solvents such as EG and ionic liquids (ILs) [10]. ILs have the advantage of having a good ability for separation, easy handling and low contamination in distilled products [11,12]. Examples of the ILs used for dehydration of ethanol are: 1-butyl-3-methylimidazolium tetrafluoroborate and 1-ethyl-3-methylimidazolium tetrafluoroborate [13], 1-butyl-3-methylimidazolium chloride [14], 1-ethyl-3-ethylimidazolium diethyl phosphate [15] and 1-hexyl-3-methylimidazole chloride [16]. A modeling and simulation study on extractive distillation using ILs showed advantages with respect to the distillate purity and recovery [17]. Imidazolium-based ILs were compared and the process optimized using a univariate procedure of sensitivity analysis [18]. A high-purity (>99.9 mol%) ethanol was achieved with a lower energy consumption compared to conventional solvents.

Optimization through sensitivity analysis is a univariate procedure. Generally, this approach is not suitable for the evaluation of phenomena that depend on many variables as it cannot estimate the interdependency among the variables. By neglecting the interaction among variables, the resulting optimum does not necessarily correspond to the global optimum.

The optimization of a process can be accomplished, in general, by means of deterministic or stochastic approaches. In the first class of methods, all the steps can be predicted if the starting points are known. In other words, a deterministic method always leads to the same response if it starts from the same initial point. In contrast, stochastic methods have a random character. Several choices are made based on random numbers, drawn at runtime. Both approaches are widely used in optimization problems in chemical engineering when the goal is to maximize or minimize a given response while keeping others subjected to certain constraints [19,20].

The deterministic approach is composed of traditional optimization methods (direct and gradient-based methods) and has the disadvantages of requiring the first and/or second order derivatives of the objective function and/or constraints, and not being efficient in non-differentiable or discontinuous problems. In addition, the deterministic methods are dependent on the initial conditions chosen. The stochastic approach does not have these disadvantages, since it does not need to have any information about the search space, requiring only an objective/adequacy function that assigns a value to any solution [20]. However, even if starting from the same initial point, each run will follow its path, possibly leading to a different final response. It is important to remark that global optimization can only be guaranteed with deterministic methods. This is not guaranteed beforehand with stochastic techniques due to their probabilistic character. Both approaches are used when optimizing many factors and responses simultaneously. The application of these optimization approaches to separation processes has been reported by several authors [21-27].

Another optimization strategy is the use of a multivariate statistical optimization methodology, which consists of experimental design strategies to explore efficiently the space of the process variables; and empirical statistical modeling to develop an approximate relationship among the response (dependent variables) and the process variables (independent variables) in order to find optimized conditions [28]. Using this approach, interpretation of the models' coefficients (or main and interaction effects) contributes to enhancing process understanding.

The use of multivariate statistical optimization techniques along with process simulation still has not gained widespread usage. The ethanol dehydration process simulation and the use of response surface methodology to evaluate the interaction of the variables and their effects on the process can be found in the literature [29-32]. Their objective was to maximize the distilled ethanol concentration and to minimize the energy consumption. For these purposes, different surfaces were evaluated separately in order to identify a condition that would simultaneously satisfy the responses studied. This strategy may be satisfactory when different responses show similar behavior upon changing factor levels. When the responses have a certain degree of divergence, however, it is difficult to find a combination of the factor levels that simultaneously satisfies all the responses under investigation. A change in the level of one factor may improve a specific response while it may have a deleterious effect on the other responses [33]. A better approach to deal with multiple responses is to use mathematical functions to combine different responses into one, such as the desirability function proposed by [34]. Derringer's desirability function has proved to be efficient in optimizing processes [35,36]. However, the usefulness of the desirability function together with process simulation has not yet been reported in the literature.

In this work, the ethanol dehydration process by extractive distillation was optimized using multivariate statistical techniques, which consisted of simultaneously evaluating the relationship among several process variables through experimental design and sta-

tistical empirical modelling. The goal was to improve the performance of the process by means of simple modifications in an existing industrial plant. The desirability function was used to identify the set of factors that simultaneously optimize multiple responses related to the purity of the produced ethanol fuel and energy consumption. Results were compared to azeotropic distillation using cyclohexane, this still being a common process in the sugarcane ethanol industry. The Aspen Plus® simulator was employed to carry out the simulations with conventional process plant configurations. The following ILs were used as extractive distillation entrainers: 1-methylimidazolium chloride ([Mim][Cl]), 1-ethyl-3-methylimidazolium chloride ([Emim][Cl]), 1-butyl-3-methylimidazolium chloride ([Bmim][Cl]) and 1-hexyl-3-methylimidazolium chloride ([Hmim][Cl]).

METHODOLOGY

Process simulation

Figure 1a shows the simulated process flowsheet of the extractive distillation process [17]. The process is composed of the extractive distillation column (C-Column), which is fed with HEF and the solvent. Its distillate is DEF and the bottom stream is a mixture of water and solvent (water + solvent) which in turn is sent to the second column, the solvent recovery column (P-Column). The P-column separates the water (as the distillate), from the solvent, which is recovered at its base and recycled to C-column along with the pure solvent make up (MKUP stream).

The simulated azeotropic distillation process is shown in Figure 1b [6,37]. Cyclohexane was used as the separation agent. The process consists of two distillation columns: the first column (C-Column) is the azeotropic column where ethanol is rectified from the HEF feed, reflux and recycle streams. The bottom product is the DEF. The distillate is an azeotropic mixture of solvent, ethanol and water, separated into organic and aqueous phases in a decanter. The majority of the solvent is recovered in the organic phase which returns to the C-column as a reflux stream along with the pure solvent make up (MKUP feed). The aqueous phase is fed to the P-column for solvent recovery; its bottom product is recovered water and the distillate is a mixture rich in ethanol and cyclohexane which is then recycled to the C-column. The column model used for the simulations was the rigorous RadFrac module available in Aspen Plus®.

Thermodynamic model

A simplified vapor-liquid equilibrium (VLE) relation for the ethanol/water/solvent ternary mixture was used because of the low pressures involved:

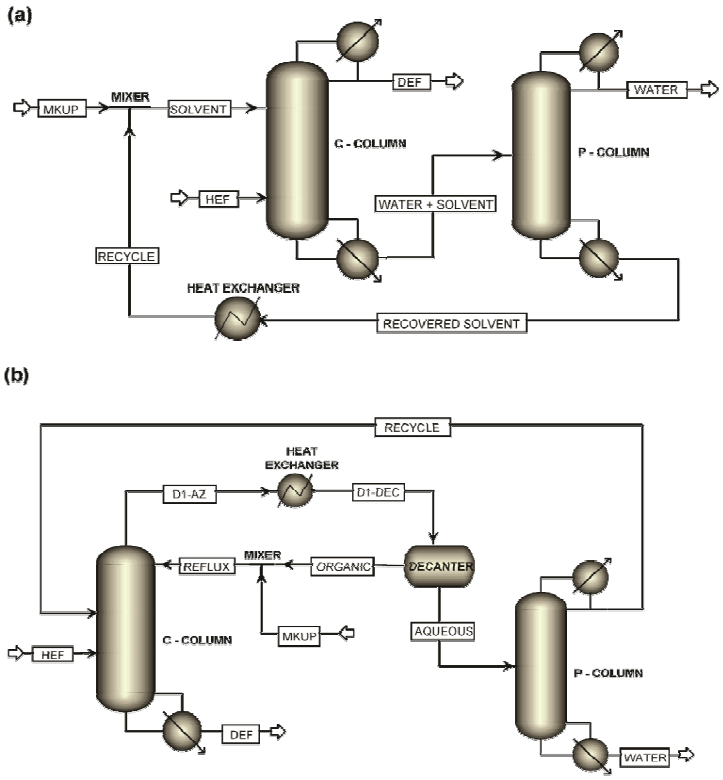

Figure 1. Process flowsheet of the extractive (a) and azeotropic (b) distillation processes.

$$Py_i = x_i \gamma_i P_i^{vap} \quad (1)$$

where P is the total pressure, y_i is the vapor phase mole fraction of component i, x_i is the liquid phase mole fraction of component i, γ_i is the activity coefficient of component i, and P_i^{vap} is the pure component i vapor pressure. Activity coefficients were calculated using the NRTL model [38]. Despite the fact that this model was developed for systems involving non-electrolytes [39], it has been widely used for mixtures with ILs [14,18,40,41].

The pure component properties were used as given in the Aspen Plus® databank, except for the ILs, not found in the database. In this case, the ILs were inserted into the simulator as pseudo-components. In order to estimate their vapor pressure, the data shown in Table 1 are introduced along with their pseudo-component definition.

The NRTL binary interaction parameters available in the Aspen Plus®.databases were used for the well-known ethanol/water/cyclohexane and ethanol/ /water/ethylene glycol ternary mixtures. For the systems with ILs, the NRTL binary interaction parameters were used as presented by [47] ([Mim][Cl]), [40] ([Emim][Cl]), [14] ([Bmim][Cl]) and [16] ([Hmim][Cl]).

Simulation setup

Table 2 presents the operational conditions for the simulated azeotropic [37] and extractive [17] distillation processes. In all cases, a flow rate of 100 kmol/h with a mass fraction of 95.2% ethanol was adopted for the HEF feed stream. A mass fraction greater than 99.3% ethanol was also specified for the DEF stream. Pressure in all distillation columns was set at 101.3 kPa [18,30,31].

Experimental design

Simultaneous evaluation of process factors was carried out using the Statistica® software, version 8. The factors evaluated were: reflux ratio of the dehydration (C-column) and recovery (P-column) columns, solvent to feed ratio (*S/F*), HEF feed stage, solvent feed stage and the recovery column (P-column) feed stage. The evaluated responses were: DEF purity (% mass), solvent recovery (%), purity of recovered solvent (% mass) and energy consumption per unit mass of DEF produced.

Initially, a screening of the six factors studied was performed through an experimental design, in order to choose the most significant factors. Then, using these most-significant variables, central composite designs were used to find the optimized condition. In the screening step, a six-factor full factorial design (with a central point) was used for each solvent, except for the azeotropic distillation process using cyclohexane in which only five factors could be studied. This is justified by the fact that the reflux ratio of the C-column is determined by the liquid-liquid phase splitting in the decanter. The C-column condenser was represented by a combination of a heat exchanger and a decanter (Figure 1b). Table 3 presents the levels of the factors studied, which were defined based on a previous sensitivity analysis.

Normal probability plots were employed in order to identify the significant factors for the process, as it is not possible, in simulations, to estimate the experimental random error. After selecting the most significant factors, factor levels were expanded using central composite designs (CCD), and the desirability function was used to find the optimal conditions.

Table 1. IL basic properties used in the creation of the pseudo-components in the simulator; NBP – normal boiling point

IL	Molecular formula	Molar mass (g/mol)	Density (kg/m^3)	*NBP* / K	Reference
[Mim][Cl]	$C_4H_7ClN_2$	118.56	1183.0	504.8	[42,43]
[Emim][Cl]	$C_6H_{11}ClN_2$	146.62	1186.0	484.6	[44]
[Bmim][Cl]	$C_8H_{15}ClN_2$	174.67	1080.0	547.5	[45]
[Hmim][Cl]	$C_{10}H_{19}ClN_2$	202.73	1040.4	593.2	[46]

Table 2. Process data used in the simulations

Specification	[Mim][Cl]	[Emim][Cl]	[Bmim][Cl]	[Hmim][Cl]	EG	Cyclohexane
Number of stages of C-column	33	33	33	33	33	31
HEF feed stage	20	20	20	20	20	15
Solvent feed stage	6	6	6	6	4	10
C-Column reflux ratio	2	2	2	2	1.4	-
Number of stages of P-column	12	12	12	12	12	22
Feed stage of P-column	11	9	9	11	4	11
P-Column reflux ratio	2	2	2	2	1.5	0.35

Table 3. Design factors and levels used in the screening step

Factor	[Mim][Cl]			[Emim][Cl]			[Bmim][Cl]			[Hmim][Cl]			EG			Cyclohexane		
	−	0	+	−	0	+	−	0	+	−	0	+	−	0	+	−	0	+
(1) HEF feed stage	16	24	32	20	26	32	18	25	32	20	26	32	22	27	32	11	14	17
(2) Solvent feed stage	4	11	18	2	5	8	2	7	12	2	5	8	3	6	9	2	6	10
(3) Feed stage of P-column	3	7	11	3	6	9	3	6	9	2	6	10	2	5	7	2	11	20
(4) Reflux ratio of C-column	0.5	1.25	2.0	0.5	1.25	2.0	1.2	1.6	2.0	0.5	1.25	2.0	0.8	1.22	1.65	-	-	-
(5) Reflux ratio of P-column	0.9	1.45	2.0	0.9	1.45	2.0	0.9	1.45	2.0	0.5	1.25	2.0	0.5	1.0	1.5	0.1	0.45	0.8
(6) *S/F*	0.19	0.24	0.28	0.25	0.28	0.31	0.30	0.35	0.40	0.44	0.46	0.48	0.55	0.60	0.65	0.110	0.115	0.121

In this approach, the individual responses were converted into values between 0 and 1, called individual desirability (d_i), where 0 and 1 represent undesirable and desirable responses, respectively [48]. In cases of response maximization, d_i was calculated by:

$$d_i = \begin{cases} 0, & y < L \\ \left(\dfrac{y-L}{T-L}\right)^s, & L \le y \le T \\ 1, & y > T \end{cases} \quad (2)$$

where y is the response being monitored, L is the lowest acceptable response and T is the target response. In addition, it is possible to weigh the response through the exponent s. In the cases of minimization of the response, d_i was given by:

$$d_i = \begin{cases} 1, & y < T \\ \left(\dfrac{U-y}{U-T}\right)^t, & T \le y \le U \\ 0, & y > U \end{cases} \quad (3)$$

U is the highest acceptable response and t is the response weighing parameter. A third possibility can be evaluated when the target value (T) is between the lowest (L) and the highest (U) values [48].

All the individual desirabilities were then combined by means of a geometric mean to calculate the global desirability D, given by:

$$D = \left(\prod_{i=1}^{m} d_i\right)^{1/m} \quad (4)$$

where m is the number of individual desirabilities. After the set of conditions that maximize the global desirability has been determined, the individual behavior of each response should be examined to ascertain that they are all within acceptable regions and with all constraints satisfied, and then analyze the practical feasibility [49].

RESULTS AND DISCUSSION

Residual curve maps analysis

The separation ability of the ILs as extractive distillation entrainers was initially evaluated by means of residual curve maps, as shown in Figure 2a-d. For comparison purposes, residual curve maps are also shown for EG and cyclohexane in Figure 2e and f, respectively. As can be observed, the ILs under study presented the same behavior as EG. As there are no stationary points in Figure 2a-e, a ternary mixture separation by extractive distillation is feasible.

For the ethanol/water/cyclohexane ternary (Figure 2f), on the other hand, there are three stationary points: binary azeotropes ethanol/cyclohexane at 64.92 °C, water/cyclohexane at 69.49 °C and ethanol/ /water at 78.15 °C. The unstable node for the ternary mixture at 62.39 °C defines three regions where the fed compositions will result in pure ethanol (region 1), pure water (region 2) and pure cyclohexane (region 3).

Factorial design screening

The complete factorial design with six factors shown in Table 3 was carried out in a preliminary screening stage for all solvents, except for cyclohexane where only five factors were taken into consideration. In all cases, the factorial design was performed again taking into consideration only the statistically significant factors from the previous step. This procedure was repeated until all remaining factors were significant. Analysis of the normal probability plots led to the results summarized in Table 4.

For illustration purposes, the normal probability plots for [Bmim][Cl] are shown in Figure 3. As can be seen, main effects 1, 2 and 4 and interaction between factors 1 and 4 are the most significant for the DEF purity and the recovered solvent purity responses (Figure 3a and c). For the recovered solvent purity, factor 6 also appears to be significant. In the case of the recovered solvent response (Figure 2b), the main effects 3, 4 and 5 and the interactions 3*4 and 3*5 were significant. For the energy consumption res

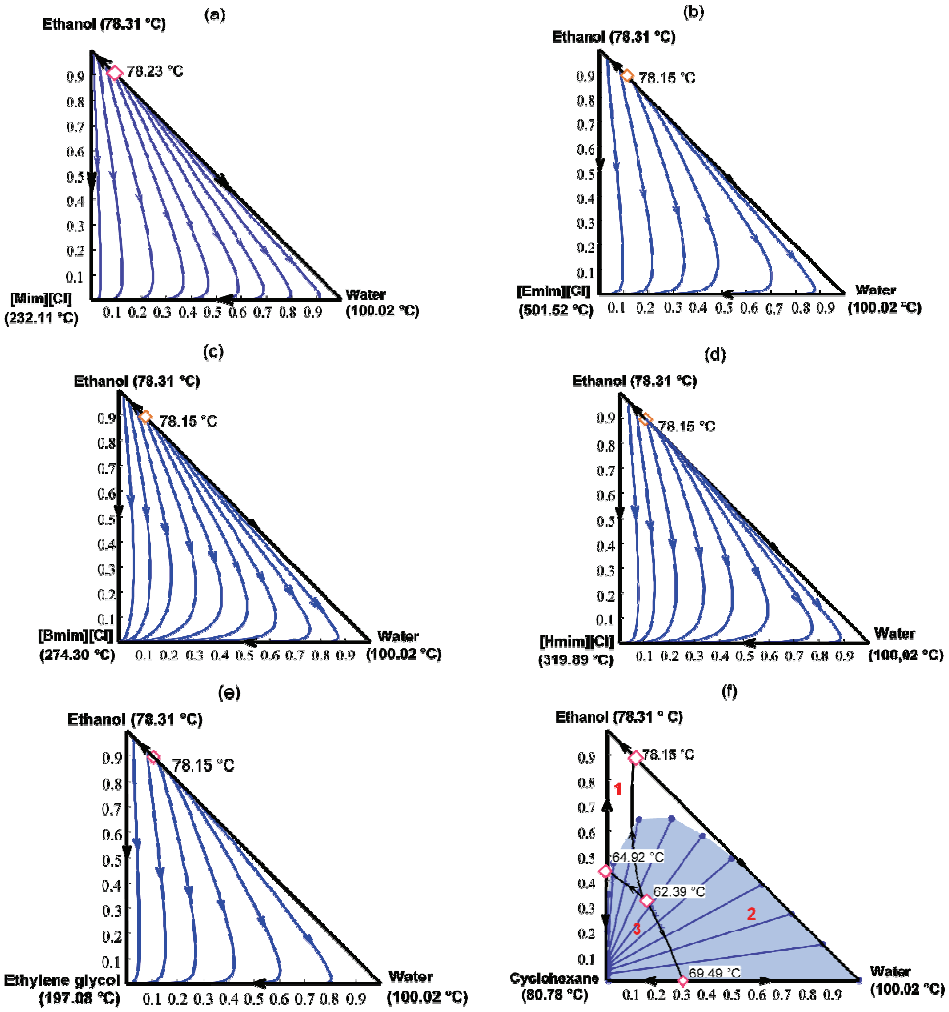

Figure 2. Residual curve maps for ethanol-water-solvent, where the solvent is: a) [Mim][Cl], b) [Emim][Cl], c) [Bmim][Cl], d) [Hmim][Cl], e) EG and f) cyclohexane.

Table 4. Factors and levels after the screening step

Factor	[Mim][Cl]			[Emim][Cl]			[Bmim][Cl]			[Hmim][Cl]			EG			Cyclohexane		
	−	0	+	−	0	+	−	0	+	−	0	+	−	0	+	−	0	+
(1) HEF feed stage	-	-	-	20	26	32	-	-	-	-	-	-	-	-	-	-	-	-
(2) Solvent feed stage	-	-	-	-	-	-	2	7	12	2	5	8	-	-	-	2	6	10
(3) Feed stage of P-column	-	-	-	-	-	-	-	-	-	-	-	-	2	5	7	2	11	20
(4) Reflux ratio of C-column	0.5	1.25	2.0	0.5	1.25	2.0	1.2	1.6	2.0	0.5	1.25	2.0	0.80	1.22	1.65	-	-	-
(5) Reflux ratio of P-column	0.9	1.45	2.0	-	-	-	-	-	-	-	-	-	0.5	1.0	1.5	-	-	-
(6) *S/F*	0.19	0.24	0.28	0.25	0.28	0.31	0.30	0.35	0.40	0.44	0.46	0.48	-	-	-	0.110	0.115	0.121

ponse, the main effects of factors 4, 5, 6 and 2 are clearly significant.

Factor 3 seems not to be significant for any of the responses investigated. Factor 1 is only significant for the following responses: purity of anhydrous ethanol and purity of recovered solvent, showing a negative signal for each. Thus, after observing the normal graphs and the responses for the design matrix, factor 3 was the positive level and factor 1 at the negative level, as at these levels the best results show.

A new design was proposed for the remaining factors (factors 2, 4, 5 and 6). In this design, factor 5 only showed significance for the response of energy consumption, and by setting this factor at the negative level, lower values of energy were obtained. And

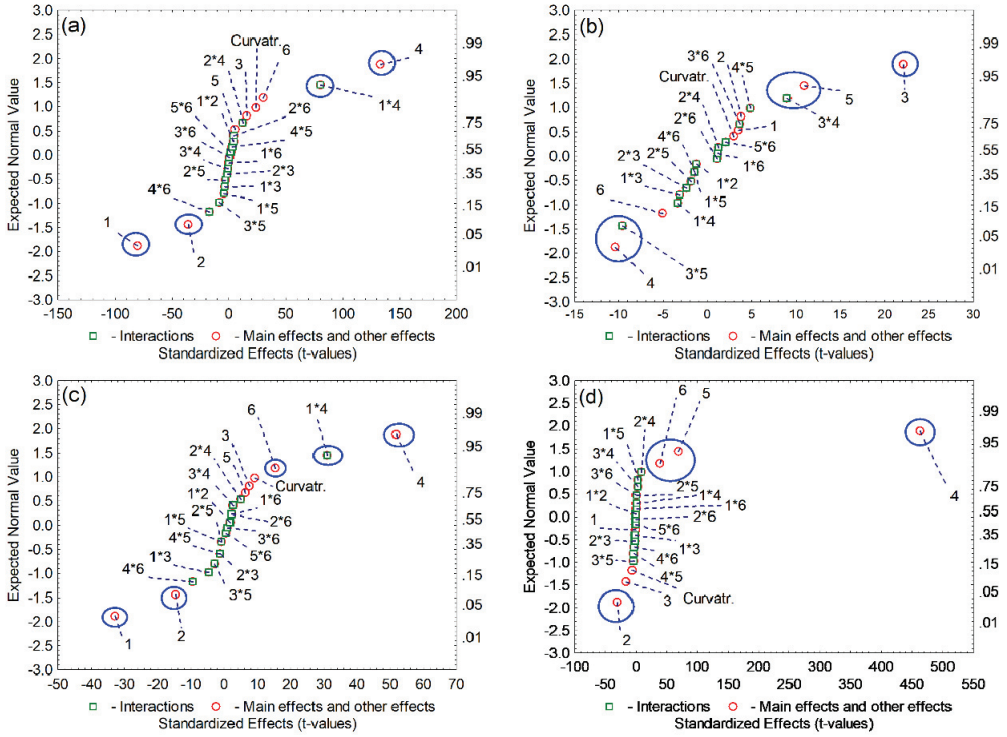

Figure 3. Normal probability plots for the 2^6 factorial design for the extractive distillation using [Hmim][Cl]; responses are: a) DEF purity, b) solvent recovery, c) purity of recovered solvent and d) energy consumption.

finally, a face-centered design of three factors (2, 4 and 6) was proposed.

In order to carry out the simulations, values for some factors, including the non-significant factors, were chosen as described next. [Mim][Cl]: non-significant factors 1 (HEF feed stage), 2 (solvent feed stage) and 3 (P-column feed stage) were all set at the negative level, 16, 4 and 3, respectively. [Emim][Cl]: non-significant factors 2 (solvent feed stage), 3 (P--column feed stage) and 5 (reflux ratio of P-column) were set at the positive (8), positive (9) and negative (0.5) levels, respectively. [Bmim][Cl]: non-significant factors 1 (HEF feed stage), 3 (P-column feed stage) and 5 (reflux ratio of P-column) were set at the positive (32), negative (3) and negative (0.9) levels, respectively. EG: non-significant factors 1 (HEF feed stage), 2 (solvent feed stage) and 6 (*S/F*) were set at the negative (22), negative (3) and positive (0.65) levels, respectively. Cyclohexane: non-significant factors 1 (HEF feed stage) and 5 (P-column reflux ratio) were set at 15 and 0.45, respectively.

Desirability function

Following the desirability definition, undesirable conditions (d_i = 0) were chosen as DEF purity less than 99.3% and purity of recovered solvent less than 99%. On the other hand, the desirable conditions (d_i = = 1) were defined as DEF purity greater than 99.7% and purity of recovered solvent greater than 99.6%. Energy consumption and solvent recovery specifications were defined according to the results obtained for each experimental design. In the processes in which ionic liquids were used, it was not necessary to evaluate the response of the recovered solvent, since the recovery was 100% for all cases. The desirability function was generated in the Statistica® software. For illustration purposes, results for the extractive distillation process using the [Mim][Cl] IL are shown in Figure 4.

The curves in Figure 4 show the effect of each factor on the responses while the levels of the remaining factors are held at the specified values. The last column of graphs in Figure 4 shows the desirability previously set for each response. Taking factor 4 (C-Column reflux ratio) as an example, its effects on the responses can be observed in the first column on the graphs, where the first graph corresponds to the DEF purity. Its optimal point is located at level -1 of the design. A similar behavior was observed for the purity of the recovered solvent. At level -1, the energy consumption was minimized. Thus, level -1 meets the best combination of optimal conditions for factor 4, which is endorsed by the global desirability shown at the bottom left in Figure 4.

The second column of graphs in Figure 4 shows the effects of factor 5 (P-Column reflux ratio). As can

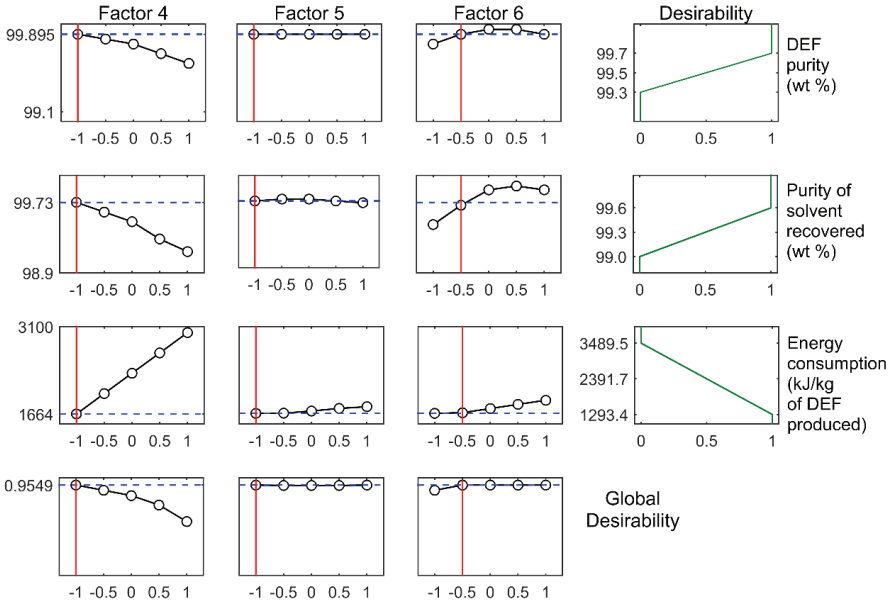

Figure 4. Desirability function results for the extractive distillation process using [Mim][Cl] IL.

be observed, the response variation is smaller in comparison to factor 4, but DEF purity, purity of the recovered solvent and energy consumption also reach optimal conditions at level −1. As a result, the global desirability indicates that factor 5 meets all specifications at level −1.

Finally, the third column of graphs in Figure 4 presents the effects of factor 6 (S/F ratio). Here, the optimal conditions are observed at level -0.5 for DEF purity, purity of the recovered solvent and energy consumption. Thus, the best condition for all the responses is located at level -0.5 as given by the global desirability.

The analysis described above was repeated for each process. Results are summarized in Figure 5. The decoded optimal levels are presented in Table 5 along with the responses obtained from process simulations at the corresponding levels. Table 5 also

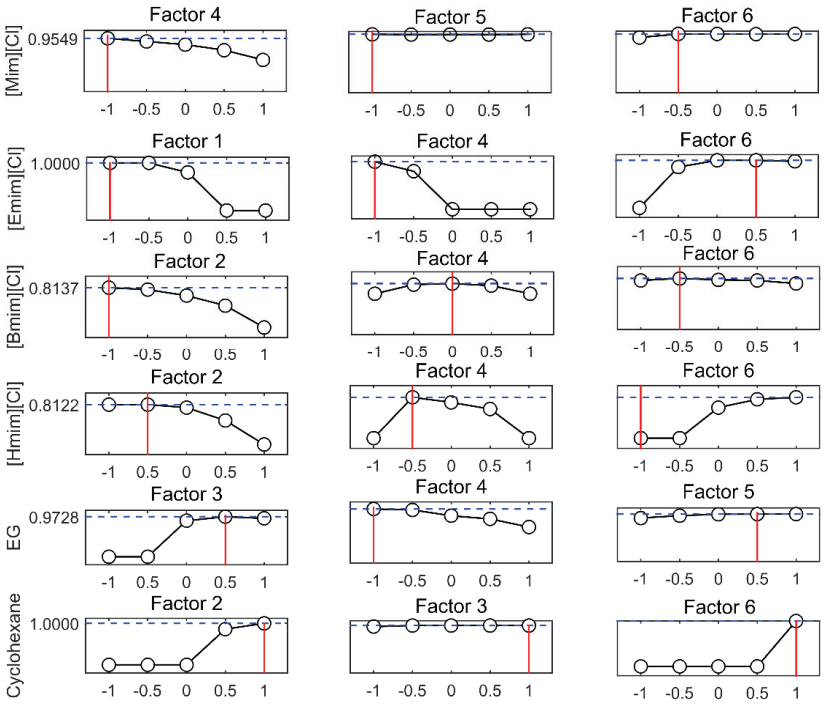

Figure 5. Global desirability for each simulated process.

Table 5. Comparison of simulation results for starting (S) and optimized (O) process conditions

Factor	[Mim][Cl]		[Emim][Cl]		[Bmim][Cl]		[Hmim][Cl]		EG		Cyclohexane	
	S	O	S	O	S	O	S	O	S	O	S	O
(1) HEF feed stage	20	16	20	20	20	32	20	20	20	22	15	15
(2) Solvent feed stage	6	4	6	8	6	2	6	4	4	3	10	10
(3) P-Column feed stage	11	3	9	9	9	3	11	10	6	6	11	20
(4) C-Column reflux ratio	2	0.5	2	0.5	2	1.6	2	0.9	1.4	0.8	-	-
(5) P-Column reflux ratio	2	0.9	2	0.5	2	0.9	2	0.5	1.5	1.25	0.35	0.45
(6) *S/F* ratio	0.19	0.22	0.25	0.295	0.30	0.325	0.44	0.48	0.60	0.65	1.20	1.21
						Response						
DEF purity (mass fraction, %)	99.6	99.9	99.4	99.9	99.4	99.6	99.3	99.6	99.9	99.6	99.9	99.9
Solvent recovery (%)	100	100	100	100	100	100	100	100	100	99.2	97.08	97.25
Purity of solvent recovered (mass fraction, %)	99.3	99.7	99.3	99.9	99.6	99.7	99.6	99.8	99.9	99.6	95.2	95.3
Energy consumption (kJ/kg of DEF produced)	3078	1665	3631	2495	3482	3065	4072	3045	2340	1818	3101	3248

presents factors and the corresponding responses from simulations based on the data used for the screening step (Table 3). Detailed information for each optimized flowsheet is available upon request to corresponding author as the supplementary material.

As can be observed in Table 5, a DEF mass fraction purity ≥99.3% was obtained in all cases as well as a high solvent recovery, thus, reducing the amount of solvent needed make up. With respect to energy consumption, a decrease was observed in all cases under the optimized conditions, reaching 45.9% for the [Mim][Cl] process, except for the azeotropic distillation using cyclohexane where an increase of 4.7% was obtained. This observation can be rationalized by the fact that the feasible operating conditions for the azeotropic distillation process are constrained to a narrow region (Figure 2f) so that the starting setup can be used as the optimal set of conditions. However, for the majority of cases, the multivariate statistical technique used was effective in producing the specified DEF accompanied by a decrease in the energy consumption and requiring only small modifications of an existing process plant.

The optimized results obtained were compared with the literature from an extensive review of recent advances in the development of bioethanol recovery and dehydration processes [50]. Fifty-four publications were identified on the topic. They were classified according to the concentration of ethanol used in the process feed. Sixteen papers reported a process feed close to the azeotrope point of the ethanol/water mixture (90-95%), which was the EHF concentration we used in this article. These works were also classified according to the type of technology used for dehydration, all of them used distillation.

Hence, an approximate comparison was made with the cases that used hydrated ethanol feeds close to the azeotrope point. Table 6 presents a comparison of the energy consumption and DEF purity obtained in our study in relation to the most relevant works in the literature as well as other information about these publications.

The azeotropic distillation process simulated in this work presented energy consumption 36.1% lower than that presented by [6]. In the case of extractive distillation with EG, the energy consumption obtained in this study was 3.3% higher than that reported by [7] who used the same solvent, the difference being due to different simulation configurations. The use of the EG/calcium chloride mixture [30] presented an energy consumption 27.6% lower than the extractive distillation process with EG. Relative to EG and tetraethylene glycol [10], higher values of energy consumption were observed. However, in these cases only the energy used by the dehydration column was reported, so that the energy used in the solvent recovery step was not taken into account. Finally, EG [51], EG/glycerol mixture [52] and glycerol [53] presented higher energy consumptions when compared to EG case studied in this work.

In the case of IL, in our work, especially for [Emim][Cl] and [Bmim][Cl], based on the [17], there was a reduction of 23.9% and 29.7% in relation to energy consumption, respectively. Unfortunately, the same was not observed for [Hmim][Cl], with only a small difference of 1.2% between the cases studied relative to the results from [17]. Other ILs found in the

Table 6. Comparison of the energy consumption, DEF purity and HEF feed results for ethanol dehydration

Solvent	HEF feed wt.%	DEF purity wt.%	Energy consumption (kJ/kg of anhydrous ethanol)	Remarks	Reference
[Mim][Cl]	95.2	99.9	1665	-	Authors
[Emim][Cl]	95.2	99.9	2495	-	
[Bmim][Cl]	95.2	99.6	3065	-	
[Hmim][Cl]	95.2	99.6	3045	-	
EG	95.2	99.6	1818	-	
Cyclohexane	95.2	99.9	3101	-	
[Emim][Cl]	89.0	99.5	3278	-	[17]
[Bmim][Cl]	90.0	99.6	4359		
[Hmim][Cl]	93.0	99.6	3008		
[Bmim][SO4]	93.0	99.6	4118		
[Bmim][BF4]	93.0	99.5	8689		
[Emim][BF4]	93.5	99.9	2270	-	[18]
Tetraethylene-glycol	93.5	99.6	4600*	*Energy consumption calculation based on the dehydration column only	[10]
EG	93.5	99.6	3600*		
EG	93.5	99.9	2200	New operating flowsheet was proposed including three columns: an extractive distillation column, solvent recovery column, and a concentrator.	[51]
EG	93.5	99.9	1760	Simulation based on laboratory experiments and a pilot plant.	[7]
EG + Calcium Chloride	94.9	99.9	1425	Vacuum distillation used on the solvent recovery column	[30]
60% EG + 40% Glycerol	94.9	99.9	2018	Vacuum distillation used on the solvent recovery column	[52]
Glycerol	93.5	99.5	1900	Vacuum distillation used on the solvent recovery column	[53]
Cyclohexane	90.0	99.9	7900-14000	Dividing-wall column used for heterogeneous azeotropic distillation	[54]
Cyclohexane	93.5	*	4853	*Anhydrous ethanol obtained within specification	[6]
Gasoline	93.5	*	3180		

literature are included on the table in order to compare with energy consumption, indicating that all IL proposed in this article showed lower energy consumption.

The lowest energy consumption among the ILs presented was observed for [Mim][Cl], about 8% lower than that obtained for the optimized process with EG. Among the IL, the following order of increasing energy was obtained: [Mim][Cl] (1665 kJ/kg DEF) < [Emim][Cl] (2495 kJ/kg DEF) < [Hmim][Cl] (3045 kJ/kg DEF) ≈ [Bmim][Cl] (3065 kJ/kg DEF). The difference between the energy consumption of the last two ionic liquids is less than 1%. Among the studied ILs, [Mim][Cl] was found to be the most promising solvent for the production of anhydrous ethanol with high purity at lower energy levels, having the lowest *S/F* (0.22) required to separate the ethanol--water mixture.

CONCLUSIONS

The suitability of the ILs used for ethanol dehydration was evaluated with optimized process conditions presenting improvements when compared to base cases, except for azeotropic distillation using cyclohexane. This process is still used in the Brazilian industry, although its operational conditions are constrained to quite narrow ranges. As a result, the proposed starting setup may be taken to seamlessly be included at the optimal point. For the extractive distillation processes, however, it was possible to find optimal conditions meeting the specified goals. Among the ILs used as entrainers in the extractive distillation, [Mim][Cl] presented the best results with 8% less energy use when compared to the optimized process using EG. The use of the multivariate statistical technique and the desirability function made it possible to evaluate simultaneously the relationships among several process variables and their effects on the spe-

cified responses. This approach was effective in finding the optimal process conditions, making significant improvements possible in the processes studied with only minor modifications of a preexisting process plant. The application of this methodology to the energy intensive ethanol dehydration process is an important contribution to the sustainability of the sugarcane industry by increasing ethanol fuel competitiveness against fossil fuels.

Acknowledgments

This work was supported by NUQAAPE/ /FACEPE [process No.: APQ-0346-1.06/14]; INCTAA [processes No.: CNPq 573894/2008-6; FAPESP 2008/57808-1], CNPq [process No.: 428891/2018-7] and CAPES. The English text of this paper has been revised by Sidney Pratt, Canadian, MAT (The Johns Hopkins University), RSAdip - TESL (Cambridge University).

Abbreviations list

[Mim][Cl]	1-Methylimidazolium chloride
[Emim][Cl]	1-Ethyl-3-methylimidazolium chloride
[Bmim][Cl]	1-Butyl-3-methylimidazolium chloride
[Hmim][Cl]	1-Hexyl-3-methylimidazolium chloride
EG	Ethylene glycol
HEF	Hydrated ethanol fuel
DEF	Dehydrated ethanol fuel
IL	Ionic liquid
NRTL	Non-Random Two Liquid
S/F	Solvent-to-feed ratio
CCD	Central composite design

REFERENCES

[1] J. Belincanta, J.A. Alchorne, M.T. Silva, Braz. J. Chem. Eng. 33 (2016) 1091-1102

[2] Renewable Fuels Association (RFA). Leading the U.S. Ethanol Industry: 2016 (http://www.ethanolrfa.org/resources/industry/ statistics/)

[3] L.C.B.A. Bessa, F.R.M. Batista, A.J.A. Meirelles, Energy 45 (2012) 603–612

[4] G.H.S.F. Ponce, M. Alves, J.C.C. Miranda, R.M. Filho, M.R.W. Maciel, Chem. Eng. Res. Des. 95 (2015) 55–63

[5] R. Palacios-Bereche, A.V. Ensinas, M. Modesto, S.A. Nebra, Energy 82(2015) 1–12

[6] A. Chianese, F. Zinnamosca, Chem. Eng. J. Netherlands (1990) 59-65

[7] A. Meirelles, S. Weiss, H.J. Herfurth, Chem. Technol. Biotechnol. 53 (1992) 181-188

[8] R. Pinto, M. Wolf-Maciel, L. Lintomen, Comput. Chem. Eng. 24 (2000) 1689-1694

[9] J. Fu, Ind. Eng. Chem. Res. 43 (2004) 1274-1278

[10] M.A.S.S. Ravagnani, M.H.M. Reis, R. Maciel Filho, M. R. Wolf-Maciel, Process Saf. Environ. 88 (2009) 67-73

[11] L.C. Branco, Sociedade Portuguesa de Química, Lisboa, 1 (2015) 15-22

[12] M. Seiler C. Jork, A. Kavarnou, W. Arlt, R. Hirsch, AIChE J. 50 (2004) 2439-2454

[13] C. Jork, M. Seiler, Y.A. Beste, W. Arlt, J. Chem. Eng. Data (2004) 852-857

[14] N. Calvar, B. González, E. Gómez, Á. Domínguez, J.. Chem. Eng. Data (2006) 2178-2181

[15] X.C. Jiang, J.F. Wang, C.X. Li, L.M. Wang, Z.H. Wang, J. Chem. Thermodyn. (2007) 841-846

[16] L. Zhang, Y. Ge, D. Ji, J. Chem. Eng. Data (2009) 2322--2329

[17] J.J. Figueroa, B.H. Lunelli, R. Maciel Filho, M.R. Wolf Maciel, Procedia Eng. (2012) 1016-1026

[18] Z. Zhu, Y. Ri, M. Li, H. Jia, Y. Wang, Y. Wang, Chem. Eng. Process, China 1 (2016) 190-198

[19] T.F. Edgar, D.M. Himmelblau, L.S. Lasdon, Optimization Of Chemical Processes, McGraw-Hill International, 2nd ed., 2001

[20] K. Deb, Optimization For Engineering Design : Algorithms And Examples, Phi Learning Private Limited, New Delhi, 2nd ed., 2012

[21] M. Martín, I.E. Grossmann, AIChE J. 57 (2011) 3408--3428

[22] R. Brunet, G. Guillén-Gosálbez, L. Jiménez, AIChE J. 60 (2013) 500-506

[23] P. Kanchanalai, R.P. Lively, M.J. Realff, Y. Kawajiri, Ind. Eng. Chem. Res. 52 (2013) 11132-11141

[24] M.B. Franke, Comput. Chem. Eng. 89 (2016) 204-221

[25] X.L. Yang, J.D. Ward, Ind. Eng. Chem. Res. 57 (2018), 11050-11060

[26] A. Yang, H. Zou, I. Chien, D. Wang, S. Wei, J. Ren, W.; Shen, Ind. Eng. Chem. Res. 58 (2019) 7265-7283

[27] Y. Cui, Z. Zhang, X. Shi, C. Guang, J. Gao, Sep. Purif. Technol. 236 (2020) 116303

[28] R.H. Myers, D.C. Montgomery, Response Surface Methodology: Process and Product Optimization Using Designed Experiments, Wiley Series in Probability and Statistics, New York, 2016

[29] A.M. Uyazán, I.D. Gil, J. Aguilar, G. Rodríguez, L.A. Caicedo, Ing Invest. Bogotá 26 (2006) 45-50

[30] I.D. Gil, A.M. Uyazán, J. Aguilar, G. Rodríguez, L.A. Caicedo, Braz. J. Chem. Eng. (2008) 207-215

[31] I.D. Gil, J. M. Gómez, G. Rodríguez, Comput. Chem. Eng. (2012) 129-142

[32] E. Ebrahimiaqda, K.L. Ogden, ACS Sustain. Chem. Eng, 5 (2017) 6854-6862

[33] M.A. Bezerra, S.L.C. Ferreira, C.G. Novaes, A.M.P. Santos, G.S. Valassques, U.M.F.M. Cerqueira, J.P.S. Alves, Talanta (2018) 941-959

[34] G. Derringer, R.J. Suich, Qual. Technol. 12 (1980) 214-219

[35] C. Buratti, M. Barbanera, E. Lascaro, F. Cotana, Waste Manage. 71 (2017) 523-534

[36] L. Mesa, Y. Martínez, E. Barrio, E. González, Appl.. Energy (2017) 299-311

[37] I.D.G. Chaves, J.R.G. López, J.L.G. Zapata, A.L. Robayo, G.R. Niño, Process Analysis and Simulation in Chemical Engineering, Springer, 1st ed., London, 2016

[38] H. Renon, J. M. Prausnitz, (). Local compositions in thermodynamic excess functions for liquid mixtures. AIChE J. 14 (1968) 135-144

[39] E.C. Carlson, Chem. Eng. Prog. 92 (1996) 35-46

[40] Y. Ge, L. Zhang, X. Yuan, W. Geng, J. Ji, J. Chem. Thermodyn. 40(2008) 1248-1252

[41] N. Calvar, B. González, E. Gómez, G. Domínguez, J. Chem. Eng. Data 1 (2009) 1004-1008

[42] J.N.C. Lopes, A.A.H. Pádua, J. Phys. Chem. 110 (2006) 19586-19592

[43] GUIDECHEM - Chemical Trading Guide, Chemical Dictionary: CAS No. 35487-17-3, https://www.guidechem.com/encyclopedia/1h-imidazole-1-methyl-hydrochldic44712.html#Properties, (accessed on July 2020)

[44] S. A. Bolkan J. T. Yoke, J. Chem. Eng. Data 31 (1986)194-197

[45] J.G. Huddleston, A.E. Visser, W.M. Reichert, H.D. Willauer, G.A. Broker R.D. Rogers, Green Chem. 3 (2001) 156-164

[46] E. Gomez N. Calvar, I. Dominguez, A. Dominguez,Phys. Chem. Liq. 44 (2006) 409-417

[47] C. Shen, X. Li, Y. Lu, C. Li, J. Chem. Thermodyn. 43 (2011) 1748-1753

[48] E.R.P. Filho, Editora UFSCar, 1ª. Ed., São Carlos, 2015. p. 88

[49] B. Barros Neto, I.S. Scarminio, R.E. Bruns, Bookman, , Porto Alegre, 4. ed., 2010, p. 414

[50] A. Singh, G. P. Rangaiah, Ind. Eng. Chem. Res. 56 (2017) 5147-5163

[51] G. Li, P. Bai, Ind. Eng. Chem. Res. 51 (2012), 2723−2729

[52] I.D. Gil, L.C. García, G. Rodríguez, Braz. J. Chem. Eng. 31 (2014) 259−270

[53] P. García-Herreros, J.M. Gómez, I.D. Gil, G. Rodríguez,, Ind. Eng. Chem. Res. 50 (2011) 3977−3985

[54] L.-Y. Sun, X.-W. Chang, C.-X. Qi, Q.-S. Li, Sep. Sci. Technol. 46 (2011) 1365−1375.

CLÁUDIA JÉSSICA DA SILVA CAVALCANTI[1]
JOÃO PAULO DA SILVA QUEIROZ[2]
LUIZ STRAGEVITCH[1]
FLORIVAL RODRIGUES DE CARVALHO[1]
MARIA FERNANDA PIMENTEL[1]

[1]Department of Chemical Engineering, Federal University of Pernambuco, Recife-PE, Brazil
[2]Department of Chemical Engineering, Federal University of São Carlos, São Carlos-SP, Brazil

NAUČNI RAD

MULTIVARIJABILNA STATISTIČKA OPTIMIZACIJA PROCESA DEHIDRATACIJE ETANOLA KORIŠĆENJEM JONSKIH TEČNOSTI

U ovom radu, optimizovan je postupak dehidratacije etanola pomoću simulatora Aspen Plus® i multivarijabilne statističke tehnike zasnovane na funkciji poželjnosti. Pogodnosti jonskih tečnosti 1-metilimidazolijum-hlorida ([Mim] [Cl]), 1-etil-3-metilimidazolijum-hlorida ([Emim] [Cl]), 1-butil-3-metilimidazolijum-hlorida ([Bmim] [Cl]) i 1-heksil-3-metilimidazolijum-hlorida ([Hmim] [Cl]), kao modifikatora ekstraktivne destilacije, su procenjene i upoređene sa konvencionalnim rastvaračima, etilen-glikolom i cikloheksanom. Među korišćenim rastvaračima, [Mim] [Cl] je zahtevao najmanju potrošnju energije, oko 8% manje u odnosu na etilen-glikol. Korišćene multivarijabilne statističke tehnike bile su efikasne u optimizaciji procesa ekstraktivne destilacije, jer se potrošnja energije u procesu može svesti na minimum, dok se postiže čistoća etanola u skladu sa važećim specifikacijama i visok povraćaj rastvarača. Ovim pristupom bilo je moguće poboljšati učinak procesa sa malo ili bez modifikacije postojećih procesnih postrojenja.

Ključne reči: bioetanol, poželjnost, energija, ekstraktivna destilacija, jonska tečnost, optimizacija.

CI&CEQ
Chemical Industry & Chemical Engineering Quarterly

Available on line at
Association of the Chemical Engineers of Serbia *AChE*
www.ache.org.rs/CICEQ

Chem. Ind. Chem. Eng. Q. 27 (2) 177–187 (2021) CI&CEQ

SRINIVASAN PERIASAMY MANIKANDAN[1]
RAJOO BASKAR[2]

[1]Department of Chemical Engineering, Kongu Engineering College, Erode, India
[2]Department of Food Technology, Kongu Engineering College, Erode, India

SCIENTIFIC PAPER

UDC 661.666:66.03:54

STUDIES ON THERMOPHYSICAL PROPERTY VARIATIONS OF GRAPHENE NANOPARTICLE SUSPENDED ETHYLENE GLYCOL/WATER

Article Highlights

- Graphene/ethylene glycol/water mixed nanofluids were prepared
- The thermophysical characteristics of the graphene suspended base fluid was studied
- Obtained results were compared with models proposed in the literature

Abstract

The objective of the study is to determine the thermophysical property variations (such as viscosity, density, specific heat capacity and thermal conductivity) of graphene suspended base fluid (ethylene glycol (EG)/water (W)), with respect to graphene nanoparticle concentration and hot fluid inlet temperature. Graphene nanoparticle concentrations (0.2, 0.4, 0.6, 0.8 and 1 vol.%) and the base fluid of 30:70 vol.% of EG: Water is prepared initially. The impact of graphene nanoparticle addition on base fluids based on experimentation in the commercial plate heat exchanger was studied. In this experiment, the hot fluid inlet temperature was varied at 55, 65 and 75 °C. The experimental results of thermophysical properties were compared with the selected models proposed in the literature. Einstein (1956), Kitano (1981) and Bachelor models (1977) have been used to consider the effect of viscosity. The measured density and specific heat capacity were validated with Pak and Cho and Xuan models, respectively. To consider the effect of thermal conductivity, three different models (Maxwell (1954), Vajjah (2010) and Sahoo (2012)) have been used. Study revealed that the thermophysical properties of base fluid significantly affect the graphene nanoparticle suspension.

Keywords: graphene, nanoparticle, thermophysical property, ethylene glycol, water.

Viscosity, density, specific heat capacity and thermal conductivity are significant thermophysical properties, which alter the properties of conventional heat transfer fluids. Viscosity is a significant property which measures a fluid friction and its internal flow resistance. Density of a fluid is directly proportionate with respect to pressure and indirectly proportionate with respect to temperature. Also, this property is important in the stage of preparation of nanoparticle suspensions, since for materials with different densities is difficult to get a homogeneous mixture. Specific heat capacity represents the quantity of heat needed to increase the temperature of one kg of mass by 1 K. It is a significant factor since it decides the requirement of heat transfer fluid. Among the four properties, thermal conductivity is a very significant factor, since it is expected, when high thermal conductivity nanometer-sized particles are added to a conventional heat transfer fluid, to reach for achieving higher value of thermal conductivity of the nanoparticle mixture. This property plays important role in the design and fabrication of energy-efficient heat transfer equipment. From the available literature, it was found that low thermal conductivity is a primary drawback in the growth of energy-efficient heat transfer fluids. Hence, nanoparticle suspended base fluids are needed to show high thermal conductivities compared to those of base heat transfer fluids for efficient utilization in heat transfer processes. These fluids are beneficial in

Correspondence: S.P. Manikandan, Department of Chemical Engineering, Kongu Engineering College, Erode-638 060, India.
E-mail: sriperiasamy@gmail.com
Paper received: 4 May, 2020
Paper revised: 25 July, 2020
Paper accepted: 24 September, 2020

https://doi.org/10.2298/CICEQ200504036P

various industries such as transportation, chemical, electronics cooling, space, nuclear and food industries [1]. Corrugated heat exchangers are very useful in dairy industries because of their outstanding heat transfer coefficient characteristics and compact designs [2].

The following literature are studies based on the effect of thermophysical properties with respect to nanofluid: the initial idea was proposed by Choi *et al.* [3] for enhancing the thermal conductivity of base heat transfer fluids by adding and mixing nanoparticles in a base fluid. They observed that metals and metal oxides possess higher thermal conductivity than the base fluids. Sarafraz *et al.* [4] framed a research work for studying the pool boiling heat transfer behaviour of MEG/DEG/water ternary mixture suspended nanofluid and developed a new correlation. Rasher *et al.* [5] studied the viscosity effect on aluminium oxide suspended pure propylene glycol at a temperature range of 30 to 60 °C and a nanoparticle volume fraction of 0.5 to 3%; they varied the nanoparticle size (27, 40 and 50 nm). They reported incremental effect on viscosity of nanoparticle suspension. Kulkarni *et al.* [6] performed investigation on rheological properties with copper oxide nanoparticles suspended in a propylene glycol/water mixture. Their operating temperature ranged between -35 and 50 °C; they have also varied the particle volume fraction (0-5.9%). They made comparative analysis of experimental data with ASHRAE data (2005) and Bachelor's correlation equation (1977), and observed better agreement with ASHRAE data, whereas the Bachelor's correlation showed substantial deviation. The thermodynamic feasibility of the liquid chemical looping gasification (LCLG) in syngas production was made by Sarafraz *et al.* [7]. In this study, copper oxide is implemented as an oxygen carrier for chemical looping gasification process. The proposed system offers a potential benefit to avoid agglomeration and sintering, which implies that no further process is required in separation of the evaporated copper oxide from the syngas.

Aluminium oxide and copper oxide suspended water nanofluid was analysed by Nguyen *et al.* [8] for the effect of nanoparticle addition on viscosity of base fluids. They have conducted the study by varying the nanoparticle volume fraction, size of the nanoparticle and operating temperature. The obtained results revealed that viscosity is strongly influenced by the volume concentration of the nanoparticle. However, with respect to particle size the dependency of the viscosity is less significant. The experimental study was conducted by Namburu *et al.* [9] with SiO_2 nanoparticle suspended in a base fluid of water and ethylene glycol mixture. Their objective was to find the viscosity effect on the addition of SiO_2 nanoparticle with 20, 50 and 100 nm. They observed lowest viscosity 100--nm-sized SiO_2 nanoparticle at 8% volume fraction. Silver nanoparticle suspension in water was used by Godson *et al.* [10] to find the viscosity effect of silver nanoparticle dispersed in deionized water. Their operating conditions were experimental temperature of 50 to 90 °C and the nanoparticle volume concentration of 0.3-0.9%. The study demonstrates the effect of Brownian motion and thermophoresis on the thermophysical properties of base fluid. They also developed an experimental correlation for viscosity relating with the temperature and nanoparticle volume fraction. Sarafraz [11] prepared dispersions of CuO nanoparticles in water/ethylene glycol mixture at 50-50 volumetric concentrations, in order to study the sedimentation effects and convective boiling characteristics of the prepared fluid. Comparative analysis was made between the experimental results and correlations (Chen, Gun-gor-Winterson, Rohsenow) and the study recommends Chen correlation is suitable to determine the convective flow boiling heat transfer coefficient of prepared nanofluid. The study was conducted by Sarafraz *et al.* [12] with biologically produced silver/coconut oil nanofluid. The objective of the study was to quantify the thermal conductivity, viscosity and boiling heat transfer coefficient of biologically produced nanofluid. The assessment of thermal performance is also made with the prepared nanofluid in annular heat exchanger. Due to the enhancement in thermal conductivity and viscosity of the base fluid, the study reveals that this nanofluid can be used as a lubricant as well as a coolant in engines.

The density variation with ZnO, Sb_2O_5:SnO_2 and Al_2O_3 nanoparticles suspended in ethylene glycol/ /water mixture base fluid was studied by Vajjha *et al.* [13]. They measured the changes in density of nanoparticle suspended base fluid. They operated at the temperature range between 0 and 50 °C with 1-10 % volume fraction of nanoparticle suspension. Their experimental results were compared by Pak and Cho model and obtained better agreement with the measured values at all temperatures. They have noted 1.2% deviation for Al_2O_3 and Sb_2O_5:SnO_2 nanoparticles and 8% deviation for ZnO nanoparticle. The effect of ZnO nanoparticle suspension on density of water/ethylene glycol mixture base fluid was done by Mahian *et al.* [14]. They have prepared EG/water mixture of weight ratio 40-60, their temperature range between 25 and 40 °C and the ZnO volume fraction was 4.0%. They observed maximum density of 1328

kg/m^3 at a temperature of 25 °C for a 4.0% nanoparticle volume fraction.

The specific heat capacity of titanium oxide and aluminium oxide nanoparticles suspended in a base fluid mixture of water and ethylene glycol (20/80 wt.%) was measured by Yiamsawasd *et al.* [15]. They have determined specific heat based on a differential thermal analysis technique with a temperature between 15 and 65 °C and nanoparticle volume fraction of 8.0 vol.%. They framed new correlation to estimate the specific heat capacity of suspended nanoparticles in a form of specific heat ratio between nanofluid and base fluid. Satti *et al.* [16] prepared CuO, Al_2O_3, SiO_2, ZnO and TiO_2 nanoparticles diluted in water/propylene glycol (40:60 volume ratio) base fluid. They measured the variation in specific heat capacity with respect to the effects of nanoparticle volume fraction between 0.5 and 6 vol.%, operating temperature ranges between 243 and 363 K and particle sizes of 15 and 76 nm. The results revealed that the specific heat capacity decreases with increase in nanoparticle volume fraction and the specific heat capacity increases with increase in temperature, which were in good agreement with already published results.

The experiment was performed by Lee *et al.* [17] to study the thermal conductivity effect on Al_2O_3/ /ethylene glycol, Al_2O_3/water, CuO/water and CuO/ /ethylene glycol base fluids with vol.% from 1 to 5. They reported that only a small amount of nanoparticles have considerably high values of thermal conductivities than the base fluid without nanoparticles. The study conducted by Xuan and Li [18] by the suspension of copper nanoparticle, reported that the thermal conductivity of nanofluid is affected by the shape, size, volume fraction, and properties of the nanoparticle. Eastman *et al.* [19] studied the performance of copper nanoparticles directly suspended in ethylene glycol and reported significant enhancement in thermal conductivity of the base fluid containing smaller-sized copper nanoparticles. An experiment study was conducted by Das *et al.* [20] to determine the effects of temperature variation on thermal conductivity. They have used Al_2O_3/CuO nanoparticles suspended in water base fluid. By applying wavering method, they have calculated the thermal conductivity. They observed an increasing trend of thermal conductivity with an increase in temperature. Their finding also reveals that nanoparticle suspensions will be better at high temperature. Murshed *et al.* [21] studied the thermal conductivity effect of TiO_2 suspended deionized water and reported that nanoparticles in small quantity have much higher thermal conductivities than conventional fluid. Evans *et al.* [22] studied the variations of temperature and Al_2O_3 nanoparticle size and demonstrated the hydrodynamics effects associated with Brownian motion on the thermal conductivity of the nanoparticle suspended base fluid. Their finding shows that a nanoparticle is approximately 10 times more conductive than base fluid. Li and Peterson [23] investigated with copper oxide and aluminium oxide suspension in water with 2 to 10 vol.% of nanoparticle volume fraction and 27.5 to 34.7 °C of temperatures. A linear regression equation was proposed to determine the thermal conductivity ratio based on temperature and nanoparticle volume fraction. The experimental study was conducted by Vajjah and Das [24] for Al_2O_3, CuO and ZnO nanoparticle suspension in a base fluid of water and ethylene glycol. Their test conditions were 10% of nano particle volume fraction and 298 to 363 K temperature range. Their study reveals there is an increase in thermal conductivity of nanofluid with respect to nanoparticle volume fraction and temperature, and 18% thermal conductivity ratio enhancement was observed for ZnO suspension at the 7% volume fraction of nanoparticle. Xie *et al.* [25] studied with ethylene glycol (EG) suspended with TiO_2, MgO, ZnO, Al_2O_3 and SiO_2 nanoparticles and reported that the MgO/EG suspension has the highest thermal conductivity and the lowest viscosity. They concluded that at 30 °C the thermal conductivity enhancement was 40.6% for a 5% volume concentration for MgO nanoparticle. The thermal conductivity study with titanium dioxide and aluminium oxide nanoparticle suspended in propylene glycol base fluid was made by Palabiyik *et al.* [26]. Their observation was different to the many literature results, since they have reported results of nonlinear behaviour with the selected nanoparticle volume fraction. They also reported that with respect to temperature, the enhancement in thermal conductivity was not varying significantly. The rheological behavior and heat transfer performance of various metal-based nanofluids (silver, copper, alumina, TiO_2) were studied by Pourmehran *et al.* [27] and reported that the Brownian motion is considered to simulate viscosity of nanofluid. They have used the Patel model to predict the thermal conductivity. According to their results it was observed that maximum value of heat transfer enhancement is obtained by selecting the silver (Ag) as nanoparticle.

Silicon dioxide and EG/water were used by Sahoo *et al.* [28] to investigate the impact of nanoparticle suspension in EG/water base fluid on the thermal conductivity. They observed 20% enhancement in a base fluid thermal conductivity. Their pro-

cess conditions were 20 to 90 °C temperature and a nanoparticle concentration of 10 vol.%.

The thermal conductivity behaviour of deionized water and ethylene glycol after ing graphene and graphene multi-walled carbon nano-tubes (MWCNTs) was studied by Aravind and Ramaprabhu [29]. They reported that 9.2 and 73% improvement in deionized water for nanoparticle concentration of 0.04% at temperature of 25 and 50 °C, respectively. The enhancement was 6.9 and 20% for ethylene glycol base fluid at the same nanoparticle volume fraction and temperature, respectively. They concluded that the increase in nanoparticle volume fraction increases thermal conductivity of nanofluid. Manikandan *et al.* [30] performed heat transfer studies in a corrugated plate heat exchanger with TiO_2 and ZnO diluted in a base fluid mixture of water and ethylene glycol and reported there is a significant improvement in the heat transfer rate by the nanoparticle suspension. The experimental study performed by Sundar *et al.* [31] with the prepared magnetic Fe_3O_4 nanoparticle dispersed in water, showed 8.4 and 17% enhancement in thermal conductivity at temperatures of 20 and 60 °C, respectively. They have prepared 0 to 2% volume fraction of nanoparticle suspension. Barbés *et al.* [32] measured the thermal conductivity and specific heat capacity for aluminium oxide suspended in water as well as ethylene glycol base fluid. Their study conditions were 298 to 338 K temperatures and a nanoparticle volume fraction of 1.0-10.0%. Their results reveal that thermal conductivity of suspension increased but the specific heat capacity of suspension decreased with respect to nanoparticle concentration. Graphene suspended water base fluid was prepared by Ahammed *et al.* [33] to study the thermal conductivity variation of a nanoparticle addition. Their concentrations of nanoparticle were 0.05, 0.1 and 0.15 vol.% and temperatures were in the range of 10–50 °C. They have noted that the thermal conductivity ratio was improved by 6.7 and 18.6% at 10 and 50 °C, respectively, for a nanoparticle volume fraction of 0.05%. The result confirmed that the thermal conductivity of graphene based nanofluid has a considerable impact against process temperature. It was also noted from the study that 3.3% higher thermal conductivity enhancement occurred with the increase in volume concentration. Graphene and copper suspended ethylene glycol/water base fluid used by Periasamy *et al.* [34,35] observed that the nanoparticle volume fraction has the significant effect on thermal conductivity of base fluids. A new correlation was proposed by Sarafraz [36] for the determination of the Nusselt number based on the investigation of the thermal performance and pressure drop characteristics of liquid indium mixed with copper oxide nanoparticles in a rectangular micro-channel.

Different metal oxide nanoparticles (CuO, Al_2O_3, SiO_2 and ZnO) were suspended by Satti *et al.* [37] in a propylene glycol and water mixture. They determined the thermal conductivity at a 6% volumetric fraction of nanoparticles and 30 to 90 °C temperature range. They observed an increase in thermal conductivity of nanoparticle suspension with increasing nanoparticle volume fraction and fluid temperature. The effect of ethanol/MEG/DEG ternary mixture suspension on nucleate pool boiling heat transfer characteristics were studied by Sarafraz *et al.* [38] and observed significant changes in thermophysical properties. They summarized the factors affecting the thermal conductivity of nanoparticle suspensions which are properties of particles and the base fluid, nanoparticle volumetric concentration, particle size and temperature. This result is helpful because the thermal conductivity improved working fluids may be utilized at higher temperature applications. The potential application of a liquid metal enriched with Al_2O_3 nanoparticle was studied by Sarafraz *et al.* [39] in a micro-channel solar thermal receiver with 5, 10 and 15% (mass fractions). They investigated thermal performance of the suspended nanoparticle and achieved the highest thermal performance index of 3.5 and 2.9 for the laminar and turbulent flow, respectively, at mass fraction of 10%. In order to study the heat transfer coefficient, thermal resistance and the thermal performance of a thermosyphon heat pipe, zirconia-acetone nanofluid was prepared by Sarafraz *et al.* [40]. Results showed that the presence of the nanofluid decreases the total thermal resistance and enhanced the boiling heat transfer mechanism, which resulted in the thermal performance enhancement of the heat pipe. To assess the thermal performance, a new correlation was proposed from the study to predict the Kutateladze number. Sarafraz *et al.* [41] made an experimental investigation on the thermal performance and efficiency of an evacuated tube solar collector (ETSC) with graphene-methanol nanofluid. It was revealed from the study that the presence of nanoparticles improved the thermal conductivity of methanol, while the heat capacity of the nanofluid decreased by a decrease in the mass fraction of the graphene. The different concentrations of Fe_3O_4 nanoparticles in water were used by Sarafraz *et al.* [42] to quantify the heat transfer coefficient of nanofluid under constant magnetic field. Results showed that the magnetic field can lower the fouling resistance providing that the nanosuspension is

stable. Hence the heat transfer coefficient value was also improved with the Fe_3O_4 nanosuspensions.

Some of the significant studies with respect to graphene nanoparticles are given in the following section; graphene oxide/water nanofluid was synthesized by Liu *et al.* [43] using modified Hummers' method. They have investigated the stability of the prepared nanofluids using UV spectroscopy and showed that nanofluid stability is >3 months and also that 1.0 mg/ml nanofluid can work in applications with an operational range up to 1000 °C. The study provides new correlation to calculate thermal conductivity of nanofluids. It is revealed from the study that graphene oxide nanoparticles synthesized by modified Hummers' method, can be used as a stable nanofluid with acceptable heat transfer potential in thermal systems. Heat transfer studies in a three-dimensional spiral heat exchanger were performed by Bahiraei *et al.* [44]. In this study, thermal and hydraulic attributes of a graphene nanofluid in a countercurrent spiral heat exchanger were evaluated. They determined the performance index (ratio of heat transfer rate to pressure drop) and reports that performance index enhances with increase in either nanoparticle concentration or Reynolds number. Bahiraei *et al.* [45] made an investigation on thermo-hydraulic performance of graphene nanoplatelets. They performed the test within a tube enhanced with rotating twisted tape. The results revealed that the convective heat transfer coefficient and pumping power increase by increasing the rotational speed and weight fraction, while they decrease by increasing the twisted ratio. The effect of nitrogen-doped graphene (NDG) nanofluids concentration on heat transfer and fluid flow in double-pipe heat exchangers was made by Marjan Goodarzi *et al.* [46]. A novel MATLAB code solved the governing equations were used to analyze the resulting heat transfer coefficient, pressure drop, wall temperature reduction and pumping power. Khan *et al.* [47] investigated a blend of *Nigella sativa* biodiesel, diesel, n-butanol, and graphene oxide nanoparticles to enhance the performance, combustion and symmetric characteristics and to reduce the emissions from the diesel engine of a modified common rail direct injection (CRDI). The results obtained indicate that 90 ppm of graphene oxide nanoparticles and 10% *n*-butanol in *Nigella sativa* biodiesel are comparable with diesel fuel. Safaei *et al.* [48,49] used graphene oxide nanofluids in solar-driven water desalination process and developed an empirical equation to correlate the average Nusselt number as a function of Rayleigh number (Ra), the Stefan number (Ste), the sub-cooling factor (Sb), and the Fourier number (Fo). Sarafraz *et al.* [50] conducted an experimental investigation on heat transfer performance of graphene nanoplatelets/pentane nanofluid in a gravity-assisted heat pipe. They observed enhancement in heat transfer coefficient by increasing the heat flux. Experimental heat transfer studies were conducted by Sarafraz *et al.* [51] by using graphene nano-platelets dispersed in water-ethylene glycol mixture and reported that the thermal performance of the system increased by 21% in terms of heat transfer coefficient. The new preparation method for the decoration of platinum (Pt) on the functionalized graphene nanoplatelet (GNP) was introduced by Yarmand *et al.* [52]. Based on the stability analysis, it was noticed that nanofluids were stable and no significant sedimentation was observed for a long time (22 days).

According to the published articles, extensive research was conducted only on thermal conductivity measurement of nanofluids. The influence of other thermophysical properties such as viscosity, density and specific heat capacity variations were not studied much with added nanoparticles. Since these thermophysical properties may improve the heat transfer performance of the conventional base fluids, and also improve the application of nanofluid in heat exchangers, a complete understanding of the thermophysical properties is necessary. Also, from the published literature, it was identified that ethylene glycol is a viable heat transfer fluid because of its thermal characteristics, but it was noticed that only limited studies were performed with ethylene glycol as a base fluid.

Graphene is one of the most studied carbon-based nanofluids because of its larger surface/volume ratio, higher thermal conductivity, lower erosion, corrosion and clogging. It was found from the literature that mostly thermal conductivity studies were performed with graphene nanofluid. Since there will be a scope for exploring other thermophysical properties (viscosity, density and specific heat capacity) of graphene nanoparticle, this study was chosen. The novelty of the present study is considering graphene as a nanoparticle and performing the thermophysical characteristics analysis of the graphene suspended ethylene glycol/water mixture.

MATERIALS AND METHODS

Experimental setup

In order to study the thermophysical characteristics of graphene nanoparticle suspended EG/water base fluid, the experimental setup consists of a hot and cold fluid tank (20 L), four thermocouples, two pumps, two flow meters, and a corrugated plate heat

exchanger (PHE) was fabricated and the outline and photograph of the experimental setup is shown in Figures 1 and 2, respectively.

Figure 2. Photograph of experimental setup.

Experimental procedure

The water is pumped from the hot fluid tank and its temperature is constantly maintained at approximately 55 °C using a thermostat and the outlet is returned to the outlet tank.

Hummers' method was employed for producing graphene nanoparticles.

The prepared nanoparticle suspension (graphene/EG/water) in the cold fluid tank is also pumped into the plate heat exchanger.

The inlet and outlet temperatures of cold and hot fluid were measured using the inserted thermocouples.

A rotameter was used to measure and control the flow rates.

Experiments were repeated by varying the hot fluid temperatures to 65 and 75 °C and the nanoparticle suspension volume fractions of 0.2, 0.4, 0.6, 0.8 and 1%.

In order to compare the results, experiments with base fluid (EG/water) used as cold fluid were carried out first and the results were compared with the graphene suspended base fluid.

Nanofluid preparation and characterization

Graphene nanoparticles were produced by the Hummers' method [53]. The prepared nanoparticles were dispersed in the base fluid (ethylene glycol/ /water mixture) as per the proposed ratio and the nanofluids were used in our study. Figure 3 provides the TEM image of graphene nanofluids at 1.0 volume fraction.

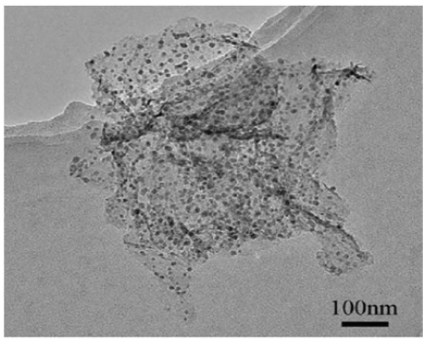

Figure 3. TEM image of graphene nanofluids at 1.0 volume fraction.

Calculation of thermophysical properties

In order to calculate thermo physical properties such as viscosity, density, specific heat capacity and

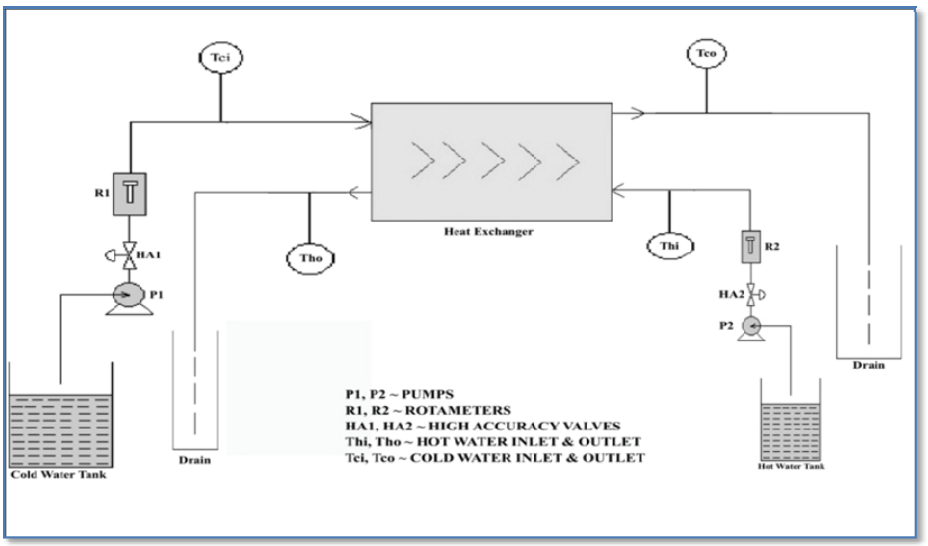

Figure 1. Outline of experimental setup.

thermal conductivity of nanoparticle suspension, the following thermophysical property models were used in the present study.

(i) Viscosity models

1. Einstein model

$$\mu_{nano} = (1+2.5\varphi)\,\mu_{base}$$

2. Kitano model

$$\mu_{nano} = \left[\left(1-\frac{\varphi}{\varphi m}\right)\right]\mu_{base}$$

3. Bachelor model

$$\mu_{nano} = (1+2.5\varphi+6.2\varphi_2)\,\mu_{base}$$

(ii) Density model

1. Pak and Cho model

$$\rho_{nano} = (1-\varphi)\,\rho_{base} + \varphi\rho_{base}$$

(iii) Specific heat capacity model

1. Xuan model

$$C_{p\,nano} = \frac{\left((1-\varphi)\rho_{base}C_{p\,base} + \varphi_{base}\rho_{nano}C_{p\,nano}\right)}{((1-\varphi)\rho_{base} + \varphi\rho_{nano}}$$

2. Pak and Cho model

$$Cp_{nano} = (1-\varphi)\,C_{p\,base} + \varphi C_{p\,particle}$$

(iv) Thermal conductivity models

1. Maxwell model

$$\frac{K_{fluid}}{K_{base}} = \frac{K_{particle} + 2K_{base} + 2\varphi(K_{particle} - K_{base})}{K_{particle} + 2_{Kbase} - \varphi(K_{particle} - K_{base})}$$

2. Vajjha Model

$$\frac{K_{fluid}}{K_{base}} = (0.0282\varphi + 0.0039)\left(\frac{T}{T_0}\right) + \\ +(-0.0307\varphi - 0.0039)$$

3. Sahoo Model

$$\frac{K_{fluid}}{K_{base}} = (-0.4557)\left(\frac{T}{T_0}\right)^2 + 1.72837\left(\frac{T}{T_0}\right) - 0.18559$$

RESULTS AND DISCUSSION

Impact of graphene nanoparticle concentration on viscosity of base fluid suspension

Viscosity indicates the resistance offered by the fluid. To consider the effect on viscosity, Einstein (1956), Kitano (1981) and Bachelor (1977) models have been taken to compare experimental results.

Figure 4a shows the influence of graphene nanoparticle suspension on the viscosity of base fluid at a hot fluid inlet temperature of 55 °C and base fluid concentrations of 30:70 (EG:W). From the figure, it was observed that the viscosity increases with the increase in graphene nanoparticle concentration. This is due to the fact that viscosity is strongly influenced by the volume concentration of the nanoparticle. Figure 4b presents the effect of nanoparticle addition on viscosity of base fluid at a hot fluid inlet temperature of 65 °C. At this temperature, an increase in nanoparticle volume fraction increased the viscosity in all the selected models with approximately equal values. It was also observed that the magnitude of viscosity decreases with increase in hot fluid inlet temperature. Figure 4c provides the plot for the influence of nanoparticle concentration on viscosity of base fluid suspension at the hot fluid inlet temperature of 75 °C. It was observed that at a hot fluid inlet temperature of 75 °C, an increase in nanoparticle concentration increased the viscosity of base fluid at the prepared base fluid concentration. This behaviour is attributed to the fact that the increase in nanoparticle concentration increases the viscosity of base fluids but the increase

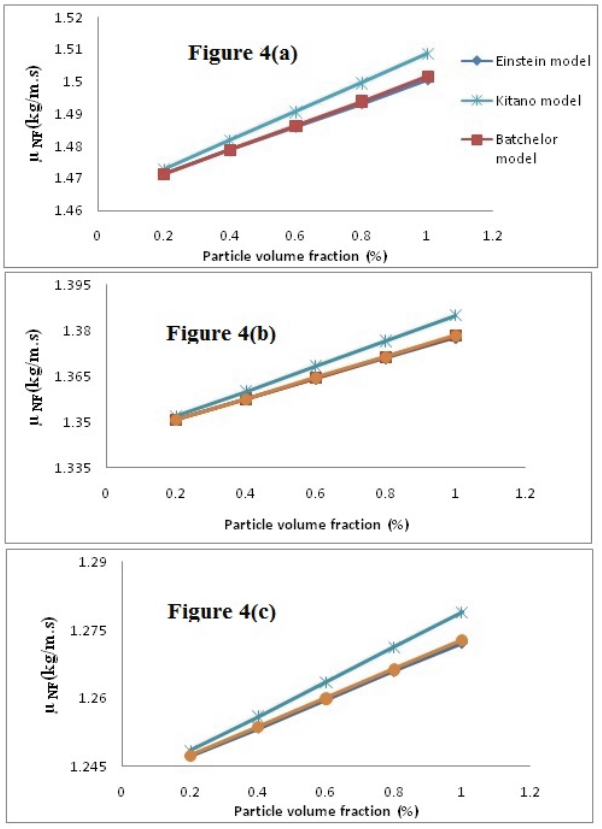

Figure 4. The influence of graphene nanoparticle concentration on viscosity of a base fluid concentration of 30:70 (EG:W) at a hot fluid inlet temperature of: a) 55, b) 65 and c) 75 °C.

in hot fluid inlet temperature decreases the viscosity of nanoparticle suspended base fluids.

Impact of graphene nanoparticle concentration on density of nanofluid

The density of metal oxides is greater than that of liquids. Density and specific heat capacity are determined as a function of particle volume fraction on the principle of two-phase mixtures. Density is considered an important parameter for evaluating the heat transfer performance of nanofluid. Figure 5a-c presents the effect of graphene nanoparticle addition on the density of nanofluid for the base fluid concentrations of 30:70 (EG:W) at the hot fluid inlet temperature of 55, 65 and 75 °C, respectively. The measured density data was validated with the Pak and Cho model.

The addition of graphene nanoparticle increased the density of the base fluid mixture. The reason for this is the nanofluid density is higher than that of the base fluid. It was noticed that the density of base fluid increased gradually with respect to the entire particle volume fraction, but the density decreases with respect to all the three hot fluid temperatures. The maximum density was observed at 1.0 vol.% for all the base fluid concentrations. The maximum density observed in the Pak and Cho model is 1037 kg/m^3 for 30:70 (EG:W). The result shows that nanofluid density increases with increase in nanoparticle concentration and decreases with increase in hot fluid inlet temperature.

Effect of graphene nanoparticle concentration on specific heat capacity of nanofluid

Specific heat is the amount of heat required to raise the temperature of one gram of nanofluid by one degree centigrade. Specific heat is one of the important properties and plays an important role in influencing the heat transfer rate of nanofluid. Figure 6a-c presents the effects of graphene nanoparticle volume fraction on specific heat capacity of nanoparticle suspension at a hot fluid inlet temperature of 55 °C and base fluid concentrations of 30:70 (EG:W) at a hot fluid inlet temperatures of 55, 65 and 75 °C, respectively.

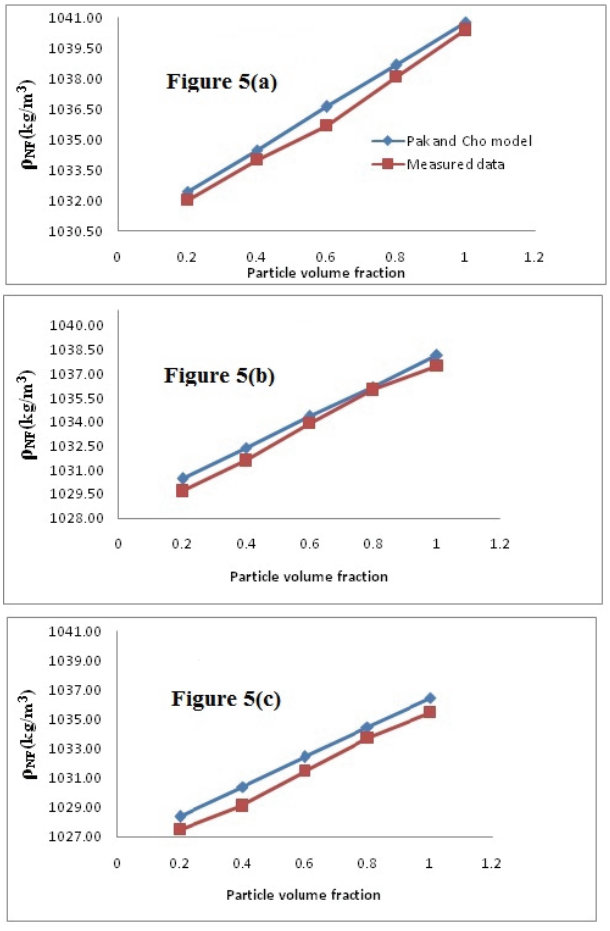

Figure 5. The influence of graphene nanoparticle concentration on density of a base fluid concentration of 30:70 (EG:W) and a hot fluid inlet temperature of: a) 55, b) 65 and c) 75 °C.

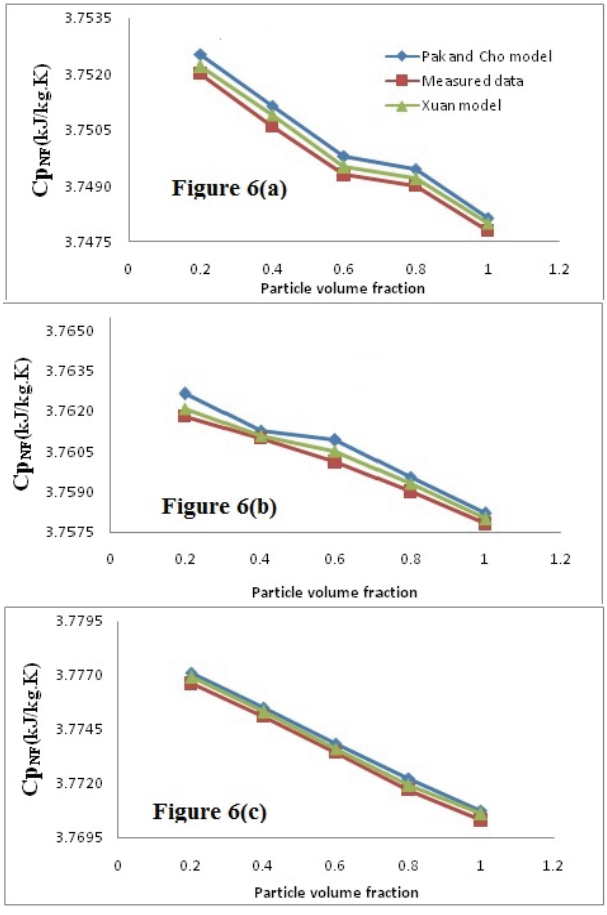

Figure 6. The influence of graphene nanoparticle concentration on specific heat capacity of base fluid concentration of 30:70 (EG:W) at a hot fluid inlet temperature of: a) 55, b) 65 and c) 75 °C.

Increase in nanoparticle concentration leads to decrease in specific heat capacity. It can be observed from the results that the values of specific heat capacity decreased from 3.762 to 3.7582 kJ/(kg K) with increase in volume concentration between 0.2 and 1.0% as per the Pak and Cho model for a base fluid concentration of 30:70 (EG:W) and a temperature of 65 °C. The reason for this is due to the fact that specific heat capacity is a mass specific quantity and this effect depends on the density of components and its mixture. The effect of graphene nanoparticle addition on specific heat capacity of nanofluid at a hot fluid inlet temperature of 75 °C and a base fluid concentration of 30 vol.% of ethylene glycol base fluids is shown in Figure 5c. The nanoparticle specific heat capacity decreased with increase in nanoparticle concentration for all the three base fluid concentrations. No significant variations were observed in specific heat capacity of nanofluid with respect to temperature. The experimental result was validated with Pak and Cho, and Xuan models. A better agreement was obtained between the measured values with selected models at all base fluid concentrations.

Effect of graphene nanoparticle concentration on thermal conductivity ratio of nanofluid

Thermal conductivity ratio (K_{nf}/K_{bf}) is an important parameter in measuring the effectiveness of the nanoparticle addition in the base fluid. For this purpose, comparisons between thermal conductivity ratio values of graphene nanoparticle with respect to base fluid concentration (30:70 (EG:W)) and at a hot fluid inlet temperatures of 55, 65 and 75 °C were plotted in Figure 6a-c, respectively. To consider the effect of Thermal conductivity ratio, three different models (Maxwell model (1954), Vajjah model (2010), and Sahoo model (2012)) have been used to compare experimental results with base fluids.

Figure 7a depicts the effects of nanoparticle addition on thermal conductivity ratio of the nanofluid at a hot fluid inlet temperature of 55 °C. The thermal conductivity ratio increased gradually at all the nanofluid concentrations due to the fact that nanoparticle volume fraction is directly proportional to thermal conductivity. At the variation of hot fluid inlet temperature at 65 °C (Figure 7b, the thermal conductivity increases with increase in volume fraction of nanoparticle in the base fluid concentration of 30:70 (EG:W). The improvement is higher than at the hot fluid temperature of 55 °C, due to the temperature effect (if temperature increases then thermal conductivity also increases). Further increase of hot fluid inlet temperature at 75 °C (Figure 7c) shows significant increases in thermal conductivity ratio. This is due to the fact that thermal conductivity is significantly affected by temperature and nanoparticle volume fraction, because of the expanded surface area of the dispersed nanoparticle in base fluid. The thermal conductivity predictions based on the selected published models were compared. Thermal conductivity increased gradually in all the selected models, which is due to the addition of nanoparticle to the base fluid. From the comparison of the thermal conductivity with the standard correlations (Maxwell model (1954), Vajjah model (2010) and Sahoo model (2012)) it is evident that increase in volume fraction of nanoparticle improved the thermal conductivity due to random Brownian motion, particle morphology, inter-particulate diffusion effects, and possible decrease in the boundary layer thickness.

There exists good agreement between the results calculated from experimental and different models. It was noticed that the density and specific heat capacity variations fall within ±5% deviation with experimental results and ±8 % deviation for viscosity and thermal conductivity variations. Hence, there exists good agreement between the correlation

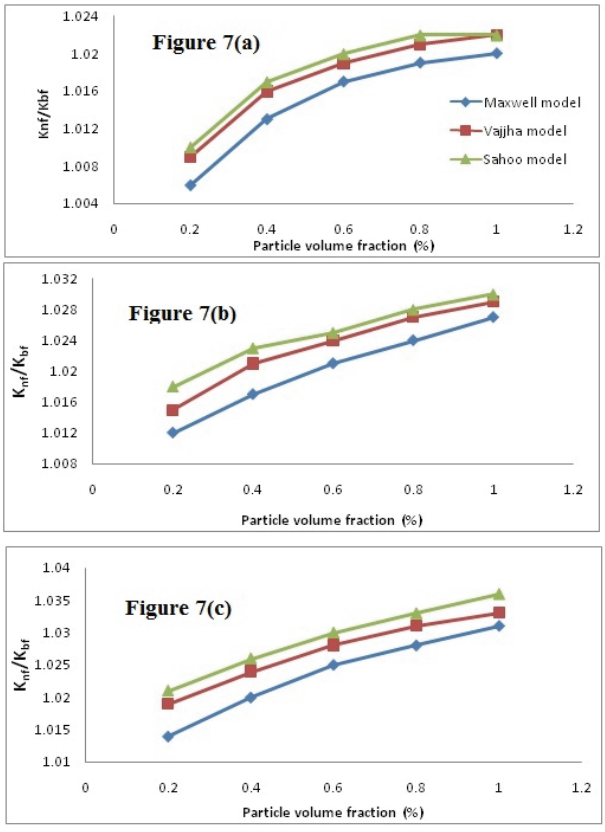

Figure 7. The influence of graphene nanoparticle concentration on thermal conductivity ratio of a base fluid concentration of 30:70 (EG:W) and a hot fluid inlet temperature of: a) 55, b) 65 and c) 75 °C.

results and experimental results, which shows the accuracy of the results of the experiment.

CONCLUSION

The study revealed that the hot fluid inlet temperature and nanofluid concentration have significant effects on the thermophysical properties of graphene suspended base fluids. There is an increase in viscosity from 1.247 to 1.272 kg/(m s) with respect to 75 °C of inlet temperature. At 55 °C, the base fluid has a higher density of 1041 kg/m^3 at 1.0 vol.%, however, the density of the mixture has the lowest value of 1028 kg/m^3 at 75 °C. Hence, the density increases with nanoparticle concentration and decreases with hot fluid inlet temperature. The dispersed nanoparticle shows lower specific heat than the values of base liquid. The observed specific heat capacity at 55 °C is 3.752 kJ/(kg K) (at 0.2 vol.%) which is reduced to 3.747 kJ/(kg K) (1.0 vol.%). Hence, the specific heat of nanofluid decreases with the increase in nanoparticle concentration, and the specific heat of nanofluid does not vary significantly with hot fluid inlet temperature. The obtained thermal conductivity ratios of base fluid are maximum at 75 °C and 1.0 vol.% with a value of 1.031, which is higher than those of base fluid. For all the thermophysical properties, the selected correlation models showed good agreement with the experimental results.

Acknowledgment

The authors thank the management of Kongu Engineering College and Department of Chemical Engineering for the facility provided.

Nomenclature

Vol.%	Volume %
EG	Ethylene glycol
W	Water
C_p	Specific heat capacity, J/(kg.K)

Greek symbols

k	Thermal conductivity, W/(m.K)
μ	Viscosity, kg/m.s
ρ	Density, kg/m3
φ	Particle volume fraction

Subscripts

nano	Nanofluid
base	Base fluid

REFERENCES

[1] M. Sabiha, R. Saidur, S. Mekhilef, O. Mahian, Renewable Sustainable Energy Rev.51 (2015) 1038-1054

[2] S. Sarafraz, M. Peyghambarzadeh, N. Vaeli, Chem. Ind. Chem. Eng. Q. 18 (2012) 315-327

[3] S.U.S. Choi, S. Lee, S. Li, J.A. Eastman, J. Heat Transfer 121 (1999) 280-289

[4] M. Sarafraz, A.S. Fazel, Y. Hasanzadeh, A. Arabshamsabadi, S. Bahram, Chem. Ind. Chem. Eng. Q. 18 (2012) 11-18

[5] R. Prasher, D. Song, J. Wang, P. Phelan, Appl. Phys. Lett. 89 (2006) 133108

[6] D.P. Kulkarni, D.K. Das, S.L. Patil, J. Nanosci. Nanotechnol. 7 (2007) 2318-2322

[7] M.M. Sarafraz, M. Jafarian, M. Arjomandi, G.J. Nathan, Appl. Energy 195(2017) 702-712

[8] C.T. Nguyen, F. Desgranges, G. Roy, N. Galanis, T. Maré, S. Boucher, Int. J. Heat Fluid Flow 28 (2007) 1492--1506

[9] P. Namburu, D. Kulkarni, A. Dandekar, D. Das, Micro Nano Lett. 2 (2007) 67-71

[10] L. Godson, B. Raja, D.M. Lal, S. Wongwises, Exp. Heat Transfer 23 (2010) 317-332

[11] M.M. Sarafraz, F. Hormozi, M. Kamalgharibi, Heat Mass Transf. 50(2014) 1237-1249

[12] M.M. Sarafraz, Chem. Biochem. Eng. Q. 30 (2017) 489--500

[13] R.S. Vajjha, D.K. Das, B.M. Mahagaonkar, Pet. Sci. Technol. 27 (2009) 612-624

[14] O. Mahian, A. Kianifar, S.A. Kalogirou, I. Pop, S. Wongwises, Int. J. Heat Mass Transfer 57 (2013) 582-594

[15] T. Yiamsawasd, A.S. Dalkilic, S. Wongwises, Curr. Nanosci. 8 (2012) 939-944

[16] J.R. Satti, D.K. Das, D. Ray, Int. J. Heat Mass Transfer 94 (2016) 343-353

[17] G.J. Lee, C.K. Kim, M.K. Lee, C.K. Rhee, S. Kim, C. Kim, Thermochim. Acta. 542 (2012) 24-27

[18] Y. Xuan, Q. Li, J. Heat Transfer 125 (2003) 151-155

[19] J.A. Eastman, S.U.S Choi, S. Li, W. Yu, L.J. Thompson, Appl. Phys. Lett. 78 (2001) 718-720

[20] S.K. Das, N. Putra, P. Thiesen, W. Roetzel, J. Heat Transfer 125 (2003) 567-574

[21] S.M.S. Murshed, Heat Transfer Eng. 33 (2012) 722-731

[22] W. Evans, J. Fish, P. Keblinsk, Appl. Phys. Lett. 88 (2006) 093116

[23] C.H. Li, G. Peterson J. Appl. Phys. 99 (2006) 084314

[24] R.S. Vajjha, D.K. Das, Int. J. Heat Mass Transfer 52 (2009) 4675-4682

[25] H. Xie, J. Wang, T. Xi, Y. Liu, Int. J. Thermophys. 23 (2002) 571-580

[26] I. Palabiyik, Z. Musina, S. Witharana, Y. Ding, J. Nanopart. Res. 13 (2011) 5049-5055

[27] O. Pourmehran, M. M. Sarafraz, M. Rahimi-Gojiri, D. D. Ganji, J. Taiwan Inst. Chem. Eng., 2018, Article in press

[28] B.C. Sahoo, D.K. Das, R.S. Vajjha, J.R. Satti, J. Nanotechnol. Eng. Med. 3 (2012) 041006

[29] S.S.J. Aravind, S. Ramaprabh. RSC Adv. 3 (2013) 4199--4206

[30] S.P. Manikandan, R. Baskar, Chem. Ind. Chem. Eng. Q. 24 (2018) 309-318

[31] L.S. Sundar, M.K. Singh, A.C.M Sousa, Int. Commun. Mass Transfer 49 (2013) 17-24

[32] B. Barbés, R. Páramo, E. Blanco, M.J. Pastoriza-Gallego, M.M. Piñeiro, J.L. Legido, J. Therm. Anal. Calorim. 111 (2013) 1615–1625

[33] N. Ahmed, L.G. Asirvatham, J. Titus, J.R. Bose, S. Wongwises, Int. Commun. Heat Mass Transfer 70 (2016) 66-74

[34] S.P. Manikandan, R. Baskar, Period. Polytech., Chem. Eng. 62 (2018) 317-322

[35] S.P. Manikandan, R. Baskar, Chem. Ind. Chem. Eng. Q. 27 (2021) 15-20

[36] M. M. Sarafraz, M. Arjomandi, Appl. Therm. Eng. 137 (2018) 700-709

[37] J.R. Satti, D.K. Das, D. Ray, Int. J. Heat Mass Trans. 107 (2017) 871-881

[38] M.M. Sarafraz, S. Peyghambarzadeh, F.S. Alavi, Chem. Ind. Chem. Eng. Q. 18 (2012) 577-586

[39] M.M. Sarafraz, M. Arjomandi, Int. Commun. Mass Transfer 94 (2018) 39-46

[40] M.M. Sarafraz, O. Pourmehran, B. Yang, M. Arjomandi, Renew. Energy 136(2019) 884-895

[41] M. Sarafraz, M.R. Safaei, Renew. Energy 142(2019) 364--372

[42] M.M. Sarafraz, O. Pourmehran, B. Yang, M. Arjomandi, R. Ellahi, Int. J. Therm. Sci. 147(2020) 106131

[43] W.I. Liu, O. Malekahmadi, S.A. Bagherzadeh, M. Ghashang, A. Karimipour, S. Hasani, T. Iskander, M. Goodarzi, Int. Commun. Mass Transfer 109(2019) 104333

[44] M. Bahiraei, H. Kiani Salmi, M.R. Safaei, Energy Convers. Manage. 180(2018) 72-82

[45] M. Bahiraei, N. Mazaheri, F. Aliee, M.R. Safaei, Powder Technol. 355(2019) 278-288

[46] M. Goodarzi, A.S. Kherbeet, M Afrand, E. Sadeghinezhad, M. Mahrali, P. Zahedi, S. Wongwises, M. Dahari, Int. Commun. Mass Transfer 76(2016) 16-23

[47] H. Khan, M.E.M. Soudagar, R.H. Kumar, M.R. Safaei, M. Farooq, A. Khidmatgar, N.R. Banapurmath, R.A. Farade, M.M. Abbas, A. Afsal, W. Ahmed, M. Goodarzi, S.N. Taqui, Symmetry 12(2020) 961

[48] M.R. Safaei, M. Safdari Shadloo, M.S. Goodarzi, A. Hadjadj, H.R. Goshayeshi, M. Afrand, S.N. Kazi, Adv. Mech. Eng. (London, U. K.) 8 (2016) 1-14

[49] M.R. Safaei, H.R. Goshayeshi, I. Chaer, Energies (Basel, Switz.) 12 (2019) 1-13

[50] M.M. Sarafraz, M.R. Safaei, Z. Tian, M. Goodarzi, E.P. Bandarra Filho, M. Arjomandi, Energies (Basel, Switz.) 12 (2019) 1-17

[51] M.M. Sarafraz, I. Tlili, Z. Tian, M. Bakouri, M.R. Safaei, M.S. Goodarzi, Appl. Sci. 9 (2019) 1-11

[52] H. Yarmand, S. Gharehkhani, S.F. Seyed Shirazi, M. Goodarzi, A. Amiri, W.S. Sarsama, M.S. Alehashem, M. Dahari, S.N. Kazi, Int. Commun. Heat Mass Transfer 77 (2016) 15-21

[53] W.S. Hummers, R.E. Offeman, J. Amer. Chem. Soc. 80 (1958) 1339.

SRINIVASAN PERIASAMY MANIKANDAN[1]
RAJOO BASKAR[2]

[1]Department of Chemical Engineering, Kongu Engineering College, Erode, India
[2]Department of Food Technology, Kongu Engineering College,Erode, India

NAUČNI RAD

PROUČAVANJE PROMENA TERMOFIZIČKIH SVOJSTAVA NANOČESTICA GRAFENA SUSPENDOVANIH U SMEŠI ETILEN-GLIKOLA I VODE

Cilj ovog rada je bio da se utvrde promene termofizičkih svojstava (kao što su viskoznost, gustina, specifični toplotni kapacitet i toplotna provodljivost) bazne tečnosti (etilen-glikol/voda, EG/V) sa koncentracijom nanočestica grafena i ulaznom temperaturom vruće tečnosti. Korišćene koncentracije nanočestica grafena su 0,2, 0,4, 0,6, 0,8 i 1 vol.%, a bazna tečnost je sa 30 vol.% EG. Istraživan je uticaj dodavanja nanočestica grafena baznoj tečnosti u komercijalnom pločastom razmenjivaču toplote. U ovom eksperimentu temperatura ulaska vruće tečnosti bila je na 55, 65 i 75 °C. Eksperimentalni rezultati termofizičkih svojstava upoređeni su sa odabranim modelima predloženim u literaturi. Modeli Ajnštajna, Kitanoa i Bačelora korišćeni su za razmatranje uticaja na viskozitet. Izmerene vrednosti gustine, odnosno specifičnog toplotnog kapaciteta potvrđeni su modelima Paka i Ćua, odnosno Ksuana. Za toplotnu provodljivost korišćena su tri različita modela. Istraživanja su otkrila da se termofizička svojstva bazne tečnosti značajno menjaju dodtakom nanočestica grafena.

Ključne reči: grafen, nanočestice, termofizička svojstva, etilen-glikol, voda.

CI&CEQ
Chemical Industry & Chemical Engineering Quarterly

Available on line at
Association of the Chemical Engineers of Serbia *AChE*
www.ache.org.rs/CICEQ

Chem. Ind. Chem. Eng. Q. 27 (2) 189–197 (2021) CI&CEQ

BERK TIRNAKCI
YAVUZ SALT

Department of Chemical Engineering, Faculty of Chemical and Metallurgical, Yildiz Technical University, Davutpasa Campus, Esenler-Istanbul, Turkey

SCIENTIFIC PAPER

UDC 628.165:551.463:678.744.7

PREPARATION AND CHARACTERIZATION OF PVA-SiO_2 NANOCOMPOSITE MEMBRANES FOR SEAWATER DESALINATION BY PERVAPORATION

Article Highlights

- For PVA-SiO_2 membrane, a permeate flux of 4.93 kg m^{-2} h^{-1} was obtained at 50 °C
- The highest selectivity value was calculated as 99.8% at 30 °C
- The nano-SiO_2 incorporation into a PVA matrix increased the water flux value more than two-fold
- The pervaporation performance of PVA membrane was enhanced remarkably

Abstract

Pervaporation is a membrane process that offers high separation performance and has an important potential for the treatment of saline water sources. In this study, poly(vinyl alcohol) (PVA) and PVA-SiO_2 nanocomposite membranes were prepared by the solution-casting method, and pervaporative water desalination studies were carried out for synthetic seawater (35 g L^{-1}) at 30, 40 and 50 °C. Effects of the temperatures and the incorporation of SiO_2 on the pervaporation performance of polymeric nanocomposite membranes were investigated. Membranes were characterized by scanning electron microscopy (SEM), Fourier-transform infrared spectroscopy (FT-IR) and thermogravimetric analysis (TGA). In experiments conducted at 50 °C, a permeate flux of 4.93 kg m^{-2} h^{-1} with a salt rejection of 99.3% were obtained. The highest salt rejection was 99.8% at temperature of 30 °C. The results showed that the pervaporation performance of PVA membranes was remarkably enhanced with the incorporation of nano-SiO_2 into polymeric matrix.

Keywords: desalination, nano-SiO_2, nanocomposite, pervaporation, poly(vinyl alcohol), seawater.

Freshwater demand is rapidly increasing for industrial, agricultural, and domestic use. In addition, the amount of water per capita is decreasing rapidly due to the lack of underground and surface water resources (about 1% of all water sources), increased industrialization, global warming, and population growth rate. Seawater is the most abundant water source compared to other natural freshwater resources, and seawater desalination is an important process for meeting freshwater demands. Among desalination technologies, membrane-based technologies are becoming increasingly important as membrane processes have advantages such as great separation performance, energy-saving, high operational stability, and easy integration with industrial systems [1,2].

For the desalination of seawater and brackish water, reverse osmosis (RO), multi-stage flash (MSF), multi-effect distillation (MED), electrodialysis (ED) and vapor compression distillation (VCD) technologies are commonly used worldwide [3,4]. RO and MSF dominate the market, together constituting >90% of the global desalination capacity [5]. However, RO has major disadvantages such as high capital and operating costs, high energy requirements, and membrane fouling [6].

PV is a promising membrane process for desalination studies due to its non-pressure-driven separ-

Correspondence: Y. Salt, Department of Chemical Engineering, Faculty of Chemical and Metallurgical, Yildiz Technical University, Davutpasa Campus, 34220 Esenler-Istanbul, Turkey.
E-mail: salt@yildiz.edu.tr
Paper received: 8 May, 2020
Paper revised: 1 October, 2020
Paper accepted: 7 October, 2020

https://doi.org/10.2298/CICEQ200505037T

ation mechanism, high selectivity, energy efficiency, and durability for pollutants [7]. In this process, the driving force is the chemical potential gradient between the two sides of the membrane, applying either vacuum or sweeping gas at the permeate side of the membrane [8]. The transport mechanism through the nonporous membrane is explained by the solution-diffusion model consisting of three steps: sorption, diffusion and desorption. The feed liquid is brought into contact with one side of the membrane at atmospheric pressure and permeate is continuously removed in vapour form from its other side [9].

The key component in pervaporation as with all other membrane processes is the membrane itself and selecting an appropriate membrane material is a crucial step in membrane studies. In the pervaporation process, water-selective membranes are prepared using polymers with hydrophilic characteristics. For the pervaporation separation of water from feed mixture, PVA is one of the best choices due to its high hydrophilic nature, which is provided by the hydroxyl (-OH) groups on its chain segments. Additionally, PVA has excellent membrane-forming properties, good thermal stability, chemical and mechanical strength, and commercial availability and is nontoxic, biocompatible and biodegradable [8,10].

Inorganic fillers can be incorporated into polymeric matrices to improve the membrane separation performance. Inorganic-organic composite membranes prepared using materials with different structures and properties, namely mixed matrix membranes (MMMs), combine the separation properties of inorganic and organic materials [11,12]. Nanocomposites have an important role in membrane applications. In membrane technology, inorganic nanomaterials such as TiO_2, SiO_2, Al_2O_3, Si, Ag, ZnO and ZrO_2 and organic nano-materials such as graphene oxide (GO), carbon nanotubes (CNT), and carbon nanofibers (CNF) are used as nano-sized fillers to provide thermal, physical, and chemical resistance and improve the membrane separation performance [13,14].

Xie *et al.* [15] prepared PVA/maleic anhydride/ /silica hybrid membranes via the sol-gel method and investigated the effects of temperature, salinity and pressure on the desalination of a NaCl/water solution. They reported a water flux of 11.7 kg m^{-2} h^{-1} and salt rejection values of 99.9% with hybrid membranes containing silica particles (<10 nm) for the pervaporation desalination of NaCl/water solution with NaCl concentrations of 0.2-5.0 wt.% at permeate pressures of 2-40 Torr and temperatures of 20-65 °C. In another study, they also investigated the effect of the thickness of PVA/maleic anhydride/silica membrane on the desalination performance [16] and obtained a water flux of 6.93 kg m^{-2} h^{-1} with >99.5% salt rejection at 22 °C and 6 Torr for a 2000 ppm NaCl solution. Cho *et al.* [17] prepared an inorganic NaA zeolite membrane for the pervaporative desalination of seawater. Water flux and salt rejection were 1.9 kg m^{-2} h^{-1} and 99.9%, respectively. Chaudhri *et al.* [18] prepared hollow-fiber PVA membranes on a polysulfone support and reported a water flux of approximately 7.4 L m^{-2} h^{-1} at 71 °C. Liang *et al.* [19] used the electrospinning/electrospraying technique to prepare thin-film nanofibrous pervaporation composite (TFNPVC) membranes using poly(vinyl alcohol), polyacrylonitrile (PAN) nanofibrous scaffold and polyethylene terephthalate (PET) to make a three-layered composite membrane. They obtained water fluxes of 8.53, 7.24 and 5.57 L m^{-2} h^{-1} for 5000, 35000 and 50000 ppm NaCl solutions, respectively, with salt rejection of > 99.5%.

In the present study, a nano SiO_2-filled PVA membrane was prepared by the solution-casting method and pervaporation desalination studies were carried out at different temperatures. Glutaraldehyde (GA) was used as the cross-linking agent for PVA. The effects of temperature and nano-SiO_2 incorporation on pervaporation performance were investigated for synthetic seawater desalination. Experiments were carried out at 30, 40, and 50 °C and the permeate flux, rejection, permeance and selectivity results were compared with pristine PVA membranes [20].

EXPERIMENTAL

Materials

PVA (98-99% hydrolyzed, average M.W. 88000--97000) and GA (25% aq. sln.) were purchased from Alfa Aesar. GA was used as the cross-linking agent for PVA. Sulfuric acid was used as a catalyst for cross-linking reaction, and sulfuric acid and methanol were purchased from J.T. Baker and Lab Scan, respectively. Sodium chloride (NaCl) was purchased from Merck. SiO_2 (99.65%, P-Type) with a particle size of 13-23 nm was supplied by Nanografi Nano Technology. Synthetic seawater (35 g L^{-1}) was prepared in the laboratory.

Membrane preparation

In this study, pristine PVA and PVA-SiO_2 nanocomposite membranes were prepared by a solution casting method. PVA (10 wt.%) was dissolved in deionized water by mixing at a moderate stirring speed for 2 h in a glass reactor placed in a water bath at 90 °C. Subsequently, nano-SiO_2 solution was added to the PVA solution while stirring, and the

whole solution was stirred again for a further 1 hour to ensure a well dispersion. SiO_2 nanoparticle was incurporated into polymer matrix in an amount of 10 wt.% with respect to weight of PVA to avoid an agglomeration of the nanoparticles, and a brittle membrane. The nanomaterial was dispersed in water using a magnetic stirrer and an ultrasonic bath before adding it to the polymer solution. The membrane solution was cast onto glass plates as a thin film and was then dried at 40 °C for 24 h. The drying temperature was determined as 40 °C, as the changes in ambient temperature can affect the membrane drying process. The dried membranes were peeled-off from the glass plates and were immersed in a mixture containing 3% GA, 5% H_2SO_4, 23% water, 69% methanol for 24 h and were cross-linked [21]. The cross-linked membranes were removed from the mixture. Figure 1 shows a schematic representation of the cross-linking reaction between PVA and GA [22].

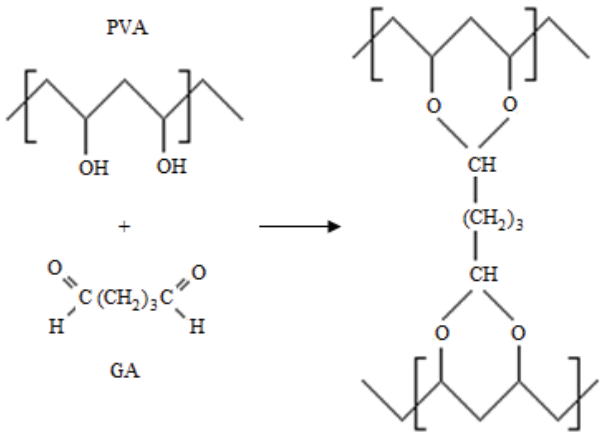

Figure 1. Cross-linking reaction between PVA and GA [22].

The membranes were weighed, and then kept in deionized (DI) water overnight to remove the residues of the cross-linking mixture. After washing with deionized water, the membranes were dried again in an oven at 105 °C for 2 h to remove the water content of the membranes [23]. There was no weight loss in the prepared membranes. For the pristine PVA membranes, the PVA solution (10 wt.%) was prepared by stirring at a moderate speed for 3 h in a reactor placed in a water bath at 90 °C. The membrane solution was cast onto glass plates, and the resulting membrane films were dried at 40 °C for 24 h. A similar procedure was used to prepare the pristine PVA membranes. The membrane thicknesses were measured with a digital micrometer, and the flux values were normalized to 100 μm.

Characterization

Scanning electron microscopy (SEM)

Cross-sectional morphologies of the PVA and PVA-SiO_2 nanocomposite membranes were observed by scanning electron microscopy. Membranes were immersed in liquid nitrogen, and then fractured and gold sputter-coated before the SEM analysis.

Fourier-transform infrared (FT-IR)

A Perkin-Elmer Spectrum 100 FT-IR instrument was used to characterize the functional structure and the chemical groups in the PVA and PVA-SiO_2 nanocomposite membranes. The wave range of the FTIR spectra was between 4000 and 650 cm^{-1}.

Thermogravimetric analysis

The thermal properties of the PVA and PVA-SiO_2 nanocomposite membranes were investigated using Exstar TG/DTA 6300. TGA studies were conducted under a continuous nitrogen flow with a 10 °C min^{-1} heating rate from 25 to 600 °C.

Pervaporation experiments

Pervaporation experiments for PVA and PVA-SiO_2 nanocomposite membranes were carried out at 30, 40 and 50 °C. The schematic representation of the pervaporation setup is given elsewhere [23]. The feed tank was kept at a constant temperature in a water bath, and the feed mixture was fed to the stainless-steel membrane cell with a peristaltic pump. The effective membrane area of the membrane cell was 23 cm^2. The synthetic seawater mixture was prepared in our laboratory, and the salt concentration was 35 g L^{-1} [7,24]. The pressures on the feed and permeate sides of the membrane were kept at atmospheric pressure and ≤1 Torr, respectively, and the pressure on the permeate side was measured by a Vacuubrand DVR-2 digital vacuum meter. Samples were collected every hour in Dewar traps containing liquid nitrogen and were weighed accurately. Permeation fluxes (J) were calculated using the following equation:

$$J = \frac{W}{At} \tag{1}$$

where W, A and t are the permeate amount (g), membrane's effective area (m^2) and the time interval (h), respectively. The salt rejection (R) was calculated by the conductivity method using the following equation:

$$R(\%) = 100\frac{C_f - C_p}{C_f} \tag{2}$$

where C_f and C_p are salt concentrations in the feed and permeate, respectively. The pervaporation select-

ivity (α_i) was calculated using the following equation [25,26]:

$$\alpha_i = \frac{x_i / (1 - x_i)}{y_i / (1 - y_i)} \quad (3)$$

where x and y are the weight fraction of component i in feed and permeate, respectively. The permeance of membrane (P_i/l) was determined according to Eq. (4) [25,27], assuming ideal solution (γ_{water} =1) for NaCl solution of 35 g/L [28]:

$$\frac{P_i}{l} = \frac{J_i}{x_i \gamma_i P_i^{sat} - y_i P^p} \quad (4)$$

where P_h, l, γ_i and P^p are the membrane permeability, membrane thickness, activity coefficient and permeate pressure, respectively. The term $y_i P^p$ was ignored, as the permeate pressure was maintained at ≤1 Torr. The saturated vapor pressure (P_i^{sat}) can be calculated with the Antoine equation [29]:

$$\log(P_i^{sat} / \text{bar}) = A - \frac{B}{T + C - 273.15} \quad (5)$$

where T is the temperature in Kelvin. A, B and C are the Antoine constants, and are given in Table 1 [29].

Table 1. Antoine constants for water [29]

Antoine coefficient		
A	*B*	*C*
5.11564	1687.537	230.17

RESULTS AND DISCUSSION

SEM Results

The cross-sectional SEM images of pristine PVA membranes (a) and PVA-SiO_2 nanocomposite membranes (b) are presented in Figure 2.

Figure 2a shows that the structure of the pristine PVA membrane is defect-free and smooth. Figure 2b shows homogeneous distribution of the nanomaterials within the polymer matrix. No particle agglomeration was observed.

FT-IR Results

The FT-IR spectra of the PVA and PVA-SiO_2 nanocomposite membranes are shown in Figure 3. The spectra can be divided into 4 main regions: I. hydroxyl groups (-OH), II. methylene groups (-CH_2), III. aldehyde groups (-CHO) and IV. acetal/ether groups (-COC), corresponding to 3000-3600 cm^{-1}, 2900-3000 cm^{-1}, 1650-1750 cm^{-1} and 1000-1100 cm^{-1} wavenumbers, respectively.

The FT-IR analysis of both PVA and PVA-SiO_2 nanocomposite membranes showed a broad peak between 3200 and 3300 cm^{-1}, indicating stretching of the hydroxyl groups of the polymer. In all spectra, the reflection peaks at approximately 2910, 2940 and 1418 cm^{-1} were assigned to a stretching vibration and flexural vibration of methylene (-CH) (the main structure of PVA), respectively [30]. The sharp peak observed at approximately 1700 cm^{-1} is assigned to C=O expansion band caused by ester groups [31]. This stretch is smaller in PVA with a higher degree of hydrolysis due to the lower number of acetate groups. The appearance of the ether/acetal peak indicates that crosslinking occurs between aldehyde groups and hydroxyl groups in the polymer [32-34]. The intensity of the peak at 1141 cm^{-1} is controlled by the crystalline segment of the polymer chains. This peak is related to the C-C and C-O bonds in the main carbon chain [22] and is constant for both PVA and PVA-SiO_2 nanocomposite membranes because the crystal structure of the polymer is the same for all samples. The peaks observed at approximately 3300 and 1100

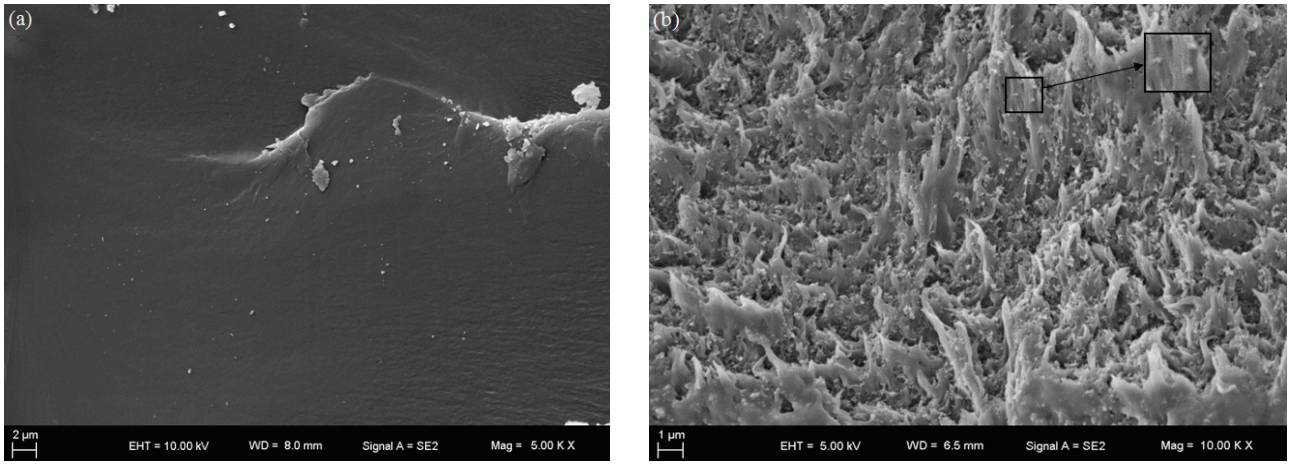

Figure 2. SEM images of PVA (a) and PVA-SiO_2 nanocomposite membranes (b).

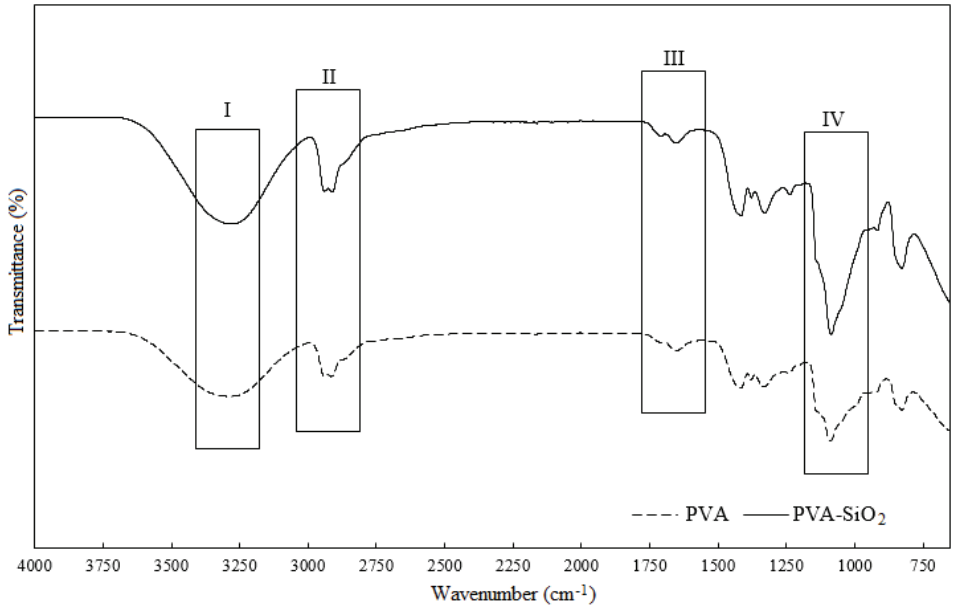

Figure 3. FT-IR spectra of PVA and PVA-SiO_2 nanocomposite membranes.

cm^{-1} are attributed to hydroxyl (-OH) groups and Si-O-Si stretching modes for PVA-SiO_2. A reduction in the intensity of the -OH and Si-O-Si groups was observed [34]. The peaks between 1000-450 cm^{-1} are attributed to the stretching vibrations of Si-O-Si. The peak at approximately 3440 cm^{-1} shifted to a lower wave number with the increase in nano-SiO_2 content, indicating an increase in intermolecular hydrogen bonds between nano-SiO_2 and PVA [35].

TGA Results

Figure 4 shows the TGA thermographs of the PVA and PVA-SiO_2 nanocomposite membranes. The thermal degradation profiles of both membranes revealed three weight loss stages.

The first weight loss step observed between 80-160 °C is due to the evaporation of bound and free water in the polymeric matrix and resulted in a loss of approximately 8.2 wt.% for PVA and for 26.3 wt.% PVA-SiO_2 (weight losses not shown). Primary decomposition of the PVA chain started at approximately 250 °C and is assigned to the elimination of side-groups of the polymer chain [36]. Total weight loss of the PVA membrane was approximately 74 wt.% and occurred at 400 °C. This first degradation step of PVA was followed by a final decomposition corresponding to the breakdown of the main polymer chain [37]. The decomposition of the main PVA chain started at 400 °C for PVA and 500 °C for PVA-SiO_2, and the weight

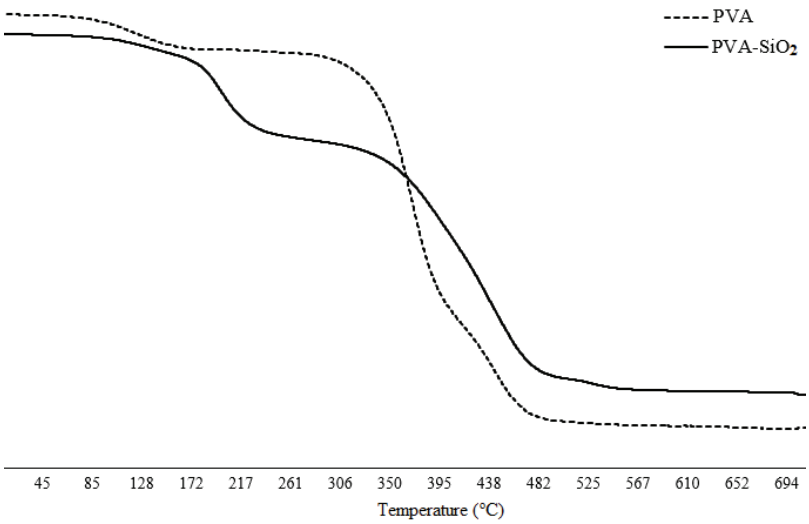

Figure 4. TGA thermographs of the PVA and PVA-SiO_2 nanocomposite membranes.

loss profiles of the PVA and PVA/SiO_2 nanocomposite membranes were similar. The shift towards the higher degradation temperature for the PVA-SiO_2 nanocomposite membrane is assigned to improved thermal stability due to the incorporation of SiO_2 nanomaterial into the PVA matrix.

Pervaporation results

The pervaporation desalination experiments were carried out at 30, 40, and 50 °C for PVA and PVA-SiO_2 nanocomposite membranes. Figure 5 shows the permeate water flux (a) and salt rejection (b) values of the PVA and PVA-SiO_2 membranes as a function of temperature for desalination of 35 g L^{-1} synthetic seawater.

Figure 5a shows that permeation rates increase with increasing temperature for both membranes as the mobility of the polymer chain and the solubility and diffusivity of water molecules through the polymeric matrix increase [38]. Salt rejection values obtained for PVA and PVA-SiO_2 membranes are shown in Figure 5b. Owing to the trade-off relationship between flux and selectivity for membrane processes, salt rejection values decrease with increasing temperature. This is related to the enhanced polymer chain mobility that allows free ion transit. It is clear from Figure 5a and b that, with the nano-SiO_2 incorporation into the PVA matrix, both water flux and salt rejection increased due to the nanoporous and highly hydrophilic structure of the nanomaterial that rejects salt passage. A permeate flux of 4.93 kg m^{-2} h^{-1} was obtained for the PVA-SiO_2 membranes at 50 °C, and a salt rejection rate of >99% was observed for all temperatures.

Figure 6a and b illustrate the effects of temperature on permeance and selectivity, respectively. Based on the solution-diffusion model, the permeation flux depends on the solubility and diffusivity of components in the membrane. The permeances of both membranes decrease with the increasing of temperature, except for the permeance of PVA-SiO_2 membrane at temperature of 50 °C because the decrease in solubility is higher than the increase in diffusivity [39]. In contrast, the permeance of PVA-SiO_2 membrane increase at 50 °C as the permeation flux through PVA-SiO_2 membrane increases significantly from 40 to 50 °C. This also implies that the increase in the diffusivity is able to compensate the decreasing in the solubility [39,40]. As can be seen from Figure 6b, the selectivity of the PVA-SiO_2 membrane evidently dec-

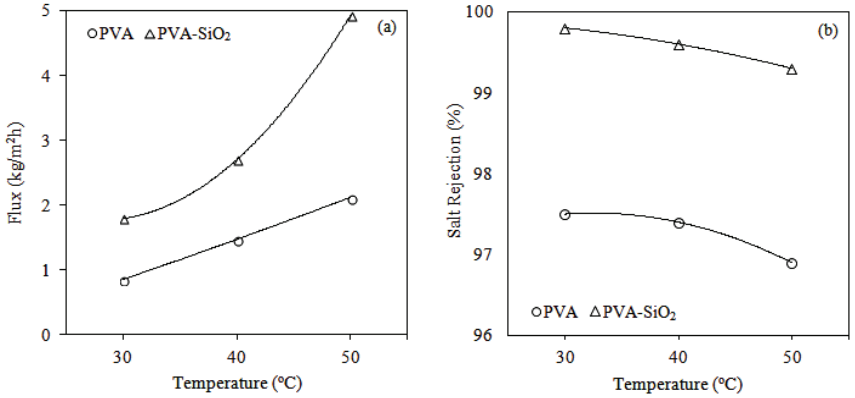

Figure 5. Flux (a) and salt rejection (b) results of PVA and PVA-SiO_2 nanocomposite membranes.

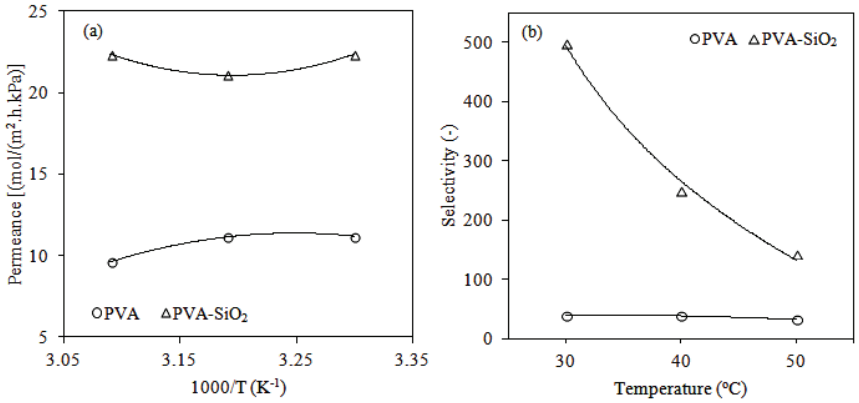

Figure 6. Permeance (a) and selectivity (b) results of PVA and PVA-SiO_2 nanocomposite membranes.

reases with an increase in temperature, while selectivity decreases slightly for the PVA membrane, as the frequency and amplitude of the polymer chain mobility increase with increasing temperature.

Table 2 compares the desalination performance of the PVA-SiO_2 nanocomposite membrane with literature results based on pervaporation-based desalination. Considering the membrane thickness and temperature values, the PVA-SiO_2 membranes exhibited a good performance with high salt rejection and water flux.

CONCLUSION

The aim of this study was to prepare a membrane with high desalination performance. PVA was selected as the polymer matrix for its high hydrophilic nature, high thermal, mechanical, and chemical resistance, and great film-forming properties. Nanocomposite membranes were prepared with nano-sized SiO_2 and the effects of nanomaterial incorporation into a PVA matrix and temperature on water flux and salt rejection were investigated. Pervaporation experiments were carried out at different temperatures and the performance data for PVA-SiO_2 nanocomposite membranes were compared with pristine PVA membranes.

The pervaporation results exhibited that nano SiO_2 filler positively affected the membrane separation performance. The nano-SiO_2 incorporation into the PVA matrix increased the permeate flux values for all temperatures and salt rejection values >99% were obtained. The nanocomposite membrane seems to have much better salt rejection compared to pristine membranes. In addition, the TGA profiles showed that the decomposition temperature of the PVA membranes was improved with nano-SiO_2 incorporation. In conclusion, the pervaporation desalination results obtained using nano-SiO_2-filled PVA membranes are promising for seawater desalination.

REFERENCES

[1] E. Drioli, A.I. Stankiewicz, F. Macedonio, J. Membr. Sci. 380 (2011) 1-8

[2] Y. Li, L. Zhu, J. Taiwan Inst. Chem. Eng. 80 (2017) 867–874

[3] H. Cherif, J. Belhadj, In Sustainable Desalination Handbook-Plant Selection, Design and Implementation, Ch. 15, B.G. Gude, Ed., Butterworth-Heinemann: Oxford, 2018, pp 527-559

[4] J.O. Brotto, N. Padoin, C. R. Rambo, C. Soares, Water Supply 19 (2018) 1221-1228

[5] T. Humplik, J. Lee, S.C. O'Hern, B.A. Fellman, M.A. Baig, S.F. Hassan, M.A. Atieh, F. Rahman, T. Laoui, R. Karnik, E.N. Wang, Nanotechnology 22 (2011) 292001

[6] A.D. Khawaji, I.K. Kutubkhanah, J.M. Wie, Desalination 221 (2008) 47-69

[7] Q. Wang, N. Li, B. Bolto, M. Hoang, Z. Xie, Desalination 387 (2016) 46-60

Table 2. Performance comparison of various membranes in the pervaporation desalination studies; PVA, poly(vinylalcohol); PAN, polyacrylonitrile; GO, graphene oxide; CNT, carbon nanotube; PVDF, poly(vinylidene flouride); GA, glutaraldehyde; PEBA, poly(ether--block-amide). Model solutes are NaCl, Na_2SO_4 and $MgCl_2$

Membrane	NaCl content	Temperature (°C)	Thickness (μm)	Water flux	Salt rejection (%)	Reference
NaA zeolite	Seawater	69	-	1.9 kg m^{-2} h^{-1}	99.9	[17]
PVA/maleic anhydride/silica	2 g L^{-1}	20-65	10	6.9-11.7 kg m^{-2} h^{-1}	99.5-99.9	[15]
PVA/PAN	5 g L^{-1}	Room temperature	0.62-12.9	8.53 L m^{-2} h^{-1}	99.9	[19]
	35 g L^{-1}			7.36 L m^{-2} h^{-1}	99.8	
	50 g L^{-1}			5.81 L $m^{-2}h^{-1}$	99.8	
PVA	30 g L^{-1}	70	0.1	7.4 kg m^{-2} h^{-1}	99.9	[18]
PVA/Silica	2 g L^{-1}	60	4.9	20.6 L $m^{-2}h^{-1}$	99.9	[41]
	30 g L^{-1}			10.4 L m^{-2} h^{-1}	99.9	
PVA/PAN	35 g L^{-1}	70	-	11.2 kg m^{-2} h^{-1}	99.8	[42]
	100 g L^{-1}					
Chitosan/GO	5 wt.%	81	10-13	30.0 kg $m^{-2}h^{-1}$	99.99	[43]
PVA/GA/Laponite	3 wt%	70	-	58.6 kg m^{-2} h^{-1}	99.9	[44]
PVA/CNT	35 g L^{-1}	22	19	6.96 kg m^{-2} h^{-1}	99.91	[24]
PVA/PVDF	100 g L^{-1}	80	0.3	13.7 L m^{-2} h^{-1}	>99	[45]
			0.8	12.1 L m^{-2} h^{-1}		
			2.0	8.1 L m^{-2} h^{-1}		
PEBA	0-200 g L^{-1*}	25-65	40-90	0.5-1.7 kg m^{-2} h^{-1}	99.9	[46]
PVA/SiO_2	35 g L^{-1}	50	100	4.93 kg m^{-2} h^{-1}	99.3	This study

[8] R.Y.M. Huang, Pervaporation Membrane Separation Process, Elsevier, Amsterdam, 1991

[9] R.D. Noble, S.A. Stern, Membrane Separations Technology, Principles and Applications, Elsevier, Amsterdam, 1995

[10] B. Yilman, F.U. Nigiz, A. Aytaç, N.D. Hilmioglu, Water Supply 19 (2018) 1229-1237

[11] F.U. Nigiz, N.D. Hilmioglu, Desalin. Water Treat. 57 (2016) 4749-4755

[12] M. Maghami, A. Abdelrasul, In Zeolites and Their Applications, Ch. 7, M.N. Rashed, Ed., IntechOpen Ltd: London, 2018, pp. 115-134

[13] L.Y. Ng, A.W. Mohamad, C.P. Leo, N. Hilal, Desalination 308 (2013) 15-33

[14] J.H. Jhaveri, Z.V.P. Murthy, Desalin. Water Treat. 57 (2016) 26803-26819

[15] Z. Xie, M. Hoang, T. Duong, D. Ng, B. Dao, S. Gray, J. Membr. Sci. 383 (2011) 96-103

[16] Z. Xie, D. Ng, M. Hoang, T. Duong, S. Gray, Desalination 273 (2011) 220-225

[17] C.H. Cho, K.Y. Oh, S.K. Kim, J.G. Yeo, P. Sharma, J. Membr. Sci. 371 (2011) 226-238

[18] S.G. Chaudhri, B.H. Rajai, P.S. Singh, Desalination 367 (2015) 272-284

[19] B. Liang, K. Pan, L. Li, E.P. Giannelis, B. Cao, Desalination 347 (2014) 199-206

[20] B. Tirnakci, Master's thesis, Yildiz Technical University, Istanbul, 2017

[21] C.-K. Yeom, K.-H. Lee, J. Membr. Sci. 109 (1996) 257-265

[22] E.F. Reis, F.S. Campos, A.P. Lage, R.C. Leite, L.G. Heneine, W.L. Vasconcelos, Z.I.P. Lobato, H.S. Mansur, Mater. Res. 9 (2006) 185-191

[23] Y. Salt, E. Arcevik, B. Ekinci, Can. J. Chem. Eng. 92 (2014) 503-510

[24] G. Yang, Z. Xie, M. Cran, D. Ng, S. Gray, J. Membr. Sci. 579 (2019) 40-51

[25] P. Das, S.K. Ray, S.B. Kuila, H.S. Samanta, N.R. Singha, Sep. Purif. Technol. 81 (2011) 159-173

[26] R.S. Veerapur, M.B. Patil, K.B. Gudasi, T.M. Aminabhavi, Sep. Purif. Technol. 58 (2008) 377-385

[27] G. Jyoti, A. Keshav, and J. Anandkumar, J. Eng. (2015), Article ID 927068

[28] O. Miyawaki, A. Saito, T. Matsuo, K. Nakamura, Biosci. Biotech. Biochem., 61 (1997) 466-469

[29] B.E. Poling, J.M. Prausnitz, J.P. O'Connell, The Properties of Gases and Liquids, McGraw-Hill, NewYork, 2001

[30] L. Zhu, J. Wang, L. Guo, J. Shen, Adv. Mater. Res. 239--242 (2011) 1956-1959

[31] A. Şahin, I. Ar, J. Therm. Sci. Tech. 34 (2014) 153-162

[32] C.K. Yeom, K.H. Lee, J. Appl. Polym. Sci. 67 (1998) 209--219

[33] B. Smith, Infrared Spectral Interpretation: A Systematic Approach, CRC Press, New York, 1999

[34] O. Farid, F. Mansour, M. Habib, J. Robinson, S. Tarleton, J. Environ. Chem. Eng. 4 (2016) 293-298

[35] S. Tang, P. Zou, H. Xiong, H. Tang, Carbohydr. Polym. 72 (2008) 521-526

[36] C.C. Yang, Y.J. Li, T.H. Liou, Desalination 276 (2011) 366-372

[37] C.C. Yang, J. Membr. Sci. 288 (2007) 51-60

[38] A. Huang, B. Feng, J. Membr. Sci. 548 (2018) 59-65

[39] J. Xu, C. Gao, X. Feng, J. Membr. Sci. 352 (2010) 197-204

[40] D. T. Bui, A. Nida, K. C. Ng, K. J. Chua, J. Membr. Sci. 498 (2016) 254-262

[41] S.G. Chaudhri, J.C. Chaudhari, P.S. Singh, J. Appl. Polym. Sci. 134 (2017) 45718

[42] R. Zhang, B. Liang, T. Qu, B. Cao, P. Li, Environ. Technol. 40 (2017) 312-320

[43] X. Qian, N. Li, Q. Wang, S. Ji, Desalination 438 (2018) 83-96

[44] A. Selim, A.J. Toth, E. Haaz, D. Fozer, A., Szanyi, N. Hegyesi, P. Mizsey, Sep. Purif. Technol. 221 (2019) 201--210

[45] L. Li, J. Hou, Y. Ye, J. Mansouri, V. Chen, Desalination 422 (2017) 49-58

[46] D. Wu, A. Gao, H. Zhao, X. Feng, Chem. Eng. Res. Des. 136 (2018) 154-164.

BERK TIRNAKCI
YAVUZ SALT

Department of Chemical Engineering, Faculty of Chemical and Metallurgical, Yildiz Technical University, Davutpasa Campus, Esenler-Istanbul, Turkey

NAUČNI RAD

DOBIJANJE I KARAKTERIZACIJA PVA-SiO_2 NANOKOMPOZITNIH MEMBRANA ZA DESALINACIJU MORSKE VODE PERVAPORACIJOM

Pervaporacija je membranski proces koji nudi visok stepen razdvajanja i ima važan potencijal za tretman slanih izvora vode. U ovom radu, pripremljeni su poli(vinilalkohol) (PVA) i PVA-SiO_2 nanokompozitne membrane metodom livenja rastvora, koje su zatim korišćene u istraživanju desalinizacije sintetičke morsku vodu (35 g L^{-1}) na 30, 40 i 50 °C. Istraživani su efekti temperature i ugradnje SiO_2 na performanse pervaporacije polimernim nanokompozitnim membranama. Membrane su okarakterisane skenirajućom elektronskom mikroskopijom, infracrvenom spektroskopijom sa Furijeovom transformacijom i termogravimetrijskom analizom. U eksperimentima izvedenim na 50 °C, dobijen je fluks permeata od 4,93 kg m^{-2} h^{-1} sa uklanjanjem soli 99,3%. Najveće uklanjanje soli od 99,8% postignuto je na temperaturi od 30 °C. Rezultati su pokazali da su pervaporacione performanse PVA membrana izuzetno poboljšane ugradnjom nano-SiO_2 u polimernu matricu.

Ključne reči: desalinizacija, nano-SiO_2, nanokompozit, pervaporacija, poli(vinilalkohol), morska voda.

CI&CEQ
Chemical Industry & Chemical Engineering Quarterly

Available on line at
Association of the Chemical Engineers of Serbia *AChE*
www.ache.org.rs/CICEQ

Chem. Ind. Chem. Eng. Q. 27 (2) 199–206 (2021) CI&CEQ

NORLIZA ABDUL LATIFF[1,3]
LUQMAN CHUAH ABDULLAH[1]
PEI YING ONG[3]
NOR AMAIZA MOHD AMIN[2]

[1]Department of Chemical and Environmental Engineering, Faculty of Engineering, Universiti Putra Malaysia, Serdang, Selangor, Malaysia
[2]Department of Process and Food Engineering, Faculty of Engineering, Universiti Putra Malaysia, Serdang, Selangor, Malaysia
[3]Innovation Centre in Agritechnology, Universiti Teknologi Malaysia, Muar, Johor, Malaysia

SCIENTIFIC PAPER

UDC 66.047:58:544

THIN-LAYER DRYING MODEL OF *Cosmos caudatus*

Article Highlights

- Thin-layer mathematical models to describe the drying characteristic of *Cosmos caudatus* were studied
- Page model showed the best-fitted drying data with good statistical indicators
- D_{eff} values increased with the increase of drying temperatures (4.12×10^{-12}-24.71×10^{-12} m^2/s)
- Activation energy value calculated at 39.35 kJ/mol for drying *C. caudatus*

Abstract

Drying kinetic models and energy characteristics are well known tools to evaluate and predict the most suitable drying physiochemical conditions for a particular product. In this study, a thin-layer drying model was developed to best describe the drying kinetic behaviour of Cosmos caudatus. The drying experiments were conducted using a thermal convection oven and C. caudatus leaves were dried at five different temperatures (40, 50, 60, 70, 80 °C). Six different thin-layer drying models were proposed and applied to select the best drying model by fitting to the experimental moisture ratio data. The proposed drying models included Page, Modified Page, Lewis, Henderson-Pabis, Two Term and Weibull, and the results were statically compared and evaluated based on their goodness of fit. Among these, the Page model was found to best represent the thin-layer drying behaviour of C. caudatus with 99.76%, 5.93×10^{-5}, 9.68×10^{-5} for the coefficients determination (R^2), reduced chi-square (χ^2), and root mean square error (RMSE), respectively. The average effective moisture diffusion coefficient (D_{eff}) for the temperature 40 to 80 °C ranged from 4.12×10^{-12} to 24.71×10^{12} m^2/s, while the activation energy (E_a) was calculated at 39.35 kJ/mol based on the Arrhenius's equation.

Keywords: thin-layer drying model, Cosmos caudatus, effective moisture diffusivity, activation energy, thermal convection oven.

Cosmos caudatus, also known as Ulam Raja (King's salad), belongs to the *Asteraceae* family. *C. caudatus* has been utilised as a medicinal plant, beginning in Latin America and afterwards developed within Southeast Asian countries such as Malaysia, Indonesia and Thailand [1,2]. In Malaysia, the plant has been cultivated as a commercial crop and widely used in many applications such as for culinary and therapeutic purposes [1]. As a local delicacy, *C. caudatus* has numerous biological properties, which have been scientifically documented, including being anti-inflammatory, antihypertensive, antidiabetic, anti-osteoporosis, antiobesity and anticancer [1-4]. The presence of important bioactive compounds (polyphenols, tannins, saponins, plant sterols, terpenes, and phenylpropanoids), minerals, and vitamins is considered as an essential quality indicator for its utilisation in many potential applications. [1,5-8].

The drying process can be considered as the most important step in downstream processing. The function of drying is to remove moisture from the fresh product, particularly from agricultural produce. Drying slows down the deterioration process by reducing contamination growth of mould or microorganisms, helps to prolong the shelf-life as well as simplifies packaging, handling, storage, and delivery [9-15]. Dif-

Correspondence: N.A. Latiff*, L.C. Abdullah**, Department of Chemical and Environmental Engineering, Faculty of Engineering, Universiti Putra Malaysia, Serdang, 43400, Selangor, Malaysia.
E-mail: (*)norlizaabdlatiff@utm.my, (**)chuah@upm.edu.my
Paper received: 21 November, 2019
Paper revised: 9 August, 2020
Paper accepted: 13 October, 2020

https://doi.org/10.2298/CICEQ191121038L

ferent drying technologies have been widely introduced in the manufacturing industries. Thermal drying is one of the most conventionally used drying methods for drying biomedicinal herbal products. Compared to the traditional drying method using ambient temperature, thermal drying has greater efficiency yielding a high quality of dried product at a lower operational cost [14]. However, the thermal drying mechanism is complex, involving simultaneous heat and mass transfer for the removal of moisture content from the wet material and air [16,17]. Hence, studying the drying kinetics will aid the modelling of the drying process.

The thin-layer drying process refers to a dry layer of particles when fully exposed to drying air [16,17]. The thin-layer drying model through a mathematical solution is widely used to model drying kinetics in many agricultural products [16-21]. It is not only used to explain the drying characteristics, but also the transportation phenomena such as moisture diffusion and evaporation during the drying process [16-18]. Theoretically, thin-layer drying models are derived based on Newton's law of cooling and Fick's second law of diffusion and can be categorised into theoretical, semi-theoretical, and empirical models [16–18]. Semi-theoretical models that are modified from theoretical models have fewer assumptions and are dependent on the experimental data [16,19]. The internal factors such as drying temperature, drying air velocity, material thickness, initial moisture content, and relative humidity are the main constraints in using these models [16,20]. The Page, Newton, Midilli--Kucuk, and Henderson-Pabis models are the most used semi-theoretical models to describe the drying characteristics in many types of plant samples [16,17]. In contrast, for empirical models, the fundamental aspects are negligible, and the assumptions strongly depend on the experimental data and dimensionless analysis, meaning that the important process that takes place during drying cannot be explained [16,17,19]. Wang and Singh reported that the Weibull model is among the widely used empirical models to predict the drying process of many types of plant samples [16,17]. Among the developed thin-layer drying models, researchers found that both semi-theoretical and empirical models provided more accurate results and better prediction of drying characteristics in fruits and vegetables [17].

Although *C. caudatus* has been reported to possess numerous therapeutic potentials, the drying kinetics has yet to be studied. From an engineering point of view, the drying kinetics is crucial for the description of the drying mechanism and predicting the most suitable drying conditions. Therefore, this study has been carried out to evaluate the drying process of *C. caudatus* using a thermal convection dryer at different drying temperatures. By fitting the drying experimental data to the established mathematical drying models, the most suitable drying kinetics model of *C. caudatus* may be established. The effective moisture diffusion coefficient and activation energy of *C. caudatus* were also studied to further investigate the mass and energy characteristics throughout the drying process of *C. caudatus*.

METHODOLOGY

Preparation of *C. caudatus*

The raw materials were directly collected from the research farm of the Innovation Centre in Agritechnology for Advanced Bioprocessing (ICA), Universiti Teknologi Malaysia, Pagoh branch, Johor Bahru, Malaysia. The freshly harvested samples were randomly chosen before the drying experiment. The samples were cleaned and cut into small pieces. The initial moisture content of fresh leaf (80.5% wet basis) was measured using a moisture analyser (MX-50, A&D Instruments Ltd, Oxford shire, United Kingdom) at 105 °C for 15 min.

Preparation of drying process

The *C. caudatus* leaves were dried using a laboratory convection oven (Memmert UF110, Memmert Universal, Schwabach, Germany), and the process based on Alara *et al.* [22] with minimal modification. The oven was equipped with an adjustable temperature function that allowed the user to select the required temperature. The temperature of the ambient air was 26 °C and the relative humidity (*rh*) was in the range of 80 to 88%. The air velocity in the dryer was 1 m/s and it was measured using a digital anemometer (Digital Thermo Anemometer, Dwyer, U.S.A). Five drying temperatures of 40, 50, 60, 70 and 80 °C were used to dry the samples at a constant air velocity with three replicates for each treatment. The drying oven was firstly preheated to the chosen temperature before sample loading. An aluminium tray with a size of 22 cm×16 cm was used to place the sample (5 g) in a single layer over the tray of the dryer. Then, the sample tray was positioned in the middle of the drying chamber to ensure uniform drying. The weight loss of the sample was measured with an analytical balance (PA214C, OHAUS Corporation, USA) at selected intervals and replicated thrice. Each of the weighing processes lasted about 15 s and it was carried out near to the dryer unit. The sample was dried

until a constant weight was achieved in consecutive measurements.

Determination of the thin-layer mathematical components

Moisture content

The moisture content (M) of the samples was calculated using Eq. (1) [13]:

$$M = \frac{m_t - m_{dm}}{m_{dm}} \quad (1)$$

where M, m_t and m_{dm} are the moisture content (g water/g dry matter), mass of sample (g) at a specific time and mass of dry weight (g), respectively.

Drying rate

The drying rate (DR) of the samples was calculated using Eq. (2) [13]:

$$DR = \frac{M_{t+\Delta t} - M_t}{\Delta t} \quad (2)$$

where DR, Mt, $Mt+\Delta t$ and Δt are the drying rate (g water/g dry matter min), moisture content at time t (g water/g dry matter), moisture content at $t+\Delta t$ (g water/g dry matter), and the drying time (min), respectively.

Mathematical modeling of drying curves

The dimensionless moisture ratio (MR) was calculated from Eq. (3). Kinetic models may be used to describe the drying kinetics as a relation to the moisture transfer as shown in Table 1.

$$MR = \frac{M - M_e}{M_o - M_e} \quad (3)$$

where M is the moisture content at any drying time (dt), M_o is the initial moisture content and M_e is the moisture content at equilibrium (g water/g dry matter). For long drying, the difference of M_e is relatively small compared to M, it was therefore simplified as an Eq. (4) [13]:

$$MR = \frac{M}{M_o} \quad (4)$$

Table 1. Mathematical models for drying curves; k is drying rate constant (min^{-1}), a, b, n are constant sand t is drying time (min)

Model	Equation
Page	$MR = \exp(-kt^n)$
Lewis	$MR = \exp(-kt)$
Henderson-Pabis	$MR = a\exp(-kt)$
Modified Page	$MR = \exp(-kt)^n$
Two Term	$MR = a\exp(-k_1t)+b\exp(-k_2t)$
Weibull	$MR = \exp(-[t/b]^a)$

The experimental results of MR for *C. caudatus* were fitted to the selected six thin-layer models (Table 1) and analyzed based on statistical tools such as correlation coefficient (R^2), root square error ($RMSE$) and Chi-square (χ^2), respectively. The equations are given in Eqs. (5)-(7), respectively. The higher R^2, lower $RMSE$ and χ^2 values represent a good agreement between the experimental and predicted data [13,22]:

$$R^2 = 1 - \left[\frac{\sum_{i=1}^{N} \left(MR_{\exp,i} - MR_{pre,i} \right)^2}{\sum_{i=1}^{N} \left(MR_{\exp,i} - \overline{MR_{\exp}} \right)^2} \right] \quad (5)$$

$$RMSE = \left[\frac{1}{N} \sum_{i=1}^{N} \left(MR_{\exp,i} - MR_{pre,i} \right)^2 \right]^{1/2} \quad (6)$$

$$\chi^2 = \sum_{i=1}^{N} \left[\frac{MR_{\exp,i} - MR_{pre,i}}{MR_{pre,i}} \right]^2 \quad (7)$$

Estimation of the effective moisture diffusivity

The determination of the effective moisture diffusion coefficient during the drying process of *C. caudatus* was estimated using Fick's second law. The equation is expressed by Eq. (8) [22,26]:

$$MR = \frac{8}{\pi^2} \sum_{n=1}^{\infty} \frac{1}{(2n+1)^2} \exp\left(-\frac{(2n+1)^2 \pi^2 D_{eff} t}{4L^2} \right) \quad (8)$$

For a longer drying process, MR < 0.6 the equation is simplified to:

$$\ln MR = \ln\left(\frac{8}{\pi^2} \right) - \left(\pi^2 \frac{D_{eff}}{4L^2} t \right) \quad (9)$$

where MR, D_{eff}, L, t and n is the dimensionless moisture ratio, the effective moisture diffusion coefficient (m^2/s), half the thickness of the initial *C. caudatus* sample (m), drying time (s) and an integer value, respectively.

Estimation of the activation energy

The activation energy is measured by the Arrhenius equation and expressed accordingly in Eq. (10) [13]:

$$D_{eff} = D_0 \exp\left(-\frac{E_a}{RT} \right) \quad (10)$$

D_0 is a constant in the Arrhenius equation (m^2/s), T is the temperature in degrees Kelvin (K), R is the universal gas constant (kJ/(mol K)), E_a is the activation energy (kJ/mol). By plotting D_{eff} *versus* $1/T$, the

value of E_a can be determined using exponential regression.

Data analysis

The value of *M*, *MR*, *DR*, D_{eff} and E_a were calculated using Microsoft Excel software. The statistical value of R^2, *RMSE* and χ^2 of the parameter models was estimated by Excel Solver (Microsoft Office 2016).

RESULTS AND DISCUSSION

Drying characteristics of *C. caudatus*

In this study, *C. caudatus* leaves were dried at 40, 50, 60, 70 and 80 °C until equilibrium moisture content was reached. Figure 1 illustrates the drying curves in terms of moisture ratio *versus* drying time at different temperatures. While Figure 2 shows the reproducibility of the drying curve plot at 60 °C. The initial moisture content of the leaves before hitting their steady dry weight at 40, 50, 60, 70 and 80 °C was 81.11, 81.14, 82.13%, 81.30 and 82.10% (w.b), respectively. Such differences are possibly due to the different temperatures involved. As seen in Figure 1, the time to reach the equilibrium moisture content from its initial moisture content to dry *C. caudatus* leaves at 40, 50, 60, 70 and 80 °C were 100, 80, 40, 20, and 10 min, respectively. The results demonstrated that higher drying temperature (80 °C) entailed the shortest drying time. The lower the temperature (40 °C), the longer it took to dry the sample and resulted in slower drying rates. Similar observations were also reported when drying *Vernonia amygdalina* leaves and piper leaves samples [10,22]. The reproducibility of the drying curves weighted by the magnitude of standard deviations (*SD*) and the similarity between the curves. Higher reproducibility of drying curves has been tested under all temperature conditions. Figure 3 shows the example of equality between the curves.

The relation in terms of drying speeds and drying temperatures is shown in Figure 3. Significantly, the drying rate increased at an elevated drying

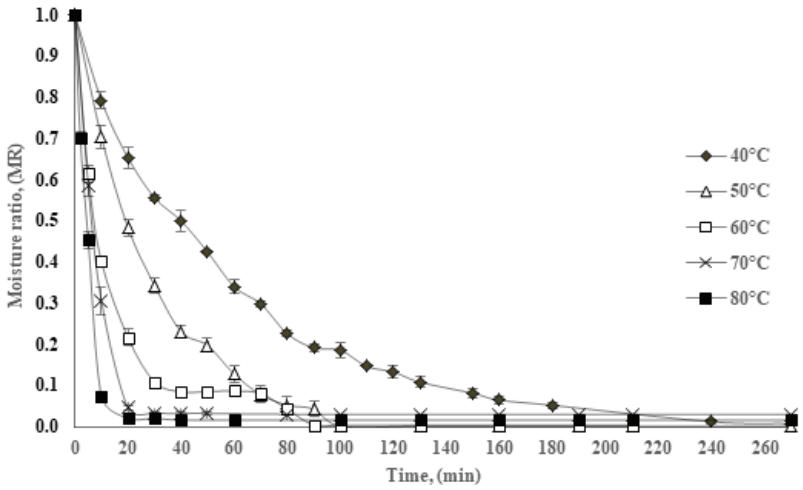

Figure 1. Drying curves of C. caudatus at different drying temperatures.

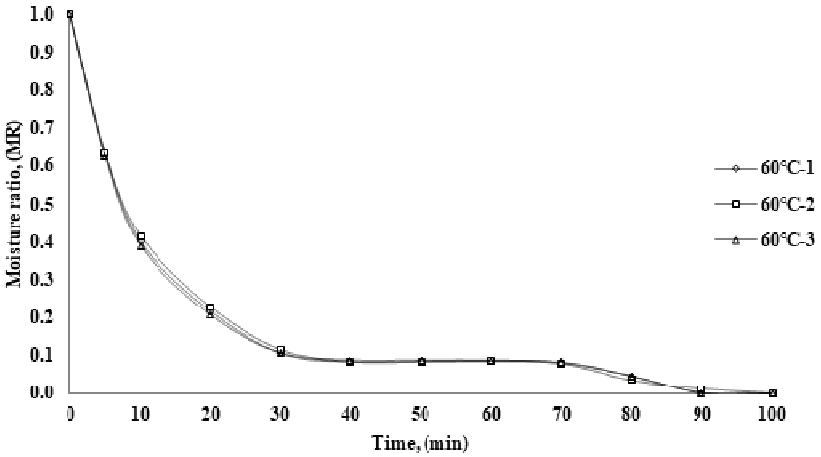

Figure 2. Example of reproducibility result (drying curve) at 60 °C.

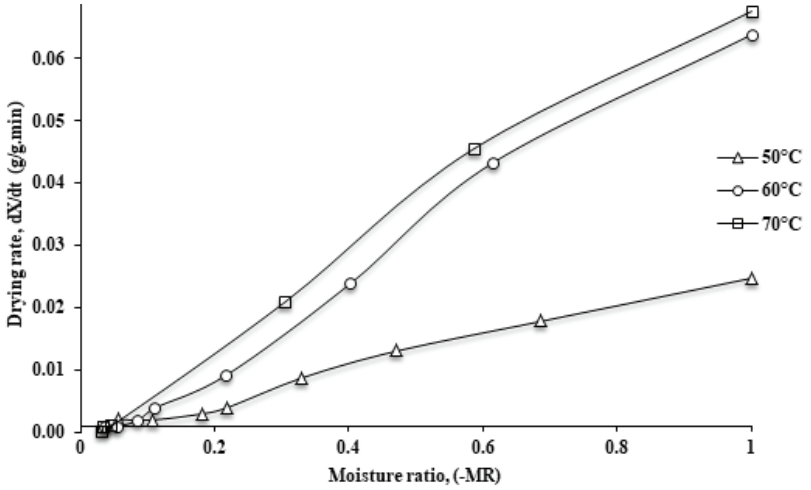

Figure 3. The drying rate curves of C. caudatus at different drying temperatures.

temperature, resulting in a rapid depletion of moisture content [15,22,26]. On the other hand, the higher drying rate accelerates further heat transfer and causes rapid removal of moisture from the material l[15,22,23]. In the drying of *Momordica charantia* slices, a fast-drying rate also occurred at 80 °C using a hot air dryer [11]. The moisture removal rate slowly reduced when approaching the equilibrium moisture content.

The entire drying process of *C. caudatus* occurred during the falling-rate period, indicating that internal moisture diffusion was the dominant factor [24]. As reported, this falling-rate period induced a shrinking effect when the surface film of the dried product appeared [17]. The results were similar to the drying behaviour reported for fruits and vegetable products [13,22,27]. As seen from Figure 3, no initial constant-rate period was observed as the evaporation process took place rapidly (negligible) at the surface of the *C. caudatus* leaves. This absence is due to the unbound moisture being insignificant in the leaves [13,14,22]. As drying continued, the material entered a second falling-rate period and then encounter a slower reduction of moisture until attaining equilibrium moisture content. The drying of *C. caudatus* stopped at this stage when no further moisture was transferred from the leaf into the surrounding air [14,15,19,24].

Thin-layer drying model

Six thin-layer models, including Page, Lewis, Henderson-Pabis, Modified Page, Two Term and Weibull, have been proposed and compared (Table 2). The suitability of the models was assessed using statistical analysis and this is shown in Table 2. The correlation coefficient (R^2) of greater than 0.9900, with the lowest root mean square error (*RMSE*), and the lowest chi-square (χ^2) values presented the most appropriate model for drying *C. caudatus*. From the results, the Page, Modified Page and Lewis models provided the appropriate results to fit the experimental data. The R^2 values of these models were estimated between 0.9900 and 0.9976. Based on the results shown in Table 1, the Page model gave an accurate prediction with the closest fit of R^2. The highest R^2 was 0.9976, with an *RMSE* of 9.68×10^{-5} and χ^2 of 5.93×10^{-5} at a drying temperature of 40 °C. Figure 4 shows the plot of the experimental data and the predicted moisture ratio by the best model for drying *C. caudatus*. The present results are in line with previous studies to best predict the drying kinetic in agricultural products such as [23] *Momordica charantia* [11], banana [29,30] and green bean [24]. This increased from 0.00246 to 0.2000 when the drying temperature was increased from 40 to 80 °C. The *k* value was linearly dependent on temperature and was consistent with the previous studies using this model [31].

The effective moisture diffusivity (D_{eff}) was calculated from the plots of ln *MR* against drying time (s) at different temperatures, and the slope of each linear regression plot was applied to estimate the D_{eff} coefficient. The change in D_{eff} coefficient at different temperatures (40 to 80 °C) is presented in Table 3. The D_{eff} coefficient showed a significant increase with an increase in temperature from 4.12×10^{-12} to 24.716×10^{-12} m^2/s. The result of this study are consistent with the reported studies, which lay within the general range of 10^{-9} to 10^{-12} m/s for food materials [13,22,32,33]. Different drying methods have been studied to investigate the change in the effective moisture diffusivity process for drying of different products. However, different drying methods, either using a thermal convection oven or a hot air dryer, also indicated an increase

Table 2. Values of the mathematical coefficients of different models for all drying temperatures

Temperature (°C)	Model	Coefficients	Statistical estimated results		
			R^2	*RMSE*	χ^2
40	Page	k = 0.0246 n = 0.9203	0.9976	9.6800×10^{-5}	5.9261×10^{-5}
50		k = 0.0542 n = 0.8648	0.9931	3.4273×10^{-4}	0.0021
60		k = 0.1529 n = 0.7402	0.9906	2.8484×10^{-4}	0.0034
70		k = 0.1300 n = 0.9001	0.9900	6.5370×10^{-4}	0.0046
80		k = 0.200 n = 0.8000	0.9904	7.6275×10^{-4}	0.0040
40	Modified Page	k = 0.1566 n = 0.1100	0.9949	2.0200×10^{-4}	0.0013
50		k = 0.3744 n = 0.1000	0.9963	1.8500×10^{-4}	0.0012
60		k = 0.3100 n = 0.3000	0.9680	7.6200×10^{-4}	0.0134
70		k = 0.400 n = 0.3020	0.9936	4.1677×10^{-4}	0.0068
80		k = 0.200 n = 0.8030	0.9885	9.1800×10^{-4}	0.0029
40	Lewis	k = 0.0180	0.9952	1.8919×10^{-5}	0.0012
50		k = 0.0400	0.9890	5.4912×10^{-4}	0.0037
60		k = 0.1200	0.9318	0.0032	0.0328
70		k = 0.1200	0.9936	4.1677×10^{-4}	0.0029
80		k = 0.1850	0.9887	8.9942×10^{-4}	0.0047
40	Henderson-Pabis	k = 0.0273 a = 1.1103	0.9187	0.0521	0.0333
50		k = 1.1046 a = 0.0605	0.9000	0.0632	0.0520
60		k = 1.0660 a = 0.0600	0.9307	0.0683	0.0301
70		k = 0.1000 a = 1.0200	0.9844	0.0010	0.0066
80		k = 0.2250 a = 1.3741	0.9000	0.1463	0.0614
40	Weibull	a = 0.0020 b = 0.1549	0.9104	0.0036	0.0200
50		a = 0.1353 b = 2.5063	0.8999	0.0045	0.0418
60		a = 0.2110 b = 2.500	0.9724	0.0013	0.0500
70		a = 0.2112 b = 1.5365	0.9860	9.1183×10^{-4}	0.0069
80		a = 0.3000 b = 1.700	0.9880	9.5623×10^{-4}	0.0049
40	Two Term	a = 0.6692 k_1 = 0.0237	0.9094	0.0667	0.0397
50		b = 0.6892 k_2 = 0.0237	0.9000	0.0041	0.0232
60		a = 0.4867 k_1 = 0.3343	0.9441	0.0030	0.0281
70		b = 0.6001 k_2 = 0.0189	0.9815	0.0012	0.0077
80		a = 0.5000 k_1 = 0.3500	0.9223	0.0054	0.0238
		b = 0.54 k_2 = 0.0665			
		a = 0.5000 k_1 = 0.200			
		b = 0.54 k_2 = 0.0665			
		a = 0.5000 k_1 = 0.4500			
		b = 0.54 k_2 = 0.0665			

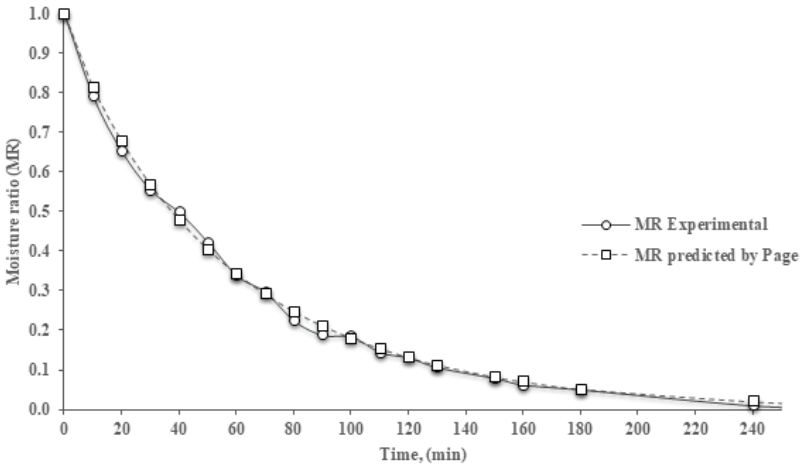

Figure 4. Experimental and theoretical moisture ratio of C. caudatus predicted by the Page model (40 °C).

Table 3. Values of D_{eff} at different drying temperatures

Temperature °C	Slope (k_o)	$D_{eff}\times10^{-12}$ m^2/s	R^2
40	-0.0003	4.1194	0.9885
50	-0.0006	8.2380	0.9906
60	-0.0007	9.6110	0.9212
70	-0.0012	16.4780	0.9013
80	-0.0018	24.7160	0.9567

in the D_{eff} coefficient when the temperature was increased [13,15,22]. This is most likely because high temperature increases heat absorption in a material that increases mass transfer and drying speed [26,28]. Hence, it can be seen that the D_{eff} coefficient highly depends on the increase in the drying temperature.

Activation energy

The activation energy (E_a) represents the minimum energy required to start the removal of moisture from a material. To investigate the activation energy for drying *C. caudatus* with respect to the drying temperature, the Arrhenius equation was used to plot the exponential regression graph of ln D_{eff} against $1/T$ [13]. Based on the exponential regression plot as shown in Figure 5, the activation energy of drying *C. caudatus* was determined at 39.35 kJ/mol by thermal convection oven dryer. According to the literature review, more than 90% of the activation energy to dry a food product falls within the range between 14.42 and 43.26 kJ/mol [13,15]. The activation energy obtained in this study is also comparable to previous studies on food products such as lemongrass (38.35 kJ/mol) [13], basil (33.21 kJ/mol) [23], quinces (38.29 kJ/mol) [27], kiwifruits (34.34 to 38.07 kJ/mol) [30] and *Andrographis paniculata* (33.4 kJ/mol) [24]. Nonetheless, the difference may be due to the drying methods, materials and operating conditions during the drying process [13,21].

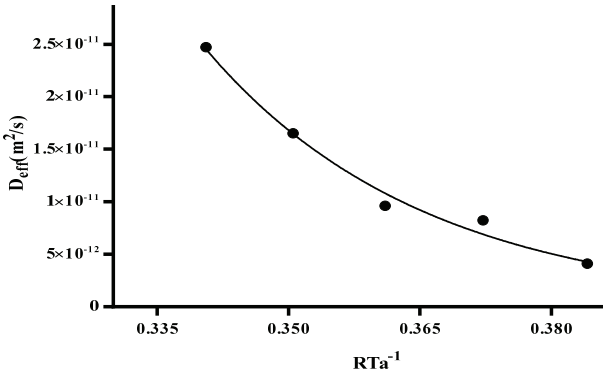

Figure 5. The relationship between change of D_{eff} and RTa^{-1} based on the Arrhenius's model (E_a =39.35 kJ/mol); $y = 2E\text{-}05e^{-39.35x}$, $R^2 = 0.9756$.

CONCLUSION

The semi-theoretical Page model was shown to be the best-fitting model for predicting the drying kinetic behavior of *C. caudatus* using a thermal convection oven. The effective moisture diffusion coefficients of the dried *C. caudatus* increased with increasing of drying temperature from 4.12×10^{-12} to 24.72×10^{-12} m^2/s and the activation energy was calculated at 39.35 kJ/mol. This study highly recommends further investigation be conducted into the physiochemical properties of *C. caudatus* and the optimisation process of drying *C. caudatus* using the selected thin-layer drying model as a benchmark. This is to improve performance and quality control of drying *C. caudatus* in terms of cost, energy and time.

Acknowledgements

The authors are grateful for the financial support received from the Malaysian Ministry of Higher Education (MOHE). Acknowledgement is also made of the excellent support of the staff of the UTM Innovation Centre in Agritechnology for Advanced Bioprocessing, especially Ms. Khairunnisa Embi for her technical assistance.

REFERENCES

[1] S. Moshawih, M.S. Cheeme, Z. Ahmad, Z.A. Zakaria, M.N. Hakim, Int. Res. J. Educ. Sci. 1 (2017) 12-31

[2] S.H. Cheng, M.Y. Barakatun-Nisak, J. Anthony, A. Ismail, J. Res. Med. Sci. (2015) 1000-1006

[3] E.W.C. Chan, S.K. Wong, H.T. Chan, J. Nat. Rem. 16 (2017) 137-147

[4] H.A. Rahman, S. Nazamid, F. Abas, A. Ismail, M.W. Muhammad, A.A. Hamid, Int. J. Food Prop. 20 (2017) 2616-2629

[5] A. Mediani, F. Abas, A. Khatib, C.P. Tan, Molecules. 18 (2013) 10452-10464

[6] A. Mediani, F. Abas, C. Tan, A. Khatib, Antioxidants 3 (2014) 358-370

[7] M.M.A. Sharifuldin, Z. Ismail, A.F.A. Aisha, E.K. Seow, H.K. Beh, Qual. Assur. Saf. Crop. Foods. 8 (2016) 617--622

[8] S.H. Cheng, A. Ismail, J. Anthony, O.C. Ng, A.A. Hamid, M.Y. Barakatun-Nisak, J. Evidence-Based Complementary Altern. Med. (2015) 1-7

[9] H. Li, L. Xie, Y. Ma, M. Zhang, Y. Zhao, X. Zhao, LWT - Food Sci. Technol. 101 (2019) 630-638

[10] K.Y. Pin, T.G. Chuah, A.A. Rashih, C.L. Law, M.A. Rasadah, T.S.Y. Choong, Dry Technol. 27 (2009) 149-155

[11] J. Chen Z. Ying, F. Sheng, M. Yuecheng, K. Xin, X. Xuejiao, Z. Xiaobo, Adv. J. Food Sci. Technol. 5 (2013) 1214-1219

[12] H. Darvishi, A.R. Asl, A. Asghari, M. Azadbakht, G. Najafi, J. Khodaei, J. Saudi Soc. Agric. Sci. 13 (2014) 130-138

[13] T.V.L. Nguyen, M.D. Nguyen, D.C. Nguyen, L.G. Bach, T.D. Lam, Processes 7 (2019) 2-11

[14] A.K. Babu, G. Kumaresan, V.A. Aroul, R. Velraj, Renew. Sustain. Energy Rev. 90 (2018) 536-556

[15] N.H.A. Tajudin, S.M. Tasirin, W.L. Ang, M.I. Rosli, L.C. Lim, Food Bioprod. Process. 118 (2019) 40-49

[16] D.I. Onwude, N. Hashim, R.B. Janius, N.M. Nawi, K. Abdan, Compr. Rev. Food Sci. Food Saf. 15 (2016) 599--618

[17] U.E. Inyang, I.O. Oboh, B.R. Etuk, Adv. Chem. Eng. Sci. 8 (2018) 27-48

[18] A. Benseddik, A. Azzi, M.N. Zidoune, K. Allaf, Eng. Agric. Environ. Food. 11 (2018) 220-231

[19] H. Kucuk, A. Midilli, A. Kilic, I. Dincer, Dry Technol. 32 (2014) 757-773

[20] P.C. Panchariya, D. Popovic, L. Sharma, J. Food Engr. 52 (2002) 349-57

[21] A.K. Karthikeyan, S. Murugavelh, Renew. Energy 128 (2018) 305-312

[22] O.R. Alara, N.H. Abdurahman, O.A. Olalere, J. Saudi Soc. Agric. Sci. 18 (2019) 309-315

[23] O. Bensebia, K. Allia, J. Essent. Oil-Bear. Plants. 18 (2015) 99-111

[24] D.M. Kadam, R.K. Goyal, M.K. Gupta, J. Med. Plant. Res. 5 (2011) 4721-4730

[25] Y.Y. Hee, G.H. Chong, Int. Food Res. J. 22 (2015) 393--397

[26] N. Karakaplan, E. Goz, E. Tosun, and M. Yuceer, J. Food Process. Preserv. 43 (2019) 1-10

[27] A. Maskan, S. Kaya, M. Maskan, J. Food Eng. 54 (2002) 81-88

[28] D.P.M. Dimitrios A. Tzempelikos, Alexandros P. Vourus, Archilleas V. Bardaks, Andronikos E. Filios, J. Med. Plant. Res. 5 (2011) 4721-4730

[29] W.P. da Silva, C.M.D.P.S. e Silva, F.J.A. Gama, J.P. Gomes, J. Saudi Soc. Agric. Sci. 13 (2014) 67-74

[30] I. Doymaz, Int. J. Food Prop. 13 (2010) 486-497

[31] A. Mohammadi, S. Rafiee, A. Keyhani, Am.-Eurasian J. Agric. Environ. Sci. 3 (2008) 802-805

[32] S. Darıcı, S. Şen, Heat Mass Transf. 51 (2015)1167-1176

[33] M. Younis, D. Abdelkarim, A. Zein El-Abdein, Saudi J. Biol. Sci. 25 (2018) 332-338.

NORLIZA ABDUL LATIFF[1,3]
LUQMAN CHUAH ABDULLAH[1]
PEI YING ONG[3]
NOR AMAIZA MOHD AMIN[2]

[1]Department of Chemical and Environmental Engineering, Faculty of Engineering, Universiti Putra Malaysia, Serdang, Selangor, Malaysia
[2]Department of Process and Food Engineering, Faculty of Engineering, Universiti Putra Malaysia, Serdang, Selangor, Malaysia
[3]Innovation Centre in Agritechnology, Universiti Teknologi Malaysia, Muar, Johor, Malaysia

NAUČNI RAD

MODEL SUŠENJA LIŠĆA *Cosmos caudatus* U TANKOM SLOJU

Kinetički modeli sušenja i energetske karakteristike dobro su poznati kao alati za procenu i predviđanje najprikladnijih fizičkohemijskih uslova sušenja za određeni proizvod. U ovom radu, razvijen je model sušenja u tankom sloju koji najbolje opisuje kinetičko ponašanje sušenja Cosmos caudatus. Eksperimenti sušenja su izvedeni pomoću termokonvekcione peći, a lišće C. caudatus sušeni je na pet različitih temperatura (40, 50, 60, 70, 80 °C). Šest različitih modela sušenja u tankom sloju (Pejdžov, modifikovani Pejdžov, Levisov, Henderson-Pabisov, dvočlani i Vajbulov) su analizirani radi izbor najboljeg modela sušenja u odnosu na slaganje sa eksperimentalnim podacima o vlagi. Utvrđeno da je Pejdžov model najbolje opisuje kinetiku sušenja lišća C. caudatus u tankom sloju sa koeficijentom detreminacije 99,76%, redukovanim hi-kvadratom $5{,}93\times10^{-5}$ i korenom srednje kvadratne greške $9{,}68\times10^{-5}$. Prosečni efektivni koeficijent difuzije vlage za temperaturu od 40 do 80 °C kretao se od $4{,}12\times10^{-12}$ do $24{,}71\times10^{-12}$ m^2/s, dok je vrednost energije aktivacije bila na 39,35 kJ/mol na osnovu Arenijusove jednačine.

Ključne reči: model sušenja u tankom sloju, Cosmos caudatus, efektivna difuznost vlage, energija aktivacije, termokonvekciona peć.